ARTERIAL FLUID MECHANICS AND ENHANCED PERMEABILITY IN THE NORMAL RABBIT AORTA

by

ABDUL I. BARAKAT

B.S., Nuclear Engineering
North Carolina State University
(1985)

M.S., Nuclear Engineering
Massachusetts Institute of Technology (1988)

Submitted to the Department of Nuclear Engineering
in partial fulfillment of the requirements for the degree of

DOCTOR OF PHILOSOPHY

at the

MASSACHUSETTS INSTITUTE OF TECHNOLOGY

February 1994

Signature of Author _____
Department of Nuclear Engineering
February 15, 1993

Certified by _____
Clark K. Colton
Thesis Supervisor

Certified by _____
Gordon L. Brownell
Thesis Reader

Accepted by _____
Allan F. Henry
Chairman, Committee for Graduate Students
Science

ARTERIAL FLUID MECHANICS AND ENHANCED PERMEABILITY IN THE NORMAL RABBIT AORTA

by

ABDUL I. BARAKAT

Submitted to the Department of Nuclear Engineering
on February 15, 1994 in partial fulfillment of the requirements
for the Degree of Doctor of Philosophy in Biofluid Dynamics

ABSTRACT

The focal nature of early atherosclerotic lesions has motivated the notion of the importance of localizing factors, most notably the detailed flow field within the affected vessel. Despite extensive study, very few generalizations regarding the potential role of hemodynamics in atherogenesis can be made at the present time. The focus of this work has been on investigating possible relationships between the distribution of focal sites of enhanced macromolecular permeability in the normal rabbit aorta and the detailed flow field within the aorta,

A quantitative topographical mapping of the distribution of the enhanced permeability sites revealed that their highest density occurs in the aortic arch, decreases as one proceeds distally reaching a minimum in the intercostal artery region, and then increases again in the abdominal aorta. The sites occur in streaks, and their density is high in the vicinity of aortic ostia. The distribution of site density around ostia generally resembles that of early atherosclerotic lesions experimentally induced in hypercholesterolemic rabbits.

The flow field in the rabbit aorta was studied in excised natural aortas made transparent to allow flow visualization. Steady and pulsatile flow were studied in the aortic arch, while the experiments in the abdominal aorta were confined to steady flow. The flow visualization results revealed the existence of a zone of clockwise helical flow along the ventral wall of the aortic arch. In the abdominal aorta, a pair of slowly-moving recirculation zones was observed lateral to most ostia. The flow field is generally complex with regions of boundary layer separation and flow recirculation. Vessels in close anatomic proximity interact fluid mechanically leading to considerably more complex flow behavior. No generalizations can be made regarding wall shear stresses proximal and distal to aortic ostia due to frequent skewness of aortic velocity profiles. The enhanced permeability site topography around the major branches of the abdominal aorta does not correlate with any specific features of steady flow shear stress distribution.

The velocity profiles in the rabbit abdominal aorta between the celiac and superior mesenteric arteries were measured *in vivo* using high resolution pulsed Doppler ultrasound velocimetry. A 15 MHz system with associated probes was used. Each probe was equipped with two ultrasonic transducers, and the information from both transducers could be combined to yield both the axial and transverse components of the velocity vector within the measurement volume. The results revealed large transverse velocity components in the aorta suggesting the presence of extensive secondary flow motion. The measured velocity profiles are consistent with the presence of multiple zones of helical flow motion within the aortic cross-section.

Two-dimensional steady and sinusoidal pulsatile flow numerical simulations were performed in a model of an idealized arterial branching. The purpose of this study was to elucidate fundamental fluid mechanical differences between steady and pulsatile flow. Steady flow recirculation zones periodically appear and disappear with pulsatility. Moreover, additional recirculation zones not present in steady flow are observed in pulsatile flow. Pulsatile flow wall shear stresses may be significantly larger or smaller than their steady flow counterparts depending on the specific portion of the cardiac cycle. Finally, the steady flow generalization that wall shear stresses within recirculation zones are always low cannot be made in pulsatile flow.

Thesis Supervisor: Clark K. Colton
Professor of Chemical Engineering

ACKNOWLEDGMENTS

I would like to thank my thesis supervisor, Professor Clark Colton, for his guidance and support throughout the course of this thesis. I admire his attention to detail and appreciate his emphasis on quality and his willingness to come in for discussions at any hour of the day. I believe that both Clark and I are "night persons" and that we have developed some of our most productive ideas between midnight and 2 a.m. I also appreciate Clark's willingness to allow me to explore any ideas I had regardless of how crazy they seemed.

I would also like to thank Professors Ken Smith and Gordon Brownell for serving on my thesis committee and providing me with useful suggestions along the way. I believe I have learned considerably from Ken's fluid mechanical insight.

I would like to thank Dr. Takeshi Karino for giving me the opportunity to work in his laboratory at the Montreal General Hospital. I would also like to thank Shunsuke Endo and Hiroshi Abe for surgical expertise and for their friendship and kindness during my stay in Montreal.

I would like to thank Dr. Pierre Peronneau for giving me the opportunity to work in his laboratory at the Broussais Hospital in Paris. Special thanks to Jean-Paul Guglielmi, Alain Barbet, and Philippe Delouche for their help in the design and fabrication of the Doppler probes. Thanks also to my French friends: Dominique, Marie-Claire, Nathalie, Francoise, and Alain Herment.

I have spent 29% of my life to date at MIT. I will leave with many memories that I will cherish for the rest of my life. There are more people to acknowledge than I will ever to manage to fit into this limited section, but here it goes anyway:

Thanks to Kin Cheung and Tze Poon for great friendship back during the early Bldg. 12 days. Kin, I appreciate the fact that you stay in touch. By the way, I have not been canoeing since "The Incident." Scarred for life, I guess!!

Thanks to Dan Morin for great friendship and many, many, many basketball games. If Dan ever cuts down on his trash-talking and works on his outside shot, he may have a chance in our one-on-one games.

Thanks to Hojoon Park for being an all-around great guy.

Thanks to Mustapha Khemira for the many "Campus House of Pizza" dinners and associated discussions.

Thanks to Bill Olson for all the REM tapes (Sorry, I cannot get into O^+ despite your attempts) and to Keith Dionne for his "can-do" attitude.

Thanks to Nelson Lin for giving me the satisfaction of having won the '80s (I'm planning a comeback in the '90s).

Thanks to the GBA (Greek Basketball Association) for many enjoyable games and for playing zone all the time.

Thanks to the old Friday evening basketball gang (not including labbies who will be acknowledged separately): L^2, Xinjin Zhao, Luhong Bo, Joy "The Infidel" Mendoza, Hiroshi Saito, David Chang, and Marc Moran.

Thanks to current (and a few ex-) labbies: Stat-Man Avgoustiniatos for B-Ball, Fresco's, backgammon, etc.; Suju Karoor for her willingness to help at all time and for many Indian dishes, desserts, candy, etc.; Brian "Corn" Laffey for PICKS on the court and for remembering all the SNL lines; Rabbit-Mate Susan Lessner for all the discussions we have had; for Bobby Padera (although he is a Bulls' fan) for basketball insight and Celtics' tickets; for Mike Pomianek for his willingness to help and his sense of humor; for Zhiguo Su for his kindness; and for Haiyan Wu for Tetris lessons.

Thanks to Costas Patrickios (TOG) for being such a great friend at all time. I am sure we will always stay in touch.

Thanks to Edna Yamasaki for her kindness and for the Brazilian chocolates.

I have saved this last paragraph for the people most dear to me. Claire Pellot has truly brightened my life and has supported me constantly. My two sisters, Suzy and Hala (and their husbands), have been there from day one. With the passing of every day, I realize more and more how truly important they are to me and how lucky I am to have siblings like them. Finally, none of this could have been possible without mom and dad. They have been there every step of the way and have always given their full love and support. My parents have dedicated their entire lives to their children; I love them dearly, and I dedicate this thesis to them.

TABLE OF CONTENTS

Title Page 1

Abstract 2

Acknowledgments 4

Table of Contents 6

List of Figures 11

List of Tables 19

1. Introduction and Motivation 20

1.1 Introduction 20

1.1.1 Atherosclerosis: Definition and Characteristics 20

1.1.2 Lipid Hypothesis 22

1.1.3 Response to Injury Hypothesis 23

1.2 Hemodynamics and Atherogenesis: Background 24

1.2.1 General Considerations 24

1.2.2 Pathological Observations 25

1.2.3 Endothelial Cell Response to Flow 26

1.2.4 In Vitro Studies of Physiological Flow Fields 27

1.2.5 In Vivo Measurements 28

1.2.6 Numerical Simulations 29

1.3 Focal Phenomena in Rabbits 30

1.4 Thesis Objectives and Scope 31

1.5 References 36

2. Topographical Mapping of Sites of Enhanced HRP Permeability in the Normal Rabbit Aorta 44

2.1 Introduction 44

2.2 Materials and Methods 45

2.2.1 Animal Experiments 45

2.2.2 Longitudinal Opening of Aorta 47

2.2.3 HRP Processing 48

2.2.4 HRP Spot Localization 49

2.3 Results 51

2.3.1 Size Distribution of HRP Spots 51

2.3.2 En Face Spatial Distribution of HRP Spots 51

2.3.3 Spatial Distribution of HRP Spots Around Ostia 53

2.3.3.1 Abdominal Region 54

2.3.3.2 Intercostal Region 56

2.3.3.3 Aortic Arch Region 57

2.4 Discussion 57

2.5 References 61

3. Measurement of Flowrates Through Aortic Branches in the Rabbit *In Vivo* 82

3.1 Introduction 82

3.1.1 Background 82

3.1.2 Rabbit Aortic Anatomy 84

3.2 Materials and Methods 85

3.2.1 Flowrate Measurement System 85

3.2.2 Animal Experiments 86

3.2.2.1 Animal Preparation 86

3.2.2.2 Surgical Procedures 86

3.2.2.3 Flowrate Measurements 88

3.3 Results 90

3.3.1 Blood Pressure and Heart Rate 90

3.3.2 Variation of Aortic Flowrate with Time 91

3.3.3 Mean Flow Splits 91

3.3.4 Pulsatile Flowrate Profiles 92

3.3.5 Peak Pulsatile Flow Splits 93

3.3.6 Peak Pulsatile to Mean Flowrate Ratios 93

3.4 Discussion 94

3.5 References 98

4. Detailed Flow Patterns in the Transparent Rabbit Aorta 110

4.1 Introduction 110

4.1.1 Background and Motivation 110

4.1.2 Rabbit Aortic Anatomy 111

4.2 Materials and Methods 112

4.2.1 Preparation of Transparent Aorta 112

4.2.2 Experimental Procedure and Data Analysis 114

4.3 Results 116

4.3.1 Aortic Arch 116

4.3.1.1 Steady Flow 116

4.3.1.2 Pulsatile Flow 119

4.3.2 Abdominal Aorta 122

4.3.2.1 Celiac Artery 122

4.3.2.2 Superior Mesenteric Artery 125

4.3.2.3 Right and Left Renal Arteries 128

4.4 Discussion 131

4.4.1 Aortic Arch 131

4.4.2 Abdominal Aorta 134

4.5 References 139

5. Simulation of the Two-Dimensional Steady and Pulsatile Flow Field in a Model Arterial Branching 172

5.1 Introduction 172

5.2 Numerical Model and Solution Procedure 174

5.3 Results 177

5.3.1 Steady Flow Simulations 177

5.3.2 Pulsatile Flow Simulations 181

5.4 Discussion 185

5.5 References 191

6. *In Vivo* Velocity Profiles in the Rabbit Abdominal Aorta 232

6.1 Introduction 232

6.2 Materials and Methods 235

6.2.1 Flow Rate Measurement System 235

6.2.2 Animal Experiments 237

6.2.2.1 Animal Preparation 237

6.2.2.2 Surgical Procedures 238

6.2.2.3 Velocity Profile Measurements 238

6.3 Results 240

6.3.1 Straight Tube Velocity Profiles 240

6.3.2 Abdominal Aorta Velocity Profiles 242

6.4 Discussion 247

6.5 References 252

7. Conclusions and Recommendations for Future Work 274

7.1 Conclusions 274

7.2 Recommendations for Future Work 277

LIST OF FIGURES

Figure 2.1 (A) Anatomy of a typical rabbit aorta illustrating the major branches. (B) Pattern of cuts used to longitudinally open aorta after branches have been cut flush with adventitial surface. (C) Aorta pinned flat, illustrating typical relative positions of major branches.

Figure 2.2 Size distribution of enhanced HRP permeability sites (pooled data from eight rabbits). An equivalent circular diameter was calculated from the area of each HRP spot.

Figure 2.3 *En face* spatial distribution of enhanced HRP permeability sites in aortas of rabbits 1-4 as reconstructed by image analysis. Each dot on the aorta represents an actual HRP spot. At the right of each aorta is plotted the spot density in the five regions into which each aorta was divided: (1) arch, (2) upper descending thoracic, (3) middle descending thoracic, (4) lower descending thoracic (intercostal region), and (5) abdominal. The average spot density over the enire aorta is tabulated at the bottom of each aorta. The extent of xerographic/photographic reduction of the aortic image varies from rabbit to rabbit.

Figure 2.4 *En face* spatial distribution of enhanced HRP permeability sites in aortas of rabbits 5-8 as reconstructed by image analysis. See caption for Figure 2.3 for further details.

Figure 2.5 *En face* spatial distribution of enhanced HRP permeability sites in portions of abdominal aortas of rabbits 4 and 5. Three regions of HRP streaks are observed: (1) proximal to the celiac ostium along the anatomical right lateral wall of the aorta; (2) proximal to the celiac ostium along the anatomical left lateral wall of the aorta; and (3) between the celiac and superior mesenteric ostia spanning the anatomical ventral and left lateral walls of the aorta. Streak numbers on figure correspond to these regions.

Figure 2.6 Representative polar coordinate system around ostia. The center of the coordinate system is the center of gravity of the ostium under consideration. The angle θ is measured in the clockwise direction. $\theta=0^{o}$ is proximal; $\theta=180^{o}$ is distal; $\theta=90^{o}$ is anatomical right for a ventral ostium, anatomical left for a dorsal ostium, dorsal for a lateral ostium on the right side, and ventral for a lateral ostium on the left side; $\theta=270^{o}$ is anatomically opposite to 90^{o}. The two dashed lines divide the domain into four 90^{o} quadrants centered about $\theta=0^{o}$, 90^{o}, 180^{o}, and 270^{o}. Spot patterns are plotted as aorta is viewed *en face* and lateral orientations shown here are anatomically correct for the case of a vessel on the ventral surface or on the right side. The coordinate

axes are marked off by tick marks in 1 mm increments, and each axis goes out to a maximum of 6 mm. The coordinate "d" denotes the distance from the ostium edge along the major axis of the ellipse, and the circles represent equally spaced increments along coordinate d.

Figure 2.7 *En face* spatial distribution of HRP spots around abdominal ostia (pooled data from eight rabbits). Region of "No Data" denotes end of aortic tissue at cut edge. Region labelled "Influenced by Sup. Mes." denotes region of probable HRP spot overlap between the superior mesenteric and right renal branches. Region labelled "Influenced by Ventral Streak" denotes region believed to be associated with streak between celiac and superior mesenteric ostia. The outline of each ostium represents an ellipse whosemajor and minor axes are determined by averaging the eight pairs of major and minor axes obtained by image analysis. Circles drawn around the ostiacorrespond to 1/2 mm increments in d, the distance from the ostium edge along the major axis of the elliptical ostium; therefore, the innermost circle corresponds to d=0.5 mm, the next circle to d=1.0 mm, the third to d=1.5 mm, and the outermost circle to d=2.0 mm.

Figure 2.8 Radial distribution of HRP spots around abdominal ostia as a function of the distance from ostium edge d (pooled data from eight rabbits). Regions labelled "Incomplete Data" are associated with end of aortic tissue at cut edge. Region labelled "Part of Ventral Streak" refers to spots believed to be primarily associated with the streak seen *en face* in the region between the celiac and superior mesenteric ostia. Each data point represents all the data from eight rabbits in a single quadrant. The data points at d=0.5 mm correspond to all the spots between the periphery of the ostium and the first circle in Figure 2.7. The data points at d=1.0 mm correpsond to all of the spots between the first and second circles in Figure 2.7, and so forth.

Figure 2.9 Angular distribution of HRP spots around abdominal ostia for the region $0<d\leq 2$ mm (pooled data from eight rabbits). Also plotted is the distributionof length of experimentally-induced atherosclerotic lesions in rabbits [16,17].

Figure 2.10 *En face* spatial distribution of HRP spots around the superior mesenteric and right renal ostia in each of the eight rabbits studied. Both vessels and their corresponding HRP spots are shown on the same plot in their relative anatomical locations. Dashed contours represent actual shapes of ostia; solid contours represent ellipses used to approximate shapes of ostia.

Figure 2.11 *En face* spatial distribution of HRP spots around anatomically right and left intercostal ostia (pooled data from eight rabbits, eight pairs per rabbit). Innermost circle represents ostium. Additional circles correspond to d=0.5 and 1.0 mm.

Figure 2.12 Radial distribution of HRP spots around anatomically right and left intercostal ostia as a function of the distance from ostium edge d (pooled data from eight rabbits, eight pairs per rabbit). Each data point represents all the data from eight rabbits in a single quadrant. The data points at d=0.5 mm correspond to all the spots between the periphery of the ostium and the first circle in Figure 2.11. The data points at d=1.0 mm correpsond to all of the spots between the first and second circles in Figure 2.11.

Figure 2.13 Angular distribution of HRP spots around anatomically right and left intercostal ostia for the region $0<d\leq1$ mm (pooled data from eight rabbits, eight pairs per rabbit). Also plotted is the distribution of length of experimentally-induced atherosclerotic lesions in rabbits [17].

Figure 2.14 *En face* spatial distribution of HRP spots around aortic arch ostia (pooled data from seven rabbits). Exact location and size of ostia are unknown. Circles with radii of 4 mm around the brachiocephalic center of gravity and 3 mm around the left subclavian center of gravity are drawn to define the region of interest. Regions of "No Data" arise as a result of manner in which aortic arch is cut and pinned flat.

Figure 2.15 Angular distribution of HRP spots around aortic arch ostia (pooled data from seven rabbits). HRP spots within 4 mm of the center of gravity of the brachiocephalic artery and 3 mm of the center of gravity of the left subclavian are used to construct the figure. Regions of "Incomplete Data" are associated with regions of "No Data" in Figure 2.14.

Figure 3.1 Anatomy of a typical rabbit aorta illustrating the major aortic branches.

Figure 3.2 Mean blood pressure as a function of time from the beginning of surgery. Mean blood pressure in each animal was calculated as one-third of the maximum systolic value plus two-thirds of the minimum diastolic value; the result agreed with the time-mean blood pressure displayed by the pressure monitor. Data represent mean±standard deviation of measurements from the nine rabbits studied.

Figure 3.3 Heart rate as a function of time from the beginning of surgery. Data represent mean±standard deviation of measurements from the nine rabbits studied.

Figure 3.4 Typical pulsatile volumetric flowrate profiles in the ascending aorta, the isolated section of the abdominal aorta proximal to the iliac bifurcation, and each of the eight aortic branches studied.

Figure 4.1 Anatomical schematic of the rabbit aorta and its major branches.

Figure 4.2 Typical transparent aortic arch and branches.

Figure 4.3 Detailed steady flow patterns in the aortic arch. The different line weights give a sense of three-dimensionality: solid lines represent streamlines in, long dashed lines represent streamlines slightly above or below, and short dashed lines represent streamlines furthest from the common median plane. The central figure is a composite of the various streamline categories, while the surrounding panels depict a breakup of these categories. The trajectories of the individual streamline categories have been described in the text. Plane A-A' shows a view of the aortic cross-section illustrating the approximate origin of the various streamline categories.

Figure 4.4 Steady flow velocity profiles in the common median plane at selected locations of the aortic arch and its branches. Numbers on the aortic wall are wall shear stresses in dyne/cm^2, while numbers on the profiles at every plane are the maximum velocities in mm/sec in that plane. Negative values of shear stress denote flow in the direction opposite to that of the bulk flow.

Figure 4.5 Pulsatile flow velocity profiles in the common median plane at selected locations of the aortic arch and its branches at five equally-spaced time points within a single pulsatile cycle. t=0 corresponds to the beginning of the cycle. See caption for Figure 4.4 for further details.

Figure 4.6 Distal to proximal shear stress ratio at the brachiocephalic and left subclavian arteries as a function of time for one pulsatile cycle. The steady flow values are also indicated.

Figure 4.7 Pulsatile to steady flow shear stress ratio as a function of time for one pulsatile cycle at both the lesser and greater curvature of the aortic arch at selected locations. The straight unity lines indicate where the pulsatile and steady flow shear stresses are equal.

Figure 4.8 Typical transparent aorto-celiac junction. The curvature is sharper at the distal tip of the branch than at the proximal tip.

Figure 4.9 Detailed steady flow patterns in the vicinity of the celiac artery. See caption for Figure 4.3 for further details.

Figure 4.10 Steady flow velocity profiles in the common median plane at selected locations in the vicinity of the celiac artery. See caption for Figure 4.4 for further details.

Figure 4.11 Typical transparent aorto-superior mesenteric junction illustrating the close anatomical proximity to the right renal artery. The superior mesenteric and right renal arteries emerge from the aorta almost at right angles to one another; therefore, the portion of the right renal artery shown is the projection of the right renal artery in the plane of the superior mesenteric artery. The curvature is sharper at the distal tip of the branch than at the proximal tip.

Figure 4.12 Detailed steady flow patterns in the vicinity of the superior mesenteric artery. See caption for Figure 4.3 for further details.

Figure 4.13 Steady flow velocity profiles in the common median plane at selected locations in the vicinity of the superior mesenteric artery. See caption for Figure 4.4 for further details.

Figure 4.14 Typical transparent aorto-renal junction. The curvature is sharper at the distal tips of the branches than at the proximal tips.

Figure 4.15 Detailed steady flow patterns in the vicinity of the right and left renal arteries. See caption for Figure 4.3 for further details.

Figure 4.16 Steady flow velocity profiles in the common median plane at selected locations in the vicinity of the right and left renal arteries. See caption for Figure 4.4 for further details.

Figure 5.1 Flow field simulation geometry illustrating the division of the computational domain into 96 macro-elements and the imposed parabolic velocity profile boundary conditions.

Figure 5.2 Steady state flow field illustrating the two recirculation zones A and B.

Figure 5.3 Close-up view of steady state fluid streamlines in the immediate vicinity of the branching.

Figure 5.4 Steady state wall shear rate field in the horizontal section of the T-junction along the bottom wall (4a), top wall proximal to the branching (4b), and top wall distal to the branching (4c). Positive values denote forward flow along the bottom wall and

backward flow along the towall. Negative values denote backward flow along the bottom wall and forward flow along the top wall.

Figure 5.5 Steady state shear rate field in the vertical section of the T-junction along the left (5a) and right (5b) walls. Positive values denote forward flow along the left wall and backward flow along the right wall, while negative values denote backward flow along the left wall and forward flow along the right wall.

Figure 5.6 Close-up view of fluid streamlines in the immediate vicinity of the branching at 20 equally-spaced time intervals within the pulsatile cycle.

Figure 5.7 Time variation of shear rate at the proximal and distal corners of the branching during the course of the pulsatile cycle. Also shown are the constant values computed under steady flow conditions.

Figure 5.8 Time variation of the magnitude of the distal to proximal shear rate ratio during the course of the pulsatile cycle. Also shown is the constant value computed under steady flow conditions.

Figure 5.9 Magnitudes of the spatial shear rate and shear stress gradients in the immediate vicinity of the branching during the course of the pulsatile cycle.

Figure 5.10 Time variation of the global maximum shear rate within the horizontal section of the flow field during the course of the pulsatile cycle. Also shown is the constant value computed under steady flow conditions.

Figure 5.11 Time variation of the maximum shear rate along the bottom wall of the horizontal section of the T-junction during the course of the pulsatile cycle. Also shown is the constant value computed under steady flow conditions.

Figure 5.12 Time variation of the ratio of the shear rate within recirculation zone B in pulsatile flow to the constant value of this parameter in steady flow during the course of the pulsatile cycle.

Figure 6.1 Method of velocity measurement in two orthogonal midplanes of the aorta. Two probes (1 and 2), each equipped with two transducers, are used. Data from the two transducers are combined to yield both axial and transverse velocity components.

Figure 6.2 Probe 1 axial and transverse velocity profiles for steady, fully developed flow in a straignt polyethylene tube.

Figure 6.3 Probe 2 axial and transverse velocity profiles for steady, fully developed flow in a straignt polyethylene tube.

Figure 6.4 Position 1 (corresponding to probe 1) axial and transverse velocity profiles as a function of time during the course of a cardiac cycle in the rabbit abdominal aorta shortly distal to the celiac artery. "V" refers to the ventral wall of the aorta and "D" to the dorsal wall.

Figure 6.5 Position 2 (corresponding to probe 2) axial and transverse velocity profiles as a function of time during the course of a cardiac cycle in the rabbit abdominal aorta shortly distal to the celiac artery. "R" refers to the right lateral wall of the aorta and "L" to the left lateral wall.

Figure 6.6 Aortic cross-sections indicating directions of transverse velocities in the two orthogonal measurement midplanes at selected time points within the cardiac cycle shortly distal to the celiac artery. Also shown are helical flow patterns consistent with the measured transverse velocities.

Figure 6.7 Position 1 (corresponding to probe 1) axial and transverse velocity profiles as a function of time during the course of a cardiac cycle in the rabbit abdominal aorta midway between the celiac and superior mesenteric arteries. "V" refers to the ventral wall of the aorta and "D" to the dorsal wall.

Figure 6.8 Position 2 (corresponding to probe 2) axial and transverse velocity profiles as a function of time during the course of a cardiac cycle in the rabbit abdominal aorta midway between the celiac and superior mesenteric arteries. "R" refers to the right lateral wall of the aorta and "L" to the left lateral wall.

Figure 6.9 Aortic cross-sections indicating directions of transverse velocities in the two orthogonal measurement midplanes at selected time points within the cardiac cycle midway between the celiac and superior mesenteric arteries . Also shown are helical flow patterns consistent with the measured transverse velocities.

Figure 6.10 Position 1 (corresponding to probe 1) axial and transverse velocity profiles as a function of time during the course of a cardiac cycle in the rabbit abdominal aorta shortly proximal to the superior mesenteric artery. "V" refers to the ventral wall of the aorta and "D" to the dorsal wall.

Figure 6.11 Position 2 (corresponding to probe 2) axial and transverse velocity profiles as a function of time during the course of a cardiac cycle in the rabbit abdominal aorta shortly proximal to the

superior mesenteric artery. "R" refers to the right lateral wall of the aorta and "L" to the left lateral wall.

Figure 6.12 Aortic cross-sections indicating directions of transverse velocities in the two orthogonal measurement midplanes at selected time points within the cardiac cycle shortly proximal to the superior mesenteric artery. Also shown are helical flow patterns consistent with the measured transverse velocities.

Figure 6.13 Axial velocity shear stresses at the ventral, dorsal, right lateral, and left lateral aortic walls shortly distal to celiac artery as a function of time during the course of a cardiac cycle.

Figure 6.14 Axial velocity shear stresses at the ventral, dorsal, right lateral, and left lateral aortic walls midway between the celiac and superior mesenteric arteris as a function of time during the course of a cardiac cycle.

Figure 6.15 Axial velocity shear stresses at the ventral, dorsal, right lateral, and left lateral aortic walls shortly proximal to superior mesenteric artery as a function of time during the course of a cardiac cycle.

Figure 6.16 Axial and transverse velocity profiles in the superior mesenteric artery. Note that the axial velocity becomes negative during a portion of diastole indicating reverse flow from the branch into the aorta.

LIST OF TABLES

Table 4.1. Volumetric flowrate (ml/min) in the ascending thoracic aorta as a function of measurement number.

Table 4.2. Mean flow splits in the eight aortic branches, expressed as per cent of mean flowrate in the ascending thoracic aorta.

Table 4.3. Peak pulsatile flow splits in the eight aortic branches, expressed as per cent of mean flowrate in the ascending thoracic aorta.

Table 4.4. Ratio of peak pulsatile to mean flowrate in the aorta and eight aortic branches.

Chapter One

Introduction and Motivation

1.1 Introduction

1.1.1 Atherosclerosis: Definition and Characteristics

Atherosclerosis is an arterial disease characterized by the focal accumulation of a variety of complex lipids, proteins, carbohydrates, cellular components, and blood constituents within the arterial wall. The pathological complications of atherosclerosis, namely coronary heart disease and stroke, represent the leading cause of human death in the western world.

The arterial wall is structurally arranged in three layers. The innermost layer, the *tunica intima,* consists of the endothelium and a thin layer of collagen and elastin fibers. The endothelium is the monolayer of cells lining all blood vessels and is therefore in constant contact with flowing blood. The endothelium has a myriad of very complex functions, not all of which are well-understood at the present time. Two well-established functions of the endothelium, however, are the provision of a non-thrombogenic surface compatible with blood and the presentation of a selectively permeable membrane for substances which get transported from the bloodstream into the arterial wall. The selective nature of endothelial permeability is determined by the presence of tight junctions between endothelial cells (EC) as well as pinocytotic vesicles. Molecules as large as about 2 nm in diameter pass through endothelial junctions, but much larger molecules can be transported across the endothelium exclusively by pinocytotic vesicles [1]. The collagen and elastin fibers within the *intima* are central to determining the mechanical properties of the arterial wall.

The middle layer of the arterial wall, the *tunica media,* comprises a large portion of the wall and is generally composed of tight extracellular matrix interspersed with smooth muscle cells. The outermost layer, the *tunica adventitia,* consists primarily of collagen and elastin fibers which merge with secondary tissue.

The Working Group on Atherosclerosis of the National Heart, Lung, and Blood Institute in 1981 declared the fatty streak as the first pathological change in atherosclerosis. Although considerable debate exists over the validity of this definition, it represents a useful starting point. These fatty streaks contain both intracellular (foam cells) as well as extracellular lipids, especially in the *intima.* This leads to only a minor elevation of the normal intimal surface. An extensive study of the fatty streaks in individuals from nineteen different countries spanning a spectrum of racial, ethnic, and economic backgrounds has been performed [2]. This study established that the fatty streaks develop to virtually the same extent regardless of the population considered during the first two decades of life. The streaks found in the coronary arteries tend to be localized at the same sites where the more advanced fibrous atherosclerotic plaques are found upon examination of older individuals. In the aorta, on the other hand, the fatty streaks are found to be most prevalent in the proximal portion, while it is well-established that the fully-developed plaques tend to be more extensive in the abdominal region of the aorta. This suggests that fatty streaks develop into fibrous plaques only under certain conditions or that there are alternate channels for the development of the plaques other than through the fatty streaks.

The uncertainties associated with the progression of the disease present difficult problems in studies of its etiology and pathogenesis. What is certain about the early stages of atherosclerosis, however, is the existence of

particular sites of predilection for lesion formation within the vasculature [3]. In particular, the earliest lesions localize in regions of arterial branching and curvature. This focal nature of the disease has motivated the notion of the importance of localizing factors, including arterial hemodynamics and focal variations in arterial wall structure.

1.1.2 Lipid Hypothesis

The "lipid hypothesis" has dominated the vast majority of atherosclerosis research to date. This hypothesis, in its simplest form, attributes the disease to the inability of the arterial wall to fully metabolize the lipids transported into it from the bloodstream thereby resulting in the net accumulation of these lipids in the vessel wall. It has been stated that the hallmark of atherosclerosis is the accumulation of cholesterol in the arterial wall [2]. This cholesterol is derived virtually entirely from plasma, and it is transported by low density lipoprotein (LDL). The major mechanism of LDL cholesterol uptake by the cells of the arterial wall is *via* the LDL receptor pathway [4] in which LDL binds to the receptors on the plasma membrane, gets absorbed into the cells by endocytosis, and is then delivered to lysosomes where the proteins and cholesteryl esters are hydrolyzed and free cholesterol is released to be used by the cell. Once the cell has acquired the cholesterol it needs, the synthesis of LDL receptors is reduced thereby limiting cholesterol uptake by the arterial wall. This is accompanied by a decrease in the level of cholesterol synthesis in the blood. An abnormality in any of the steps of this entire process may lead to cholesterol accumulation within the wall.

In the initial stages of atherosclerosis, cholesteryl esters accumulate within foam cells, but as the lesions progress into the fibrous plaques, large amounts of extracellular cholesteryl esters are also found. Moreover, there is

an enhancement of unesterified extracellular cholesterol within the fibrous plaques [5]. Besides the accumulation of cholesterol, there are several other biochemical changes which take place in the atherosclerotic lesion. These include an increase in the synthesis and accumulation of phospholipids, an increase in fatty acid synthesis, an increase in glucose utilization, an increase in lactate production, an increase in collagen synthesis, and an increase in collagen content.

1.1.3 Response to Injury Hypothesis

The "response to injury" hypothesis was proposed by Ross and Glomset [6,7]. This hypothesis postulates that the first event of atherogenesis is caused by some focal injury to the endothelium. This injury could be induced by a number of factors of which hyperlipidemia and hemodynamics are examples. The injury results in EC desquamation which exposes some of the underlying connective arterial tissue. Platelets then adhere to the exposed EC and release a mitogen (platelet derived growth factor or PDGF) which stimulates the proliferation of the smooth muscle cells in the arterial wall. The loss of endothelial lining also greatly facilitates the transport of macromolecules from the bloodstream into the vessel wall. LDL itself has been shown to be mitogenic [6].

The "response to injury" hypothesis as described above considers the denudation of the endothelium as a prerequisite for atherogenesis. Experimental mechanical deendothelialization can in some cases result in the development of atherosclerotic plaques [8-16], and spontaneously-occurring EC loss, in the few instances in which it has been observed [17-20], has also been closely correlated with the sites at which plaques localize. However, in light of pathological evidence that the earliest stages of atherosclerosis occur

in the presence of an intact endothelium [21], the endothelial injury concept has evolved into an endothelial dysfunction postulate. This dysfunction may be caused by mechanical or biochemical mechanisms which alter cell function without causing any cell loss.

Morrel [1] has considered the following four mechanisms by which endothelial dysfunction can lead to the development of atherosclerosis: 1) enhanced arterial permeability, 2) increased production of growth factors by dysfunctional endothelium, 3) LDL alteration by dysfunctional endothelium, and 4) attraction of monocytes and macrophages to the site of plaque development. These four mechanisms may be caused and/or influenced by a number of physiological factors including arterial hemodynamics, EC turnover, changes in endothelial structure due to monocytes and macrophages, and many others.

1.2 Hemodynamics and Atherogenesis: Background

1.2.1 General Considerations

The notion of hemodynamic involvement in atherosclerosis is motivated by the focal nature of the disease. One problem is that, depending on the species investigated, early atherosclerotic lesions are observed at different sites within the vasculature, and these sites are generally expected to be exposed to radically different fluid mechanical conditions. This has led to conflicting explanations and contradictory hypotheses regarding the potential role of hemodynamics in atherogenesis.

The specific literature on early atherosclerotic lesion localization can be summed up in the following fashion [22]: In human fetuses, neonates, and infants [23] and in animal models in which the disease is experimentally induced [24-26], lesions localize generally distal to major aortic branches. On

the other hand, in the adult human [27-33] and in the White Carneau pigeon [34], a species which develops spontaneous atherosclerosis, the early lesions localize generally proximal to major branches.

A consistent hemodynamic theory must explain these differences in lesion localization within the various species. The difficulty in formulating such a theory stems from the tremendous complexity of arterial flow fields. Blood flow in arteries represents a fluid mechanical system involving the pulsatile flow of a non-Newtonian fluid within a compliant vessel having a very complex geometry. *In vitro* hemodynamic studies, despite their general accuracy, are always open to the question of how closely they simulate actual physiological conditions, while *in vivo* measurements, whether invasive or noninvasive, generally present access and resolution problems. Next, we briefly discuss the earliest hemodynamic theories of atherogenesis which were generally based on pathological evidence. Subsequently, we turn our attention to more recent work on the cellular response of the endothelium to flow as well as on more macroscopic aspects of physiological flow fields.

1.2.2 Pathological Observations

The earliest hemodynamic hypotheses concentrated on wall shear stress levels, and they were based primarily on pathological evidence of lesion localization in combination with fundamental assumptions on arterial flow fields. These assumptions had their basis in early fluid mechanical observations made on idealized models of arterial branching so that it was generally assumed that regions proximal to arterial branches experienced lower wall shear stresses than those distal. Hence, the inter-species differences in lesion localization around branches described above led to two contradictory hypotheses regarding the role of hemodynamics in

atherogenesis. The first implicated regions of high shear stress as the culprit in the localization of early lesions, and it was initially advanced by Fry [35] and supported by the pathological observations of several other investigators [34,36-38]. The second hypothesis implicated low shear stress regions and was introduced by Caro *et al.* [39,27]. Pathological evidence in general support of this hypothesis includes observations made in [31,34,40].

Although wall shear stress hypotheses have dominated the literature on the relationship of hemodynamics to atherogenesis, several other hemodynamic mechanisms have been postulated to play an important role. These include low arterial blood pressure [41], boundary layer separation [42], turbulence [43], arterial wall fatigue and consequent loss of tensile strength [44], and impedance mismatching [45].

1.2.3 Endothelial Cell Response to Flow

In the early studies above, the role of arterial fluid mechanics in the atherogenic process was generally defined in terms of a hemodynamic damage mechanism to the endothelium. However, the observation that the earliest stages of atherogenesis occur in the presence of an intact endothelium [21] has motivated fundamental studies aimed at elucidating EC response to fluid mechanical stresses. These studies have revealed that the endothelium is an active structure with sophisticated response mechanisms to stimuli and an extensive network of communication with both adjacent cells and subjacent smooth muscle cells. EC exhibit specific humoral, metabolic, and structural responses which vary with shear stress level. Examples of phenomena that respond to shear stress are production of interleukin-6 [46]; expression of endothelin [47]; rate of prostacyclin production, intracellular Ca^{2+} concentration, and microtubule realignment [48]; pinocytotic rate, cell

alignment in flow direction, and redistribution of microfilaments or stress fibers [49]; EC proliferation and DNA synthesis [50]; deendothelialization and cell detachment [35]; redistribution of focal adhesion sites [51]; and reorientation of extracellular fibronectin deposition [52]. These EC phenomena respond to mechanical stimuli over time scales ranging from seconds to days [53]. Although their direct applicability to physiological situations is uncertain, these observations suggest that mechanical forces can stimulate EC *in vivo.*

1.2.4 *In Vitro* Studies of Physiological Flow Fields

The very different and often contradictory fluid mechanical hypotheses that have been postulated have motivated detailed *in vitro* investigations of the flow field in models of arterial branching. The earliest studies were in idealized models which failed to account for many of the subtle geometric and hydrodynamic details that give rise to the tremendous complexity of arterial flow fields but which nevertheless provided important fundamental fluid mechanical insight into the effect of various parameters on the flow field. Examples of these studies are model stenosis and bifurcation investigations in which steady or pulsatile flow fields and resulting wall shear stress distributions as well as regions of boundary layer separation and flow recirculation were visualized at different flow Reynolds numbers and various vessel dimensions and branching angles [54-68].

The emergence of several studies emphasizing the importance of incorporating realistic geometric details into arterial flow model studies [69,70] has led to more recent investigations in glass models, vascular casts, or excised natural vessels. The emphasis of these studies has been on capturing true arterial geometry, physiological pulsatility, and even wall compliance, and they have revealed the existence of complex flow fields, especially in the

vicinity of arterial branches. For example, flow in models of the human abdominal aorta [71,72] demonstrated more complex flow patterns in the infrarenal than in the suprarenal section as well as time-varying helical vortex motions initiating at the renal arteries and propagating to the iliac bifurcation.

Pulsatile flow experiments in models of the carotid artery [73] have shown that the common carotid and distal internal carotid arteries undergo axial, unidirectional flow, while the region within the carotid sinus undergoes boundary layer separation, helical flow, and reverse flow. Finally, within coronary arteries, disturbed flow patterns have been observed along the outer walls of bifurcations, while the inner walls have been found to be generally exposed to unidirectional flow [74]. These studies have suggested that lesion development correlates with regions of low or oscillatory wall shear stress, boundary layer separation, and/or flow reversal.

1.2.5 *In Vivo* Measurements

A relatively small number of *in vivo* studies of the flow field and wall shear stresses have been reported in the literature. Noninvasive pulsed Doppler [75] and magnetic resonance [76] measurements of velocity profiles have been made in peripheral arteries; however, the level of detail that can be resolved remains limited at this point. There have been several studies with invasive pulsed Doppler ultrasound in dogs, and these studies have shed some light on the arterial velocity profiles *in vivo.* For example, Farthing and Peronneau [77] studied the velocity profiles at several locations in the aortic arch at various points within the cardiac cycle and estimated wall shear stresses. Hutchison *et al.* [78] studied the flow patterns in the dog abdominal aorta and reported regions of transient flow recirculation opposite the superior mesenteric and left renal arteries in the post-systolic phase of the cardiac

cycle. No recirculation was observed at peak systole although the velocity profiles were asymmetric. Bell *et al.* [79] examined the velocity profiles in the left circumflex and left anterior descending coronary arteries and consistently observed higher wall shear rates along the outer walls than along the inner walls. However, even with *in vivo* pulsed Doppler measurements, there is a large uncertainty in the immediate vicinity of the wall due to wall motion, and it is this region, unfortunately, that is of most interest from the standpoint of studies on atherogenesis. *In vivo* studies also suffer from limitations on spatial resolution which prevent the study of fluid mechanical interactions with the arterial wall at a microscopic level.

1.2.6 Numerical Simulations

In principle, numerical simulations of arterial fluid dynamics offer arbitrarily fine spatial and temporal resolution. The advent of finite element methods has led to unprecedented versatility in simulating complex geometries. Moreover, advances in algorithmic techniques and computer architecture have finally made the simulation of complex flow fields feasible, leading to an increase in numerical simulations of steady and pulsatile flow that attempt to shed light onto the details of arterial velocity fields. However, virtually all published simulations deal with oversimplified geometries, use idealized and often non-physiological boundary conditions, and rarely incorporate the effect of wall motion. Despite these limitations, the computational studies have provided useful insight into fundamental fluid mechanical phenomena by offering spatial and temporal resolutions that are far superior to any that could be accessed experimentally.

There are several examples in the literature of two-dimensional steady and pulsatile flow simulations in the aortic bifurcation [80,81] which produced

transient flow reversal in the daughter vessels. Thiriet *et al.* [82] simulated steady flow through a three-dimensional finite element model of the aortic bifurcation and demonstrated the existence of secondary helical motion within the daughter branches. Simulation of steady and pulsatile flow patterns in three-dimensional models of the carotid artery bifurcation yielded complex disturbed flow patterns in the carotid sinus [83,84]. Perktold *et al.* [85] modeled the three-dimensional unsteady flow in the left main coronary arteries and have reported secondary flow velocities of 3 to 4% of the maximum axial velocity.

One important advancement within the field of computational fluid dynamics within the last decade has been the emergence of fluid dynamic programs for performing sophisticated simulations. These programs, of which NEKTON and FIDAP are examples, are generally based on the finite element method and are in principle capable of solving any time-dependent, three-dimensional fluid dynamic problem in arbitrarily complex geometries. The emergence of powerful personal workstations has rendered previously prohibitively expensive numerical simulations possible. The numerical codes are also equipped with very powerful and robust pre- and post-processing packages capable of manipulating the output data and displaying it in very useful graphical format. Moreover, they can often be easily interfaced with powerful computer aided design capabilities for generating a wide range of visualization graphics. These may be very useful in understanding basic fluid flow phenomena as well as for examining the interactions of the fluid flow with the walls of the simulated flow domain.

1.3 Focal Phenomena in Rabbits

The hypercholesterolemic rabbit is a good model in which to study focal phenomena because it exhibits a relatively predictable pattern of early atherosclerotic fatty lesions [86-89]. Early lesions occur diffusely in the aortic arch and ascending aorta, in a streak in the upper descending thoracic aorta and along the ventral wall between the celiac and superior mesenteric arteries, and distal and lateral to branch orifices in the abdominal aorta and descending thoracic aorta. In addition, previous work in our laboratory has led to the discvery of other focal phenomena in the normal rabbit.

In the course of prior research on mechanisms governing the transport, accumulation, and metabolism of LDL and other proteins in the aorta of the normal New Zealand White (NZW) rabbit (and squirrel monkey), we have found punctate foci of greatly enhanced permeability to various proteins, including radiolabeled LDL, horseradish peroxidase (HRP), and biotinylated bovine serum albumin [90-94]. These sites also occur in the hypercholesterolemic rabbit [95]. After 1-min circulation of HRP, 10-min circulation of LDL, the enhanced permeability sites range from about 100 to 200 μm in diameter and each site of permeability dysfunction is associated with one or at most a few EC. About one-third of these sites are associated with abnormal, enlarged EC or possess other morphological features different from normal arterial tissue. Others have now replicated our findings concerning focal sites of increased LDL uptake [96,97]; focal elevation of LDL degradation in the same regions of normal rabbits has been reported [87]. Focal differences in EC shape have been observed over distances of 100 to 200 μm immediately distal to the aortic branches in the rabbit [98]. Focal sites of enhanced LDL permeability have also been observed in the rat [99].

1.4 Thesis Objectives and Scope

We hypothesize that the sites of these highly localized cellular phenomena are representative of the sites of the earliest atherosclerotic processes. The objectives of this work were to quantitatively establish the topography of these sites within the aorta, to compare the topography to that of early atherosclerotic lesions experimentally induced in hypercholesterolemic rabbits, and to probe whether the localization of these apparent cellular dysfunctions is associated with mechanical forces exerted by hemodynamic phenomena. The specific organization of the thesis is as follows:

Chapter Two is a quantitative topographical mapping study of the distribution of the enhanced permeability sites on the surface of the normal rabbit aorta using image analysis. The rabbit experiments and image analysis data acquisition were performed by Peter A.F. Uhthoff (formerly of our group). Peter and I collaborated on data analysis and interpretation. This study revealed reproducible aorta-wide trends in enhanced permeability site localization as well as preferred radial and angular distributions around individual aortic ostia. The existence of these preferred distributions is consistent with the notion of the importance of localizing phenomena, particularly hemodynamics. This motivated all the fluid mechanical studies described in subsequent chapters.

We decided to investigate the detailed flow field in the rabbit aorta using a technique developed by Karino and Motomiya [100] in which the natural aorta is excised from the animal and rendered transparent to allow flow visualization. Prior to performing this study, however, we needed information on the flow divisions in the rabbit aortic branches *in vivo,* i.e. the fractions of cardiac output within each of the major aortic branches. The detailed flow field within the aorta is expected to be sensitive to these flow divisions. Chapter Three describes a study of these flow divisions using transit-time ultrasound

flowmetry. The results revealed that the superior mesenteric and celiac arteries receive the bulk of aortic flow (about 55% combined), while each of the other branches receives significantly less flow (5 to 8% of the cardiac output). Another finding was the existence of reverse flow from some of the branches back into the aorta during a portion of diastole. This reverse flow, when present, would be expected to have important implications on the *in vivo* wall shear stress in the aorta in the immediate vicinity of the branches.

The flow division results of Chapter Three were then imposed on preparations of transparent rabbit aortas, and the details of the flow visualization results are described in Chapter Four. Both steady and pulsatile flow were studied in the aortic arch, while only steady flow was studied in the abdominal aorta. A zone of clockwise helical motion was observed along the ventral wall of the aortic arch both in steady and pulsatile flow. Flow separation was present at the inlets of the aortic arch branches, and helical flow was observed within the branches. Pulsatility led to periodic appearance and disappearance of the flow separation zones. Within the abdominal aorta, a pair of slowly-moving flow recirculation zones were observed lateral to all ostia. The flow field in the vicinity of the superior mesenteric and right renal arteries was very complex due to the anatomic proximity of these vessels to one another. A comparison of the steady flow wall shear stress distribution with the enhanced permeability site topography around branches revealed no apparent correlation.

The lack of apparent correlation between the steady flow visualization results of Chapter Four with the enhanced permeability site distribution motivated the numerical study detailed in Chapter Five. The computer code NEKTON was used to study the two-dimensional steady and sinusoidal pulsatile flow fields in a 90° T-junction representing an idealized model of an

arterial branching. The purpose of this study was to elucidate fundamental differences that may exist between steady and pulsatile flow. The results indicated that steady flow recirculation zones periodically appear and disappear with pulsatility. Additional recirculation zones not present in steady flow were observed in pulsatile flow. Depending on the specific time within the pulsatile cycle, the wall shear stress levels could be significantly larger or smaller than their steady flow counterparts. Unlike steady flow, shear stress levels within pulsatile recirculation zones were not necessarily low. The results therefore suggest important fundamental differences between steady and pulsatile flow behavior.

The importance of pulsatility and the questions that may be raised regarding how closely model studies approach the actual physiological conditions motivated the preliminary study described in Chapter Six. High resolution 15 MHz pulsed Doppler ultrasound velocimetry was used to establish the *in vivo* velocity profiles in the rabbit abdominal aorta between the celiac and superior mesenteric arteries. The uniqueness of the system used lies in the design of its perivascular probes each of which is equipped with two ultrasonic transducers. The information from the two transducers can be combined to yield both the axial and transverse components of the velocity vector [101] within the measurement volume.

Measurements were made in two orthogonal midplanes in the aorta. The axial velocities indicated the presence of forward flow in the aorta during the entire course of the pulsatile cycle. Large transverse velocity components were present suggesting extensive secondary flow motion. The measured velocity profiles are consistent with the presence of multiple zones of forward-moving helical flow within the aorta.

The fluid mechanical studies described in this thesis indicate that the flow field within the rabbit aorta is extremely complex. The steady flow results did not correlate with the localization of enhanced permeability sites in the aorta, while the spatial resolution of the *in vivo* measurements near the wall is not sufficiently high to allow meaningful comparison of velocity profiles with localized phenomena. Chapter Seven discusses the conclusions of this work as well as its contributions to the field and recommends directions for future investigations.

1.5 References

1. Morrel EM. Sites of enhanced ^{125}I-Low Density Lipoprotein permeability in the rabbit aorta *in vivo*. Ph.D. Thesis. MIT, 1987.

2. St. Clair RW. Pathogenesis of the atherosclerotic lesion: Current concepts of cellular and biochemical events. In *Recent Advances in Arterial Diseases: Atherosclerosis, Hypertension, and Vasopasm*, Alan R. Liss, Inc., New York, NY, pp.1-29, 1986.

3. Schwartz CJ, Mitchell JRA. Observation on localizations of arterial plaques. *Circ. Res.* **11:** 63, 1972.

4. Goldstein JL, Anderson RG, Brown MS. Receptor-mediated endocytosis and the cellular uptake of low density lipoprotein. Ciba Found. Symp. **92:** 77, 1982.

5. Small DM. Cellular mechanisms for lipid deposition in atherosclerosis. *N. Engl. J. Med.* **297:** 873, 1977.

6. Ross R, Glomset JA. The pathogenesis of atherosclerosis (first of two parts). *N. Engl. J. Med.* **295:** 369, 1976.

7. Ross R, Glomset JA. The pathogenesis of atherosclerosis (second of two parts). *N. Engl. J. Med.* **295:** 420, 1976.

8. Davignon J. The lipid hypothesis - pathophysiological basis. *Arch. Surg.* **113:** 28, 1978.

9. Spaet TH, Rhee C, Geiger C. Delayed consequences of endothelial removal from rabbit aorta. *Adv. Exp. Med. Biol.* **102:** 165, 1978.

10. Minick CR, Stemerman MB, Insull Jr. W. Role of endothelium and hypercholesterolemia in intimal thickening and lipid accumulation. *Am. J. Pathol.* **95:** 131, 1979.

11. Ross R, Harker L. Hyperlipidemia and atherosclerosis. Chronic hyperlipidemia initiates and maintains lesions by endothelial cell desquamation and lipid accumulation. *Science.* **193:** 1094, 1976.

12. Nam SC, Lee WM, Jarmolych J, Lee KT, Thomas WA. Rapid production of advanced atherosclerosis in swine by a combination of endothelial injury and cholesterol feeding. *Exp. Mol. Pathol.* **18:** 369, 1973.

13. Stemerman MB. Thrombogenesis of the rabbit arterial plaque. An electron microscope study. *Am. J. Pathol.* **73:** 7, 1973.

14. Bjorkerud S. Atherosclerosis iniated by mechanical trauma in normolipidemic rabbits. *J. Atherscler. Res.* **9:** 209, 1969.

15. Bjorkerud S, Bondjers G. Arterial repair and atherosclerosis after mechanical injury. Part I. Permeability and light microscope characteristics of endothelium in non-atherosclerotic and atherosclerotic lesions. *Atherosclerosis.* **13:** 355, 1971.

16. Bjorkerud S, Bondjers G. Arterial repair and atherosclerosis after mechanical injury. Part 5. Tissue response after induction of large superficial transverse injury. *Atherosclerosis.* **18:** 235, 1973.

17. Lewis JC, Kottke BA. Endothelial damage and thrombocyte adhesion in pigeon atherosclerosis. *Science.* **196:** 1007, 1977.

18. Gutstein WH, Farrell GA, Armellini C. Blood flow disturbance and endothelial cell injury in preatherosclerotic swine. *Lab. Invest.* **29:** 134, 1973.

19. Osborne-Pellegrin MJ, Weill D. "Spontaneous" endothelial injury in the rat caudal artery. *Exp. Mol. Pathol.* **39:** 61, 1983.

20. Fry DL. Hemodynamic forces in atherogenesis. In *Cerebrovascular Diseases*, Raven Press, New York, NY, pp.77-95, 1976.

21. Goode TS, Davies PF, Reidy MA, Bowyer DE. Aortic endothelial cell morphology observed in situ by scanning electron microscopy during atherogenesis in the rabbit. *Atherosclerosis.* **27:** 235, 1977.

22. Nerem RM, Levesque MJ. Fluid Mechanics in Atherosclerosis. *Handbook of Bioengineering.* Ch. 21, 1987.

23. Sinzinger H, Silberbauer K, Auerswald W. A quantitative investigation of sudanophilic lesions around the aortic ostia of human fetuses, newborns, and children. *Blood Vessels.* **17:** 44, 1980.

24. Cornhill JF, Roach MR. A quantitative study of the localization of atherosclerotic lesions in the rabbit aorta. *Atherosclerosis.* **23:** 489, 1976.

25. Flaherty JT, Ferrans VJ, Pierce JE, Carew TE, Fry DL. Localizing factors in experimental atherosclerosis. In *Atherosclerosis and Coronary Heart Disease.* Grune and Stratton, New York, NY, pp.40-83, 1972.

26. Schwenke DC, Carew TE. Quantification *in vivo* of increased LDL content and rate of LDL degradation in normal rabbit aorta occurring at sites susceptable to early atherosclerotic lesions. *Circulation Res.* **62:** 699, 1988.

27. Caro CG, Fitz-Gerald JM, Schroter RC. Atheroma and arterial wall shear: Observation, correlation and proposal of a shear dependent mass transfer mechanism for atherogenesis. *Proc. Roy. Soc. Lond. B.* **177:** 109, 1971.

28. Texon M. The role of vascular dynamics in the development of atherosclerosis. In *Atherosclerosis and its Origin.* Academic Press, New York, NY, 1963.

29. Mustard JF, Packham MA. Thrombosis and the development of atherosclerosis. In *The Pathogenesis of Atherosclerosis.* Williams and Wilkins, Baltimore, MD, 1972.

30. Mitchell JRA, Schwartz CJ. *Arterial Disease.* F.A. Davis Co., Philadelphia, PA, 1965.

31. Kjaernes MA, Svindland A, Walle L, Wille SO. Localization of early atherosclerotic lesions in the arterial bifurcation in humans. *Acta Path. Microbiol. Scand. A.* **89:** 35, 1981.

32. Svindland AD, Walloe L. Localization of early atherosclerotic lesions in carotid and coronary bifurcations: A refutation of the high shear hypothesis. In *Proc. on Fluid Dynamics as a Localizing Factor in Atherosclerosis.* Springer-Verlag, Heidelberg, 1987.

33. Friedman MH, Hutchins GM, Bargeron CB, Deters OJ, Mark FF. Correlation of human arterial morphology with hemodynamic measurements in arterial casts. *J. Biomech. Eng.* **103:** 204, 1981.

34. Cornhill JF, Levesque MJ, Nerem RM. Quantitative study of the localization of sudanophilic coeliac lesions in the white Carneau pigeon. *Atherosclerosis.* **35:** 103, 1980.

35. Fry DL. Acute vascular endothelial changes associated with increased blood velocity gradients. *Circ. Res.* **22:** 165, 1968.

36. Reidy MA, Bowyer DE. Scanning electron microscopy of arteries: The morphology of aortic endothelium in hemodynamically stressed areas associated with branches. *Atherosclerosis.* **26:** 181, 1977.

37. Bondjers G, Bjorkerud S. Cholesterol accumulation and content in regions with defined endothelial integrity in the normal rabbit aorta. *Athersclerosis.* **17:** 71, 1973.

38. Newman HAI, Zilversmit DB. Quantitative aspects of cholesterol flux in rabbit atheromatous lesions. *J. Biol. Chem.* **237:** 2078, 1962.

39. Caro CG, Fitz-Gerald JM, Schroter RC. Arterial wall shear and distribution of early atheroma in man. *Nature.* **223:** 1159, 1969.

40. Zarins CK, Giddens DP, Bharadvaj BK, Sottiurai VS, Mabon RF, Glagov S. Carotid bifurcation atherosclerosis: Quantitative correlation of plaque localization with flow velocity profiles and wall shear stress. *Circ. Res.* **53:** 502, 1983.

41. Texon M. *Hemodynamic Basis of Ahterosclerosis.* Hemisphere Publishing Corp., Washington, 1980.

42. Fox JA, Hugh AE. Localization of atheroma: A theory based on boundary layer separation. *Br. Heart J.* **28:** 388, 1966.

43. Wesolowski SA, Fries CC, Sabini AM, Sawyer PN. The significance of turbulence in hemic systems and in the distribution of atherosclerotic lesion. *Surgery.* **57:** 155, 1965.

44. Stehbens WE. Hemodynamics and atherosclerosis. *Biorheology.* **19:** 95, 1982.

45. Gosling RG, Newman DL, Bowden NLR, Twinn KW. The area ratio of normal aortic junctions: Aortic configuration and pulse-wave reflection. *Brit. J. Radiol.* **44:** 850, 1971.

46. Massop DW, Wright JG, Smead WL, Sadoun ET, Cornhill JF. Interleukin-6 production by human aortic endothelial cells is regulated by shear stress. *Arteriosclerosis.* 10: 760a, 1990.

47. Malek A, Izumo S. Physiological fluid shear stress causes downregulation of endothelin-1 mRNA in bovine aortic endothelium. *Am. J. Physiol. 263* (Cell Physiol. **32**): C389, 1992.

48. Frangos JA, Eskin SG, McIntyre LV, Ives CL. Flow effects on prostacyclin production by cultured human endothelial cells. *Science.* **227:** 1477, 1989.

49. Dewey CF, Bussolari SR, Glimbrone MA Davies PF. The dynamic response of vascular endothelial cells to fluid shear stress. *J. Biomech. Eng.* **103:** 177, 1981.

50. Davies PF, Remuzzi A, Gordon EJ, Dewey EJ, Gimbrone MA. Turbulent fluid shear stress induces vascular endothelial cell turnover *in vitro.* *Proc. Natl. Acad. Sci. USA.* **83:** 2114, 1986.

51. Davies PF. Mechanical sensing mechanisms: Shear stress and endothelial cells. *J. Vasc. Surg.* **13:** 729, 1991.

52. Wick TM, Doty SD, Nerem RM. Influence of fluid mechanical stresses on vascular cell adhesion. In *Biomedical Transport Processes.* Plenum Press, New York, NY, pp.283-292, 1990.

53. Davies PF, Tripathi SC. Mechanical stress mechanisms and the cell: An endothelial paradigm. *Circ. Res.* **72:** 239, 1993.

54. Azuma T, Fukushima T. Flow patterns in stenotic blood vellel models. *Biorheology.* **13:** 337, 1976.

55. Yongchareon W, Young DF. Initiation of turbulence in models of arterial stenoses. *J. Biomechanics.* **12:** 185, 1979.

56. Tickner EG, Sacks AH. Slow flow of rigid particle suspensions through simulated stenoses. *Biorhelogy.* 5: 275, 1968.

57. Forrester JH, Young DF. Flow through a converging-diverging tube and its implications in occlusive vascular disease-I: Theoretical development. *J. Biomechanics.* **3:** 297, 1970.

58. Forrester JH, Young DF. Flow through a converging-diverging tube and its implications in occlusive vascular disease-II: Theoretical and experimental results and their implications. *J. Biomechanics.* **3:** 307, 1970.

59. Young DF, Tsai FY. Flow characteristics in models of arterial stenosis-I: Steady Flow. *J. Biomechanics.* **6:** 395, 1973.

60. Young DF, Tsai FY. Flow characteristics in models of arterial stenosis-II: Unsteady Flow. *J. Biomechanics.* **6:** 547, 1973.

61. Zeller H, Talukder N, Lorenz J. Model studies of pulsating flow in arterial branches and wave propagation in blood vessels. In *AGARD Conference Proceedings on Fluid Dynamics of Blood Circulation and Respiratory Flow.* 1970.

62. Walburn FJ, Stein PD. Flow in a symmetrically branched tube simulating the aortic bifurcation: The effects of unevenly distributed flow. *Annals of Biomed. Engr.* **8:** 159, 1980.

63. Walburn FJ, Stein PD. The shear rate at the wall in a symetrically branched tube simulating the aortic bifurcation. *Biorheology.* **19:** 307, 1982.

64. Fukushima T, Homma T, Azuma T, Harakawa K. Characteristics of secondary flow in steady and pulsatile flows through a symmetrical bifurcation. *Biorheology.* **24:** 3, 1987.

65. Balasubramanian K, Mabon RF, Giddens DP. Flow in the carotid bifurcation. In *Hemodynamics and the Arterial Wall.* University of Houston, Houston, TX, 1980.

66. Bharadvaj BK, Mabon RF, Giddens DP. Steady flow in a model of the human carotid bifurcation: Part I-flow visualization. *J. Biomechanics.* **15:** 349, 1982.

67. Bharadvaj BK, Mabon RF, Giddens DP. Steady flow in a model of the human carotid bifurcation: Part II-laser-Doppler measurements. *J. Biomechanics.* **15:** 363, 1982.

68. Rindt CCM, Vosse FNvd, Steenhoven AAv, Janssen JD, Reneman RS. A numerical and experimental analysis of the flow field in a two-dimensional model of the human carotid artery bifurcation. *J. Biomechanics.* **20:** 499, 1987.

69. Lutz RJ, Cannon JN, Bischoff KB, Dedrick RL, Stiles RK, Fry DL. Wall shear stress distribution in a model canine artery during steady flow. *Circ. Res.* **41:** 391, 1977.

70. Friedman MH, Deters OJ, Mark FF, Bargeron CB, Hutchins GM. Arterial geometry affects hemodynamics - A potential risk factor for atherosclerosis. *Atherosclerosis.* **46:** 225, 1983.

71. Moore JE, Ku DN, Zarins CK, Glagov S. Pulsatile flow visualization in the abdominal aorta under differing physiologic conditions: Implications for increased susceptibility to atherosclerosis. *J. Biomech. Eng.* **114:** 391, 1991.

72. Pedersen EM, Yoganathan AP, Lefebvre XP. Pulsatile flow visualization in a model of the human abdominal aorta and aortic bifurcation. *J. Biomechanics.* **25:** 935, 1992.

73. Ku DN, Giddens DP. Pulsatile flow in a model carotid bifurcation. *Arteriosclerosis.* **3:** 31, 1983.

74. Asakura T, Karino T. Flow patterns and spatial distribution of atherosclerotic lesions in human coronary arteries. *Circ. Res.* **66:** 1045, 1990.

75. Simon AC, Levenson J, Flaud P. Pulsatile flow and oscillating wall shear stress in the brachial artery of normotensive and hypertensive subjects. *Cardiovascular Res.* **24:** 129, 1990.

76. Moore JE, Ku DN. Wall shear stress measurements in model abdominal aorta using magnetic resonance imaging. *ASME BED Advances in Bioengineering.* **20:** 375, 1991.

77. Farthing S, Peronneau P. Flow in the thoracic aorta. *Cardiovascular Res.* **13:** 607, 1979.

78. Hutchison KJ, Karpinski E, Campbell JD, Potemkowski AP. Aortic velocity contours at abdominal branches in anesthetized dogs. *J. Biomechanics.* **21:** 277, 1988.

79. Bell DR, Sabbah HN, Stein PD. Profiles of velocity in coronary arteries of dogs indicate lower shear rate along inner arterial curvature. *Arteriosclerosis.* **9:** 167, 1989.

80. Friedman MH, O'Brien V, Ehrlich LW. Calculations of pulsatile flow through a branch: Implications for the hemodynamics of atherosclerosis. *Circ. Res.* **36:** 277, 1975.

81. Zheng L, Yang W. A computer simulation of the non-Newtonian blood flow at the aortic bifurcation. *J. Biomechanics.* **26:** 37, 1993.

82. Thiriet M, Pares C, Saltel E, Hecht F. Numerical simulation of steady flow in a model of the aortic bifurcation. *J. Biomed. Eng.* **114:** 40, 1992.

83. Rindt CC, van Steenhoven AA, Janssen JD, Reneman RS, Segal A. A numerical analysis of steady flow in a three-dimensional model of the carotid artery bifurcation. *J. Biomechanics.* **23:** 461, 1990.

84. Perktold K, Florian H, Hilbert D, Peter R. Wall shear stress distribution in the human carotid siphon during pulsatile flow. *J Biomechanics.* **21:** 663, 1988.

85. Perktold K, Nerem RM, Peter RO. A numerical calculation of flow in a curved tube model of the left main coronary artery. *J Biomechanics.* **24:** 175, 1991.

86. Cornhill JF, Roach MR. A quantitative study of the localization of atherosclerotic lesions in the rabbit aorta. *Atherosclerosis.* **23:** 489, 1976.

87. Schwenke DC, Carew TE. Quantification in vivo of increased LDL content and rate of LDL degradation in normal rabbit aorta occurring at sites susceptible to early atherosclerotic lesions. *Circulation Res.* **62:** 699, 1988.

88. Schwenke DC, Carew TE. Initiation of atherosclerotic lesions in cholesterol-fed rabbits. I. Focal increases in arterial LDL concentration precede development of fatty streak lesions. *Arteriosclerosis.* **9:** 895, 1989.

89. Zeindler CM, Kratky RG, Roach MR. Quantitative measurements of early atherosclerotic lesions on rabbit aortae from vascular casts. *Atherosclerosis.* **76:** 245, 1989.

90. Stemerman MB, Morrel EM, Burke KR, Colton CK, Smith KA, Lees RS. Local variation in arterial wall permeability to low density lipoprotein in abnormal rabbit aorta. *Arteriosclerosis.* **6:** 64, 1986.

91. Morrel EM, Holland JA, Pritchard KA, Colton CK, Stemerman MB. Endothelial cell perturbation and low density lipoprotein: quantitative autoradiography. *Ann. N.Y. Acad. Sci.* **516:** 412, 1987.

92. Morrel EM. Sites of enhanced ^{125}I-low density lipoprotein permeability in the rabbit aorta in vivo. Ph.D. Thesis, MIT, 1987.

93. Schnitzer JJ, Yarmush ML, Tompkins RG, Smith KA, Stemerman MB. Measurement of ^{125}I-low-density lipoprotein uptake in selected tissues of the squirrel monkey. *Am. J. Pathol.* **132:** 526, 1988.

94. Tompkins RG, Yarmush ML, Schnitzer JJ, Colton CK, Smith KA, Stemerman MB. Low-density lipoprotein transport in blood vessel walls of squirrel monkeys. *Amer. Physiol. Soc.* (Heart Circ. Physiol.). **26:** H452, 1989.

95. Stemerman MB. Effects of moderate hypercholesterolemia on rabbit endothelium. *Arteriosclerosis.* **1:** 25, 1981.

96. Truskey GA, Roberts WL, Herrmann RA, Malinauskas RA. Measurement of endothelial permeability to ^{125}I-low density lipoproteins in rabbit arteries using en face preparations. *Circ. Res.* **71:** 883, 1992.

97. Herrmann RA, Malinaukas RA, Truskey GA. Characterization of elevated low density lipoprotein permeability sites at lesion-prone areas of the normal rabbit aorta. Presented at 1993 Annual Fall Meeting, Biomedical Engineering Society, October 21-24, 1993, Memphis Tennessee.

98. Okano M, Yoshida Y. Endothelial cell morphometry of atherosclerotic lesions and flow profiles at aortic bifurcations in cholesterol fed rabbits. *J. Biomech. Eng.* **114:** 301, 1992.

99. Lin S-J, Jan K-M, Weinbaum S, Chien S. Transendothelial transport of density lipoprotein in association with cell mitosis in rat aorta. *Arteriosclerosis.* **9:** 230, 1988.

100. Karino T, Motomiya M. Flow visualization in isolated transparent natural blood vessels. *Biorheology.* **20:** 119, 1983.

101. Peronneau P. *Analyse de l'ecoulement sanguin dans les gros v aisseaux par methode ultrasonore.* These Science Nat. Universite de Paris, 1977.

Chapter Two

Topographical Mapping of Sites of Enhanced HRP Permeability in the Normal Rabbit Aorta

2.1 Introduction

The detailed localization of atherosclerotic lesions, both spontaneously occurring and experimentally induced, has been studied extensively in postmortem human specimens as well as several animal models. It has long been established that atherosclerotic plaques do not occur randomly within the vasculature but rather preferentially in regions of arterial curvature, branching, and bifurcation [1-4]. This focal nature of the disease has given rise to the notion of the importance of localizing factors in atherogenesis. Among the commonly cited localizing factors are variations in hemodynamic phenomena and in arterial wall structure and function. Indeed, various studies have reported focal variation in the permeability of the arterial system to protein-bound dyes or labelled macromolecules [5-9].

Efforts in our laboratory have focused on establishing a fundamental understanding of the mechanisms governing the transport, accumulation, and metabolism of low density lipoprotein (LDL) and other proteins in the aorta of the normal New Zealand White rabbit and squirrel monkey. In the course of these studies, we have observed punctate foci in the aorta that are highly permeable to horseradish peroxidase (HRP), an enzyme with molecular weight of about 40,000 and Stokes-Einstein radius of 3.0 nm, injected into the rabbit one minute before sacrifice and subsequently visualized *en face* by reaction with diaminobenzidine (DAB) and H_2O_2 [10-12]. These sites, henceforth referred to as "HRP spots", are also highly permeable to radiolabelled LDL [13-15], and some of them have been shown to correspond to abnormal, enlarged

endothelial cellsand to possess other morphological features different from normal arterial tissue [15].

The objective of the study reported in this paper is to provide a detailed quantitative description of the distribution of the HRP spots in the aorta of the normocholesterolemic New Zealand White rabbit. The results are compared with the localization of experimentally-induced atherosclerotic lesions in hypercholesterolemic rabbits [16-20].

2.2 Materials and Methods

2.2.1 Animal Experiments

All procedures described here were reviewed and approved by the Committee on Animal Care at MIT. Eight New Zealand White rabbits (five male and three female) weighing from 2.1 to 2.9 kg were used in this investigation. Each rabbit was first placed in a standard animal restraining box, thereby allowing easy access to the ears. A catheter (22 ga, 8 in Intracath, Deseret Pharmaceutical Co., Sandy, VT) was inserted through one of the marginal ear veins and used for administering anesthesia at a dose of 10 mg diazepam (5 mg/ml, Hoffman Laroche, Inc., Nutley, NJ) and 18 mg sodium pentobarbital (1 g/ml, Lemmon Co., Sellersville, PA). Anesthesia was supplemented with diethyl ether (Mallinckrodt, Inc., Paris, KY) inhalation as needed. The animal was then placed supine on an operating table, its four extremities secured, and the neck, thorax, abdomen, and groin shaved. The left common carotid artery was dissected free and cannulated with a catheter (16 ga, 2 in Angiocath, Deseret Pharmaceutical Co., Sandy, VT) that was connected to a three-way valve. One branch of this valve was connected to a 60 ml syringe containing a 50 ml bolus of 2.5% (w/v) glutaraldehyde in 0.1 M sodium cacodylate buffer (pH 7.4). The other branch was connected to a hanging bottle containing one

liter of the same glutaraldehyde fixative and positioned 150 cm above the operating table.

One min before sacrifice, 80 mg/kg HRP (Type II, Sigma, St. Louis, MO), dissolved in 5 ml of isotonic saline, was injected via the marginal ear vein catheter with saline flushes prior to and following HRP injection. An HRP incubation time of 1 min was sufficiently long to yield punctate and well-defined spots which allowed quantitative topographical analysis but sufficiently short to avoid large regions of diffuse HRP staining. One minute after HRP injection, the rabbit was sacrificed with an overdose (>1.25 ml/kg) of sodium pentobarbital (6 g/ml, Lemmon Co., Sellersville, PA) via the same catheter. The animal died immediately.

Sacrifice was immediately followed by injecting the 50 ml bolus of 2.5% glutaraldehyde into the carotid artery catheter and simultaneously opening the abdomen by midline incision, retracting the mesentery, and isolating and cutting a segment of the vena cava to provide an outlet for egressing blood and fixative. The bolus injection was immediately followed by continuous pressure-driven perfusion at 110 mm Hg of the same fixative from the hanging bottle into the carotid catheter. The flowrate of the bottle perfusate was maintained at about 15 ml/min for 10 min, after which it was reduced to about 5 ml/min for an additional 20 min. The extent of HRP staining was sensitive to the flowrate of the perfusate from the bottle. Substantial deviations (a factor of two or more) in either direction of these flowrates led to marked reduction of average spot density (including no observable spots). Outflowing blood and fixative were removed from the abdominal cavity by suction.

After 30 min of perfusion fixation, the thorax was opened by midline incision. Beginning at the heart and proceeding distally, the entire aorta was excised as far caudally as the iliac bifurcation. In addition, about 1 cm of all the

major vascular branches was included in the excision. Care was taken to ensure that the aorta was not cut, torn, or unnecessarily stretched during the excision process, and the excised vessel was then immersed in 250 ml of glutaraldehyde/cacodylate fixative. After one hour in this fixative, the heart and aorta were transferred to a 0.1 M cacodylate (pH 7.4) solution. The heart was carefully cut away, ensuring that the coronary sinuses and proximal portion of the ascending thoracic aorta remained intact. The complete aorta from the sinuses to the proximal portion of the iliac arteries was carefully trimmed of any fat and loose tissue.

2.2.2 Longitudinal Opening of Aorta

Figure 2.1 illustrates the manner in which the aorta is opened longitudinally and pinned flat. Figure 2.1A depicts the rabbit aorta and its major branches. The greater curvature of the aortic arch gives rise to two vessels, the brachiocephalic and the left subclavian. The brachiocephalic artery immediately divides into the right subclavian and the two carotid vessels. The descending thoracic aorta gives rise along its dorsal surface to eight pairs of intercostal arteries, the most distal of which emerges approximately at the level of the diaphragm, which anatomically marks the division between the thoracic and abdominal aorta. Within the abdominal aorta, the celiac, a large vessel which branches immediately into the left gastric, hepatic, and splenic arteries, and which supplies the stomach, liver, duodenum, pancreas, and spleen, emerges ventrally immediately caudal to the diaphragm. A ninth pair of intercostal (or phrenic) arteries arises along the dorsal surface of the aorta either slightly proximal or distal to the celiac branch. Downstream of the celiac is the superior mesenteric, a large ventral artery which supplies the pancreas, small intestine, and large intestine. Immediately distal to the superior

mesenteric and emerging laterally is the right renal artery, followed by the left renal artery on the opposite side of the animal. Some distance downstream of the renals is the ventral inferior mesenteric artery which supplies the descending colon and rectum, eventually followed by the aorto-iliac bifurcation which marks the anatomical termination of the aorta.

The protocol used to longitudinally cut open the aorta is depicted in Figure 2.1B. The aorta was positioned in its proper anatomical orientation, and its dorsal surface at the iliac bifurcation was pinned down while holding the brachiocephalic trunk with a pair of forceps. Holding the aorta firmly in place, the ventral surface of the aorta was cut in one continuous motion halfway between the lesser and greater curvature in the arch and directly opposite the eight pairs of intercostal arteries in the descending thoracic aorta. Within the abdominal aorta, the cut was made such that the ostia of all the abdominal vessels were to the right of the cut. Finally, cuts were made perpendicular to the main longitudinal cut into the brachiocephalic and left subclavian vessels so that the curved aortic arch could be pinned flat as illustrated in Figure 2.1C. To ensure that the aorta was pinned flat, all vascular branches were cut flush with the adventitial surface of the aorta. The aorta, intimal surface upward, was then pinned flat with fine insect pins on a Sylgarde silicone mat (Brownell Electro, Inc., Woburn, MA) inside an insect pinning tray (Cole-Parmer Instrument Co., Chicago, IL) with care taken to use as few pins as possible to avoid any unnecessary stretching or distortion.

2.2.3 HRP Processing

The pinned aorta was bathed in a solution of 0.5 mg/ml of DAB (Sigma, St. Louis, MO) in 0.1 M sodium cacodylate buffer (pH 7.4) for 15 to 20 min. This solution was aspirated and replaced with a solution of 0.5 mg/ml DAB in

0.1 M sodium cacodylate (pH 7.4) and 0.1 g/l H_2O_2 (Mallinckrodt, Inc., Paris, KY). This last solution was prepared just prior to use, and the last step was carried out in the dark by covering the entire pinning tray with aluminum foil and working in a darkened laboratory to avoid light reactions. After 15 min of bathing with gentle agitation, the reactants were aspirated and the aorta washed with three changes of 0.1 M cacodylate buffer. This rendered the sites of enhanced HRP permeability visible in the form of focal, punctate, circular brown regions on the intimal surface. Following HRP processing, the aorta was fixed in 2.5% glutaraldehyde in 0.1 M sodium cacodylate overnight and finally immersed in 7% sucrose in 0.1 M sodium cacodylate solution for storing and imaging purposes.

2.2.4 HRP Spot Localization

The pinning tray was mounted onto an X-Y unislide assembly (Velmax, Inc., East Bloomfield, NY) that functioned as a large microscope stage micrometer. It provided accurate linear movement of the tray and a measure of the extent of movement in two directions (x and y).

Two fiber optic lights (Dolan Jenner, Series 180, Woburn, MA) were used to illuminate the aorta. These lights did not lead to a temperature rise of the bathing solution during the prolonged image analysis sessions. VG-9 green filters were placed in the light path in order to increase the resolution and differentiation between the HRP foci and the unstained light background tissue of the aortic intima. The HRP spots on the surface of the illuminated aorta were then examined under a stereomicroscope (Wild Heerbrugg, M5APO, Heerbrugg, Switzerland) onto which was mounted a video camera (Panasonic TV WV 1550). The picture from the camera was transferred to an image analysis system (Zeiss Videoplan 2, West Germany) possessing a

digitizing tablet and stylus for the manual identification of all aortic characteristics.

The entire aorta was too large to be analyzed at one time. The microscopic magnification was set at 7.5; at this setting, the aorta was divided into 40-50 square segments, roughly 8 mm by 8 mm, which were individually analyzed. The exact quantitative procedure for each segment consisted of first recording the exact position of

the segment using the X-Y unislide assembly. Each of the HRP foci within the segment was then traced, and the Videoplan system automatically determined the x- and y-centers of gravity, the area, and perimeter of each HRP spot. The same procedure was followed for all the aortic ostia within the segment. The exact shape of the aortic segment was recorded by determining the coordinates of selected points along the perimeter. This entire process was then repeated for all the segments until the entire aorta was traced, and the resultant images were printed out and reassembled to reconstruct the entire aorta with all the relevant information regarding HRP spot size and location, aortic branch size and location, and overall aortic perimeter information. Each of the resulting reassembled video printouts was about 8 ft long. The outlines of the tissue perimeters, HRP spots and aortic ostia were manually darkened with ink. Segments of these video printouts were then sequentially reduced xerographically, reassembled, and photographically reduced to yield images of the pinned aortic surface along with the ostia and the *en face* spatial distribution of HRP spots.

2.3 Results

2.3.1 Size Distribution of HRP Spots

The size distribution of the enhanced HRP permeability sites in all eight rabbits is shown in Figure 2.2. The mean diameter±SD was 158±30 μm with a range of 90 to 350 μm. Taking 300 μm^2 to be the surface area of a typical rabbit endothelial cell [21-23], an average HRP spot would circumscribe about 65 endothelial cells.

2.3.2 *En Face* Spatial Distribution of HRP Spots

The reduced images of the eight aortas studied are depicted in Figures 2.3 and 2.4. In the figures, each black dot on the aortic surface corresponds to an actual HRP spot. A large portion of the aortic arch of rabbit 2 does not exhibit punctate HRP spots but rather a diffuse staining pattern; therefore, this region is excluded from all analyses. Furthermore, large blood clots are observed on the surface of rabbit 2 in the region between the fourth and sixth pairs of intercostal arteries and on the surfaces of rabbits 6 and 7 in the regions of the first to third pairs of intercostal arteries. These clot-covered regions are also excluded from analysis.

The surface area analyzed for each rabbit ranges from about 1270 to 1950 mm^2 and totals 13,450 mm^2 for all eight rabbits. The average spot density in all eight rabbits is 0.63 spots/mm^2 and ranges from 0.06 to 1.14 spots/mm^2 for individual rabbits.

The profile adjacent to each aorta in Figures 2.3 and 2.4 gives the average spot density in each of five regions of the aorta. Although the overall average spot density varies from rabbit to rabbit, all of the profiles display a similar qualitative pattern. The highest density of HRP spots is in the aortic arch (1.7 spots/mm^2, all rabbits; as high as 2.9 in rabbit 4); the density then

decreases as one proceeds distally, reaches a minimum (0.26, all rabbits; 0.02 in rabbit 7) in the lower descending thoracic aorta (region of intercostal arteries), and then increases again in the abdominal aorta (0.61, all rabbits).

In addition to gross regional variations, on a smaller scale the HRP spots have a nonuniform topographical distribution. Within the ascending aorta, the density of spots (Figures 2.3 and 2.4) is typically highest in the middle section of the pinned tissue that corresponds to the dorsal wall of the aorta (Figure 2.1B). In the region immediately distal to the left subclavian branch, the highest spot density shifts to a region at and near the right edge of the pinned aorta that corresponds to a region along the greater curvature of the arch. Finally, in the upper descending thoracic aorta, i.e. in the portion of the descending aorta proximal to the intercostal ostia, the highest HRP spot density shifts to a region along the cut edge in the pinned aorta, corresponding to the ventral wall of the aorta. Therefore, within the aortic arch and the upper descending thoracic aorta, the region of highest HRP spot density follows a helical pattern beginning along the dorsal wall, coiling in the clockwise direction to localize along the greater curvature of the arch immediately distal to the left subclavian artery, and finally continuing further to the ventral wall in the upper descending thoracic aorta. The clockwise helical pattern from the ventral to dorsal walls suggests a persistence down to the level of the second pair of intercostal arteries in rabbits 6 and 8 and down to much lower levels of the descending thoracic aorta in rabbits 1,3, and 4.

Outside the aortic arch, the HRP spots occur in patches and streaks that are primarily oriented in the bulk flow direction. Several streaks occur within the abdominal aorta as illustrated in Figure 2.5. There is always a streak proximal to the celiac ostium at a position corresponding to the anatomical right lateral wall of the uncut aorta. In four (rabbits 1,2,4, and 5) of the eight

rabbits studied there is a similar streak of elevated spot density proximal to the celiac ostium and located along the anatomical left lateral wall of the uncut aorta (the spots along the right cut edge of the tissue are a continuation of this streak). Additionally, the region directly between the celiac and superior mesenteric ostia that lies along the ventral wall in the intact vessel contains a streak of elevated spot density in every rabbit. In five of the eight rabbits studied (rabbits 1,2,3,6, and 8), the streak is relatively wide and encompasses the lateral walls proximal to the superior mesenteric ostium.

2.3.3 Spatial Distribution of HRP Spots Around Ostia

The topography of HRP spot staining around aortic ostia is assessed using three forms of data representation: (1) *en face* spatial distribution plots that display the positions of the HRP spots relative to the individual ostia as obtained from image analysis, (2) radial distribution plots of the density of the HRP spots as a function of distance from the ostium, and (3) angular distribution plots that express the HRP spot density in terms of a polar coordinate system in a fashion similar to the method developed by Cornhill and Roach [24]. A representative coordinate system around ostia is illustrated in Figure 2.6. Each ostium in the abdominal aorta is approximated by an ellipse possessing the same area and perimeter as the actual ostium because the image analysis revealed that these ostia were not circular and could be better approximated as ellipses. Ostia of the intercostal vessels are represented by circles. The perimeters of ostia in the arch are not specified for reasons described subsequently. In all cases, for each specific vessel the HRP spot patterns are plotted as the aorta is viewed *en face*, and the orientations on each plot are anatomically correct. The HRP spot distributions around ostia

are next discussed in detail for the abdominal region, the intercostal region, and the aortic arch region.

2.3.3.1 Abdominal Region

Figures 2.7,2.8, and 2.9 respectively illustrate the *en face* spatial, radial, and angular distributions of HRP spots around the four major abdominal ostia. Each dot in Figure 2.7 represents a single HRP spot, and spots from the eight rabbits are superimposed. Regions labelled "No Data" and "Incomplete Data" in the figures represent regions beyond the edge of pinned aortic tissue which arise because ostia are often located near a cut edge.

Analysis of the distribution of enhanced HRP permeability sites around the superior mesenteric and right renal arteries is complicated because these two vessels in the rabbit are in close proximity (Figure 2.10), more so than any two other major abdominal aortic branches. In the eight rabbits studied, the average distance between the centers of gravity of these two vessels is 5.1 mm. By comparison, the average distance between the centers of gravity of the celiac and superior mesenteric arteries is 13.8 mm, and that between the right and left renal arteries is 7.4 mm. As a consequence, some of the HRP spots distal to the superior mesenteric artery are simultaneously counted as being proximal to the right renal artery. The region of overlap thought to be influenced by the presence of the superior mesenteric artery is so indicated in Figures 2.7,2.8, and 2.9.

We divide the region within the constructed circles around the abdominal ostia in Figure 2.7 into a region in the immediate vicinity of ostia and one in the general vicinity of ostia. The HRP spots are not uniformly distributed around ostia. In the case of the celiac ostium, the density of HRP spots in the immediate vicinity of the ostium within the two innermost drawn

circles (i.e. d≤1 mm) is highest distal to the ostium. In the general vicinity of the ostium (i.e. 1≤d≤2 mm), the densities of HRP spots within the proximal and distal quadrants are comparable and slightly higher than in the lateral quadrants (Figure 2.8).

In the case of the superior mesenteric artery, the HRP spot density is also highest within the distal quadrant in the immediate vicinity of the ostium (d≤0.5 mm) as illustrated in Figure 2.8. Within the general vicinity of the ostium (0.5≤d≤2 mm), the HRP spot density is substantially higher both proximal and distal to the branch than in the lateral regions. Figure 2.5 suggests that the HRP spots proximal to the superior mesenteric are primarily a part of the axial streak that localizes along the ventral wall between the ostia of the celiac and superior mesenteric arteries.

In the case of the two renal vessels, the spots in the immediate vicinity of the ostia localize primarily distal to the ostia with the spot density in the other three quadrants significantly lower. As the distance from the edge of the ostia (d) increases beyond the general vicinity of the ostia, the preferred orientations of HRP spots largely diminish around the celiac and renal arteries, and the densities in all four quadrants become similar (Figure 2.7). In the case of the superior mesenteric artery, since the higher spot density in the proximal quadrant is a part of the ventral streak, it naturally persists for larger distances.

The HRP spot topography in rabbit 2 differs from the other seven animals. The HRP spots are more randomly distributed, and their densities in the abdominal aorta are higher than in the other rabbits. It was postulated that the data from this rabbit may have skewed the findings of spot localization around ostia. Therefore, the same analysis of HRP spot distribution around abdominal ostia was repeated with the data from rabbit 2 excluded. Although the exact values of the spot densities changed, the overall conclusions were

not affected. The data from rabbit 2 had its largest effect on the findings around the celiac ostium where the exclusion of that data, despite lowering spot density in all four quadrants, accentuated the dominance of the distal component (and to a lesser extent the left lateral component) in the immediate vicinity of the ostium (i.e. $d \leq 1$ mm) by lowering the proximal and right lateral components to a greater extent. The effect on spot localization around the other ostia was minimal.

Superimposed on Figure 2.9 are the angular distributions of experimentally-induced fatty atherosclerotic lesion lengths in hypercholesterolemic rabbits after 83 days (Cornhill and Roach, 1976 [16]) and 28 days (Zeindler *et al.* , 1989 [17]) on atherogenic diets. In the case of [17], the lesions localized primarily lateral to ostia after 1 wk on the diet and eventually developed into the 4-wk lesions displayed in Figure 2.8. Comparison of the HRP spot density with that of lesion lengths indicates dissimilar trends in the cases of the celiac and superior mesenteric vessels, although the superior mesenteric data show better agreement with the 1976 study than the 1989 investigation. On the other hand, there is qualitative agreement in the case of the two renal vessels, since both HRP spots and lesions exhibit a pronounced predilection for the distal quadrant.

2.3.3.2 Intercostal Region

Figures 2.11, 2.12, and 2.13 respectively depict the *en face* spatial, radial, and angular distributions of the HRP spots around the anatomically right and left intercostal ostia. The data in each of the plots represent HRP spots around 64 ostia (eight rabbits, each having eight pairs of intercostal arteries). In the immediate proximity of the ostia defined as the region within the constructed circles in Figure 2.11, the HRP spot density is highest within the

distal quadrant. As d increases to a value of 1.5-2 mm and higher, this preferred orientation of HRP spots disappears. Hence, the angular distribution was evaluated over the region $0<d\leq1$ mm. Superimposed on Figure 2.13 are plots of the lengths of the experimentally-induced lesions of Zeindler *et al.* [17]. The angular distribution of HRP spot density and lesion length are in remarkable qualitative agreement.

2.3.3.3 Aortic Arch Region

Figures 2.14 and 2.15 respectively depict the *en face* spatial and angular distributions of HRP spots around the two arch branches. In the aortic arch, the manner in which the aorta was cut open (Figure 2.1B) included cuts made through the ostia. This led to regions containing no tissue, and hence no HRP spot data, near the ostia and to the loss of information regarding ostium shape and size. Consequently, the positions of the ostium centers of the brachiocephalic and left subclavian vessels were approximated. The analyses were performed for the region within 4 mm of the approximated center of the brachiocephalic artery and 3 mm of the approximated center of the left subclavian ostium. There is no preferred HRP spot orientation in the vicinity of the brachiocephalic ostium, while the spots tend to localize mostly in the distal quadrant in the case of the left subclavian vessel.

2.4 Discussion

This study provides a topographical mapping of the distribution of sites of enhanced permeability to HRP in the aorta of the normal New Zealand White rabbit after one min circulation. Upon processing, these sites take the form of punctate brown circular spots about 160 μm in diameter. Essentially the same size has been reported for HRP spots in Sprague-Dawley rats following one

min circulation [25]. The average HRP spot density in eight rabbits was 0.63 spots/mm^2. This result is comparable to estimates of about 0.9 and 0.3 spots/mm^2 reported for the spot density of Evans Blue dye-albumin conjugates following 5 min [26] and 10 min [25] circulation, respectively, in the rat. Using an average value of about 300 μm^2 for the surface area of a rabbit endothelial cell, and assuming that each spot is associated with enhanced permeability around or through one endothelial cell, leads to an estimate of 1.9×10^{-4} for the fraction of all of the endothelial cells that is associated with enhanced transport during the one min experiment.

Although the average HRP spot density varies substantially and the density is not uniform throughout the aorta, several qualitative trends in spot localization are observed in virtually all rabbits studied. Along the length of the aorta, the spot density is highest in the aortic arch, intermediate in the abdominal aorta, and lowest in the lower descending thoracic aorta in the region of the intercostal arteries.

The region of highest spot density in the arch follows a helical turn in the clockwise direction (from dorsal to ventral surface) into the upper descending thoracic aorta. In some rabbits, the helical pattern persists throughout the descending thoracic aorta. Outside the arch, the HRP spots often occur in streaks oriented in the bulk flow direction. In the abdominal aorta, HRP spots localize along the dorsal and lateral walls proximal to the celiac ostium, along the ventral wall in the region between the celiac and superior mesenteric ostia, and occasionally along the lateral walls proximal to the superior mesenteric ostium.

The density of spots is also often high in the general vicinity of ostia (0-2 mm from the ostium edge). With the brachiocephalic ostium where no preferred HRP spot orientation is evident being the sole exception, the density

is typically highest distally in the immediate vicinity of ostia (0-1 mm). In the general vicinity of ostia (0-2 mm) in the abdominal aorta, the proximal density becomes comparably high around the celiac and superior mesenteric arteries while the distal localization persists in the case of the right and left renal arteries. The analysis of orientation trends is complicated in the case of the superior mesenteric and right renal ostia because of their close proximity.

A substantial fraction of the HRP spots are also sites of enhanced transedothelial LDL transport [13,15]. The helical pattern of highest spot density in the arch is in qualitative agreement with the distribution of early fatty atherosclerotic lesions experimentally induced in hypercholesterolemic rabbits reported by Roach [18] and by Schwenke and Carew [19] but is in disagreement with the findings of Rodkiewicz [20]. We compared the distribution of HRP spots around intercostal and abdominal ostia to three studies of the distribution of early fatty atherosclerotic lesions experimentally induced in rabbits [16,17,19]. The first two of these studies provided detailed quantitative information on lesion angular distributions, while the third study only displayed an *en face* view of the lesion topography.

The HRP spot density exhibits an angular distribution similar to that of the length of experimentally induced fatty atherosclerotic lesions in rabbits in the vicinity of the renal and intercostal ostia but not in the vicinity of the celiac and superior mesenteric arteries. The two studies [16,17], however, are only partially consistent with one another.

Scwenke and Carew [19] reported that sudanophilic lesions in hypercholesterolemic rabbits localized distal to orifices of branch vessels of the descending thoracic and abdominal aorta although the lateral component was also significant. In the normocholesterolemic rabbit, focal elevations of arterial LDL degradation rates and of concentrations of intact LDL occurred at these

sites. These observations are consistent with our findings that the HRP spot density in the immediate vicinity of each of the abdominal ostia is highest distal to the ostium. The relatively good agreement between HRP spot distribution and the spatial distribution of induced fatty lesions around most ostia provides support for the notion that a locally high density of enhanced permeability sites may play a role in atherogenesis.

The presence of streaks and of nonuniform radial and angular HRP spot distributions around ostia is consistent with an influence of localizing factors such as local hemodynamic phenomena and/or variations in arterial wall structure and/or function. It is tempting to implicate hemodynamic phenomena solely on the basis of the location of observed lesions or enhanced permeability sites. For example, it is commonly thought that the region distal to a branch is necessarily a site of higher shear stress than that proximal to the branch. However, the complexity of arterial fluid mechanics has recently become more well-understood, and it is evident that such a generalization cannot be made *a priori.* The results of Lutz *et al.* [27] in a model canine artery demonstrate that regions of high and low shear stress can exist in very close proximity, and those of Karino and coworkers [28-30] in natural transparent vessels illustrate the complex flow patterns that can be physiologically encountered. The area distal to a branch may in fact be an area of lower shear stress than that proximal to the branch if a sufficiently large fraction of the parent vessel flow enters the branch. Thus, local fluid mechanical patterns within the rabbit aorta need to be established before hemodynamic phenomena can be correlated with the distribution of lesions or enhanced permeability sites. Studies of this nature are currently underway.

2.5 References

1. Rindfleisch E. *A Textbook of Pathologic Histology.* Translated by Kloman WC and Miles FT, p. 211, Philadelphia: Lindsay and Blakiston, 1872.

2. Mitchell JRA, Schwartz CJ. *Arterial Disease.* Philadelphia: FA Davis Co., 1965.

3. Montenegro MR, Eggen DA. Topography of atherosclerosis in the coronary arteries. *Lab. Invest.* **18:** 126, 1968.

4. Solberg LA, Eggen DA. Localization and sequence of development of atherosclerotic lesions in the carotid and vertebral arteries. *Circulation.* **43:** 711, 1971.

5. Packham MA, Rowsell HC, Jorgensen L, Mustard JG. Localized protein accumulation in the wall of the aorta. *Exp. Mol. Pathol.* **7:** 214, 1967.

6. Somer JB, Schwartz CJ. Focal ^{3}H-cholesterol uptake in the pig aorta. *Atherosclerosis.* **13:** 293, 1971.

7. Bell FP, Adamson IL, Schwartz CJ. Aortic endothelial permeability to albumin: Focal and regional patterns of uptake and transmural distribution of ^{125}I-albumin in the young pig. *Exp. Mol. Pathol.* **20:** 57, 1974.

8. Bell FP, Day AJ, Gent M, Schwartz CJ. Differing patterns of cholesterol accumulation and ^{3}H-cholesterol influx in areas of the cholesterol-fed pig aorta identified by Evans Blue Dye. *Exp. Mol. Pathol.* **22:** 366, 1975.

9. McGill HC, Geer JC, Holman RL. Sites of vascular vulnerability in dogs demonstrated by Evans Blue. *Arch. Pathol.* **64:** 303, 1957.

10. Stemerman MB. Effects of moderate hypercholesterolemia on rabbit endothelium. *Arteriosclerosis.* **1:** 25, 1981.

11. Stemerman MB, Colton CK, Morrel E. Perturbations of the endothelium. In *Progress in Hemostasis and Thrombosis,* Vol. 7, p. 289, Grune and Stratton, Inc., 1984.

12. Morrel EM, Holland JA, Pritchard KA, Colton CK, Stemerman MB. Endothelial cell perturbation and low density lipoproteins: Quantitative autoradiography. *Ann. N.Y. Acad. Sci.* **516:** 412, 1987.

13. Stemerman MB, Morrel EM, Burke KR, Colton CK, Smith KA, Lees RS. Local variation in arterial wall permeability to low density lipoprotein in normal rabbit aorta. *Arteriosclerosis.* **6:** 64, 1986.

14. Tompkins RG, Yarmush ML, Schnitzer JJ, Colton CK, Smith KA, Stemerman MB. Low-density lipoprotein transport in blood vessel walls of squirrel monkeys. *Amer. Physiol. Soc.* (Heart Circ. Physiol.). **26:** H452-H464, 1989.

15. Morrel EM. Sites of enhanced ^{125}I-low density lipoprotein permeability in the rabbit aorta in vivo. Ph.D. Thesis, MIT, 1987.

16. Cornhill JF, Roach MR. A quantitative study of the localization of atherosclerotic lesions in the rabbit aorta. *Atherosclerosis.* **23:** 489, 1976.

17. Zeindler CM, Kratky RG, Roach MR. Quantitative measurements of early atherosclerotic lesions on rabbit aortae from vascular casts. *Atherosclerosis.* **76:** 245, 1989.

18. Roach MR. The effects of bifurcations and stenoses on arterial disease. In*Cardiovascular Flow Dynamics and Measurements,* p. 489, University Press, 1977.

19. Schwenke DC, Carew TE. Initiation of atherosclerotic lesions in cholesterol-fed rabbits. I. Focal increases in arterial LDL concentration precede development of fatty streak lesions. *Arteriosclerosis.* **9:** 895, 1989.

20. Rodkiewicz CM. Localization of early atherosclerotic lesions in the aortic arch in light of fluid flow. *J. Biomechanics.* **8:** 149, 1975.

21. Goode TB, Davies PF, Reidy MA, Bowyer DE. Aortic endothelial cell morphology observed in situ by scanning electron microscopy during atherogenesis in the rabbit. *Atherosclerosis.* **27:** 235, 1977.

22. Reidy MA, Bowyer DE. Distortion of endothelial repair: The effect of hypercholesterolemia on regeneration of aortic endothelium following injury by endotoxin. *Atherosclerosis.* **29:** 459, 1978.

23. Ramsay MM, Walker LN, Bowyer DE. Narrow superficial injury to rabbit aortic endothelium: The healing process as observed by scanning electron microscopy. *Atherosclerosis.* **43:** 233, 1982.

24. Cornhill JF, Roach MR. Quantitative method for the evaluation of atherosclerotic lesions. *Atherosclerosis.* **20:** 245, 1974.

25. Chuang P-T, Cheng H-J, Lin S-J, Jan K-M, Lee MML, Chien S. Macromolecular transport across arterial and venous endothelium in rats, studies with Evans Blue-albumin and horseradish peroxidase. *Arteriosclerosis.* **10:** 188, 1990.

26. Lin S-J, Jan K-M, Schuessler G, Weinbaum S, Chien S. Enhanced macromolecular permeability of aortic endothelial cells in association with mitosis. *Atherosclerosis.* **73:** 223, 1988.

27. Lutz RJ, Cannon JN, Bischoff KB, Dedrick RL, Stiles RK, Fry DL. Wall shear stress distribution in a model canine artery during steady flow. *Circ. Res.* **41:** 391, 1977.

28. Sohara Y, Karino T. Secondary flows in the dog aortic arch. *Fluid Control and Measurement,* p. 143, 1985.

29. Asakura T, Karino T. Flow patterns and spatial distribution of atherosclerotic lesions in human coronary arteries. *Circ. Res.* **66:** 1045, 1990.

30. Karino T, Goldsmith HL, Motomiya M, Mabuchi S, Sohara Y. Flow patterns in vessels of simple and complex geometries. In *Blood in Contact with Natural and Artificial Surfaces*, p. 422, 1987.

Figure Captions

Figure 2.1 (A) Anatomy of a typical rabbit aorta illustrating the major branches. (B) Pattern of cuts used to longitudinally open aorta after branches have been cut flush with adventitial surface. (C) Aorta pinned flat, illustrating typical relative positions of major branches.

Figure 2.2 Size distribution of enhanced HRP permeability sites (pooled data from eight rabbits). An equivalent circular diameter was calculated from the area of each HRP spot.

Figure 2.3 *En face* spatial distribution of enhanced HRP permeability sites in aortas of rabbits 1-4 as reconstructed by image analysis. Each dot on the aorta represents an actual HRP spot. At the right of each aorta is plotted the spot density in the five regions into which each aorta was divided: (1) arch, (2) upper descending thoracic, (3) middle descending thoracic, (4) lower descending thoracic (intercostal region), and (5) abdominal. The average spot density over the enire aorta is tabulated at the bottom of each aorta. The extent of xerographic/photographic reduction of the aortic image varies from rabbit to rabbit.

Figure 2.4 *En face* spatial distribution of enhanced HRP permeability sites in aortas of rabbits 5-8 as reconstructed by image analysis. See caption for Figure 2.3 for further details.

Figure 2.5 *En face* spatial distribution of enhanced HRP permeability sites in portions of abdominal aortas of rabbits 4 and 5. Three regions of HRP streaks are observed: (1) proximal to the celiac ostium along the anatomical right lateral wall of the aorta; (2) proximal to the celiac ostium along the anatomical left lateral wall of the aorta; and (3) between the celiac and superior mesenteric ostia spanning the anatomical ventral and left lateral walls of the aorta. Streak numbers on figure correspond to these regions.

Figure 2.6 Representative polar coordinate system around ostia. The center of the coordinate system is the center of gravity of the ostium under consideration. The angle θ is measured in the clockwise direction. $\theta=0^{\circ}$ is proximal; $\theta=180^{\circ}$ is distal; $\theta=90^{\circ}$ is anatomical right for a ventral ostium, anatomical left for a dorsal ostium, dorsal for a lateral ostium on the right side, and ventral for a lateral ostium on the left side; $\theta=270^{\circ}$ is anatomically opposite to 90°. The two dashed lines divide the domain into four 90° quadrants centered about $\theta=0^{\circ}$, 90°, 180°, and 270°. Spot patterns are plotted as aorta is viewed *en face* and lateral orientations shown here are anatomically correct for the case of a

vessel on the ventral surface or on the right side. The coordinate axes are marked off by tick marks in 1 mm increments, and each axis goes out to a maximum of 6 mm. The coordinate "d" denotes the distance from the ostium edge along the major axis of the ellipse, and the circles represent equally spaced increments along coordinate d.

Figure 2.7 *En face* spatial distribution of HRP spots around abdominal ostia (pooled data from eight rabbits). Region of "No Data" denotes end of aortic tissue at cut edge. Region labelled "Influenced by Sup. Mes." denotes region of probable HRP spot overlap between the superior mesenteric and right renal branches. Region labelled "Influenced by Ventral Streak" denotes region believed to be associated with streak between celiac and superior mesenteric ostia. The outline of each ostium represents an ellipse whose major and minor axes are determined by averaging the eight pairs of major and minor axes obtained by image analysis. Circles drawn around the ostia correspond to 1/2 mm increments in d, the distance from the ostium edge along the major axis of the elliptical ostium; therefore, the innermost circle corresponds to d=0.5 mm, the next circle to d=1.0 mm, the third to d=1.5 mm, and the outermost circle to d=2.0 mm.

Figure 2.8 Radial distribution of HRP spots around abdominal ostia as a function of the distance from ostium edge d (pooled data from eight rabbits). Regions labelled "Incomplete Data" are associated with end of aortic tissue at cut edge. Region labelled "Part of Ventral Streak" refers to spots believed to be primarily associated with the streak seen *en face* in the region between the celiac and superior mesenteric ostia. Each data point represents all the data from eight rabbits in a single quadrant. The data points at d=0.5 mm correspond to all the spots between the periphery of the ostium and the first circle in Figure 2.7. The data points at d=1.0 mm correpsond to all of the spots between the first and second circles in Figure 2.7, and so forth.

Figure 2.9 Angular distribution of HRP spots around abdominal ostia for the region $0<d\leq 2$ mm (pooled data from eight rabbits). Also plotted is the distribution of length of experimentally-induced atherosclerotic lesions in rabbits [16,17].

Figure 2.10 *En face* spatial distribution of HRP spots around the superior mesenteric and right renal ostia in each of the eight rabbits studied. Both vessels and their corresponding HRP spots are shown on the same plot in their relative anatomical locations. Dashed contours represent actual shapes of ostia; solid contours represent ellipses used to approximate shapes of ostia.

Figure 2.11 *En face* spatial distribution of HRP spots around anatomically right and left intercostal ostia (pooled data from eight rabbits, eight pairs per rabbit). Innermost circle represents ostium. Additional circles correspond to d=0.5 and 1.0 mm.

Figure 2.12 Radial distribution of HRP spots around anatomically right and left intercostal ostia as a function of the distance from ostium edge d (pooled data from eight rabbits, eight pairs per rabbit). Each data point represents all the data from eight rabbits in a single quadrant. The data points at d=0.5 mm correspond to all the spots between the periphery of the ostium and the first circle in Figure 2.11. The data points at d=1.0 mm correpsond to all of the spots between the first and second circles in Figure 2.11.

Figure 2.13 Angular distribution of HRP spots around anatomically right and left intercostal ostia for the region $0<d\leq1$ mm (pooled data from eight rabbits, eight pairs per rabbit). Also plotted is the distribution of length of experimentally-induced atherosclerotic lesions in rabbits [17].

Figure 2.14 *En face* spatial distribution of HRP spots around aortic arch ostia (pooled data from seven rabbits). Exact location and size of ostia are unknown. Circles with radii of 4 mm around the brachiocephalic center of gravity and 3 mm around the left subclavian center of gravity are drawn to define the region of interest. Regions of "No Data" arise as a result of manner in which aortic arch is cut and pinned flat.

Figure 2.15 Angular distribution of HRP spots around aortic arch ostia (pooled data from seven rabbits). HRP spots within 4 mm of the center of gravity of the brachiocephalic artery and 3 mm of the center of gravity of the left subclavian are used to construct the figure. Regions of "Incomplete Data" are associated with regions of "No Data" in Figure 2.14.

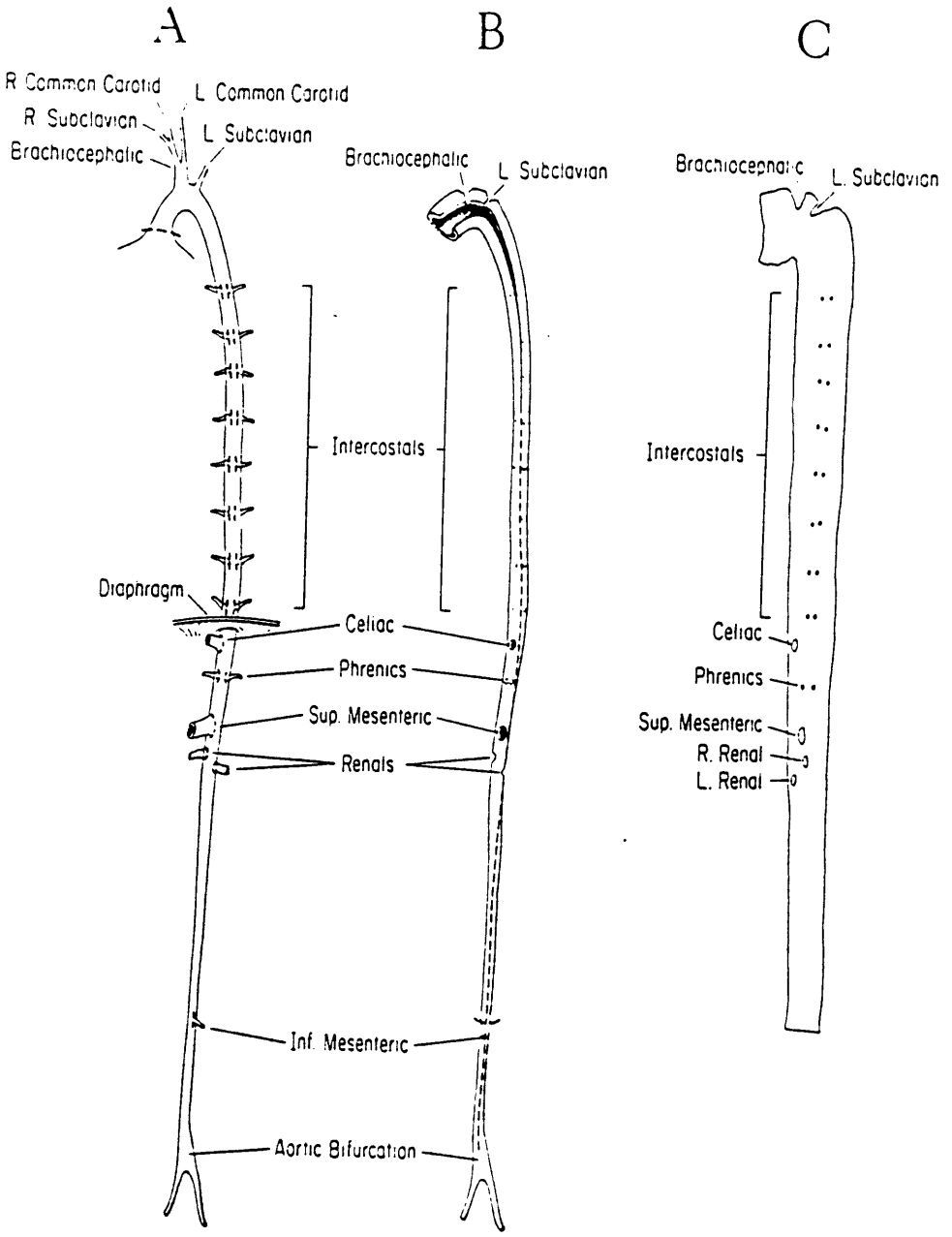
A
B
C
R Common Carotid
L Common Carotid
R Subclavian
L Subclavian
Brachiocephalic
Brachiocephalic
L Subclavian
Brachiocephalic
L. Subclavian
Intercostals
Intercostals
Diaphragm
Celiac
Phrenics
Sup. Mesenteric
Renals
Celiac
Phrenics
Sup. Mesenteric
R. Renal
L. Renal
Inf. Mesenteric
Aortic Bifurcation

Figure 2.1

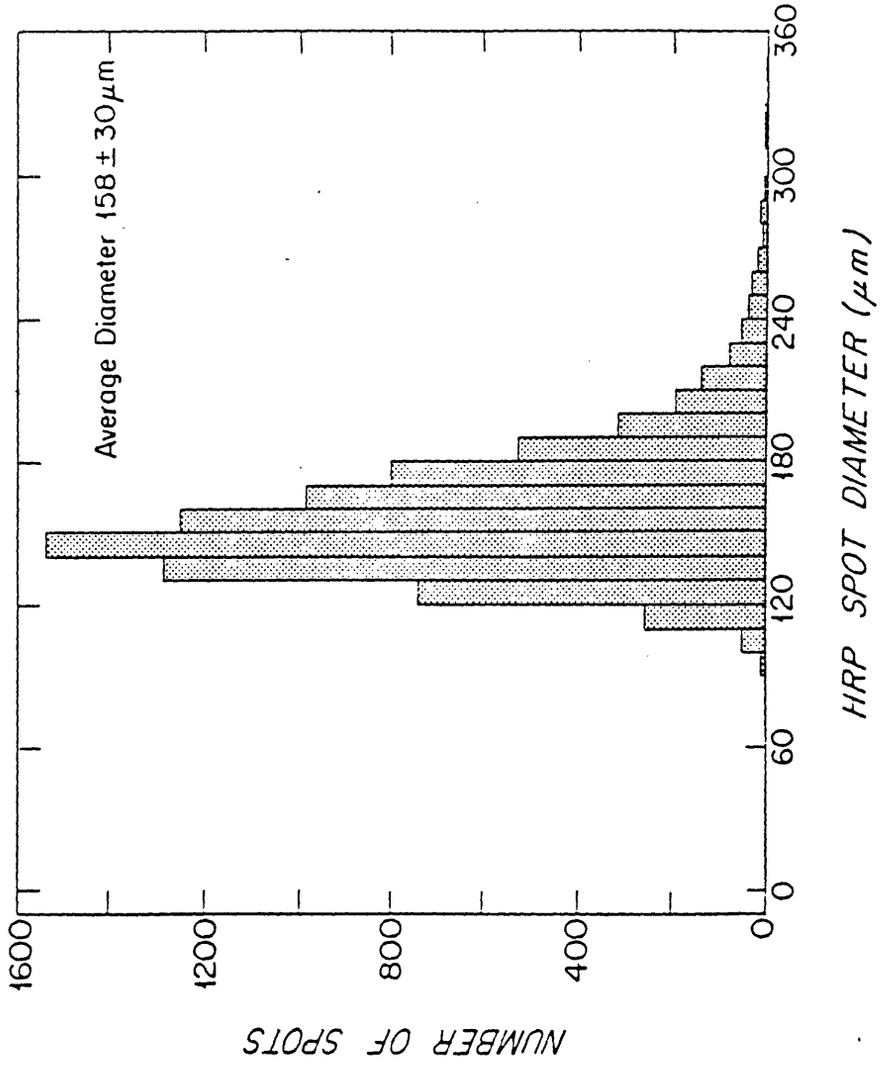
Average Diameter 158 ± 30μm
NUMBER OF SPOTS
0
400
800
1200
1600
0
60
120
180
240
300
360
HRP SPOT DIAMETER (μm)

Figure 2.2

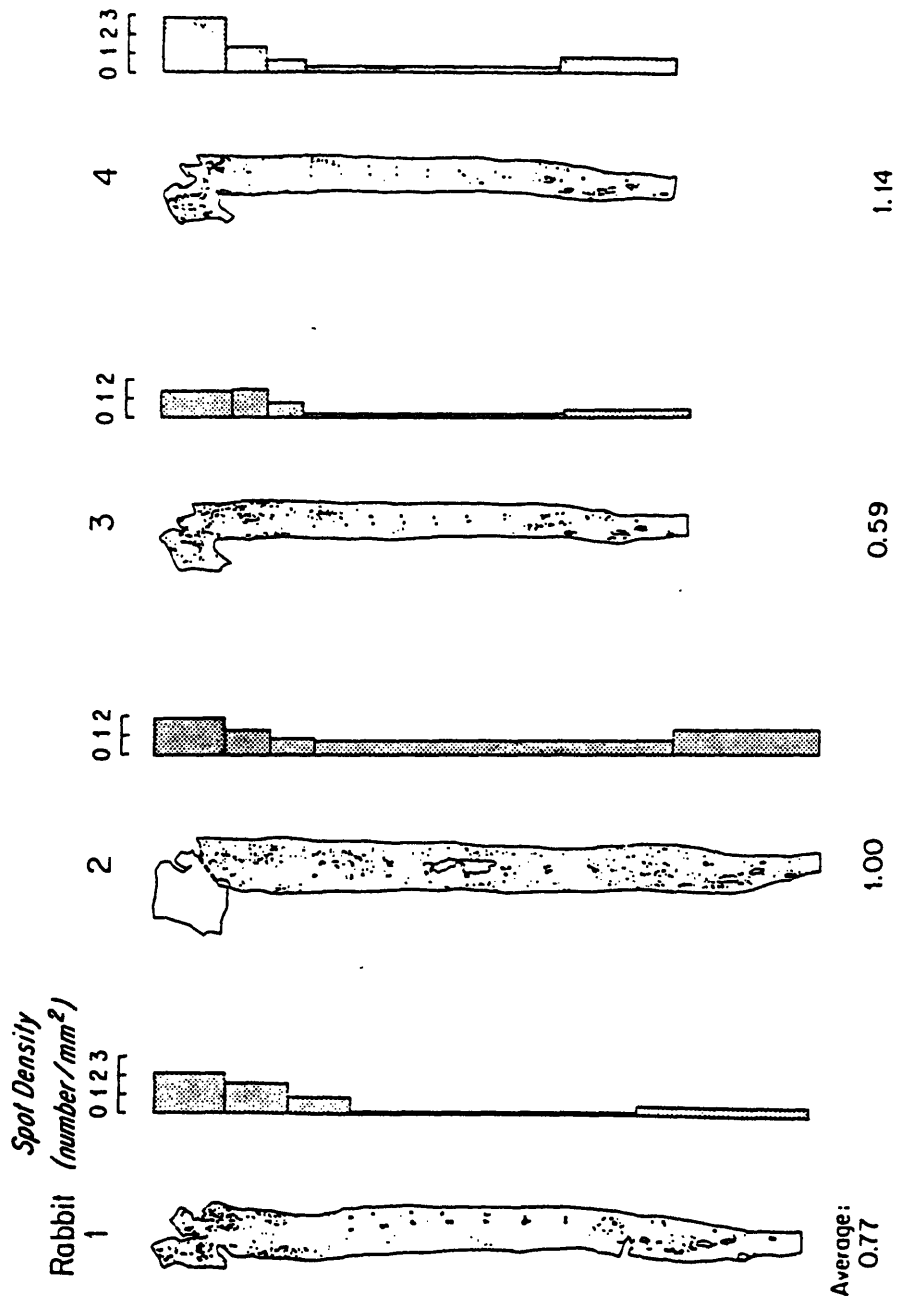
Spot Density (number/mm²)
0 1 2 3
Rabbit
1
2
3
4
0 1 2
0 1 2
0 1 2 3
1.00
0.59
1.14
Average: 0.77

Figure 2.3

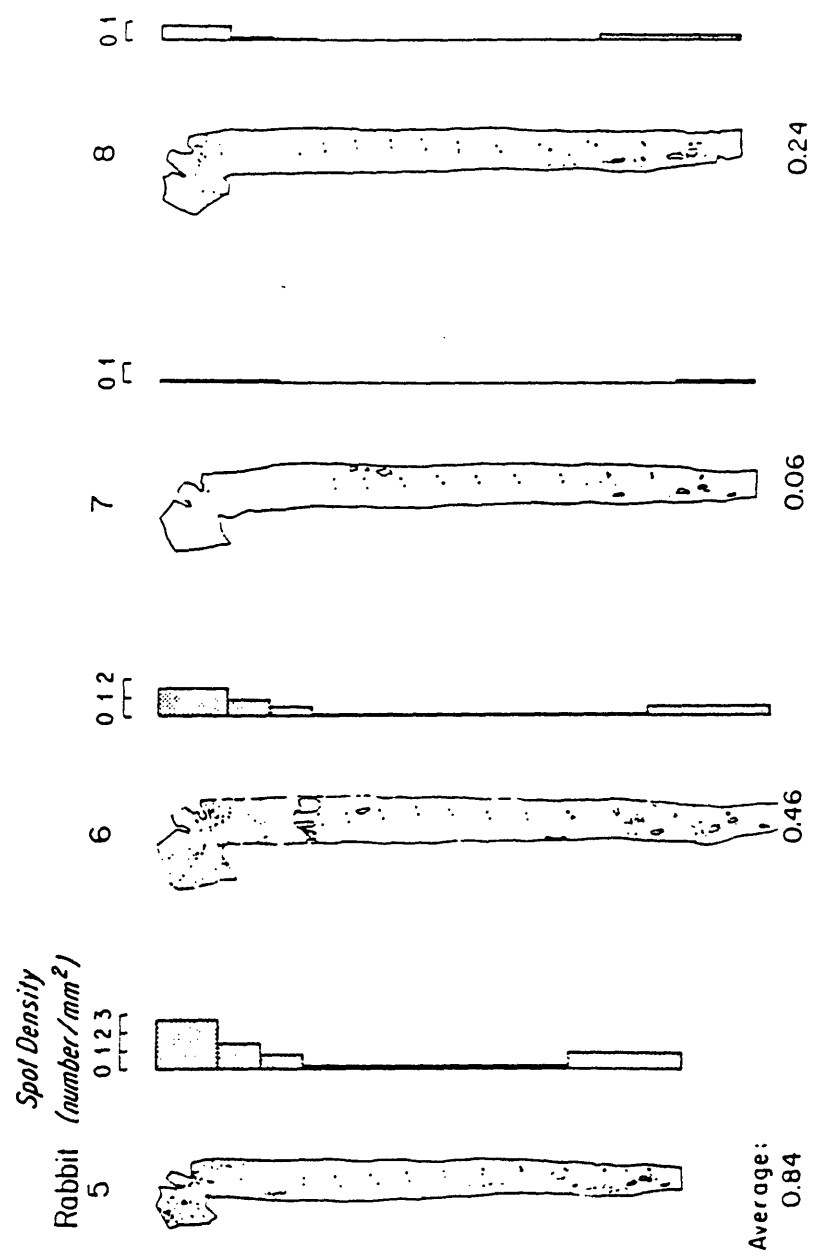
Spot Density (number/mm²)
Rabbit
5
0 1 2 3
Average: 0.84
6
0 1 2
0.46
7
0 1
0.06
8
0 1
0.24

Figure 2.4

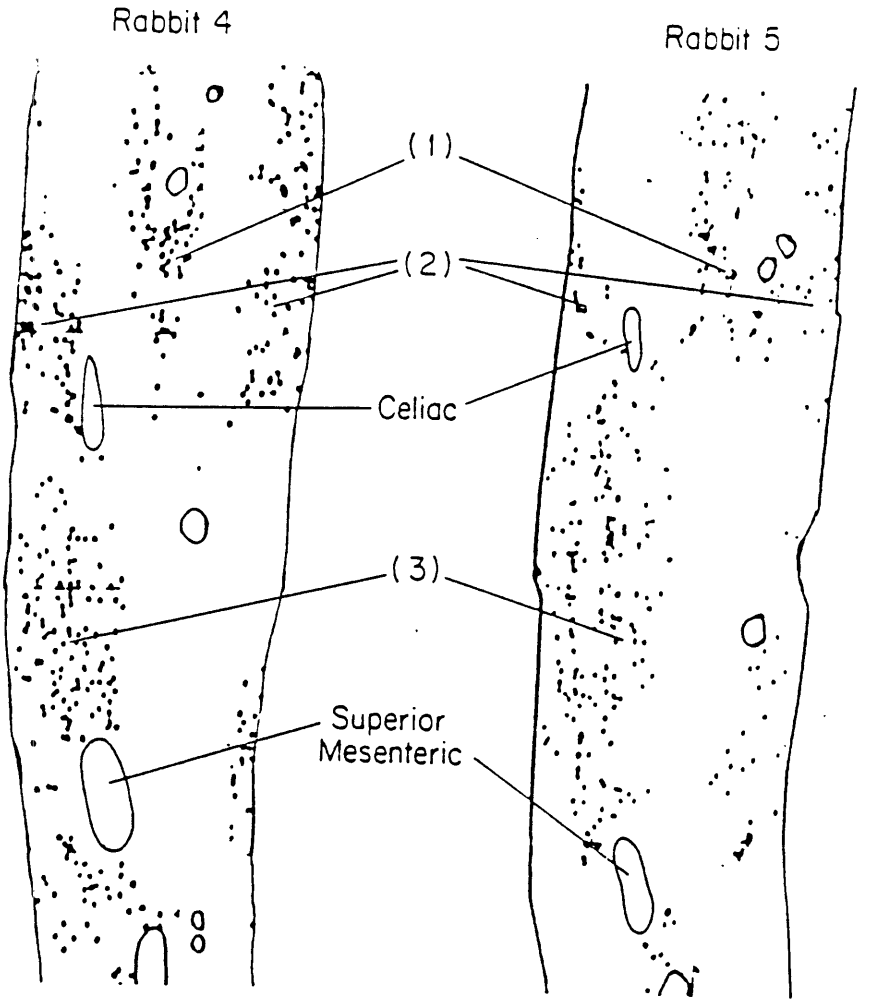

Figure 2.5

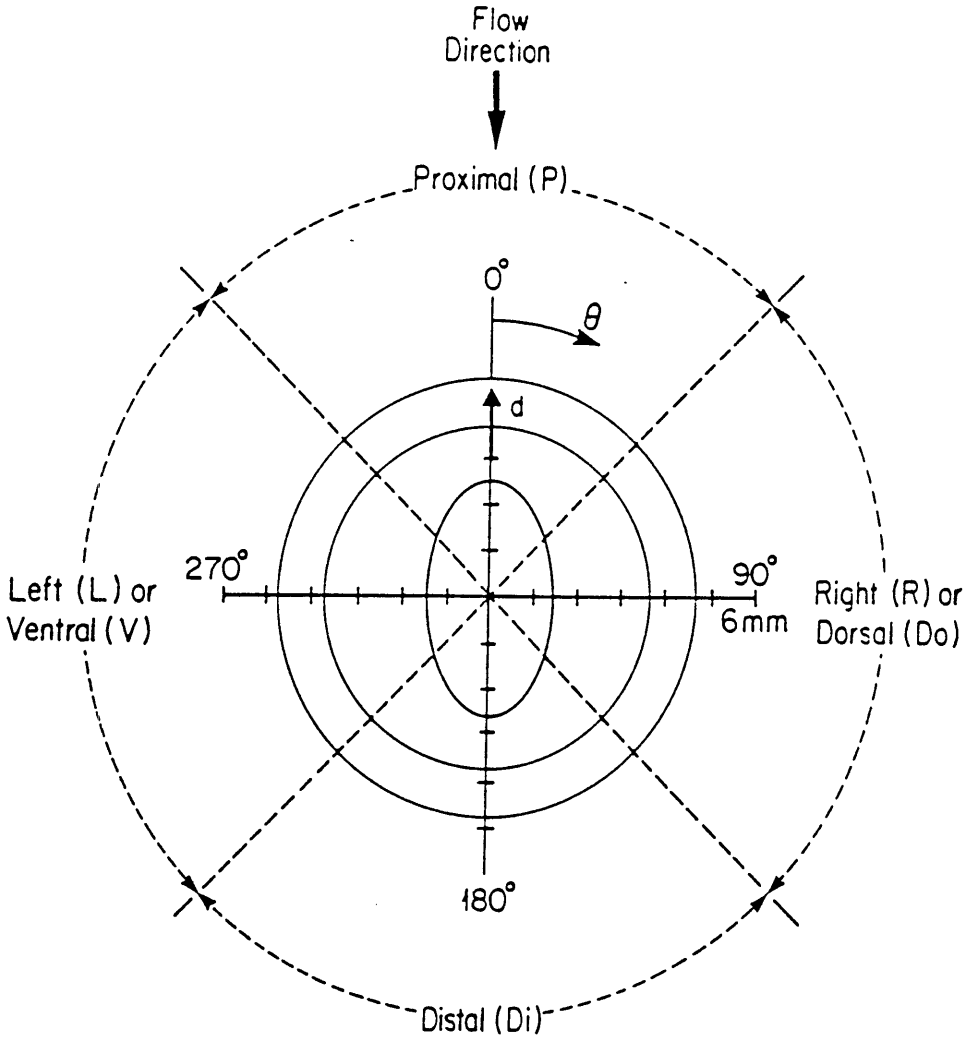
Flow
Direction
Proximal (P)
0°
θ
d
270°
90°
6mm
Left (L) or
Ventral (V)
Right (R) or
Dorsal (Do)
180°
Distal (Di)

Figure 2.6

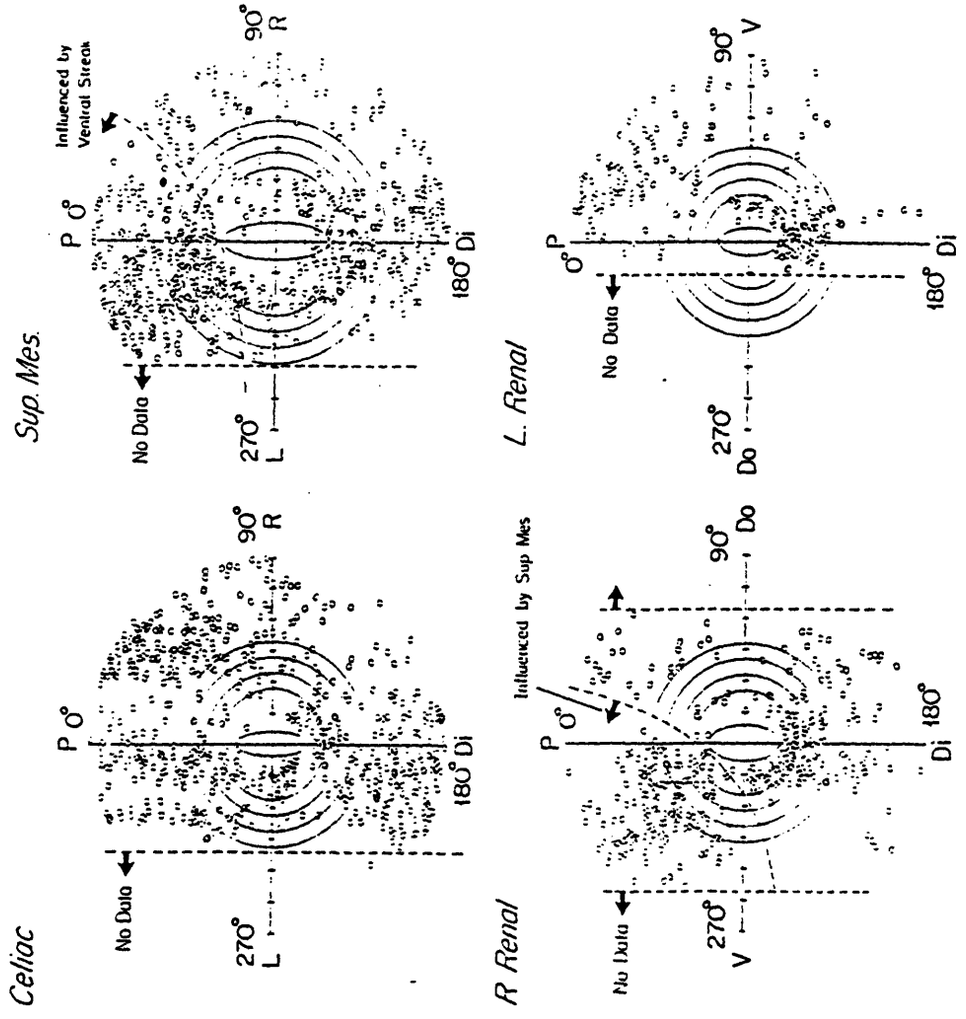
Sup. Mes.
Influenced by Ventral Streak
P 0°
90° R
180° Di
No Data
270° L
L. Renal
90° V
180° Di
No Data
270° Do
Celiac
P 0°
90° R
180° Di
No Data
270° L
R Renal
Influenced by Sup Mes
90° Do
P 0°
180° Di
No Data
270° V

Figure 2.7

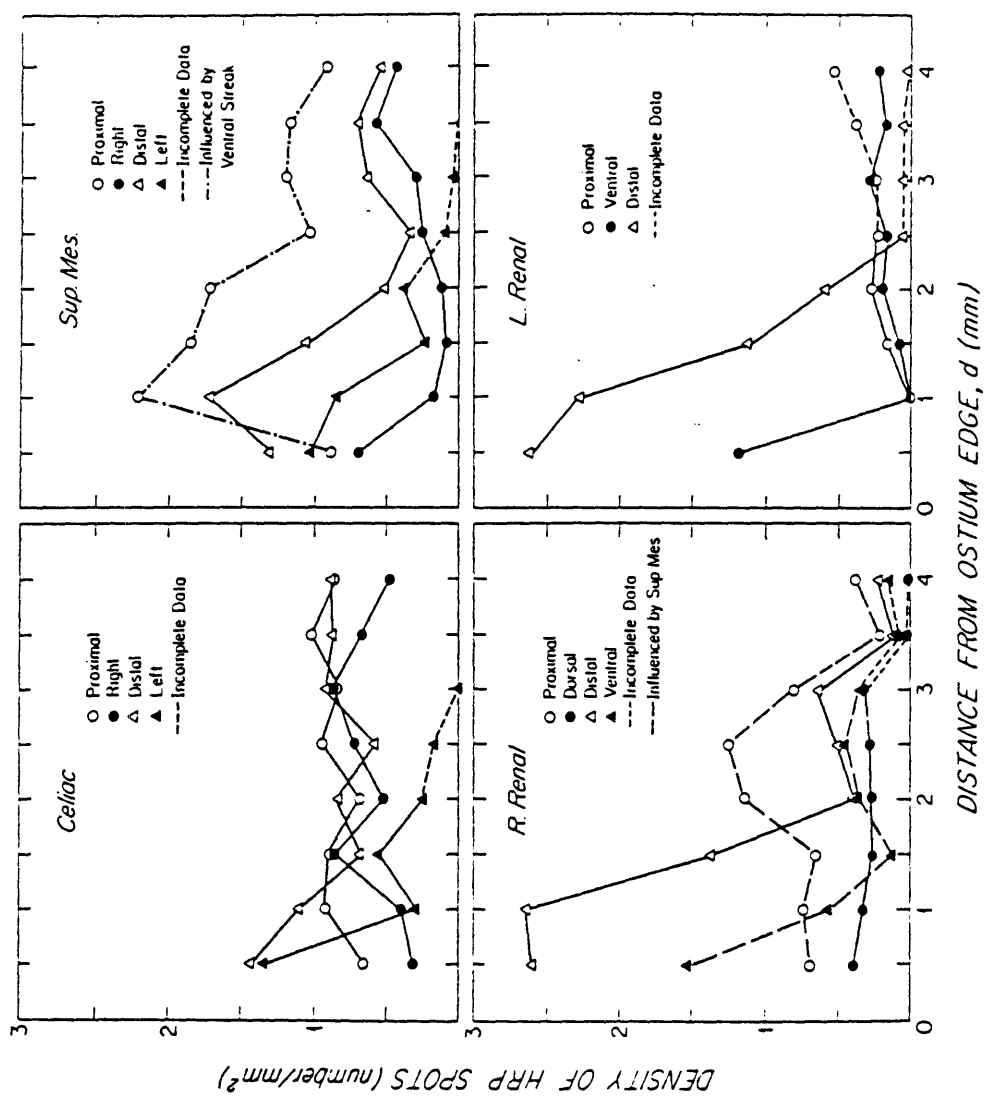
Celiac
Proximal
Right
Distal
Left
Incomplete Data
Sup. Mes.
Proximal
Right
Distal
Left
Incomplete Data
Influenced by Ventral Streak
R. Renal
Proximal
Dorsal
Distal
Ventral
Incomplete Data
Influenced by Sup Mes
L. Renal
Proximal
Ventral
Distal
Incomplete Data
DENSITY OF HRP SPOTS (number/mm²)
DISTANCE FROM OSTIUM EDGE, d (mm)

Figure 2.8

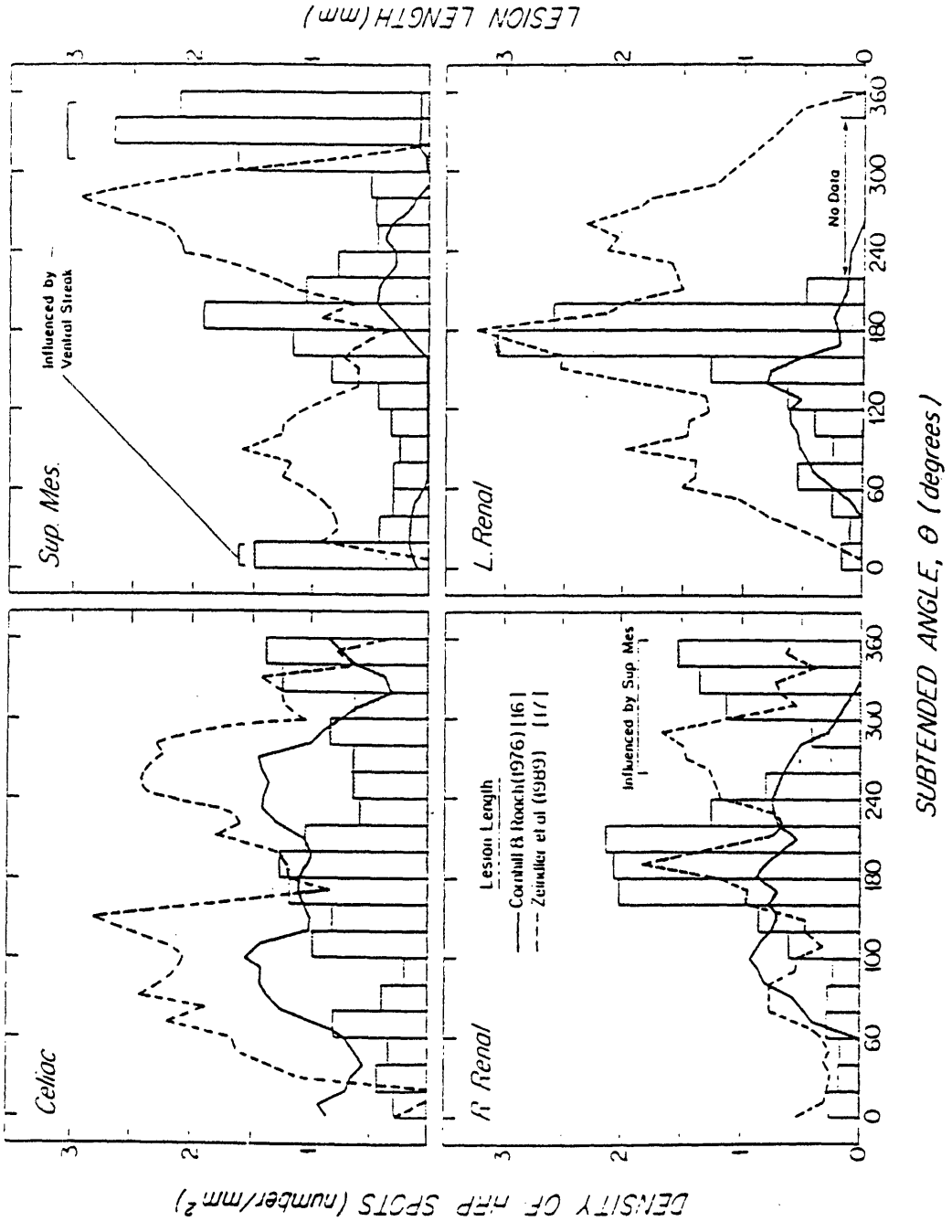
LESION LENGTH (mm)
Sup. Mes.
Influenced by Ventral Streak
Celiac
L. Renal
No Data
R. Renal
Influenced by Sup. Mes
Lesion Length
Cornhill & Roach (1976) [16]
Zeindler et al (1989) [17]
DENSITY OF HRP SPOTS (number/mm²)
SUBTENDED ANGLE, θ (degrees)

Figure 2.9

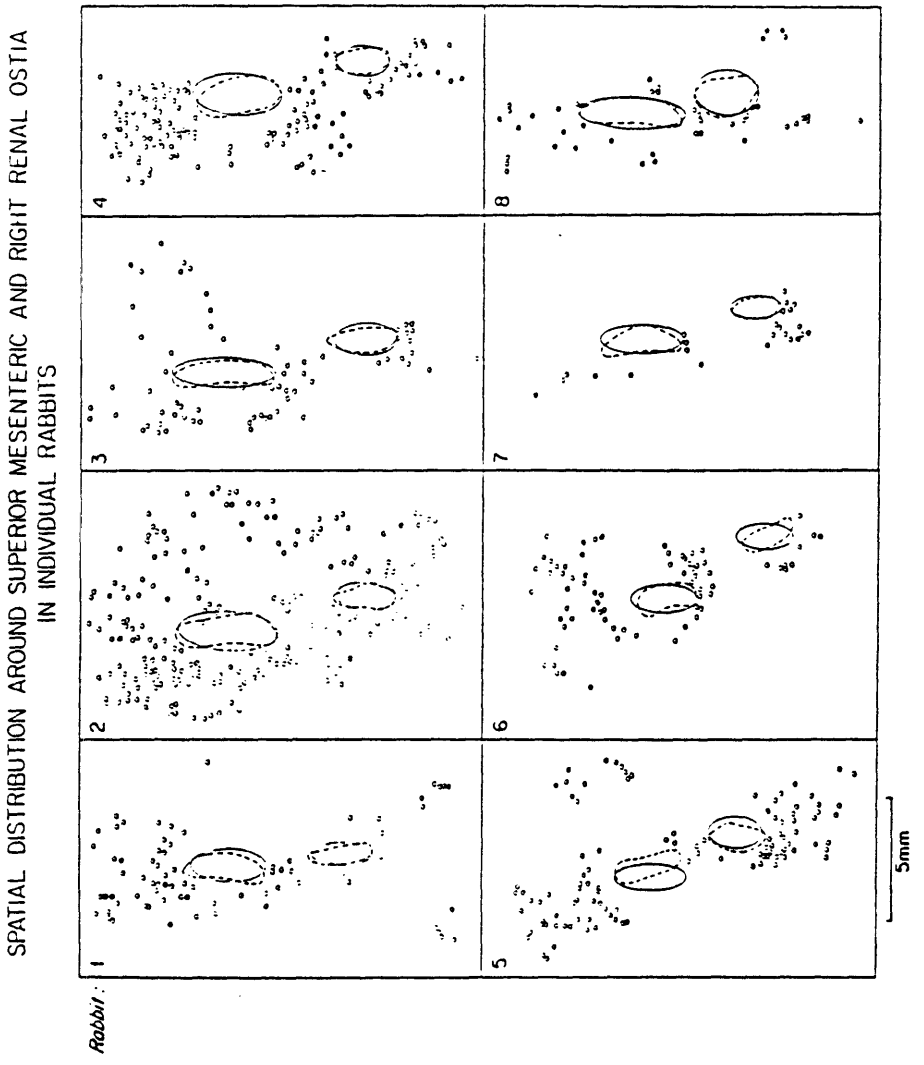
SPATIAL DISTRIBUTION AROUND SUPERIOR MESENTERIC AND RIGHT RENAL OSTIA
IN INDIVIDUAL RABBITS
Rabbit:
1
2
3
4
5
6
7
8
5mm

Figure 2.10

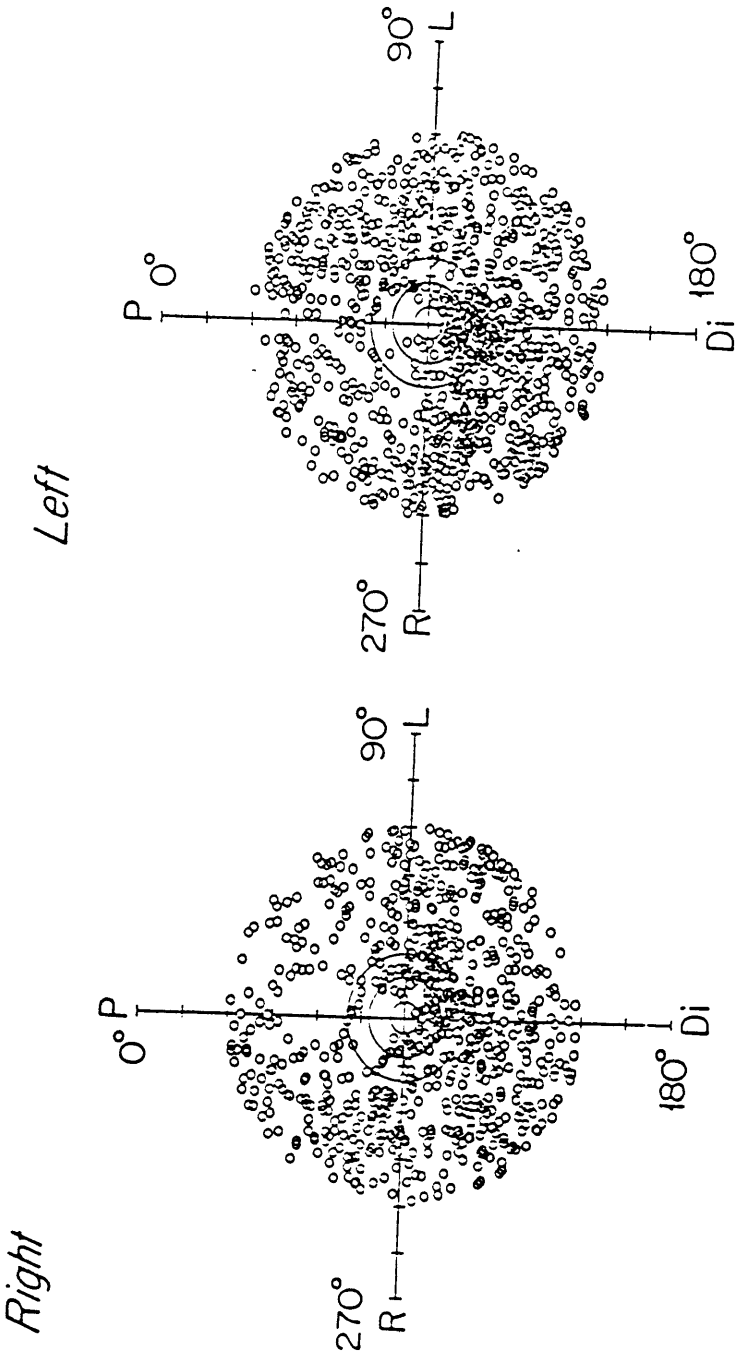

Figure 2.11

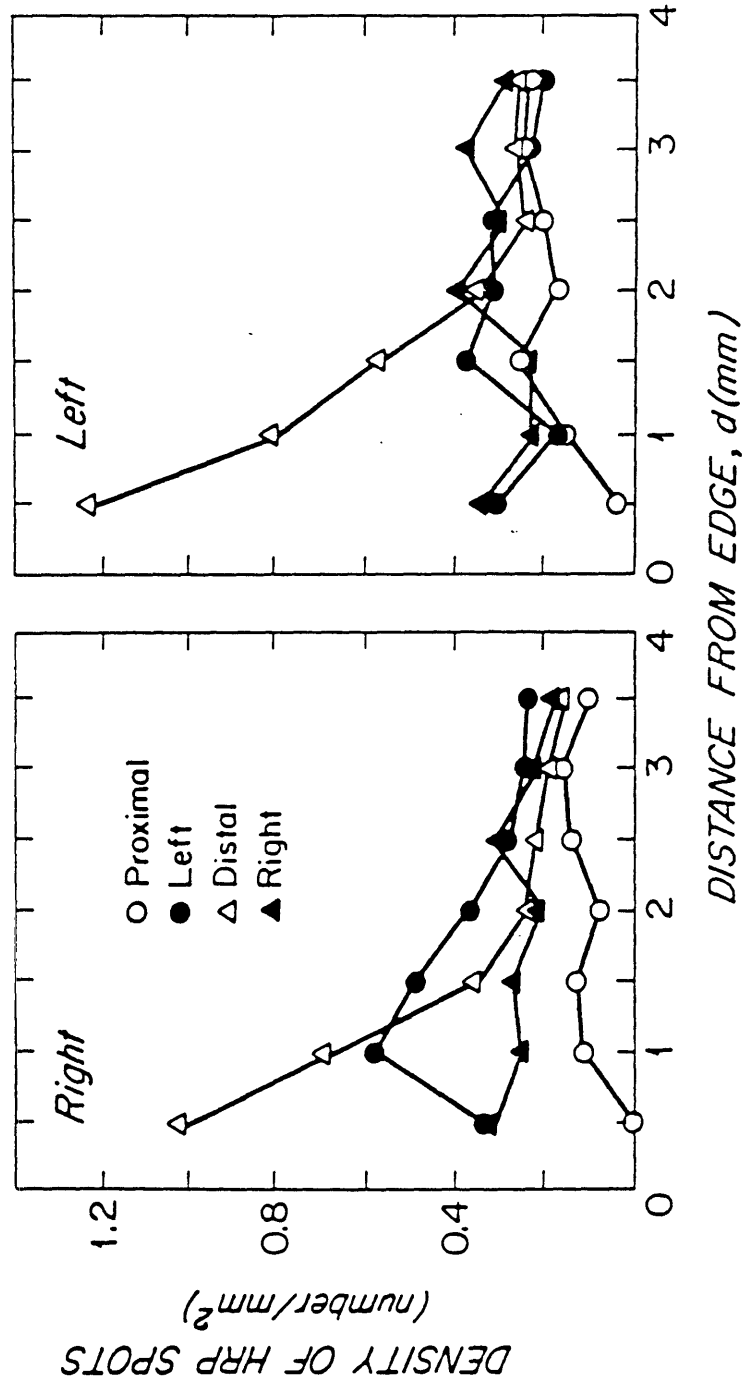
Left
Right
O Proximal
● Left
△ Distal
▲ Right
0
1
2
3
4
1.2
0.8
0.4
DENSITY OF HRP SPOTS
(number/mm²)
DISTANCE FROM EDGE, d(mm)

Figure 2.12

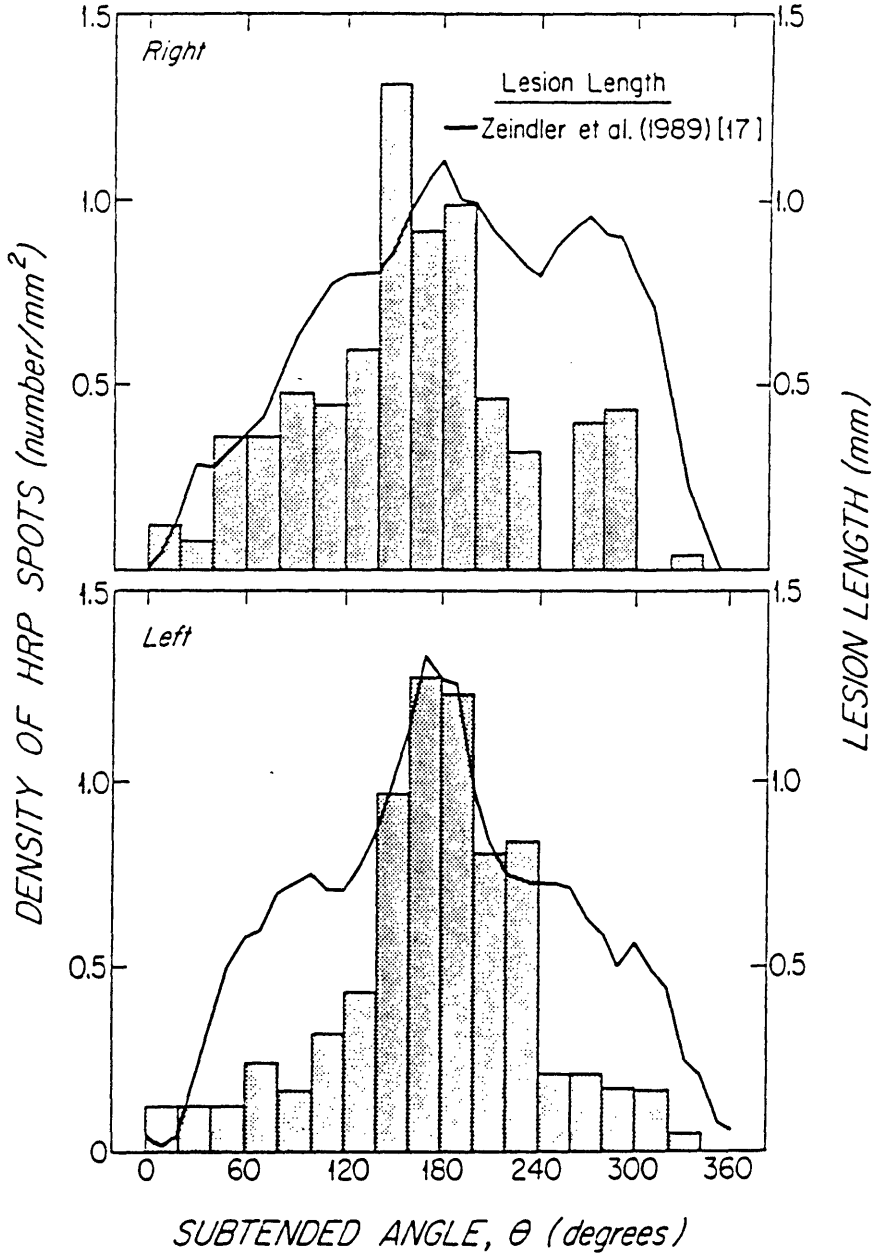
Right
Lesion Length
Zeindler et al. (1989) [17]
Left
1.5
1.0
0.5
0
0
60
120
180
240
300
360
DENSITY OF HRP SPOTS (number/mm²)
LESION LENGTH (mm)
SUBTENDED ANGLE, θ (degrees)

Figure 2.13

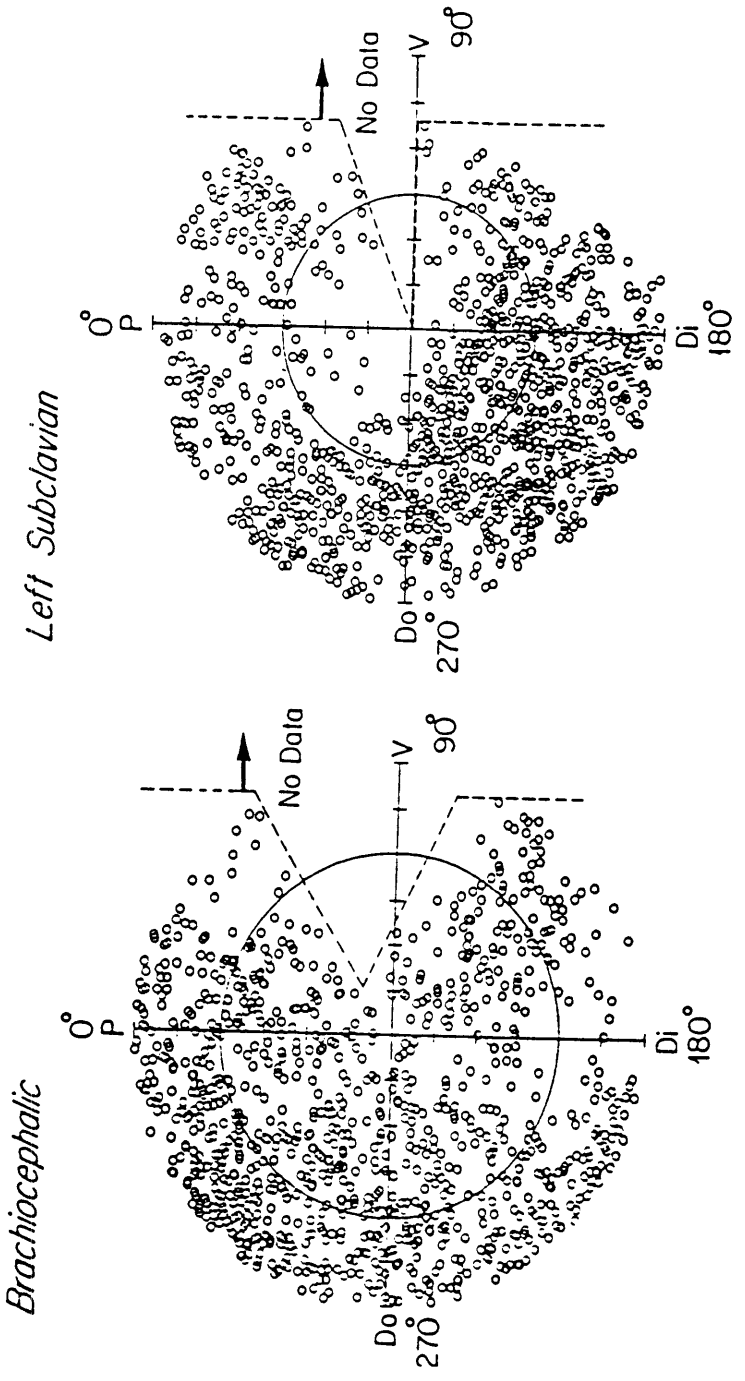
Left Subclavian
No Data
V
90°
0°
P
Di
180°
Do
270°
Brachiocephalic
No Data
V
90°
0°
P
Di
180°
Do
270°

Figure 2.14

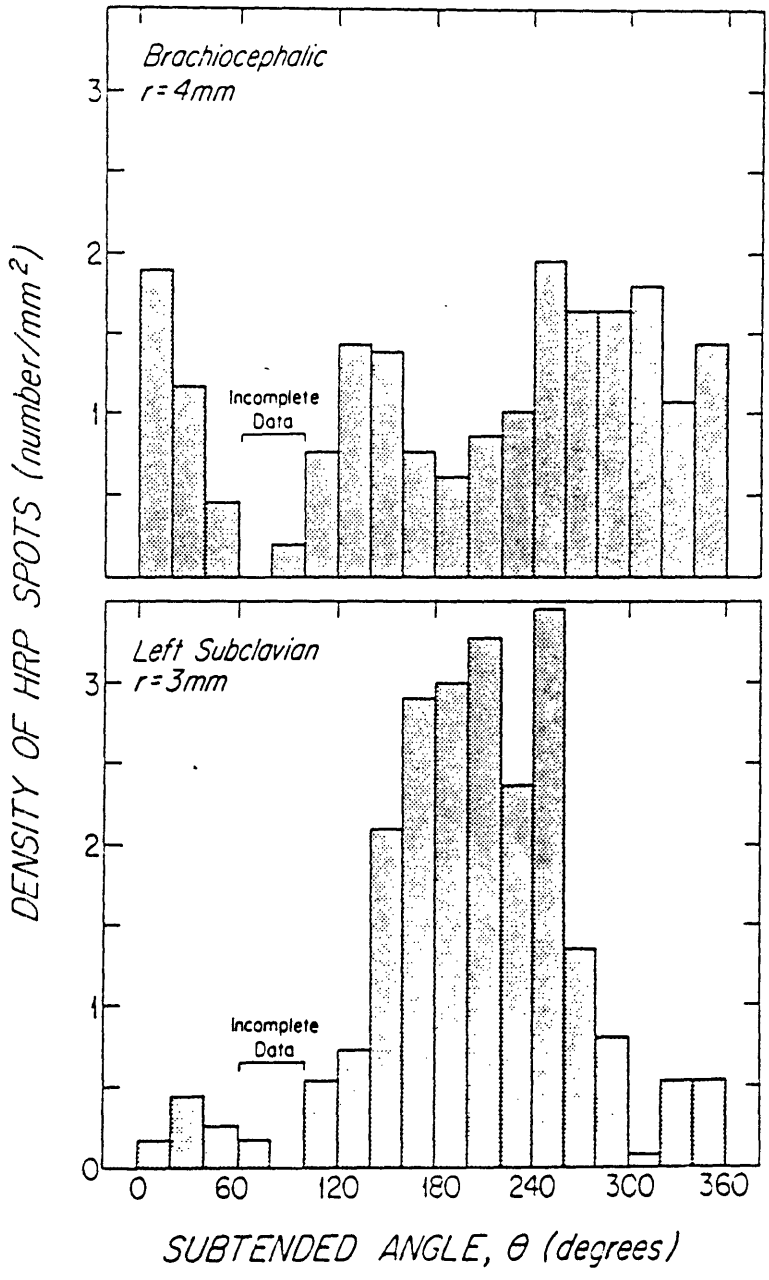
Brachiocephalic
r=4mm
Incomplete Data
Left Subclavian
r=3mm
Incomplete Data
DENSITY OF HRP SPOTS (number/mm²)
SUBTENDED ANGLE, θ (degrees)
0
1
2
3
0
60
120
180
240
300
360

Figure 2.15

Chapter Three

Measurement of Flowrates Through Aortic Branches in the Rabbit *In Vivo*

3.1 Introduction

3.1.1 Background

A knowledge of the relative flowrates in the major branches of the aorta *in-vivo* is important in studies of hemodynamics, drug delivery, and pharmacokinetics among others. Our specific interest in this problem is motivated by ongoing studies on the potential relationship of hemodynamics to atherosclerosis. We had previously reported the existence of punctate sites in the normal New Zealand White rabbit aorta that are highly permeable to horseradish peroxidase (HRP), an enzyme of molecular weight 40,000 and Stokes-Einstein radius about 3.0 nm, which is injected into the rabbit one minute before sacrifice and subsequently visualized *en face* by reaction with diaminobenzidine (DAB) and H_2O_2 [1]. These nearly-circular sites, referred to as "HRP spots", are approximately 160 μm in diameter, and they have been shown to be highly permeable to radio-labelled LDL [1]. Moreover, some of these HRP spots have been shown to correspond to abnormal, enlarged endothelial cells and to possess morphological features different from normal tissue [2]. More recently, we have used quantitative image analysis to perform a detailed mapping of the spatial distribution of the HRP spots on the aortic lumenal surface and to compute the density of the spots around the major aortic ostia [3]. That study revealed the existence of a non-random and qualitatively reproducible spot topographical distribution as well as preferred spot orientations around ostia, and these findings are consistent with an

influence of localizing factors such as detailed hemodynamics and/or arterial wall structural variations.

The experimental results of Karino and coworkers in glass models of arterial branching [4,5] and in transparent natural vessels [6-10] have revealed that the flow field within the aorta is sensitive to the values of the aortic flow splits, i.e. the fraction of the aortic flow entering each of the branches. Our interest in relating the topography of the HRP spots to the flow patterns in the rabbit aorta motivated the current study of the flow splits in the rabbit *in-vivo.* A knowledge of the flow areas of the various branches is not in itself sufficient for establishing the resulting flow splits because the actual flowrates within the various branches are primarily determined by the downstream resistance to flow in the microvasculature (the arterioles and capillaries) and hence may yield results significantly different from the geometric flow splits that are based solely on arterial dimensions. Under the assumption of Poiseuille flow, it has been shown that the arterial system accounts for only about 25% of the total resistance to flow in the human vascular bed, while the arterioles account for about 41% and the capillaries for about 27% (the entire venous system accounts for only 7%) [11].

Cardiac output and the fractions thereof comprising the cerebral, coronary, renal, and splanchnic circulation have been reported by several investigators [11-16]. Moreover, there exist data on flowrates in some of the major aortic branches of the dog [17-22]. The situation in the case of the rabbit, however, is entirely different. A detailed computerized literature search spanning the time period between 1970 and the present revealed that data on aortic flow splits in the rabbit is very sparse and scattered. Such paucity of measurements was surprising especially in view of the fact that the rabbit has long been used as an animal model in various areas of biomedical research. It

is therefore hoped that the results reported in this study may provide useful information to investigators not only in the field of atherosclerosis research, which is our group's major impetus, but also in other medical areas in which the rabbit represents an appropriate animal model.

3.1.2 Rabbit Aortic Anatomy

The anatomy of the rabbit aorta and its branches is depicted in Figure 3.1. The aorta emerges from the left ventricle and ascends dorsal to the sternum. The ascending aorta merges into the aortic arch which in turn leads to the descending thoracic aorta. The greater curvature of the aortic arch gives rise to two branches, the brachiocephalic, which shortly divides into the right subclavian and the two common carotid branches, and the left subclavian. The descending thoracic aorta gives rise along its dorsal surface to eight pairs of intercostal arteries, the most distal of which emerges approximately at the level of the diaphragm, which anatomically marks the division between the thoracic and abdominal aorta. Within the abdominal aorta, the celiac artery, a large vessel which branches into the left gastric, hepatic, and splenic arteries, emerges ventrally immediately caudal to the diaphragm. A ninth pair of dorsal intercostal (or phrenic) arteries arises either slightly proximal or distal to the celiac branch. Downstream of the celiac, the ventral superior mesenteric artery, typically the largest aortic branch, is encountered. Immediately distal to the superior mesenteric and emerging laterally is the right renal artery, followed by the left renal artery on the opposite side of the animal. Some distance downstream of the left renal is the ventral inferior mesenteric artery, and this is immediately followed by a pair of gonadal arteries which in the male rabbit are the internal spermatic arteries and in the female are the ovarian arteries. A pair of lumbar arteries is encountered some distance downstream

of the gonadal arteries, and these are eventually followed by the aorto-iliac bifurcation whose daughter vessels are the right and left common iliac arteries and which marks the anatomical termination of the aorta.

3.2 Materials and Methods

3.2.1 Flowrate Measurement System

A transit-time ultrasonic flowmeter and associated perivascular probes (Transonic Systems Inc., Ithaca, NY) was used for measuring the volumetric flowrates through the rabbit aorta and the major aortic branches *in-vivo*. Two perivascular probes were used, a larger 4S probe for the ascending thoracic aorta and a smaller 2R probe for all other locations. According to the manufacturer, the absolute accuracy was ±15% for the 4S prbe and ±10% for the 2R probe, and both probes were calibrated by the manufacturer. Each probe consisted of a body containing two ultrasonic transducers positioned on one side of a vessel and a fixed acoustic reflector bracket located on the opposite side of the vessel midway between the two transducers. The probes were connected to a single channel transit-time volume flowmeter (T101D) which displayed a digital reading of the mean flowrate. Analog outputs of both mean and pulsatile flowrates were recorded on a strip-chart recorder (Superscribe 4990, Houston Instruments, Austin, TX).

The vessel usually fit loosely within the probe window. Because the ultrasound wave must be transmitted throughout its course through a medium possessing similar acoustic properties to arterial tissue in order to yield accurate measurements, an acoustic couplant (H-R Lubricating Jelly, Transonic Systems Inc.) was applied to the window of the bracket through a 10 cc syringe.

3.2.2 Animal Experiments

3.2.2.1 Animal Preparation

Nine specific pathogen-free male, New Zealand White rabbits Hra:(NZW) SPF, *Onyctolagus Cunniculus* (Hazleton Research Products, Inc., Denver, PA) ranging in weight from 2.3 to 2.6 kg were used. The rabbits were individually housed in stainless steel cages (24"x30"x17"), fed a commercial rabbit diet (Purina Rabbit Chow HF5326, Ralston Purina Company, St. Louis, MO) and water *ad libitum,* and maintained in a controlled environment of 68-72 ^{o}F, relative humidity of 40-65%, and 12 hours light/12 hours dark. Ventilation was 100% fresh air with 12 complete room air changes per hour. The animals were fasted for 1 day prior to the experiments.

Initial anesthesia was induced by the intramuscular injection of 50 mg/kg ketamine and 10 mg/kg xylazine. After the rabbit lost consciousness, the left ear was shaved, and a catheter (24 ga, 2 in Intracath, Deseret Pharmaceutical Co., Sandy, VT) was inserted through one of the marginal ear veins, secured in place with tape, and tightly capped. The ventral surface of the rabbit was shaved, prepped with 70% isopropyl alcohol, and secured with limb ties in dorsal recumbancy. The catheter was then connected to a bag of sterile lactated Ringer's solution positioned about 100 cm above the operating table that provided continuous fluid administration averaging 10 ml/kg/hr throughout the experiment. Animals were maintained on circulating hot water heating pads (37.8 ^{o}C). ECG electrodes connected to the animal's four limbs provided continuous monitoring of heart rate.

3.2.2.2 Surgical Procedures

All procedures described here were reviewed and approved by the Committee on Animal Care at MIT. The right common carotid artery was

isolated through a 3 cm right paratracheal skin incision and cannulated with a catheter (16 ga, 2 in Angiocath, Deseret Pharmaceutical Co.). The catheter was fixed to the carotid artery with encircling ligatures of 3-0 silk and then connected to a pressure transducer (Statham Gould P231D, Gould Inc., Medical Products Division, Oxnard, CA) and monitor (Statham Gould Model SP14053, Gould Inc.) for continuous blood pressure monitoring. A tracheotomy was performed, and an uncuffed endotracheal tube (3 mm internal diameter) was inserted approximately 4 cm into the trachea, secured in place with encircling ligatures of 3-0 silk, and then connected to a respirator providing oxygen at about 1.5 liters/min. The respirator delivered a tidal volume of 25-50 ml of oxygen containing 0.5 to 2% isoflurane at 30 breaths per minute. Attempts were made to maintain heart rate and blood pressure constant by decreasing the administration rate of isoflurane and increasing the rate of lactated Ringer's solution infusion in response to decreased heart rate and blood pressure.

A ventral midline laperotomy was performed. The abdominal contents were retracted to the rabbit's left side and maintained moist by covering them with saline-soaked gauze. Various sections of the aorta and aortic branches were isolated with a combination of blunt and sharp dissections. A portion of the abdominal aorta a short distance proximal to the iliac bifurcation and the right and left iliac vessels were first isolated. Proceeding proximally, the right renal artery, superior mesenteric, and celiac arteries were isolated. The abdominal contents were then shifted to the animal's right side, and the left renal artery was isolated. The most difficult abdominal vessels to isolate were the right renal and the celiac branches. The right renal artery often lay immediately dorsal to the larger and more fragile right renal vein; on several occasions, the vein had to be retracted to provide access to the artery.

Moreover, perirenal fat often obscured the location of the artery. The primary difficulty with the celiac stemmed from access to the vessel being limited by its close proximity to the liver and stomach. Furthermore, only a short length was available for positioning the flow probe because the artery often branched immediately into its daughter vessels.

After the abdominal vessels were isolated, the abdomen was closed with a simple continuous pattern of 3-0 nylon to minimize evaporative heat and fluid losses. A sternotomy was then performed and a self-retaining retractor used to facilitate isolation of the thoracic vessels. The pericardium was incised, and a thymactomy was performed to expose the aortic arch and its branches. A section of the ascending aorta
was then isolated, followed by the brachiocephalic and the left subclavian arteries. Because the right common carotid artery was cannulated for blood pressure measurements, blood from the brachiocephalic vessel flowed only into the left common carotid and the right subclavian arteries.

Within the thoracic aorta, the most difficult branch to isolate was the left subclavian because it has intimate fascial attachments and a short length available for isolation prior to entering the rabbit's left foreleg. No attempt was made to isolate the inferior mesenteric, phrenic, intercostal, gonadal, or lumbar branches of the aorta, all of which were much smaller vessels.

3.2.2.3 Flowrate Measurements

Mean and instantaneous (pulsatile) flowrate measurements were performed after the vessels were isolated. The 4S probe was first used to measure the total flowrate entering the ascending aorta. The flowrates through the brachiocephalic and left subclavian vessels were next measured using the 2R probe. The abdomen was then reopened and the abdominal contents

again retracted to the animal's side to regain access to the abdominal vessels previously isolated. Flowrates were measured sequentially in the superior mesenteric and celiac arteries, the abdominal aorta proximal to the iliac bifurcation, and the right iliac, left iliac, right renal, and left renal arteries. Because arteries vasoconstrict upon handling, which may significantly alter the resistance to flow within a vessel, a vasodilator, 0.5% Lidocaine (Phoenix Pharmaceutical, St. Joseph, MO), was applied topically through a 5 cc syringe to the periphery of each vessel before mounting the perivascular ultrasonic probe. In addition to mounting the probe and applying the vasodilator and acoustic couplant, time was needed for the flow reading to equilibrate at every step and for recording both the mean and pulsatile flow signals. The procedure at each site averaged about 15 min, and the complete set of measurements took about 150 min. During this period, the ascending aorta flowrate decreased with time. Therefore, additional measurements of the flowrate through the ascending aorta were made at various stages during the abdominal measurement procedures to establish a more accurate assessment of the instantaneous flowrate entering the aorta.

The measured flowrates were somewhat sensitive to the angle at which the perivascular probes were mounted on the surface of the vessel. This was particularly the case in the curved aortic arch. In order to establish consistency, the probe was typically rotated through a wide range of angles, and the maximum flowrate detected was taken as the actual flowrate through the vessel. Furthermore, in certain instances, the weight of the ultrasonic probe induced a kink or bend in the vessel and hence partially obstructed the flow. This problem was most pronounced in the renal arteries where the length of the artery (i.e. the length of the vessel between the aorta and the kidney) was large, and the arteries were loosely attached to surrounding perirenal

tissue so that they could become bent easily. This problem was circumvented by ascertaining that the probe fit loosely around the vessel, and this in some instances necessitated resting the connection cable of the probe on an additional support so that its weight was primarily borne by this support and not by the artery.

Following completion of the measurements, the animal was euthanized with an overdose (about 3 ml) of sodium pentobarbital (6 g/ml, Lemmon Co., Sellersville, PA) injected either into the marginal ear vein catheter or directly into the left ventricle. The animal died immediately.

3.3 Results

3.3.1 Blood Pressure and Heart Rate

The nine-rabbit average variation of mean blood pressure and of heart rate with time from the beginning of surgery are shown in Figures 3.2 and 3.3, respectively. Blood pressure and heart rate decreased progressively with time during the course of the measurements, presumably as a result of the combined effects of evaporative fluid and heat losses and anesthesia-induced myocardial depression. These decreases were partially compensated for by increasing the lactated Ringer's solution infusion rate and by decreasing the amount of isoflurane administered. Changes in administration occasionally led to sudden jumps in both blood pressure and heart rate. However, there were limitations on the maximum fluid infusion rate imposed by the reluctance to alter the flow properties of blood and on the decrease of isoflurane imposed by the need for a sufficient amount to maintain deep anesthesia throughout the procedure. Heart rate was generally more easily maintained than blood pressure, and the flow rate measurements at branches were always collected before excessive blood pressure drop was encountered.

3.3.2 Variation of Aortic Flowrate with Time

Table 3.1 summarizes measurements of the mean volumetric flowrate in the ascending aorta for each of the nine rabbits studied. The flowrate into the aorta decreased with time throughout the course of the lengthy data acquisition sessions. The exact times at which the flowrates were measured were not recorded, and each flowrate is tabulated at its sequential measurement number. For example, the ascending aorta flowrate measurements in rabbit 1 were the first and tenth measurements made with eight branch flowrate measurements in between. The measurement number representation in Table 3.1 is roughly equivalent to displaying the data as a function of time, since each measurement took approximately 15 min.

3.3.3 Mean Flow Splits

Table 3.2 summarizes the mean aortic flow splits for the nine rabbits. The measured flowrate in each of the isolated aortic branches was divided by the flowrate in the ascending thoracic aorta of the same rabbit and expressed as per cent. The total aortic flowrate appropriate to each branch measurement was estimated by interpolating between the two nearest ascending aorta flowrate measurements in Table 3.1. Although there is considerable scatter in the flow split data among the individual rabbits, the general trends are reproducible. The flowrate through the superior mesenteric artery is the highest (32% of the total), followed by the flowrate through the celiac artery (24%). The two flow splits are significantly different ($p<0.05$). These two vessels receive on average about 56% of the total aortic flowrate. Each of the other major branches receives a much smaller fraction of the total aortic flowrate, ranging from about 5 to 8%. Flow splits for paired vessels were

symmetric. The mean flow splits through the right and left renal arteries were not significantly different ($p>0.05$), nor were those through the right and left common iliac branches. Because the right carotid artery was cannulated for blood pressure measurement, the flowrate through the brachiocephalic artery may have been significantly underestimated.

The sum of the flowrates through all eight vessels studied averaged 94±12% of the total aortic flow. Therefore, an average of only about 6% of the mean aortic flow goes into the eight pairs of intercostal arteries and the nferior mesenteric, phrenic, gonadal arteries, and lumbar arteries all together although the distribution among these vessels is not known.

The nine experiments reported here were performed on rabbits that had been fasted for about 24 hours prior to surgery and with the topical addition of a vasodilator immediately before mounting the perivascular flow probes during surgery. In addition, three exploratory experiments were performed on rabbits that had not been fasted and without vasodilator application. The absence of vasodilator had its most pronounced effect on the renal arteries for which vasoconstriction upon handling was easily observed visually. Without vasodilator, flow splits within the two renal arteries averaged 1.5%, about one-fourth of the value measured with vasodilator (Table 3.2). The effect of the vasodilator on the other vessels was not nearly as pronouned.

3.3.4 Pulsatile Flowrate Profiles

Figure 3.4 illustrates typical instantaneous pulsatile flowrate profiles in the ascending aorta, the isolated abdominal aortic section proximal to the iliac bifurcation, and each of the eight aortic branches studied. Reverse flow during diastole was always observed in the ascending thoracic aorta, was never observed in the section of the lower abdominal aorta proximal to the iliac

bifurcation or in the renal or iliac arteries, and was observed with varying frequencies in the aortic branches. Specifically, reverse flow during diastole was observed in the brachiocephalic artery in three of the nine rabbits studied (rabbits 4,6, and 9), in the left subclavian artery in one of the nine rabbits (rabbit 4), in the celiac and superior mesenteric arteries in five of the nine rabbits (rabbits 1,3,4,6, and 8 in the celiac and 2,4,5,6, and 8 in the superior mesenteric), and never in the renal or iliac arteries.

3.3.5 Peak Pulsatile Flow Splits

Flow splits in terms of the peak pulsatile flowrates are tabulated in Table 3.3. As in Table 3.2, there was considerable variability among animals. The highest flow splits were in the superior mesenteric and celiac arteries (30 and 23%, respectively) with the remaining branches receiving considerably smaller fractions (about 3 to 6%) of the aortic flowrate. The renal and iliac flow splits were substantially lower than their mean flow counterparts. Only 78% of the total peak pulsatile aortic flowrate was accounted for by the peak flowrate in the eight major branches, as compared to 94% for the mean flowrate. As in the case of mean flowrate, the peak pulsatile flow splits in paired vessels were symmetric. The right and left renal flow splits were not different ($p>0.05$), nor were the flow splits for the right and left iliac arteries ($p>0.05$).

3.3.6 Peak Pulsatile to Mean Flowrate Ratios

The occurrence of reverse flow in diastole within the aortic arch and in some of the aortic branches, but not in the abdominal aorta proximal to the iliac bifurcation or in the renal or iliac arteries, may be attributable, at least in part, to variations in the elastic properties of the arterial wall at these various locations. As an indicator of relative wall distensibility, we calculated the ratio of peak

pulsatile to mean flowrates shown in Table 3.4. The ratios of peak pulsatile to mean flowrates divide into two general groups, namely those of the ascending aorta and aortic branches down to the superior mesenteric artery, in which the ratio is higher, and those of the lower abdominal aorta and the renal and iliac branches, in which the ratio is lower. Although the superior mesenteric and right renal arteries are generally very close to one another in the rabbit, the peak pulsatile to mean flowrate ratios associated with the superior mesenteric and right renal arteries are significantly different ($p<0.05$), thereby suggesting the existence of a sharp decrease in wall distensibility beyond the superior mesenteric artery.

3.4 Discussion

This paper has reported the first known detailed *in-vivo* measurements of mean and peak pulsatile aortic flow splits in the rabbit. This information is considered vital for formulating physiologically-accurate experimental and numerical models of the flow field in the rabbit aorta which are of interest from the standpoint of investigating potential relationships between arterial hemodynamics and early atherosclerosis in the rabbit.

The measurements have demonstrated that the largest abdominal vessels, namely the superior mesenteric and celiac arteries, receive the bulk of the aortic flow (about 56% combined in mean flow), while each of the remaining aortic branches receives a significantly smaller flowrate (about 5-8% each). The flow splits in paired vessels are symmetric. Additionally, we found flow reversal from the aortic branches back into the aorta during diastole with varying frequency in the brachiocephalic, left subclavian, celiac, and superior mesenteric arteries. Reverse flow was never observed in the renal or the iliac arteries.

The peak pulsatile flow splits were also largest in the celiac and superior mesenteric arteries (about 53% combined), while the other vessels received considerably less flow (3-6% each). The finding that the peak pulsatile flow splits in the renal and iliac arteries are smaller than their mean flow counterparts is consistent with the observation that the renal and iliac arteries do not undergo reverse flow in the diastolic phase of the cardiac cycle. As flow in the celiac and superior mesenteric arteries reverses direction in diastole, blood reenters the aorta through these vessels, and some of this reverse flow probably enters the renal and iliac branches which do not undergo flow reversal. Therefore, the flow splits in the renal and iliac arteries have to be relatively large during the diastolic phase. Consequently, in order to yield the mean flow splits reported in Table 3.2, the flow splits in the renal and iliac arteries have to be relatively small during systole. This, however, only partially explains the relatively smaller renal and iliac peak pulsatile flow splits shown in Table 3.3. Another point in this regard is that the renal and iliac arteries are significantly less elastic than the other aortic branches. Therefore, at peak pulsatility the diameters of the renal and iliac arteries increase by a smaller amount than the diameters of the other branches so that the renal and iliac arteries become sites of relatively increased resistance to flow thereby leading to the smaller flow splits through them at peak pulsatility.

The ratio of peak pulsatile to mean flowrates has been used as a criterion for the assessment of vessel wall elasticity and has demonstrated that the abdominal aorta is considerably less elastic than the ascending thoracic aorta, and that the renal and iliac arteries are considerably less distensible than the other aortic branches. Harkness *et al.*[23] measured the elastin to collagen ratio in various parts of the dog aorta and aortic branches and

demonstrated an abrupt decrease in aortic distensibility at the level of the diaphragm.

In the current study, a vasodilator has been applied to the periphery of vessels prior to making the *in vivo* flowrate measurements in order to avoid problems with vessel vasoconstriction. This is particularly important in view of the fact that various vessels do not vasoconstrict equally. The effect of the vasodilator is most pronounced in the case of the renal arteries but is not nearly as significant in the other vessels. Fasting the animal prior to performing the measurements is important so as not to bias the data by having a situation where an inordinately large fraction of the aortic flow rushes to the stomach through the mesenteric vessels in order to digest freshly-consumed food. There is experimental evidence that splanchnic blood flow is higher in the fed than in the fasted animal [19,24,25] and that vessel autoregulation is somewhat sensitive to whether or not the animal has been fasted [20,21].

The relatively wide range of mean and peak pulsatile flow split values in the nine animals studied is probably a consequence of several factors. Chief among these factors is inherent variability in animal response to anesthesia as well as variations in metabolic characteristics and rates of evaporative heat and fluid losses. The flow splits associated with the celiac and superior mesenteric arteries span a larger range than those associated with the other vessels since these two vessels supply the abdominal contents of the animal, and during the course of the measurements the abdominal contents were retracted to the animal's side to gain access to the aorta. Since the retraction of the mesentery cannot be performed exactly reproducibly, the pull imposed by the mesentery on the celiac and superior mesenteric vessels was somewhat different for each animal, and therefore the measured flowrates were undoubtedly affected.

It remains unclear at this time how truly physiological the measurements reported here are for several reasons. Firstly, the animal was maintained in dorsal recumbancy throughout the course of the measurements, and this posture is clearly not physiological although it is not obvious how posture may affect flow splits. Secondly, the animal was under continuous anesthesia, and this is associated with significant decreases in blood pressure and heart rate. A conscious rabbit normally has a mean arterial blood pressure of 90-100 mm Hg, a heart rate of 250-300 beats per minute, and a respiratory rate of 250-300 respirations per minute [26,29]. The blood pressure and heart rate values shown in Figures 3.2 and 3.3 and the 30 respirations per minute imposed by the respirator setting are dramatically different from the conditions associated with the conscious state. There is experimental evidence that anesthetics can alter hemodynamics directly *via* a vascular effect or indirectly through an effect on the heart and/or neurohumoral control mechanisms [30]. Furthermore, anesthesia affects the flowrates through the various aortic branches unequally so that it probably has an effect on flow splits[30]. Lastly, the influences of evaporative heat and fluid loss, possible alterations in serum electrolytes, and potential disruptions in the integrity of vasopressor reflexes upon flow splits are unknown and should be investigated.

Comparison of the abdominal flow splits in the rabbit to those in man under resting conditions reveals that the combination of renal and iliac flow in the rabbit is about half that in man (24% vs. about 50%), while the flow splits into the superior mesenteric and celiac branches are considerably larger in the rabbit (56% vs. about 25%). It is uncertain how much of this discrepancy is attributable to true species differences and how much is due to the effects of anesthesia and surgical manipulation; however, the results point to the importance of performing *in-vivo* experiments of the type reported here.

3.5 References

1. Stemerman MB, Morrel EM, Burke KR, Colton CK, Smith KA, Lees RS. Local variation in arterial wall permeability to low density lipoprotein in normal rabbit aorta. *Arteriosclerosis.* **6:** 64, 1986.

2. Morrel EM. Sites of enhanced ^{125}I-low density lipoprotein permeability in the rabbit aorta in vivo. Ph.D. Thesis, MIT, 1987.

3. Barakat AI, Uhthoff PAF, Colton CK. Quantitative topographical mapping of sites of enhanced HRP permeability in the normal rabbit aorta. *ASME J. Biomech. Eng.* **114;** 283, 1992.

4. Karino T, Kwong HHM, Goldsmith HL. Particle flow behaviour in models of branching vessels. I. Vortices in 90° T-junctions. *Biorheology.* **16:** 231, 1979.

5. Karino T, Goldsmith HL. Particle flow behavior in models of branching vessels. II. Effects of branching angle and diameter ratio on flow patterns. *Biorheology.* **22:** 87, 1985.

6. Karino T, Motomiya M. Flow visualization in isolated transparent natural blood vessels. *Biorheology.* **20:** 119, 1983.

7. Sohara Y, Karino T. Secondary flows in the dog aortic arch. In *Fluid Control and Measurement,* New York, Pergamon Press, pp. 143-147, 1985.

8. Karino T. Microscopic structure of disturbed flows in the arterial and venous systems, and its implication in the localization of vascular diseases. *Intl. Angiol.* **5:** 297, 1986.

9. Karino T, Goldsmith HL, Motomiya M, Mabuchi S, Sohara Y. Flow patterns in vessels of simple and complex geometries. *Annals N.Y. Acad. Sci.* **516:** 422, 1987.

10. Asakura T, Karino T. Flow patterns and spatial distribution of atherosclerotic lesions in human coronary arteries: left coronary artery. *Circ. Res.* **66:** 1045, 1990.

11. Burton AC. *Physiology and Biophysics of the Circulation-An Introductory Text.* Chicago: Year Book Medical Publishers, Inc., 1965.

12. McDonald DA. *Blood Flow in Arteries.* Baltimore: Williams & Wilkens, 1974.

13. Little RC. *Physiology of the Heart & Circulation.* Chicago: Year Book Medical Publishers, Inc., Third ed., 1985.

14. O'Rourke MF. Principles of arterial hemodynamics. In *Mechanics of the Circulation,* ter Keurs HEDJ, Tyberg JV, eds., Dordrecht: Martinus Nijhoff Publishers,1987.

15. Perry MA and Parker JC. Indicator dilution measurements of splanchnic blood flow. In *Measurement of Blood Flow - Applications to the Splanchnic Circulation,* Granger DN, Bulkley GB, eds., Baltimore: Williams & Wilkens, 1981.

16. Schmidt RF, Thews G, eds. *Human Physiology.* Berlin: Springer-Verlag, 1983.

17. Milnor WR. Normal circulatory function. In *Medical Physiology.* Vol.2, Mountcastle VB, ed., St. Louis: C.V. Mosby, 1980.

18. Falsetti HL, Kiser KM, Francis GP, Belmore ER. Sequential velocity development in the ascending and descending aorta of the dog. *Circ. Res.* **31:** 328, 1972.

19. Harkness MLR, Harkness RD, McDonald DA. The collagen and elastin content of the arterial wall in the dog. *Proc. Roy. Soc. B.* **146:** 541, 1957.

20. Granger DN, Richardson PDI, Kvietys PR, Mortillaro NA. Intestinal blood flow. *Gastroenterology.* **78:** 837, 1980.

21. Kvietys PR, Gallavan RH, Chou CC. Contribution of bile to postprandial intestinal hyperemia. *Am. J. Physiol.* **238:** G284, 1980.

22. Vatner SF, Franklin D, Van Citters RL. Mesenteric vasoactivity associated with eating and digestion in the conscious dog. *Am. J. Physiol.* **219:** 170, 1970.

23. Granger HJ, Norris CP. Intrinsic regulation of intestinal oxygenation in the anesthetized dog. *Am. J. Physiol.* **238:** H836, 1980.

24. Norris CP, Barnes GE, Smith EE, Granger HJ. Autoregulation of superior mesenteric flow in fasted and fed dogs. *Am. J. Physiol.* **237:** H174, 1979.

25. O'Rourke MF. Pressure and flow waves in systemic arteries and the anatomical design of the arterial system. *J. Appl. Physiol.* **23:** 139, 1967.

26. Lipman NS, Marini RP, Erdman SE. A comparison of ketamine/xylazine and ketamine/xylazine/acepromazine anesthesia in the rabbit. *Laboratory Animal Science.* **40:** 395, 1990.

27. Wyatt JD, Scott RAW, Richardson ME. The effects of prolonged ketamine-xylazine intravenous infusion on arterial blood pH, blood gases, mean arterial blood pressure, heart and respiratory rates, rectal temperature and reflexes in the rabbit. *Laboratory Animal Science.* **39:** 411, 1989.

28. Borkowski GL, Danneman PJ, Russell GB, Lang CM. An evaluation of three intravenous anesthetic regimens in New Zealand rabbits. *Laboratory Animal Science.* **40:** 270, 1990.

29. Weisbroth SH, Flatt RE, Kraus AL, eds. *The Biology of the Laboratory Rabbit.* Ch. 3. New York: Academic Press, 1974.

30. Kvietys PR, Barrowman JA, Granger DN. Effects of anesthetics and other experimental conditions on splanchnic blood flow. In *Measurement of Blood Flow - Applications to the Splanchnic Circulation,* Granger DN, Bulkley GB, eds., Baltimore: Williams & Wilkens, 1981.

Figure Captions

Figure 3.1 Anatomy of a typical rabbit aorta illustrating the major aortic branches.

Figure 3.2 Mean blood pressure as a function of time from the beginning of surgery. Mean blood pressure in each animal was calculated as one-third of the maximum systolic value plus two-thirds of the minimum diastolic value; the result agreed with the time-mean blood pressure displayed by the pressure monitor. Data represent mean±standard deviation of measurements from the nine rabbits studied.

Figure 3.3 Heart rate as a function of time from the beginning of surgery. Data represent mean±standard deviation of measurements from the nine rabbits studied.

Figure 3.4 Typical pulsatile volumetric flowrate profiles in the ascending aorta, the isolated section of the abdominal aorta proximal to the iliac bifurcation, and each of the eight aortic branches studied.

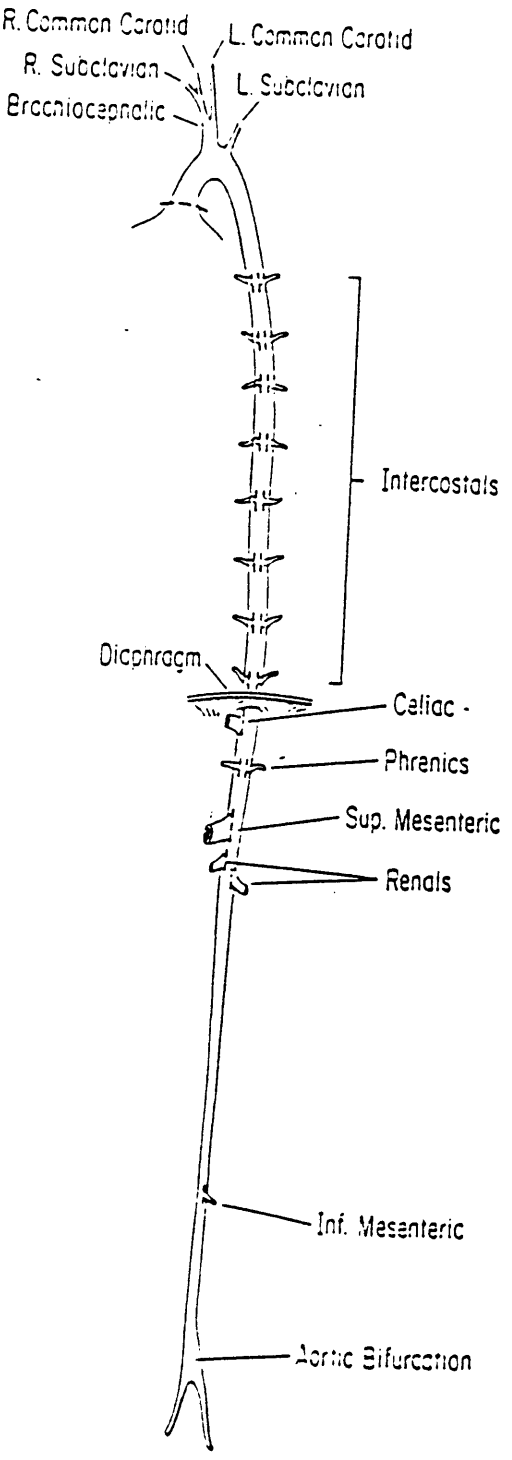
R. Common Carotid
L. Common Carotid
R. Subclavian
L. Subclavian
Brachiocephalic
Intercostals
Diaphragm
Celiac
Phrenics
Sup. Mesenteric
Renals
Inf. Mesenteric
Aortic Bifurcation

Figure 3.1

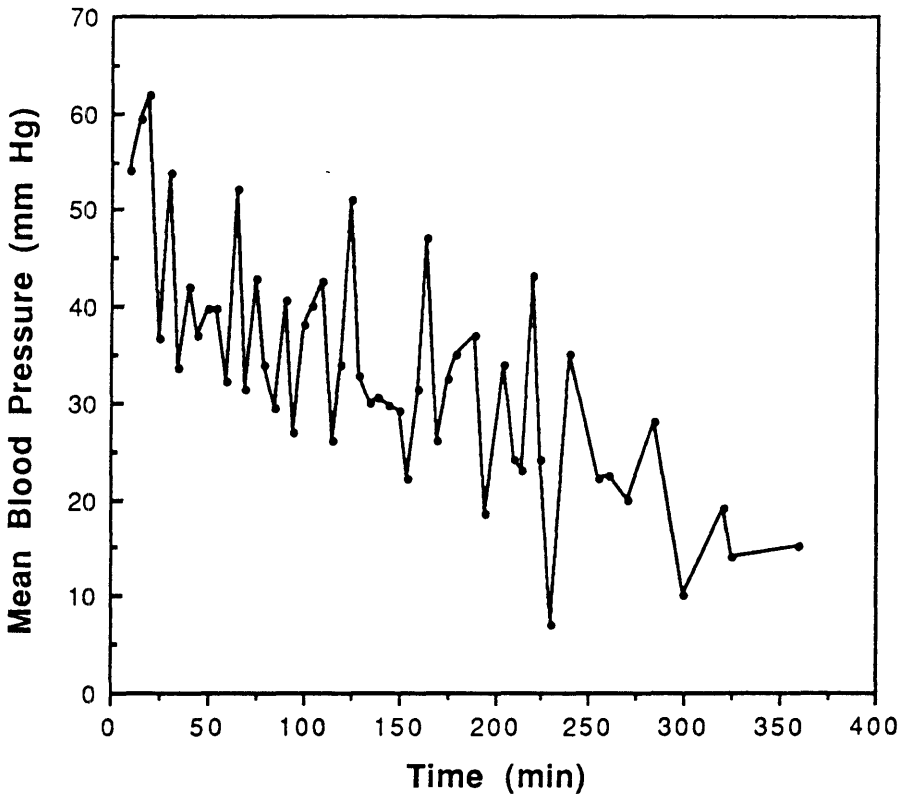
Mean Blood Pressure (mm Hg)
70
60
50
40
30
20
10
0
0
50
100
150
200
250
300
350
400
Time (min)

Figure 3.2

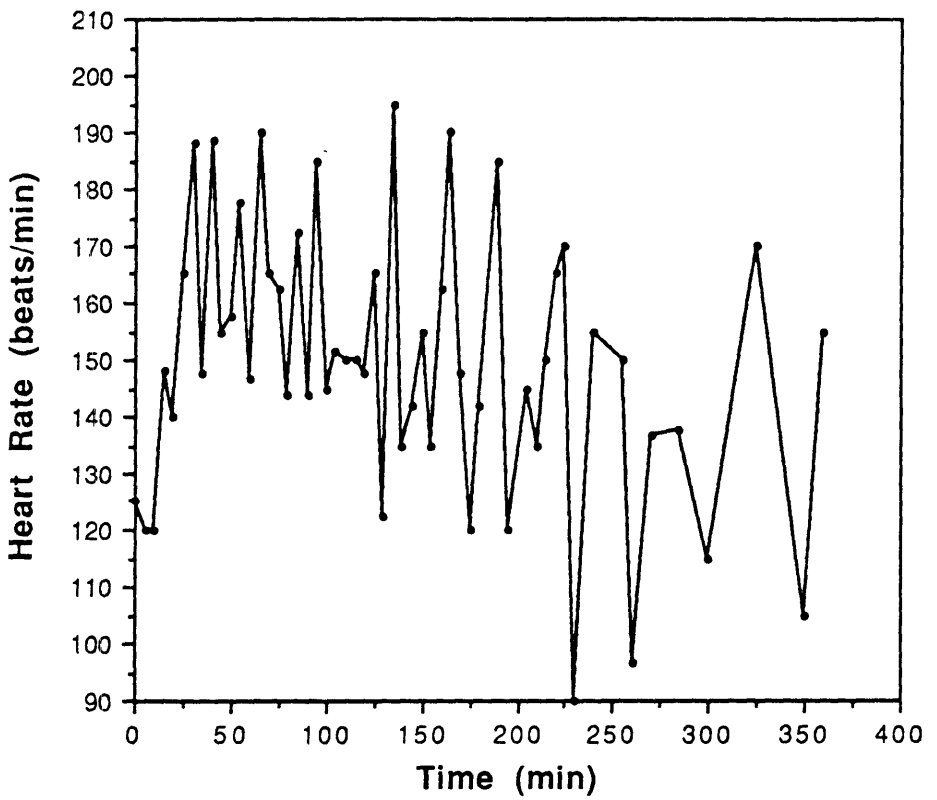
Heart Rate (beats/min)
210
200
190
180
170
160
150
140
130
120
110
100
90
0
50
100
150
200
250
300
350
400
Time (min)

Figure 3.3

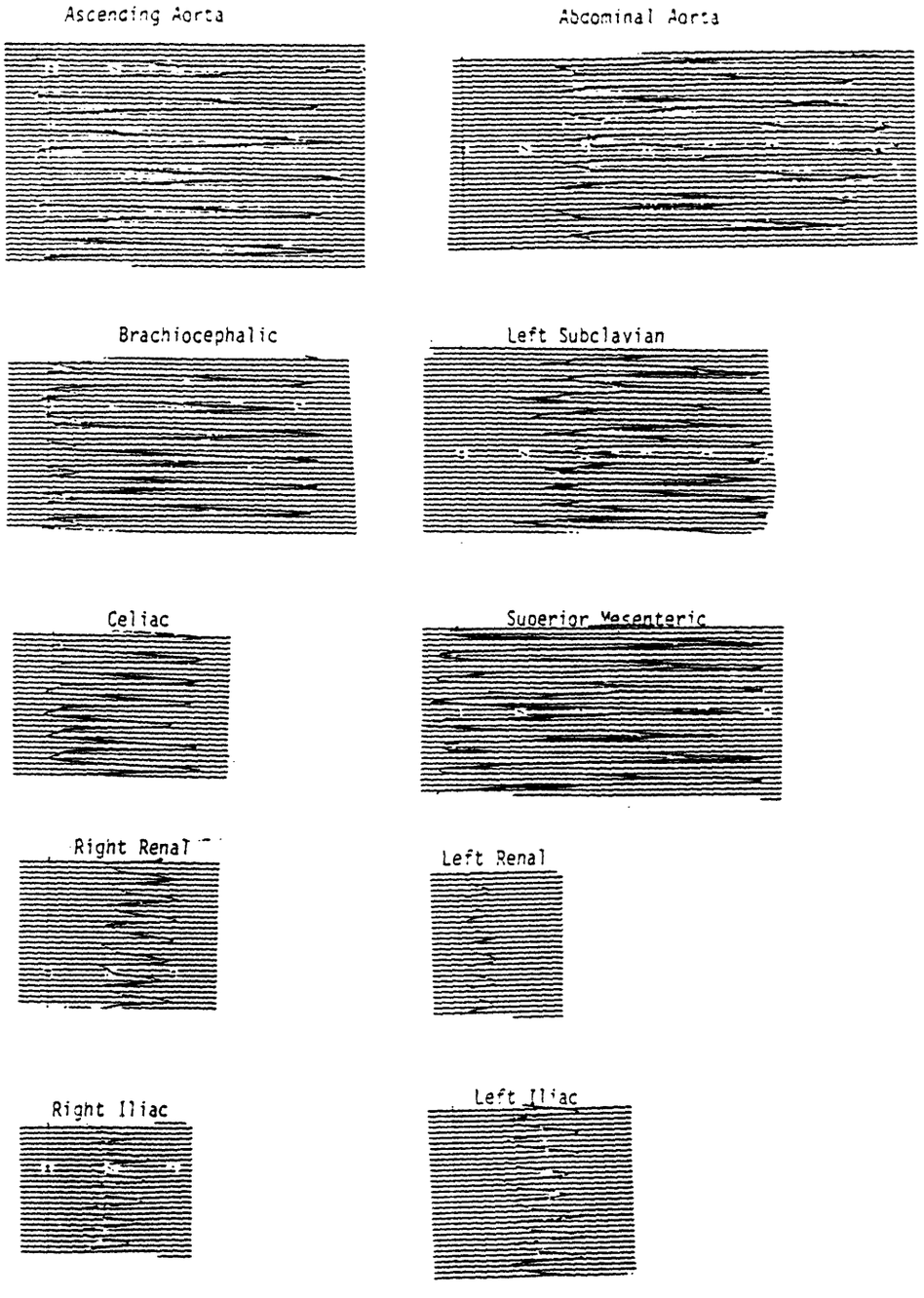
Ascending Aorta
Abdominal Aorta
Brachiocephalic
Left Subclavian
Celiac
Superior Mesenteric
Right Renal
Left Renal
Right Iliac
Left Iliac

Figure 3.4

Table 3.1 . Volumetric flowrate (ml/min) in the ascending thoracic aorta as a function of measurement number.

	Measurement Number													
Rabbit	1	2	3	4	5	6	7	8	9	10	11	12	13	14
1	160									105				
2	110										82			
3	150											50		50
4	143				100					110			96	
5	135			135			115				105			62
6	98			98			80					60		28
7	210				178									
8	140			124		118		92			70			95
9	214			183			190			161				140

Table 3.2. Mean flow splits in the eight aortic branches, expressed as per cent of mean flowrate in the ascending thoracic aorta

	Vessel								
Rabbit	Brachio-cephalic	Left Subclavian	Celiac	Superior Mesenteric	Right Renal	Left Renal	Right Iliac	Left Iliac	Total
1	5.1	5.1	28.2	46.2	7.2	6.5	1.8	1.5	101.6
2	3.4	5.9	32.4	33.5	4.1	3.9	8.3	9.1	100.6
3	6.4	2.1**	17.8	22.0	7.0	10.4	10.4	9.0	85.1
4	5.7	13.2	22.8	37.9	8.1	3.0	5.8	7.5	104.0
5	13.0*	7.6	25.5	27.3	12.4	5.0	4.7	5.5	101.0
6	4.0	9.0	14.5	28.3	3.9	1.1	4.4	4.7	69.9
7	7.4	9.3	36.0	30.6	–	–	–	–	83.3
8	6.7	7.1	18.1	30.2	4.3	4.7	9.1	7.7	87.9
9	6.8	6.1	24.0	30.8	4.7	6.0	6.1	5.6	90.1
Average ±SD	5.7±1.4	7.9±2.6	24.4±7.1	31.9±6.9	6.5±2.9	5.1±2.7	6.3±2.8	6.3±2.5	94.1±11.7

* Outlier by the Modified Three-Sigma Test

** Vessel injured during surgery

Table 3.3. Peak Pulsatile flow splits in the eight aortic branches, expressed as per cent of mean flowrate in the ascending thoracic aorta

	Vessel								
Rabbit	Brachio-cephalic	Left Subclavian	Celiac	Superior Mesenteric	Right Renal	Left Renal	Right Iliac	Left Iliac	Total
1	5.5	4.9	29.0	33.8	4.0	–	1.2	1.0	79.4
2	3.5	8.1	34.1	40.3	1.6	2.6	3.4	6.3	99.9
3	4.9	0.3**	13.4	11.2	4.0	7.2	8.9	8.1	58.0
4	5.8	7.2	15.7	32.1	3.3	1.1	2.7	3.5	71.4
5	6.9*	–	20.1	31.0	6.6	3.2	2.2	3.0	72.5
6	5.2	5.8	8.8	25.5	1.4	–	2.0	2.1	50.8
7	5.6	6.3	27.9	26.7	–	–	–	–	66.5
8	5.9	5.0	34.7	35.0	2.2	2.6	5.7	4.6	95.7
9	5.8	5.4	20.6	30.6	2.9	4.0	5.9	5.5	80.7
Average ±SD	5.5±0.9	6.1±1.2	22.7±9.2	29.6±8.2	3.3±1.7	3.4±2.1	4.0±2.6	4.3±2.3	78.1±13.2

* Outlier by the Modified Three-Sigma Test

** Vessel injured during surgery

Table 3.4 Ratio of peak pulsatile to mean flowrate in the aorta and eight aortic branches

	Vessel									
Rabbit	Ascending Aorta	Abdominal Aorta	Brachio-cephalic	Left Subclavian	Celiac	Superior Mesenteric	Right Renal	Left Renal	Right Iliac	Left Iliac
1	2.6	2.1	2.8	2.5	2.7	1.9	1.5	–	1.6	1.7
2	2.5	1.7	2.6	3.4	2.6	3.0	1.0	1.7	1.0	1.7
3	3.1	2.2	2.3	0.4 *	2.3	1.6	1.7	2.1	2.6	2.8
4	3.1	1.9	3.2	1.7	2.1	2.6	1.3	1.1	1.5	1.5
5	2.6	2.0	1.4	–	2.1	3.0	1.4	1.7	1.3	1.4
6	4.1	2.0	5.4	2.7	2.5	3.7	1.5	–	1.8	1.8
7	2.4	–	1.8	1.6	1.9	2.1	–	–	–	–
8	2.7	1.3	2.4	1.9	5.2	3.2	1.4	1.5	1.7	1.6
9	2.5	1.9	2.1	2.2	2.1	2.4	1.5	1.6	2.4	2.4
Average ±SD	2.8±0.5	1.9±0.3	2.7±1.2	2.3±0.6	2.6±1.0	2.6±0.7	1.4±0.2	1.6±0.3	1.7±0.5	1.9±0.5

* Vessel injured during surgery

Chapter Four

Detailed Flow Patterns in the Transparent Rabbit Aorta

4.1 Introduction

4.1.1 Background and Motivation

The preferred localization of early atherosclerotic lesions in regions of arterial branching, curvature, and bifurcation has given rise to the notion of the importance of localizing factors in the etiology and pathogenesis of the disease. The most frequently cited localizing factor is the detailed flow field within the affected vessels, since the flow patterns in these regions are expected to be disturbed and generally non-unidirectional. We have previously reported the existence of punctate sites of substantially enhanced permeability to macromolecules on the aortic lumenal surface of the normal New Zealand White (NZW) rabbit [1,2]. More recently, we have performed a detailed quantitative topographical mapping of these sites [3] and have demonstrated that their density is highest in the vicinity of aortic ostia and that they exhibit preferred radial and angular distributions around branches consistent with the notion of the importance of localizing factors such as detailed hemodynamics. These distributions bear some similarity to those of experimentally-induced atherosclerotic lesions in hypercholesterolemic rabbits [4-7].

Despite extensive efforts within the past 25 years to elucidate the potential role of hemodynamics in the atherogenic process, very few generalizations can be made. A detailed *in-vivo* experimental description of arterial flow patterns remains elusive due to the fluid mechanical complexity

dictated by the very tortuous vessel geometry, the very complex viscoelastic characteristics of the arterial wall, and the limited spatial resolution of flow measurement systems. The geometry and wall motion issues along with the complex non-Newtonian properties of blood and the flow pulsatility pose technical and economic constraints on the formulation of accurate predictive numerical models of arterial flow fields. There have been numerous experimental flow visualization studies in glass models and polymeric casts which, despite inherent limitations, have shed some light on the details of arterial flows (see, for example, [8-11]). More recently, with the advent of very fast computers, very efficient algorithms, and the use of the finite element method for the mathematical description of complex geometries, there has been a surge in the number of two- and three-dimensional numerical simulations of arterial fluid mechanics [12-16]. Although these computations offer superb spatial and temporal resolution as well as the ability to investigate the effects of various parameters on the resulting flow field, they remain generally confined to studies within over-simplified geometries. The objective of the study reported here is to investigate the detailed flow field in the normal rabbit aorta. The experiments were carried out on isolated natural aortas rendered transparent to allow flow visualization.

4.1.2 Rabbit Aortic Anatomy

Figure 4.1 depicts an anatomical schematic of the rabbit aorta and its major branches. A detailed description of the anatomy can be found elsewhere [17]. Briefly, the ascending aorta emerges from the left ventricle, and it merges into the aortic arch. The greater curvature of the arch gives rise to two vessels, the brachiocephalic and the left subclavian arteries. The brachiocephalic artery immediately divides into the right subclavian and the

two carotid vessels. The descending thoracic aorta gives rise along its dorsal surface to eight pairs of intercostal arteries, the most distal of which emerges approximately at the level of the diaphragm, which anatomically marks the division between the thoracic and abdominal aorta. Within the abdominal aorta, the celiac, a large vessel which branches immediately into the left gastric, hepatic, and splenic arteries, and which supplies the stomach, liver, duodenum, pancreas, and spleen emerges ventrally immediately caudal to the diaphragm. A ninth pair of intercostal (or phrenic) arteries arises along the dorsal surface of the aorta either slightly proximal or distal to the celiac branch. Downstream of the celiac is the superior mesenteric, a large ventral artery which supplies the pancreas as well as the small and large intestines. Immediately distal to the superior mesenteric and emerging laterally is the right renal artery, followed by the left renal artery on the opposite side of the animal. Some distance downstream of the renals is the ventral inferior mesenteric artery which supplies the descending colon and rectum, eventually followed by the aorto-iliac bifurcation which marks the anatomical termination of the aorta.

4.2 Materials and Methods

4.2.1 Preparation of Transparent Aorta

Transparent rabbit aortas were prepared according to the method of Karino and Motomiya [18]. Entire aortic trees including the hearts, the full lengths of the aortas, and segments of all major aortic branches were isolated from the bodies of normal NZW rabbits shortly after sacrifice. Excess connective tissue was trimmed; the eight pairs of intercostal arteries, the inferior mesenteric artery, and the lumbar and gonadal arteries in each aorta were ligated with 6-0 nylon suture paying special attention not to alter the shape of the aortic lumen as a result of the ligations. Smaller microvessels on

the aortic surfaces were occluded by ligation and/or coagulation with a fulgurator. The major aortic branches including the brachiocephalic, left subclavian, celiac, superior mesenteric, right and left renal, and right and left iliac arteries were cannulated with 2-2.5 cm long square-cut, thin-walled stainless steel catheters (8 to 16 ga) whose outer diameters approximately matched the inner diameters of the branches. The catheters were tied firmly in place with 3-0 silk suture. The left ventricles were then incised with 5-cm long 6-ga stainless steel catheters to provide inlet ports into the aortas, and the pulmonary arteries and veins were ligated with 3-0 silk suture. The catheters of the major branches were then capped, and the vessels were subjected to a water or normal saline (0.9 w/o) hydrostatic head at a physiological pressure of about 100 mm Hg at which point the vessels took on their natural physiological shapes. The entire aortic trees were then mounted in their physiological configurations onto three-dimensional stainless steel frames constructed specifically for this purpose. The frames consisted of 3 mm outer diameter stainless steel tubing which was bent and shaped so that it made firm contact with all the catheters and hence provided solid support for the aortic trees.

The tissue was fixed for about 24 hrs by pressure perfusion at about 100 mm Hg with and immersion in a solution of 2% glutaraldehyde and 4% formaldehyde in isotonic saline. Subsequently, the tissue was dehydrated over 2 to 3 days by simultaneously pressure perfusing it with and immersing it in ethanol-saline mixtures of progressively increasing ethanol concentration, and finally suspending it in pure ethanol. The cannulated branches of each aorta were then connected to flexible polyethylene tubing (Intramedic) whose inner diameter matched the outer diameter of the cannulae. The lengths of the various connection tubes were adjusted so that the fraction of total inlet flowrate into each of the aortic branches matched mean flowrates previously

measured in the rabbit *in-vivo* using transit-time ultrasound flowmetry [19]. Finally, the tissue was rendered transparent by pressure perfusion with and immersion in methyl salicylate (oil of wintergreen) containing 5% ethanol.

4.2.2 Experimental Procedure and Data Analysis

Each of the mounted transparent vessels was placed in a large square glass chamber filled with oil of wintergreen containing 5% ethanol. This chamber was then placed on a vertically-moveable horizontal stage, and the areas of interest within the aortas were trans-illuminated with condensed parallel light provided by a Reichert Binolax twin-lamp assembly supplying either low intensity light from a tungsten filament lamp or high intensity light from a 200W dc mercury arc lamp with a filter to eliminate UV illumination.

Each vessel was then subjected to the flow of a dilute suspension of 50-165 μm diameter polystyrene microspheres (s.g. 1.06, Particle Information Services, Bremerton, WA) in oil of wintergreen containing 5% ethanol (s.g. 1.16, dynamic viscosity 2.64×10^{-3} kg-m/s, and refractive index n=1.53). Steady flow was provided by gravity-feed from a head tank, while pulsatile flow studies were performed using the same head tank in combination with a sinusoidal oscillatory flow pump. The process of rendering the aortas transparent led to a complete loss of tissue compliance. This prevented performing pulsatile flow experiments in the abdominal aorta since the relatively thin wall of the abdominal aorta collapsed when a pulsatile pressure wave was imposed. In the aortic arch, on the other hand, the wall was sufficiently thick that there was no vessel collapse, and the pulsatility was imparted to the fluid thereby allowing pulsatile flow visualization. Detailed flow field visualization through various regions of interest within the transparent vessel was performed by photographing the trajectories of the suspended tracer microspheres on 16

mm cine film (Kodak double X-negative) at film speeds of 800 to 1400 frames per sec using a high-speed 16 mm cine camera (Hycam, Red Lake Labs, Santa Clara, CA) to which a zoom lens (1x to 5x) had been attached. Whenever possible, two perpendicular views of the same flow section were photographed in order to fully visualize the three-dimensional structure of the flow field. In certain cases, however, this was not possible due to anatomical geometric complexities or due to obstruction caused by the stainless steel frame on which the vessel was mounted.

Following the completion of the flow visualization procedure, each of the transparent vessels, still in the glass chamber and under physiological pressure, was trans-illuminated with condensed parallel light from a 200W ac tungsten filament white lamp through a pair of 16 cm diameter plano-convex lenses aligned in series. The arterial segments of interest were then photographed, together with a scale at the same focus, on 35 mm color or black and white film using a Nikon FE 35 mm camera equipped with close-up lenses. These photographs were used to obtain pertinent geometric data including the lengths and diameters of the various sections as well as the various branching angles.

The developed 16 mm cine films were projected on a drafting table, and the trajectories of individual tracer microspheres were analyzed frame by frame with the aid of a stop-motion 16 mm movie analyzer (Vanguard Instrument Corp., Melville, NY) to yield detailed flow patterns as well as quantitative information on fluid velocity and and resulting wall shear stress.

4.3 Results

4.3.1 Aortic Arch

4.3.1.1 Steady Flow

Figure 4.2 depicts a typical transparent rabbit aortic arch and its two major branches, the brachiocephalic and the left subclavian arteries. In this preparation, the inner diameter of the ascending thoracic aorta shortly after emerging from the left ventricle is about 6.3 mm, increases to about 6.8 mm at the apex of the aortic arch, and then tapers to about 5.5 mm in the upper descending thoracic aorta. The brachiocephalic artery has an inner diameter of about 4.6 mm at its trunk, but it divides quickly (after a length of about 4.6 mm) into the right and left carotid arteries which have inner diameters of about 2.7 and 2.4 mm, respectively. The left subclavian artery has an inner diameter of about 2.0 mm, and it emerges from the arch at an angle of approximately 60 degrees from the horizontal.

Steady flow was studied in the arch at an inlet flowrate of 305 ml/min corresponding to a Reynolds number (based on the inlet diameter of 6.3 mm and the assumption of a circular aortic cross-section) of about 440. The flow splits into the brachiocephalic artery, the left subclavian artery, and the descending thoracic aorta were 17, 7, and 76% of the inlet flowrate, respectively. The resulting detailed flow patterns are depicted in Figure 4.3, and they can be described in terms of four general streamline categories. These four categories are combined in the central portion of the figure, while the four surrounding panels display each streamline category individually for added clarity. In this and all subsequent flow pattern drawings, there are three line patterns that are used to give a sense of the three-dimensionality of the flow field. Solid lines denote streamlines in the common median plane, i.e. in

the plane of the figure; long dashed lines represent streamlines some distance either above or below the common median plane; and small dashed lines correspond to streamlines that are furthest away from the common median plane near the top and bottom walls.

The first category (Panel A) consists of relatively undeflected flow originating in or near the common median plane and flowing into the descending thoracic aorta; the tracer microspheres follow trajectories that are virtually parallel to the walls of the aortic arch. The second category (Panel B) consists of particles originating in or slightly above the common median plane and which trace helical clockwise spiral motion along the ventral (i.e. top) aspect of the arch prior to rejoining the flow in the common median plane at the level of the descending thoracic aorta. This represents a secondary flow component induced by the curvature of the aortic arch. The third category (Panel C) consists of fluid entering the brachiocephalic artery. This fluid originates in or slightly below the common median plane, and it includes streamlines which directly enter the two carotid arteries (streamlines B,C,D) as well as ones that trace helical motion into the right carotid artery (streamlines A,E). This helical motion is comprised of fluid streamlines which approach the distal (i.e. downstream) lip of the brachiocephalic branch, get deflected by the presence of the flow divider onto the lateral sides of the branch, and proceed slowly in a counter-clockwise helical fashion along the periphery of the branch before finally joining the main parallel flow within the branch. Finally, the fourth streamline category (Panel D) is comprised of both direct (streamlines A,B) and helical deflected (streamline C) flow into the left subclavian artery as well as a recirculating flow streamline into the brachiocephalic artery (streamline D). These streamlines originate in, slightly below, or far below the common median plane (at the dorsal, i.e. bottom, wall). Figure 4.3 also contains

cutaway plane A-A' which depicts a cross-sectional view of the ascending aorta proximal to (i.e. upstream of) the brachiocephalic artery illustrating schematically the approximate regions of origin of the four flow categories.

Flow separation was observed at the lesser curvature of the aortic arch slightly downsteram of the apex, but the region of separated flow was not occupied by recirculating fluid streamlines but rather by the induced helical secondary motion within the arch described above (Panel B). In addition, regions of flow separation were observed at the proximal lips of both the brachiocephalic and left subclavian arteries; the separated flow zone contained recirculating flow in the case of the brachiocephalic artery (streamline D of Panel D), while the separation zone associated with the left subclavian artery was primarily occupied by the deflected streamlines off the flow divider which spiral into the branch as described above (streamline C of Panel D). A region of strong and rather chaotic flow recirculation was observed at the entrance of the aorta slightly downstream of the aortic sinus, but this region is believed to be an artefact of the preparation caused by a partially opened aortic valve and has therefore not been shown in Figure 4.3.

Figure 4.4 depicts the steady flow velocity profiles and resulting wall shear stresses in the common median plane at various locations of the aortic arch and its branches. Flow enters the aorta slightly skewed towards the outer wall. This skewness becomes more pronounced as the flow approaches the brachiocephalic artery. Immediately distal to the brachiocephalic branch, the outer wall skewness is minimal and remains so until it becomes very marked once again immediately distal to the left subclavian artery. The sharp skewness persists for the entire section of the descending thoracic aorta photographed. The wall shear stress distal to both arch branches exceeds that proximal although the ratio of distal to proximal shear stress is significantly

larger in the case of the left subclavian artery than that of the brachiocephalic (4.1 compared to 1.6).

The shear stress along the outer wall at the entrance of the brachiocephalic artery has a small negative value due to the presence of the flow recirculation zone referred to previously within which the fluid moves very slowly. This zone has a width of 0.4 mm (9% of the branch diameter) in the common median plane. The velocity profiles in both carotid branches are skewed towards the outer walls. Within the left subclavian artery, there is a very pronounced skewness in the velocity profile towards the downstream wall as the region in the vicinity of the upstream wall corresponds to a flow separation zone that is occupied primarily by slowly-moving helical flow that is deflected off the left subclavian flow divider. The shear stress at the downstream wall within the left subclavian artery corresponds to the maximum value of shear stress observed in the entire flow field. The wall shear stress data in Figure 4.4 also indicate that the spatial shear stress gradients are generally larger along the lesser curvature of the arch than along the greater curvature.

4.3.1.2 Pulsatile Flow

Pulsatile flow in which a sinusoidal component with an oscillatory frequency of 2.5 Hz and displacement volume of 0.8 ml was superimposed on the steady flow component was also studied in the aortic arch. In general, the same four flow categories observed in steady flow persisted in pulsatile flow. At peak systole, the ventral helical flow motion (category 2 in steady flow description) was very pronounced. The flow separation zones, both the ones occupied by the forward-moving helical streamlines along the lesser curvature of the arch and proximal to the left subclavian artery as well as the one

exhibiting recirculation flow at the entrance of the brachiocephalic artery, periodically appeared and disappeared attaining their maximum extent at peak systole and disappearing completely during portions of diastole. Finally, near the end of the diastolic phase of the cardiac cycle, the flow along the lesser curvature of the arch reversed direction and flowed towards the heart. Flow along the greater curvature of the arch was much less likely to reverse direction and continued in the forward direction throughout most of the flow field. Flow within the two arch branches remained in the forward direction throughout the course of the cardiac cycle.

Figure 4.5 depicts the pulsatile flow velocity profiles and resulting wall shear stresses in the common median plane of the aortic arch and its branches at five equally-spaced time points within the cardiac cycle. At the beginning of the cycle, t=0, the velocity profile at the inlet of the aorta is relatively flat and unskewed. Immediately proximal to the brachiocephalic artery, the velocity becomes sharply skewed towards the lesser curvature, and this skewness persists throughout the remainder of the aortic arch. The recirculation zone at the entrance of the brachiocephalic artery is absent at this time point. By the next time point, $t=0.2\tau$ (where τ denotes the period of the pulsatile cycle), the flow has undergone sharp acceleration. The inlet profile remains relatively flat and unskewed, while the profile proximal to the brachiocephalic artery becomes mildly skewed towards the greater curvature of the arch. Distal to the brachiocephalic, the skewness shifts towards the lesser curvature, and this condition persists throughout the remaining portion of the arch. The recirculation zone at the entrance of the brachiocephalic artery is present at this time point and has a width of about 0.5 mm. At the next time point, $t=0.4\tau$, the inlet flow is mildly skewed towards the lesser curvature, and this skewness persists until the plane immediately proximal to the brachiocephalic artery.

Distal to the brachiocephalic, the skewness shifts to the greater curvature but then shifts back to the lesser curvature distal to the left subclavian artery and at subsequent positions. The recirculation zone at the inlet of the brachiocephalic artery has a width of about 0.6 mm at this time point. By the next time point, 0.6τ, the flow has begun decelerating. Flow enters the aorta sharply skewed towards the greater curvature, and this skewness persists until the plane immediately distal to the left subclavian artery where the skewness shifts towards the lesser curvature and remains so thereafter. The flow recirculation zone is absent at this point. Finally, at $t=0.8\tau$ corresponding to a point near the end of the pulsatile cycle, the flow throughout most of the arch is in the reverse direction. Forward flow exists, however, in a narrow region along the greater curvature around the brachiocephalic artery and proximal to the left subclavian artery. The two arch branches remain in forward flow.

Figure 4.6 illustrates the distal to proximal shear stress ratio as a function of time for both the brachiocephalic and left subclavian arteries during the course of a single pulsatile cycle. The constant steady flow values are also indicated in the figure. The results indicate that the ratio may be greater or smaller than unity depending on the portion of the cycle so that no generalizations can be made regarding the relative magnitudes of the shear stresses distal and proximal to branches in pulsatile flow. Figure 4.7 depicts the pulsatile to steady wall shear stress ratio as a function of time for one pulsatile cycle at selected planes along both the greater and lesser curvature of the arch and the right and left sides of the two aortic branches. The results show that at any one point in the flow field, the pulsatile flow shear stress may be greater or smaller than and of the same or opposite sign of its steady flow counterpart depending on the portion of the cardiac cycle. This indicates once

again that no *a priori* conclusions can be made regarding pulsatile flow shear stresses.

4.3.2 Abdominal Aorta

Steady flow in the abdominal aorta was studied in the vicinity of the four major branches - the celiac, superior mesenteric, right renal, and left renal arteries.

4.3.2.1 Celiac Artery

Figure 4.8 illustrates a typical aorto-celiac junction after it had been rendered transparent. Since the detailed geometric features are expected to play a role in determining the specific flow patterns, it is important to make several geometric observations. The celiac artery emerges from the ventral aspect of the aorta virtually symmetrically relative to the two lateral sides of the animal. The common median plane of the celiac artery forms an angle of slightly less than 90 degrees (85 degrees in the example shown in Fig. 4.8) with the horizontal. In the rabbit, the celiac artery is typically several aortic diameters away from its nearest major abdominal neighbor, the superior mesenteric artery; therefore, flow distal to the celiac artery has sufficient distance to recover from any perturbation caused by flow into the ostium of the celiac before entering the superior mesenteric artery, and there is little chance of fluid mechanical interaction between the two vessels. In the example shown in Figure 4.8, there is some tapering of the aorta distal to the celiac artery. Specifically, the aortic inner diameter immediately proximal to the celiac branch is about 4.4 mm and that immediately distal is about 3.8 mm. Finally, while the curvature of the branching at the celiac junction is very sharp at the distal lip of the branch, it is gently rounded at the proximal lip.

Steady flow at an inlet flowrate of 260 ml/min corresponding to a Reynolds number at the inlet of the abdominal aorta (based on the assumption of a circular vessel cross-section) of 570 and a celiac to total abdominal aortic flowrate ratio of 0.30 was studied. The general flow patterns are illustrated in Figure 4.9 which depicts a composite of representative particle trajectories from four streamline categories comprising the flow field as well as a breakdown of the individual categories in the four peripheral panels. The same line weight convention as described previously applies in this case.

The flow field in the aorta in the vicinity of the celiac artery is generally symmetric about the common median plane, and the detailed behavior of the four flow categories can be described as follows. Panel A represents relatively undisturbed flow in or near the common median plane which proceeds into or past the celiac branch. The fluid streamlines follow trajectories that are more or less parallel to the aortic walls. Panel B represents an annulus of flow slightly above and below the common median plane which is deflected towards the ventral aspect due to the presence of the celiac artery but whose streamlines proceed past the branch. Panel C corresponds to an annulus of flow originating at a region between the common median plane and the top and bottom walls of the aorta (corresponding to the anatomical right and left lateral walls, respectively) which encircles the core flow of Panels A and B before entering the branch, usually tracing helical trajectories. Finally, Panel D represents a flow component originating at both lateral walls which gets deflected by the flow divider and recirculates along the lateral walls at the level of the celiac before finally moving in a helical fashion into the celiac artery. This last flow category leads to the formation of a pair of thin-layered spiral secondary flow cells along the lateral walls of the aorta at the level of the celiac artery. Under the conditions illustrated in Figure 4.9, the maximum penetration

depth of the recirculation zones of Panel D into the aorta is about 2.4 mm. Figure 4.9 also depicts a cutaway cross-sectional view (A-A') of the aorta shortly proximal to the celiac artery illustrating the approximate regions of origin of each of the four flow categories described. There is a region of boundary layer separation at the proximal lip of the celiac artery, but this region does not undergo flow recirculation. Rather, the separated flow zone is occupied by the helical streamlines into the celiac branch (Panels C and D).

Figure 4.10 illustrates the velocity profiles and resulting wall shear stresses in the common median plane at various locations within the aorta in the general vicinity of the celiac artery and within the celiac artery itself. Flow approaches the celiac artery with a profile skewed towards the dorsal aspect of the vessel. The wall shear stress at the dorsal wall is 30 dyne/cm^2, while that at the ventral wall is 13 dyne/cm^2, and the peak fluid velocity is 455 mm/s. Immediately proximal to the celiac and as the fluid prepares to enter the branch, the flow skewness shifts towards the ventral wall where the shear stress is 25 dyne/cm^2, while that at the dorsal wall is 10 dyne/cm^2. The ventral skewness is even more pronounced immediately distal to the branch where the ventral shear stress is 51 dyne/cm^2 (the maximum value in this aortic segment), while the dorsal wall experiences a shear stress of only 6 dyne/cm^2. The extent of ventral skewness distal to the celiac artery decreases with distance away from the branch although it persists for the entire length of the section under study. In spite of the very low flow velocities along the dorsal wall (as low as 50 mm/s), the boundary layer does not separate from the wall, and the wall experiences forward fluid motion at all spatial locations. Within the celiac artery itself, flow is heavily skewed towards the distal wall, and this skewness persists throughout the photographed length of the celiac artery.

4.3.2.2 Superior Mesenteric Artery

Figure 4.11 shows a typical transparent aorto-superior mesenteric junction. In the rabbit, the superior mesenteric artery is typically the largest abdominal branch, and it, like the celiac, emerges ventrally from the aorta. The superior mesenteric artery is geometrically similar to the celiac artery in that it forms an angle of virtually 90 degrees (exactly 90 degrees in Figure 4.11) with the horizontal and that the curvature of the junction is very sharp at the distal lip but gently rounded at the proximal lip. The extent of aortic taper distal to the superior mesenteric artery exceeds that of the celiac; the aortic inner diameter proximal to the superior mesenteric artery in Figure 4.11 is 4.0 mm, while that distal to the branch is 3.1 mm.

In some rabbits, the superior mesenteric and right renal arteries are sufficiently far from one another that limited fluid mechanical interactions occur betwen the two vessels. In this case, the flow field in the vicinity of the superior mesenteric artery resembles that observed near the celiac artery, and it generally exhibits the same streamline groups described previously. In most rabbits, however, the superior mesenteric and right renal arteries are anatomically very close, leading to a considerably more complex and highly asymmetric flow field. An example of a typical flow field resulting from such a situation is illustrated in Figure 4.12 which depicts steady flow with a flowrate shortly proximal to the superior mesenteric artery of 180 ml/min thereby leading to a Reynolds number of 480, a superior mesenteric to inlet flowrate ratio of 0.63, and a right renal to inlet flowrate ratio of 0.11.

The resulting flow patterns divide into the six flow categories represented in the four peripheral panels of Figure 4.12. Panel A contains flow which originates in or very near the common median plane and which either proceeds down the aorta past both the superior mesenteric and right renal

arteries (streamlines A and B), enters the superior mesenteric artery directly (streamlines E,F,G), or traces helical patterns into the superior mesenteric artery (streamlines C and D). Panel B contains two groups of fluid streamlines - the first (streamlines K and L) represents flow originating slightly below (i.e. to the anatomical left of) the common median plane and which gets deflected towards the ventral wall due to the presence of the superior mesenteric artery but which then continues downstream into the aorta past both the superior mesenteric and right renal arteries, and the second (streamlines H,I,J) depicts flow originating at the dorsal wall of the aorta and which encircles the core flow before entering the superior mesenteric artery. Panel C also combines two groups of streamlines - the first (streamlines O,P) represents flow originating near the common median plane and which passes the superior mesenteric artery before entering the right renal artery, and the second (streamlines M,N,Q,R) depicts flow originating at the left lateral wall of the aorta which curls in the counterclockwise direction onto the dorsal wall before continuing on to reach the right lateral wall where it proceeds upstream until it enters the superior mesenteric artery along the right lateral wall. This last streamline group thus leads to flow recirculation along the right lateral wall. Finally, Panel D contains flow originating near the left lateral wall which curls in the clockwise direction onto the ventral wall and then continues its clockwise helical motion until it reaches the right lateral wall where it attains its maximum distal penetration. The flow then continues its clockwise helical motion until it reaches the left lateral wall while at the same time moving upstream, and it finally enters the superior mesenteric artery from the left lateral side where it spirals quickly into the branch. This flow component therefore leads to flow recirculation zones along both the dorsal and left lateral walls of the aorta. Figure 4.12 also shows a cutaway plane (A-A') proximal to the superior

mesenteric artery illustrating the regions of origin of the various streamline groups within the vessel cross-section.

A large region of flow separation is observed at the level of and distal to the superior mesenteric artery along the dorsal wall of the aorta. This separated flow zone is caused by the relatively large flowrate through the superior mesenteric artery, and it is occupied by the recirculating flow streamlines shown in Panel D of Figure 4.12. Moreover, there is a region of flow separation along the ventral wall at the proximal lip of the superior mesenteric artery, but, as in the case of the celiac artery, this region is occupied by helical flow motion from the aorta (streamlines S and T in Figure 4.12, for example) into the branch and not by recirculating fluid streamlines within the superior mesenteric artery.

Figure 4.13 illustrates the velocity profiles in the common median plane at different locations within the aorta in the vicinity of the superior mesenteric artery and within the superior mesenteric artery itself. The relatively long and straight distance between the celiac and superior mesenteric arteries allows the flow distal to the celiac to recover and hence to approach the superior mesenteric artery possessing a near-parabolic profile. Immediately proximal to the superior mesenteric artery the velocity profile becomes skewed towards the ventral aspect of the aorta due to the presence of the branch. Immediately distal to the superior mesenteric artery, the ventral skewness persists so that the shear stress is relatively high (26 dyne/cm^2) along the ventral wall of the aorta, while the dorsal wall experiences flow recirculation and hence negative values of wall shear stress (-7 dyne/cm^2). The flow past the superior mesenteric artery immediately encounters the right renal artery. Distal to the right renal artery, the ventral wall experiences a relatively high shear stress (33 dyne/cm^2), while the dorsal wall remains exposed to reverse recirculating flow

(-4 dyne/cm^2). Within the superior mesenteric artery itself, the shear stress is considerably higher along the distal wall (53 dyne/cm^2) than along the proximal wall (33 dyne/cm^2) as the flow negotiates the curvature of the branch.

4.3.2.3 Right and Left Renal Arteries

Figure 4.14 shows a typical transparent aorto-renal junction. In most rabbits, the right and left renal arteries emerge exactly from the lateral walls of the aorta, but in some rabbits they emerge slightly ventrally. The right renal artery is always proximal to the left renal artery. The two renal arteries usually have about the same diameter, and like the celiac and superior mesenteric arteries, the curvature of the renal junctions is sharper at the distal lips than at the proximal lips. In the sample studied, there is virtually no aortic taper distal to the right renal artery; the aortic diameter both proximal and distal to the right renal branch is about 3.8 mm. There is some taper, however, distal to the left renal ostium; the diameter proximal to the left renal artery is about 3.9 mm, while that immediately distal is about 3.4 mm.

As in the case of the superior mesenteric artery, a distinction has to be drawn between the situation where the superior mesenteric and right renal arteries are in close proximity and that where they are separated by a sufficiently large distance for fluid mechanical interactions to be minimal. A representative flow field in a sample within which the two vessels do not fluid mechanically interact significantly is shown in Figure 4.15. Steady flow at an inlet flowrate of 180 ml/min corresponding to a Reynolds number proximal to the right renal artery of 245, right renal to inlet flowrate ratio of 0.23, and left renal to inlet flowrate ratio of 0.22 has been studied. Representative streamlines are depicted in the central figure, and these streamlines divide into the eight groups represented in the three peripheral panels. Panel A consists

of a group of streamlines (streamlines A,B,C) in the common median plane which flow past the right and left renal arteries and continue downstream into the lower abdominal aorta and a second group (streamlines D,E,F) originating near the left lateral wall of the aorta and flowing directly into the left renal artery. Panel B contains two streamline groups - the first (streamlines G,H,J) contains streamlines originating near the right lateral wall of the aorta which get deflected at the right renal artery flow divider before entering the right renal branch. Streamline J in this group actually follows a small recirculation loop within the aorta after getting deflected off the flow divider and before entering the right renal artery. This trajectory is similar to the lateral recirculation zones that have already been reported in the case of the celiac and superior mesenteric arteries, but the recirculation loop in this case is significantly smaller in size because the flow Reynolds number at the level of the renal arteries is considerably smaller than that at the levels of the celiac and superior mesenteric arteries. The second group (strteamlines I,K) consists of streamlines originating below the common median plane (i.e. towards the dorsal aspect of the aorta) which get deflected onto the right lateral wall due to the presence of the right renal artery and then traverse the width of the aorta within the dorsal half before finally entering the left renal artery. Panel C contains four streamline groups - the first group (steramlines L and O) depicts flow originating near the right lateral wall and flowing virtually undeflected into the right renal artery. The second group (streamline R) represents flow along the top (i.e. anatomically ventral) wall which enters the right renal artery where it traces a helical trajectory. The third group (streamlines N,P) represents streamlines which originate between the common median plane and the bottom (i.e. anatomical dorsal) wall and end up in the left renal artery/. Finally, the fourth group (streamlines M,Q,S) represents flow slightly above and below

the common median plane which gets deflected towards the right lateral wall due to the presence of the right renal artery, continues past the right renal branch, gets deflected towards the left lateral wall of the aorta due to the presence of the left renal ostium, and finally continues past this branch into the lower abdominal aorta. Figure 4.15 also depicts a cutaway plane (A-A') proximal to the right renal ostium which illustrates the approximate origin of the various streamline groups within the aortic cross-section.

Figure 4.16 depicts the velocity profiles and wall shear stresses in the common median plane at various locations in the vicinity of the aorto-renal junctions and within the two renal arteries themselves. The velocity profile proximal to the right renal artery is sharply skewed towards the right lateral wall due to the presence of the right renal branch; the wall shear stress at the right lateral wall is 27 dyne/cm^2, while that at the left lateral wall is only 3 dyne/cm^2. This skewness becomes even sharper distal to the right renal branch as the shear stress along the right lateral wall is 44 dyne/cm^2, while that along the left lateral wall is 3 dyne/cm^2. As the flow prepares to enter the left renal artery, the skewness towards the right lateral wall decreases (27 dyne/cm^2 along right lateral wall and 15 dyne/cm^2 along left lateral wall). Beyond the left renal branch, the flow remains skewed towards the right lateral wall (17 dyne/cm^2 along right lateral wall and 4 dyne/cm^2 along left lateral wall), and this skewness slowly decreases as flow proceeds into the lower abdominal aorta. Within the two renal branches, the velocity profile is skewed towards the distal side of each branch although the skewness in the right renal artery is significantly more pronounced than that in the left renal artery.

As has already been mentioned, the flow field at the renal branches reported here represents a situation where the superior mesenteric and right renal arteries are anatomically relatively far apart. An example of an aorta

where these two vessels are in very close proximity (such as in Figure 4.12) has been studied (data not shown). The velocity profile and wall shear stress results follow the same general trends observed in Figure 4.16. One difference, however, is the presence of a flow recirculation zone distal to the right renal artery along the aortic left lateral wall so that the wall shear stress immediately distal to the right renal artery along the left lateral wall is negative.

4.4 Discussion

The detailed flow field has been studied in the normal rabbit aorta using microcinematographic flow visualization techniques in natural isolated aortas that had been rendered transparent. A high level of fluid mechanical detail can be obtained using this technique, and this is crucial in investigating potential relationships between arterial flow patterns and very localized phenomena within the aortic wall such as focal enhanced permeability sites or early atherosclerotic lesions.

4.4.1 Aortic Arch

Both steady and sinusoidal pulsatile flow fields have been studied in the aortic arch. The steady flow results reveal the presence of a single clockwise-rotating helical cell along the ventral wall of the arch. While induced secondary flow motion in a curved tube generally leads to a pair of counter-rotating helical cells, the presence of the two arch branches alters the flow field and leads to a single helical cell in the arch. Flow within the two arch branches contains helical components originating from fluid streamlines deflected off the branch flow dividers. Flow separation is observed at the lesser curvature of the aortic arch and proximal to both arch branches. The flow separation zones at the lesser curvature of the arch and at the entrance of the left subclavian artery

are occupied by spiral helical streamlines, while that at the entrance of the brachiocephalic artery is filled in by a recirculation zone. The velocity profiles in the entire arch in the common median plane are skewed towards the greater curvature, and the wall shear stresses distal to both branches exceed their proximal counterparts.

In the case of sinusoidal pulsatile flow, the ventral helical motion becomes very pronounced at peak systole, the flow separation zones along the inner curvature of the arch and proximal to the left subclavian artery as well as the recirculation flow zone at the entrance of the brachiocephalic artery periodically appear and disappear with pulsatility, and considerably more reverse flow is observed along the lesser curvature than along the greater curvature during the diastolic phase of the pulsatile cycle. Very few generalizations regarding the relative magnitudes of wall shear stress proximal and distal to branches can be made in pulsatile flow, and at any given point within the flow field, the pulsatile flow shear stress may be higher or lower than its steady flow counterpart depending on the specific time point within the cardiac cycle.

The steady flow results obtained here are in general agreement with the qualitative data of Rodkiewicz [20] in scaled-up plastic models of the rabbit aortic arch; however, since Rodkiewicz' models are two-dimensional, all his flow separation areas are occupied by recirculating flow streamlines. Our results indicate that most separated flow zones are actually occupied by induced secondary helical flow motion. Rodkiewicz also notes that in pulsatile flow, the general flow behavior is similar to that in steady flow but that the boundaries of the flow separation zones oscillate with pulsatility. Our results indicate that while the flow separation zones are present in systole, they disappear completely during a portion of the diastolic phase. Sohara and

Karino [21] used the method of microcinematography in transparent vessels to study the steady flow field in the dog aortic arch. Their results are qualitatively very similar to the ones we have observed in the rabbit. Our pulsatile flow results are consistent with the *in-vivo* pulsed Doppler ultrasound results of Farthing and Peronneau [22] in the dog. These results indicate reverse flow primarily along the lesser curvature of the arch during the diastolic phase, while the flow within the arch branches remains in the forward direction throughout the course of the cardiac cycle.

With the exception of the results of Rodkiewicz [20], sites of early atherosclerotic lesions experimentally induced in the aortic arch of the hypercholesterolemic rabbit follow a helical pattern [6,7]. Moreover, our previous topographical mapping studies of enhanced permeability sites in the normal rabbit aorta [3] have demonstrated that within the aortic arch and the upper descending thoracic aorta, the region of highest enhanced permeability site density follows a helical pattern beginning along the dorsal wall, coiling in the clockwise direction to localize along the greater curvature of the arch immediately distal to the left subclavian artery, and finally continuing further to the ventral wall in the upper descending thoracic aorta. The flow patterns reported in this paper have revealed the existence of a single clockwise helical secondary flow cell within the aortic arch. However, this helical motion is confined to the ventral wall of the aortic arch in steady flow. In pulsatile flow, the flow field is significantly more complicated, and the helical flow motion may well extend to the dorsal wall of the aortic arch. The exact relationship, if any, between the helical flow in the arch and the helical pattern of enhanced permeability sites and early atherosclerotic lesions remains unclear at this point.

4.4.2 Abdominal Aorta

Steady flow was studied in the abdominal aorta in the vicinity of the major aortic branches - the celiac, superior mesenteric, right renal, and left renal arteries. The results revealed the existence of very complex flow fields consisting of a number of streamline groups that exhibit drastically different behavior. In virtually every case, there are streamlines which deflect off the branch flow divider and then follow very slowly-moving recirculation trajectories within the aorta lateral to the branches before finally tracing helical paths into the branches. Boundary layer separation and consequent flow recirculation has been observed along the dorsal wall of the aorta opposite the superior mesenteric artery. Furthermore, since the superior mesenteric and right renal arteries are often in close anatomical proximity, the flow fields associated with these vessels interact thereby resulting in considerably more complex flow patterns. Finally, flow separation is frequently observed at the entrance of branches, and these separation zones are typically occupied by streamlines originating from the slowly-moving latreral recirculation cells.

Wall shear stresses are commonly higher distal to branches than proximal; however, very few generalizations can be made *a priori* in this regard. In the case of sharply skewed velocity profiles, for instance, the proximal shear stress levels may exceed their distal counterparts as was observed in the case of the left renal artery studied here.

Only steady flow was studied in the abdominal aorta; therefore, it remains unclear at this point whether or not the flow recirculation zones observed (both ones lateral to ostia and those along the dorsal wall of the aorta whenever they exist) periodically appear and disappear within the course of a cardiac cycle as was observed in the aortic arch. If this were to occur, then the aortic wall within the recirculation zones which are exposed to

very low levels of shear stress in steady flow would be exposed to shear stresses of periodically changing magnitudes and directions and hence to potentially large spatial and temporal gradients of shear stress.

The results reported here are qualitatively very similar to those of Karino *et al.* in glass models [23,24] and in the dog abdominal aorta [25]. Hutchison *et al.* [26] performed *in-vivo* pulsed Doppler ultrasound measurements on the dog abdominal aorta and reported small regions of lateral recirculation during systole and large regions of flow reversal opposite to ostia during diastole. The literature on experimentally induced atherosclerosis in hypercholesterolemic rabbits reveals that in the abdominal aorta early lesions localize virtually exclusively around branches, and that they exhibit a characteristic crescent shape spanning the lateral and distal regions around branches [7]. Zeindler *et al.* [5] followed the progression of early lesions around aortic branches in rabbits and demonstrated that the earliest deposits occur laterally with the distal involvement eventually catching up with or even exceeding the lateral component. The regions lateral to branches are the same regions where the lateral recirculation zones were observed in this study although the precise connection between specific fluid mechanical characteristics and early lesion development remains unidentified.

A direct comparison of the steady flow patterns and wall shear stresses obtained here with the topography of enhanced permeability sites in [3] reveals no correlation. For instance, the enhanced permeability sites localize distal to both right and left renal arteries. Figure 4.16 illustrates that this corresponds to a region of high wall shear stress in the case of the right renal artery and low shear stress in the case of the left renal artery. It is deemed important to establish whether or not the same conclusions apply under pulsatile flow conditions.

The method of flow visualization used here offers distinct advantages over other flow visualization techniques. Firstly, the experiments are performed on natural aortas so the exact tortuous arterial geometry is maintained. This is a very important advantage in view of the expected dependence of the flow field on geometric details. Glass models and even polymeric casts often fail to reproduce exact geometric features due to difficulties of manufacturing or polymer shrinkage. Secondly, the flow inlet conditions into the aorta are more phsiologically realistic than in other models because the hearts remain attached to the aortas in these preparations. Inlet flow conditions through the left ventricle and the aortic valve are expected to be different from those that would be obtained had an infusion tube been connected directly to the ascending thoracic aorta. Sohara and Karino [21] have demonstrated that the flow patterns in the aortic arch of the dog are sensitive to whether or not the heart remains attached to the aorta. They, in fact, have postulated that the left ventricle and/or the aortic valve is the major source of the the helical ventral flow observed. Thirdly, the vessel walls in our preparations are fully soaked in the working fluid (oil of wintergreen) and the vessel itself is placed in a large reservoir of the same fluid during the flow visualization procedure; therefore, discrepancies induced by optical distortion are minimal. Finally, the method offers a high level of spatial resolution and tremendous fluid mechanical detail with the capability to perform quantitative analyses of fluid velocities and resulting wall shear stress levels.

On the other hand, the method has specific limitations. The process of rendering the aorta transparent causes a complete loss of arterial wall compliance. In fact, the loss of compliance prevented performing pulsatile flow experiments in the abdominal aorta. Moreover, in spite of experimental

evidence that changes in aortic cross-sectional area within the cardiac cycle are only on the order of ±5% (±3% in the dog descending aorta [27]), there is evidence that wall compliance reduces the sizes of recirculation zones distal to stenoses [28]. Therefore, loss of compliance may be an important limitation of the method. Another disadvantage is that the measurements are performed in a vessel that has been excised from the body of the animal, so that the question of how closely they approximate actual *in-vivo* conditions remains unanswered. However, the qualitative agreement obtained here with the *in-vivo* data in the dog aortic arch [22] lends support to the soundness of the technique. The fact that oil of wintergreen is a Newtonian, single phase fluid which is obviously different from blood, a non-Newtonian, two-phase suspension, is not expected to be a restrictive limitation since blood at shear rates of above 100 s^{-1} has been shown to behave like a Newtonian fluid [29], and the high flowrates in the aorta generally lead to shear rates which considerably exceed 100 s^{-1}. The sole exception in this regard is within regions of flow recirculation where the fluid may move very slowly, and hence the non-Newtonian characteristics of blood may be important. Finally, the pulsatile flow studies that have been performed in the aortic arch have been based on a sinusoidal pulse shape which is non-physiological; however, since the pulsatile cycle incorporates a portion of reverse flow, the fundamental fluid mechanical phenomena are expected to be captured.

In addition to the specific flow visualization method limitations outlined above, there is a number of inherent assumptions made in the process of data analysis and reduction. A central assumption is that the tracer microspheres exactly follow the fluid streamlines. Although this assumption is generally believed to be valid since the microsphere Reynolds number (i.e. Reynolds number based on microsphere diameter, mean fluid velocity, and fluid

viscosity) is usually small, there are zones at regions of sharp curvature that remain particle-free or that only the smaller microspheres can penetrate due to the larger inertia of the larger microspheres. Another important assumption made in the analysis of the velocity profiles in the common median planes of the various aortic sections photographed is that at each spatial position the maximum particle velocity occurs in the common median plane. This would be exactly true in the case of a straight vessel; however, whenever there is curvature, the velocity profiles may be skewed so that the maximum velocity may not occur exactly in the common median plane. The limitations of the method accentuate the need for *in-vivo* flow field data in the rabbit. Experiments in this regard are currently under way.

It is interesting that the results of Karino and coworkers in the dog [21,25] and the human [30] are qualitatively similar to the findings reported here in the rabbit despite differences in aortic geometric details. The detailed quantitative data such as exact values of wall shear stress, fluid velocity, and sizes of specific recirculation zones naturally vary. In view of the fact that the patterns of early atherosclerotic lesion localization vary drastically among these species, it may very well be that the microscopic details are all-important in defining a potential role for hemodynamics, if such a role exists, in atherogenesis.

4.5 References

1. Stemerman MB, Morrel EM, Burke KR, Colton CK, Smith KA, Lees RS. Local variation in arterial wall permeability to low density lipoprotein in normal rabbit aorta. *Arteriosclerosis.* **6:** 64, 1986.

2. Tompkins RG, Yarmush ML, Schnitzer JJ, Colton CK, Smith KA, Stemerman MB. Low-density lipoprotein transport in blood vessel walls of squirrel monkeys. *Amer. Physiol. Soc.* (Heart Circ. Physiol.). **26:** H452, 1989.

3. Barakat AI, Uhthoff PAF, Colton CK. Topographical mapping of sites of enhanced HRP permeability in the normal rabbit aorta. *J. Biomech. Eng.* **114:** 283, 1992.

4. Cornhill JF, Roach MR. A quantitative study of the localization of atherosclerotic lesions in the rabbit aorta. *Atherosclerosis.* **23:** 489, 1976.

5. Zeindler CM, Kratky RG, Roach MR. Quantitative measurements of early atherosclerotic lesions on rabbit aortae from vascular casts. *Atherosclerosis.* **76:** 245, 1989.

6. Roach MR. The effects of bifurcations and stenoses on arterial disease. *Cardiovascular Flow Dynamics and Measurements.* Hwang NHC, Normann NA, eds., p. 489, Baltimore: University Press, 1977.

7. Schwenke DC, Carew TE. Initiation of atherosclerotic lesions in cholesterol-fed rabbits. I. Focal increases in arterial LDL concentration precede development of fatty streak lesions. *Arteriosclerosis.* **9:** 895, 1989.

8. Lutz RJ, Cannon JN, Bischoff KB, Dedrick RL, Stiles RK, Fry DL. Wall shear stress distribution in a model canine artery during steady flow. *Circ. Res.* **41:** 391, 1977.

9. Friedman MH, Hutchins GM, Bargeron CB, Deters OJ, Mark FF. Correlation of human arterial morphology with hemodynamic measurements in arterial casts. *J. Biomech. Eng.* **103:** 204, 1981.

10. Pedersen EM, Yoganathan AP, Lefebvre XP. Pulsatile flow visualization in a model of the human abdominal aorta and aortic bifurcation. *J. Biomechanics.* **25:** 935, 1992.

11. Ku DN, Glagov S, Moore JE, Zarins CK. Flow patterns in the abdominal aorta under simulated postprandial and exercise conditions: An experimental study. *J. Vasc. Surg.* **9:** 309, 1989.

12. Thiriet M, Pares C, Saitel E, Hecht F. Numerical simulation of steady flow in a model of the aortic bifurcation. *J. Biomech. Eng.* **114:** 40, 1992.

13. Fernandez RC, De Witt KJ, Brown MR. Pulsatile flow through a bifurcation with applications to arterial disease. *J. Biomechanics.* **9:** 575, 1976.

14. Perktold K, Florian H, Hilbert D, Peter R. Wall shear stress distribution in the human carotid siphon during pulsatile flow. *J. Biomechanics.* **21:** 663, 1988.

15. Wille SO. Numerical simulations of steady flow inside a three dimensional aortic bifurcation model. *J. Biomed. Eng.* **6:** 49, 1984.

16. O'Brien V, Ehrlich LW. Simulation of unsteady flow at renal branches. *J. Biomechanics.* **10:** 623, 1977.

17. Weisbroth SH, Flatt RE, Kraus AL, eds. *The Biology of the Laboratory Rabbit.* Ch. 3, New York: Academic Press, 1974.

18. Karino T, Motomiya M. Flow visualization in isolated transparent natural blood vessels. *Biorheology.* **20:** 119, 1983.

19. Barakat AI, Marini RP, Colton CK. Measurement of flowrates through aortic branches in the rabbit in vivo. (Manuscript in Preparation).

20. Rodkiewicz CM. Localization of early atherosclerotic lesions in the aortic arch in the light of fluid flow. *J. Biomechanics.* **8:** 149, 1975.

21. Sohara Y, Karino T. Secondary flows in the dog aortic arch. In *Fluid Control and Measurement,* Harada M, ed., p. 143, Oxford: Pergamon Press, 1985.

22. Farthing S, Peronneau P. Flow in the thoracic aorta. *Cardiovasc. Res.* **13:** 607, 1979.

23. Karino T, Kwong HHM, Goldsmith HL. Particle flow behaviour in models of branching vessels. I. Vortices in 90° T-junctions. *Biorheology.* **16:** 231, 1979.

24. Karino T, Goldsmith HL. Particle flow behavior in models of branching vessels. II. Effects of branching angle and diameter ratio on flow patterns. *Biorheology.* **22:** 87, 1985.

25. Karino T, Motomiya M, Goldsmith HL. Flow patterns at the major T-junctions of the dog descending aorta. *J. Biomech.* **23:** 537, 1990.

26. Hutchison KJ, Karpinski E, Campbell JD, Potemkowski AP. Aortic velocity contours at abdominal branches in anesthetized dogs. *J. Biomech.* **21:** 277, 1988.

27. Patel DJ, Greenfield JC Jr., Fry DL. In vivo pressure-length-radius relationship of certain blood vessels in man and dog. In *Pulsatile Blood Flow*, Atinger EO, ed., p. 293, 1964.

28. Leipsch D, Moravec S. Pulsatile flow of non-newtonian fluid in distensible models of human arteries. *Biorheology.* **21:** 571, 1984.

29. Fung YC. *Biomechanics - Mechanical Properties of Living Tissues.* New York: Springer-Verlag, 1981.

30. Endo S, Karino T. Personal Communication.

Figure Captions

Figure 4.1 Anatomical schematic of the rabbit aorta and its major branches.

Figure 4.2 Typical transparent aortic arch and branches.

Figure 4.3 Detailed steady flow patterns in the aortic arch. The different line weights give a sense of three-dimensionality: solid lines represent streamlines in, long dashed lines represent streamlines slightly above or below, and short dashed lines represent streamlines furthest from the common median plane. The central figure is a composite of the various streamline categories, while the surrounding panels depict a breakup of these categories. The trajectories of the individual streamline categories have been described in the text. Plane A-A' shows a view of the aortic cross-section illustrating the approximate origin of the various streamline categories.

Figure 4.4 Steady flow velocity profiles in the common median plane at selected locations of the aortic arch and its branches. Numbers on the aortic wall are wall shear stresses in dyne/cm^2, while numbers on the profiles at every plane are the maximum velocities in mm/sec in that plane. Negative values of shear stress denote flow in the direction opposite to that of the bulk flow.

Figure 4.5 Pulsatile flow velocity profiles in the common median plane at selected locations of the aortic arch and its branches at five equally-spaced time points within a single pulsatile cycle. t=0 corresponds to the beginning of the cycle. See caption for Figure 4.4 for further details. This vessel is the same one shown in Fig. 4.4 but photographed from a slightly different angle.

Figure 4.6 Distal to proximal shear stress ratio at the brachiocephalic and left subclavian arteries as a function of time for one pulsatile cycle. The steady flow values are also indicated.

Figure 4.7 Pulsatile to steady flow shear stress ratio as a function of time for one pulsatile cycle at both the lesser and greater curvature of the aortic arch at selected locations. The straight unity lines indicate where the pulsatile and steady flow shear stresses are equal.

Figure 4.8 Typical transparent aorto-celiac junction. The curvature is sharper at the distal tip of the branch than at the proximal tip.

Figure 4.9 Detailed steady flow patterns in the vicinity of the celiac artery. See caption for Figure 4.3 for further details.

Figure 4.10 Steady flow velocity profiles in the common median plane at selected locations in the vicinity of the celiac artery. See caption for Figure 4.4 for further details.

Figure 4.11 Typical transparent aorto-superior mesenteric junction illustrating the close anatomical proximity to the right renal artery. The superior mesenteric and right renal arteries emerge from the aorta almost at right angles to one another; therefore, the portion of the right renal artery shown is the projection of the right renal artery in the plane of the superior mesenteric artery. The curvature is sharper at the distal tip of the branch than at the proximal tip.

Figure 4.12 Detailed steady flow patterns in the vicinity of the superior mesenteric artery. See caption for Figure 4.3 for further details.

Figure 4.13 Steady flow velocity profiles in the common median plane at selected locations in the vicinity of the superior mesenteric artery. See caption for Figure 4.4 for further details.

Figure 4.14 Typical transparent aorto-renal junction. The curvature is sharper at the distal tips of the branches than at the proximal tips.

Figure 4.15 Detailed steady flow patterns in the vicinity of the right and left renal arteries. See caption for Figure 4.3 for further details.

Figure 4.16 Steady flow velocity profiles in the common median plane at selected locations in the vicinity of the right and left renal arteries. See caption for Figure 4.4 for further details.

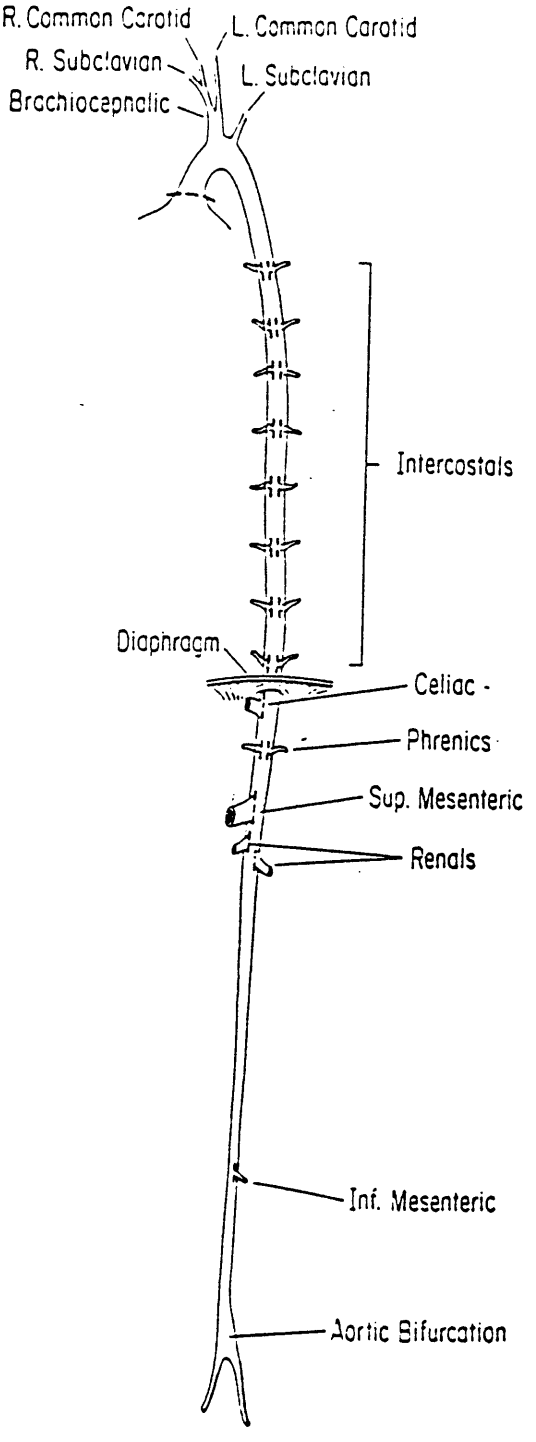
R. Common Carotid
L. Common Carotid
R. Subclavian
L. Subclavian
Brachiocephalic
Intercostals
Diaphragm
Celiac
Phrenics
Sup. Mesenteric
Renals
Inf. Mesenteric
Aortic Bifurcation

Figure 4.1

Figure 4.2

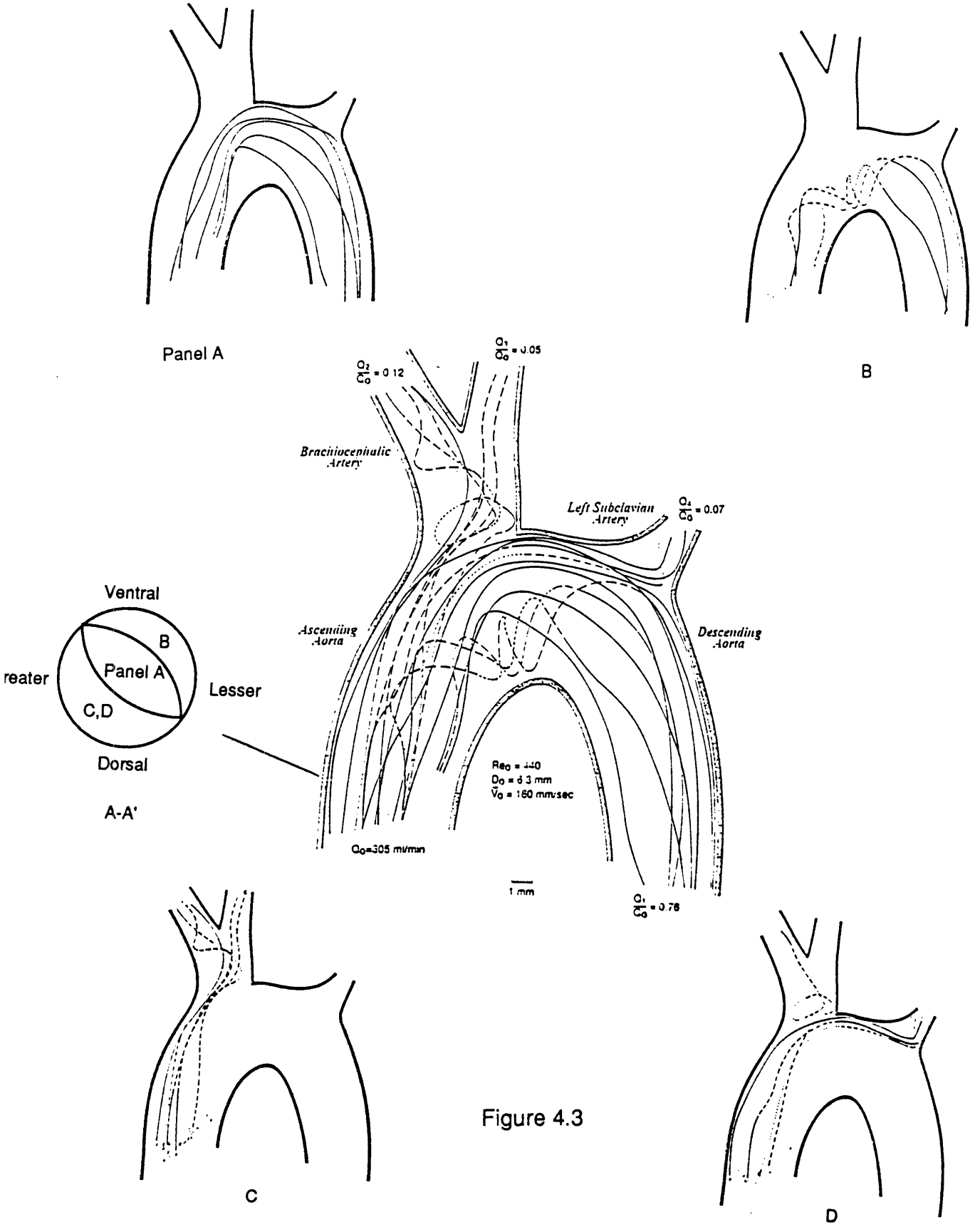
Panel A
B
Brachiocephalic Artery
Left Subclavian Artery
Ascending Aorta
Descending Aorta
Ventral
B
Panel A
reater
Lesser
C,D
Dorsal
A-A'
C
D

Figure 4.3

STEADY FLOW

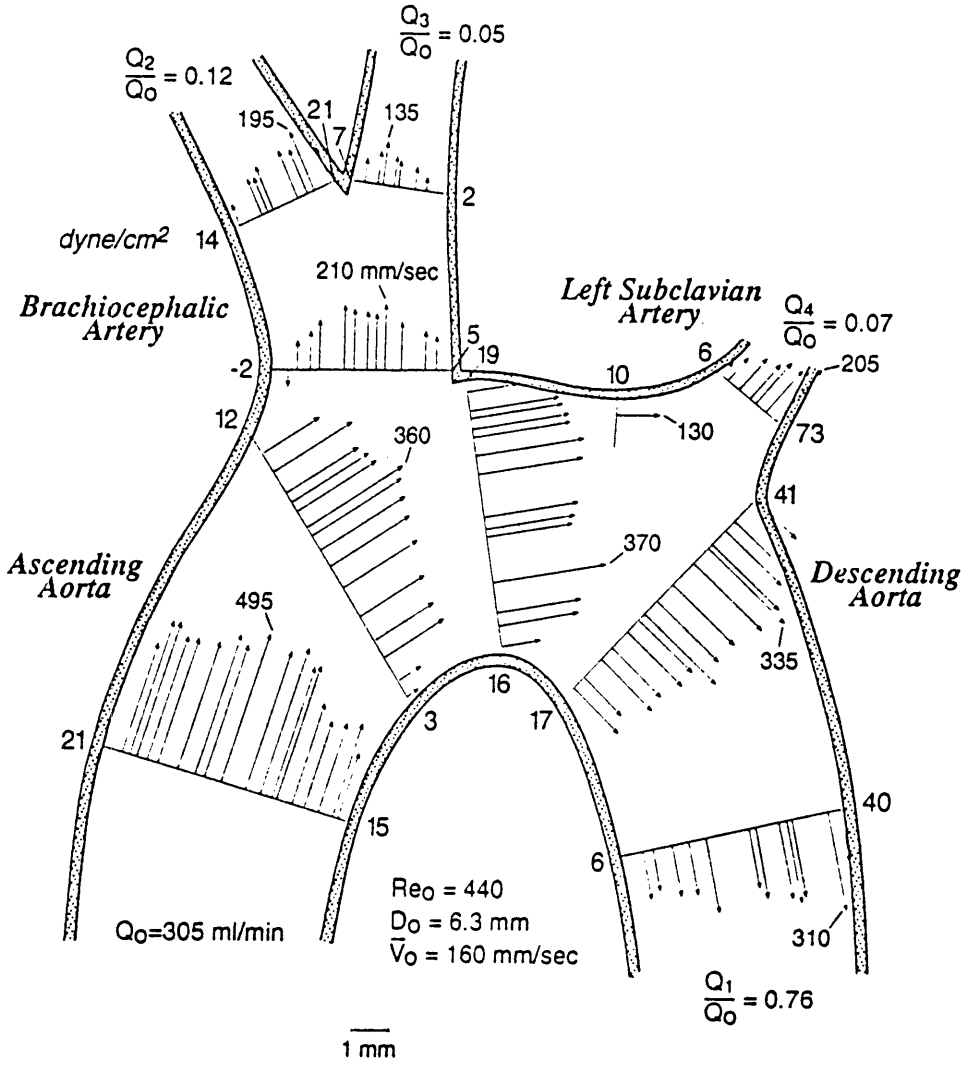

Figure 4.4

PULSATILE FLOW (t=0)

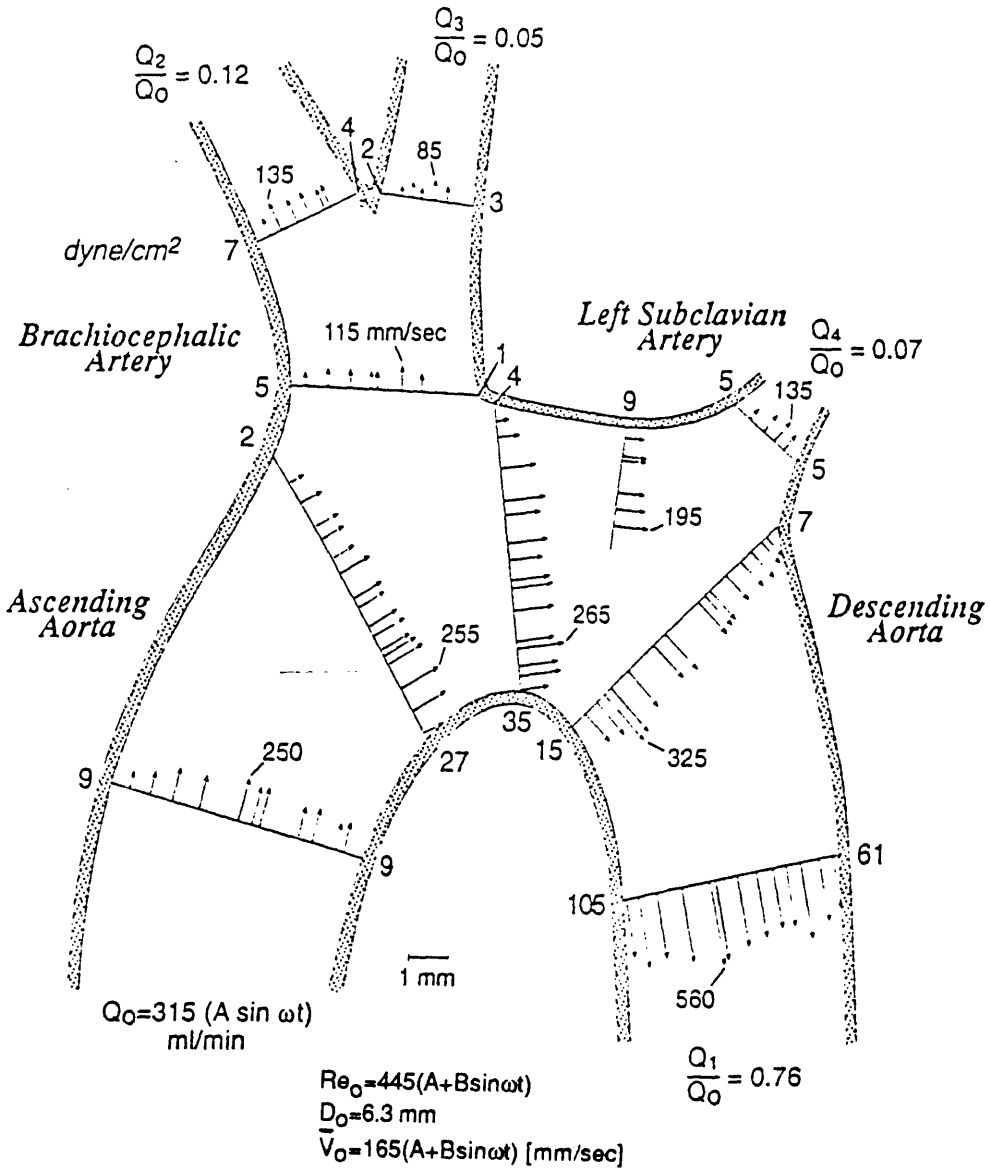

Figure 4.5 (a)

PULSATILE FLOW (t=0.2τ)

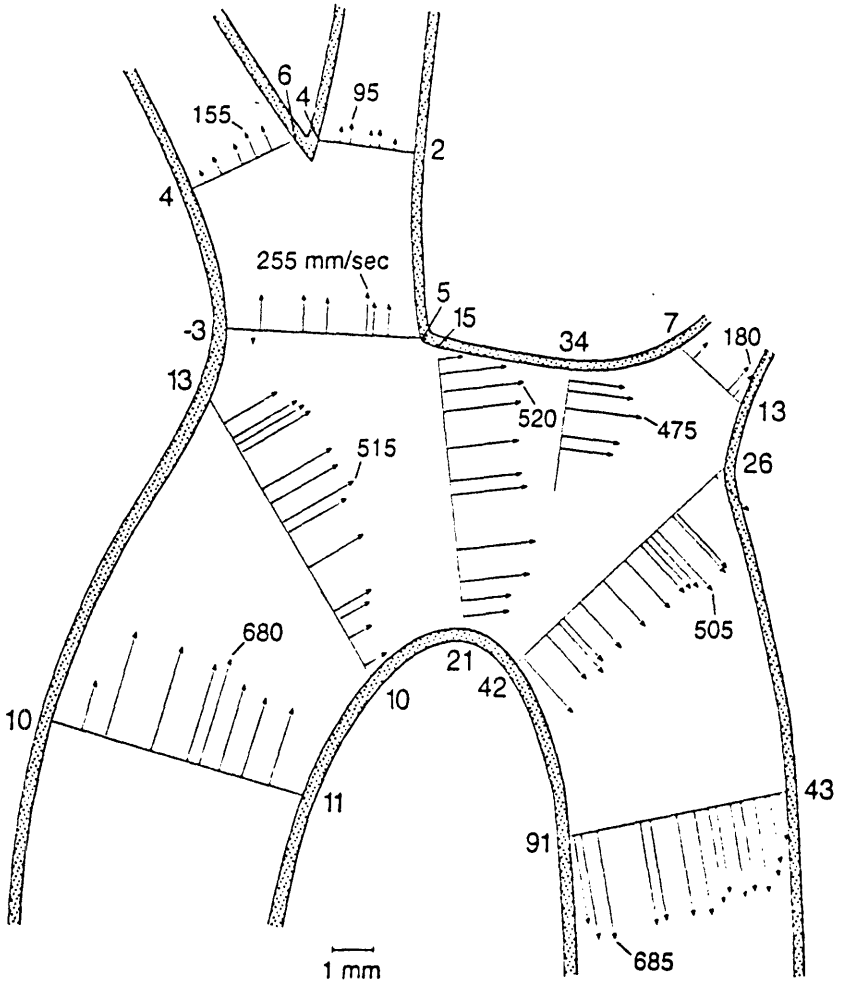

Figure 4.5 (b)

PULSATILE FLOW (t=0.4τ)

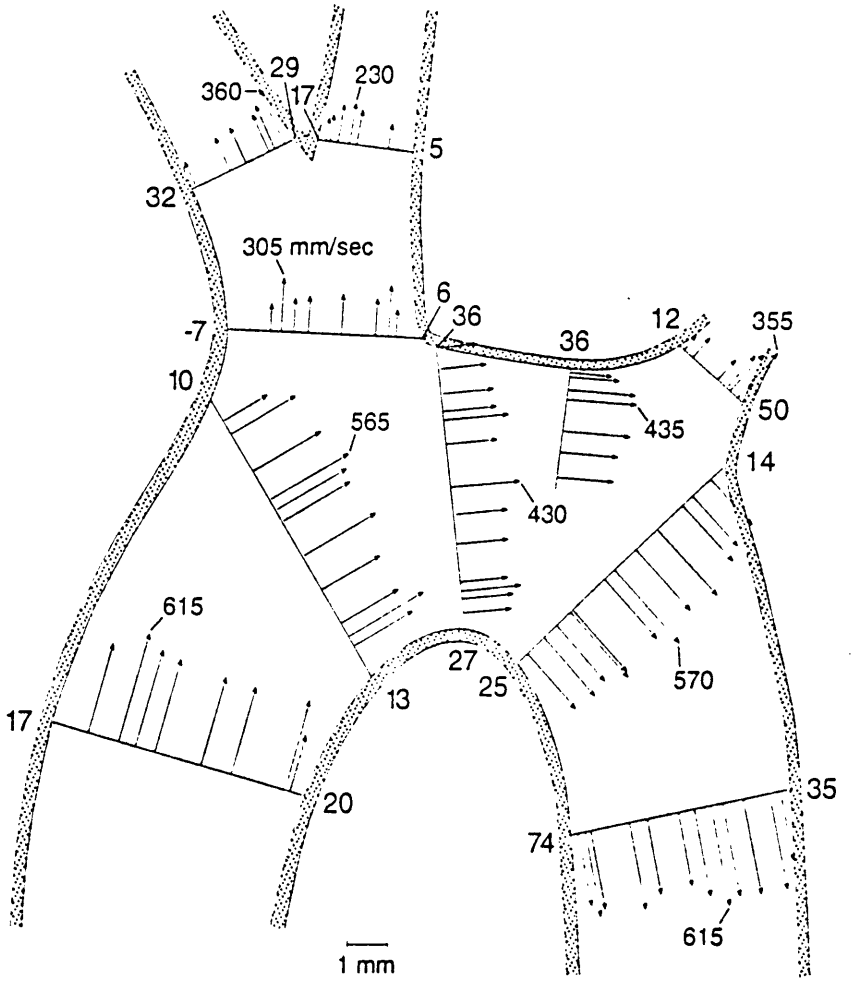

Figure 4.5 (c)

PULSATILE FLOW ($t=0.6\tau$)

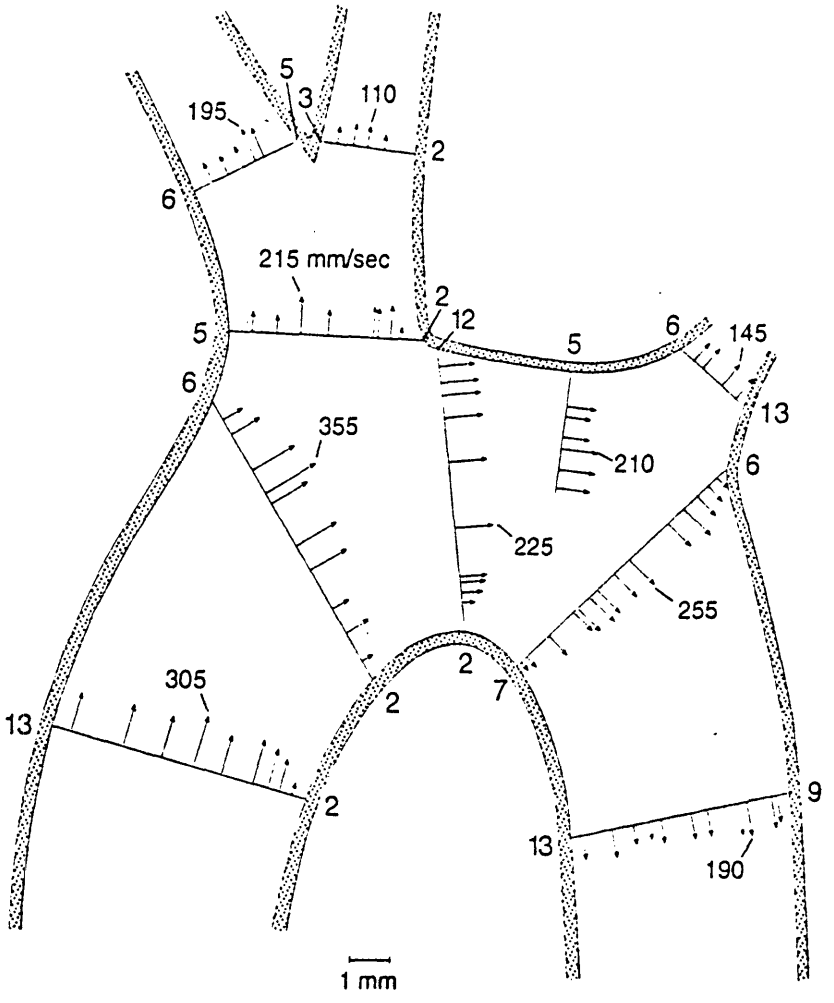

Figure 4.5 (d)

PULSATILE FLOW ($t=0.8\tau$)

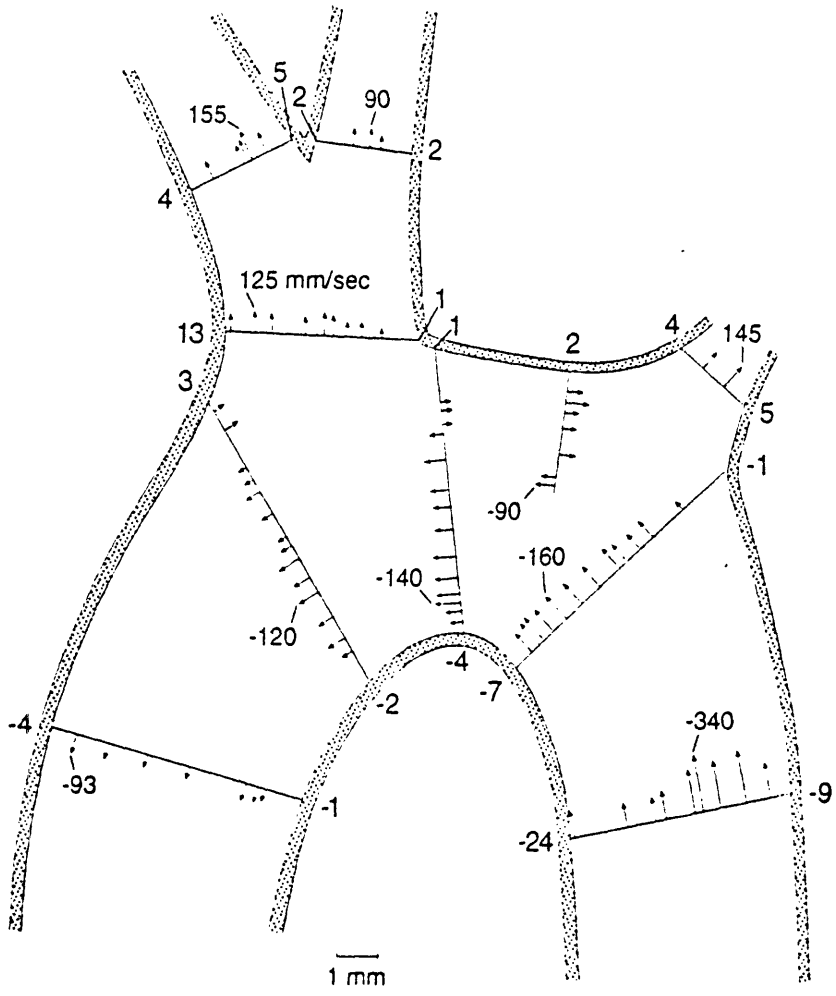

Figure 4.5 (e)

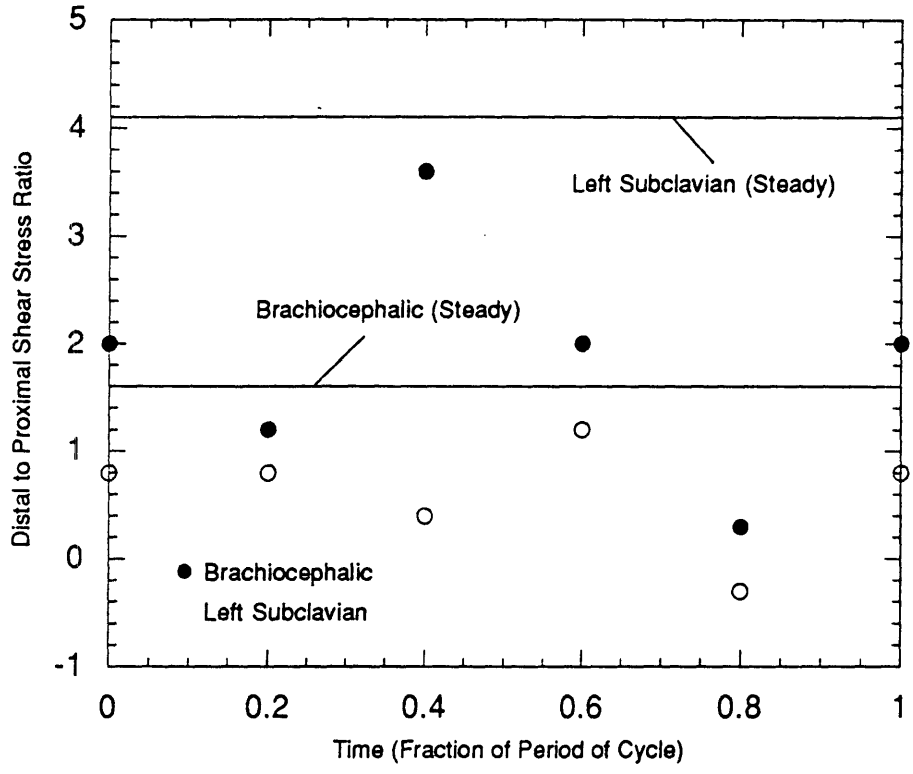
5
4
3
2
1
0
-1
0
0.2
0.4
0.6
0.8
1
Distal to Proximal Shear Stress Ratio
Time (Fraction of Period of Cycle)
Left Subclavian (Steady)
Brachiocephalic (Steady)
Brachiocephalic
Left Subclavian

Figure 4.6


1.4
1.2
1
0.8
0.6
0.4
0.2
0
-0.2
0
0.2
0.4
0.6
0.8
1
Pulsatile to Steady Flow Shear Stress Ratio
Time (Fraction of Period of Cycle)
Lesser Curvature
Greater Curvature

Figure 4.7 (a)

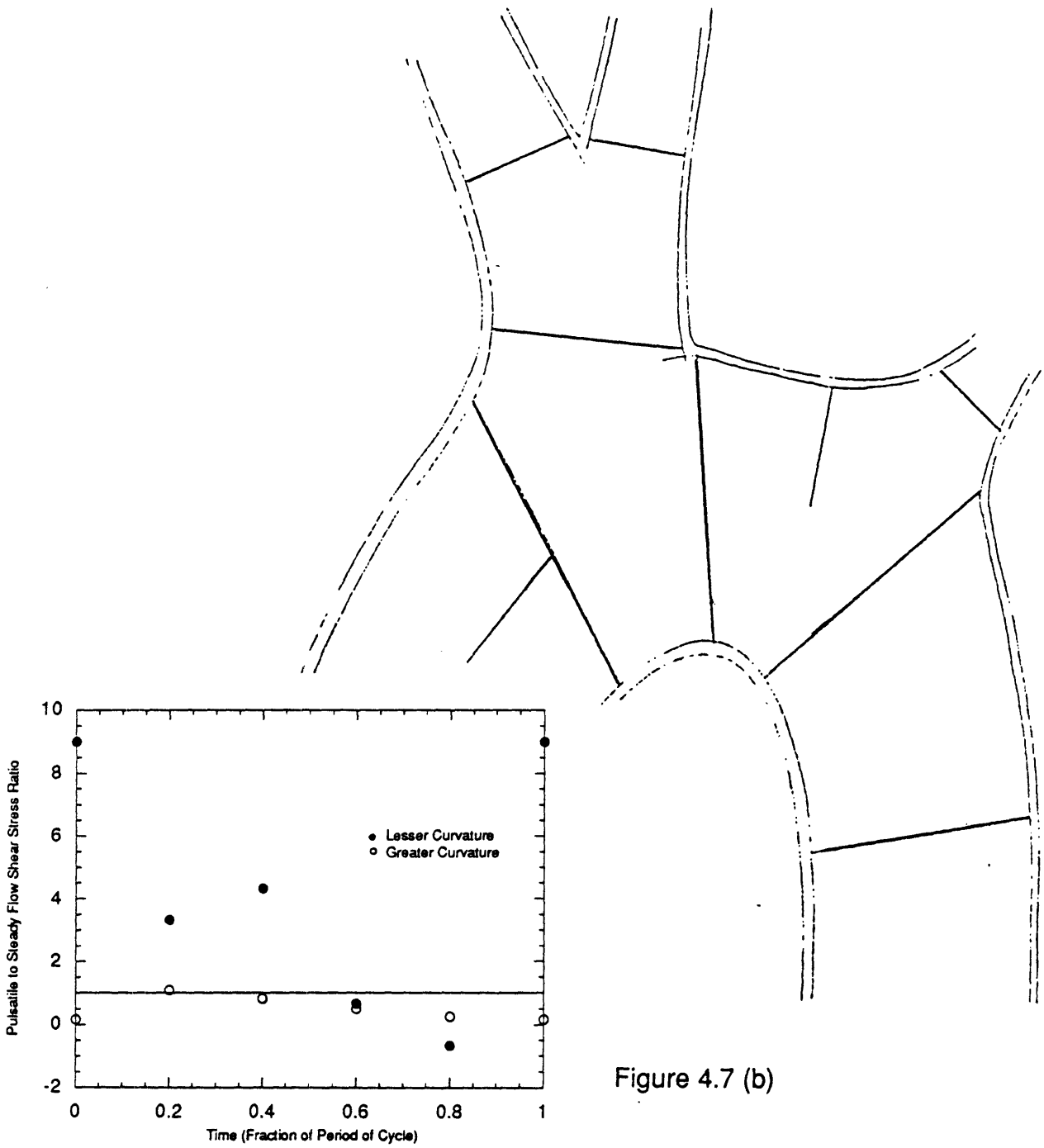
Pulsatile to Steady Flow Shear Stress Ratio
10
8
6
4
2
0
-2
0
0.2
0.4
0.6
0.8
1
Time (Fraction of Period of Cycle)
Lesser Curvature
Greater Curvature

Figure 4.7 (b)

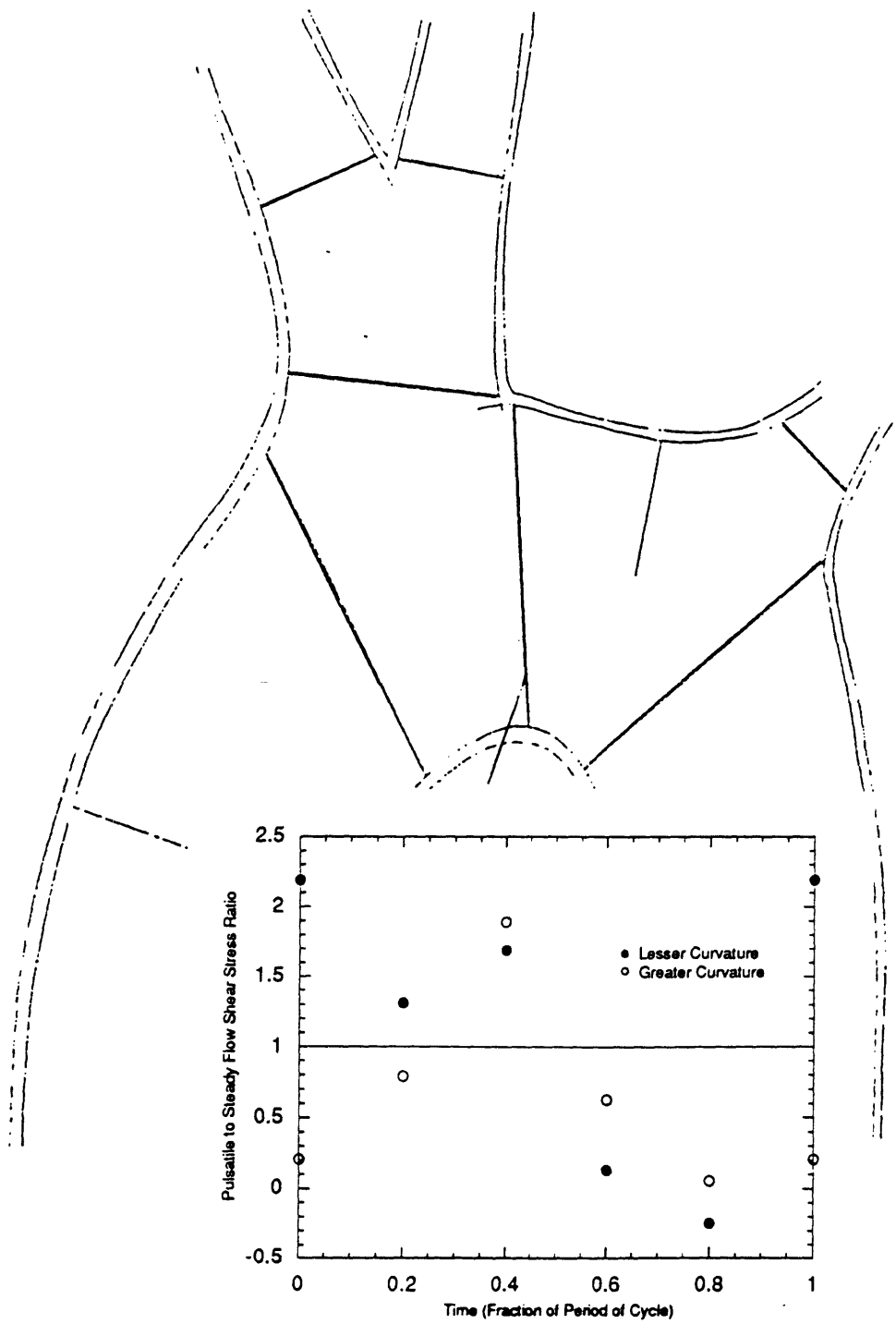
2.5
2
1.5
1
0.5
0
-0.5
0
0.2
0.4
0.6
0.8
1
Pulsatile to Steady Flow Shear Stress Ratio
Time (Fraction of Period of Cycle)
Lesser Curvature
Greater Curvature

Figure 4.7 (c)

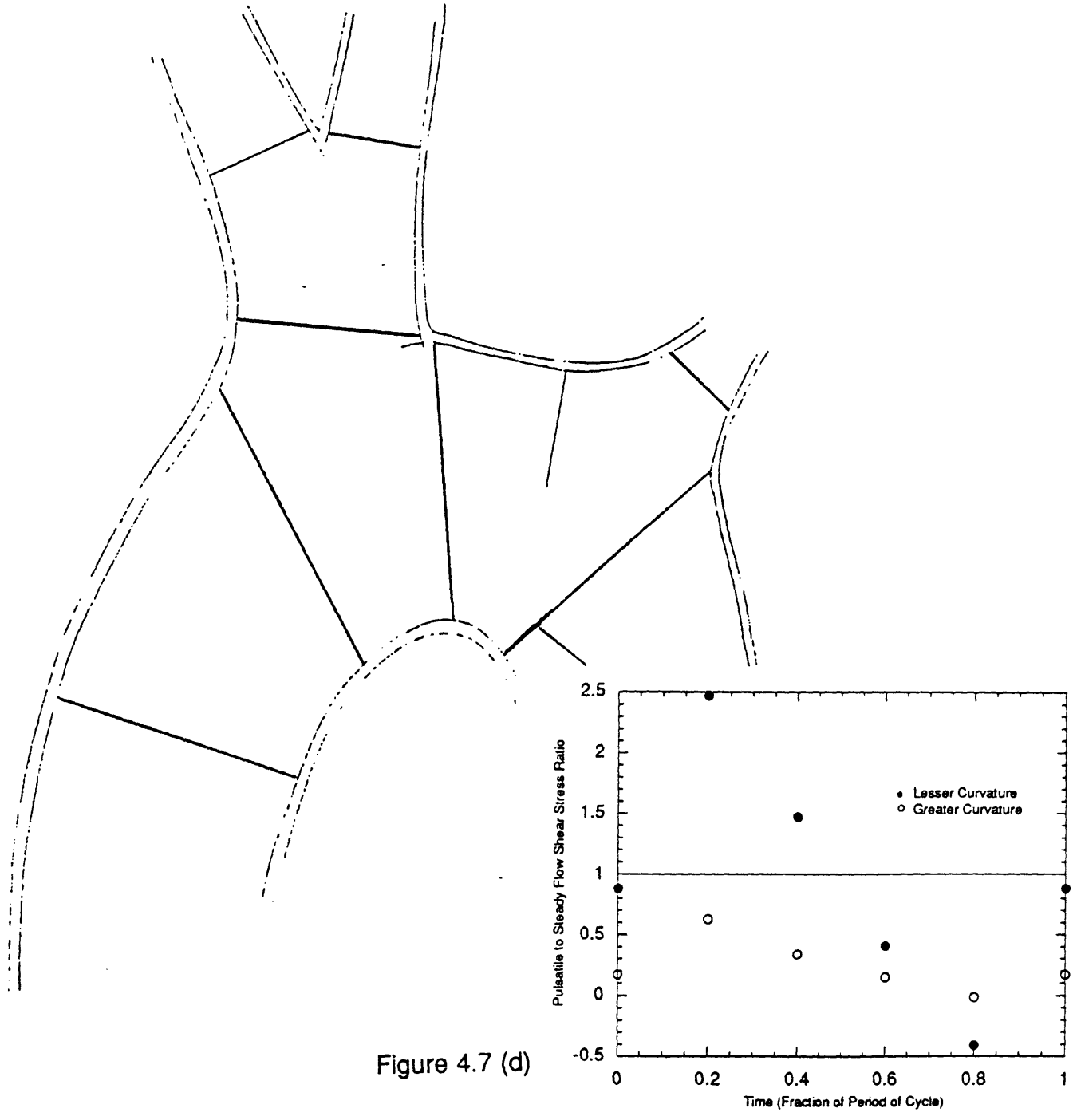
Lesser Curvature
Greater Curvature
Pulsatile to Steady Flow Shear Stress Ratio
Time (Fraction of Period of Cycle)
2.5
2
1.5
1
0.5
0
-0.5
0
0.2
0.4
0.6
0.8
1

Figure 4.7 (d)

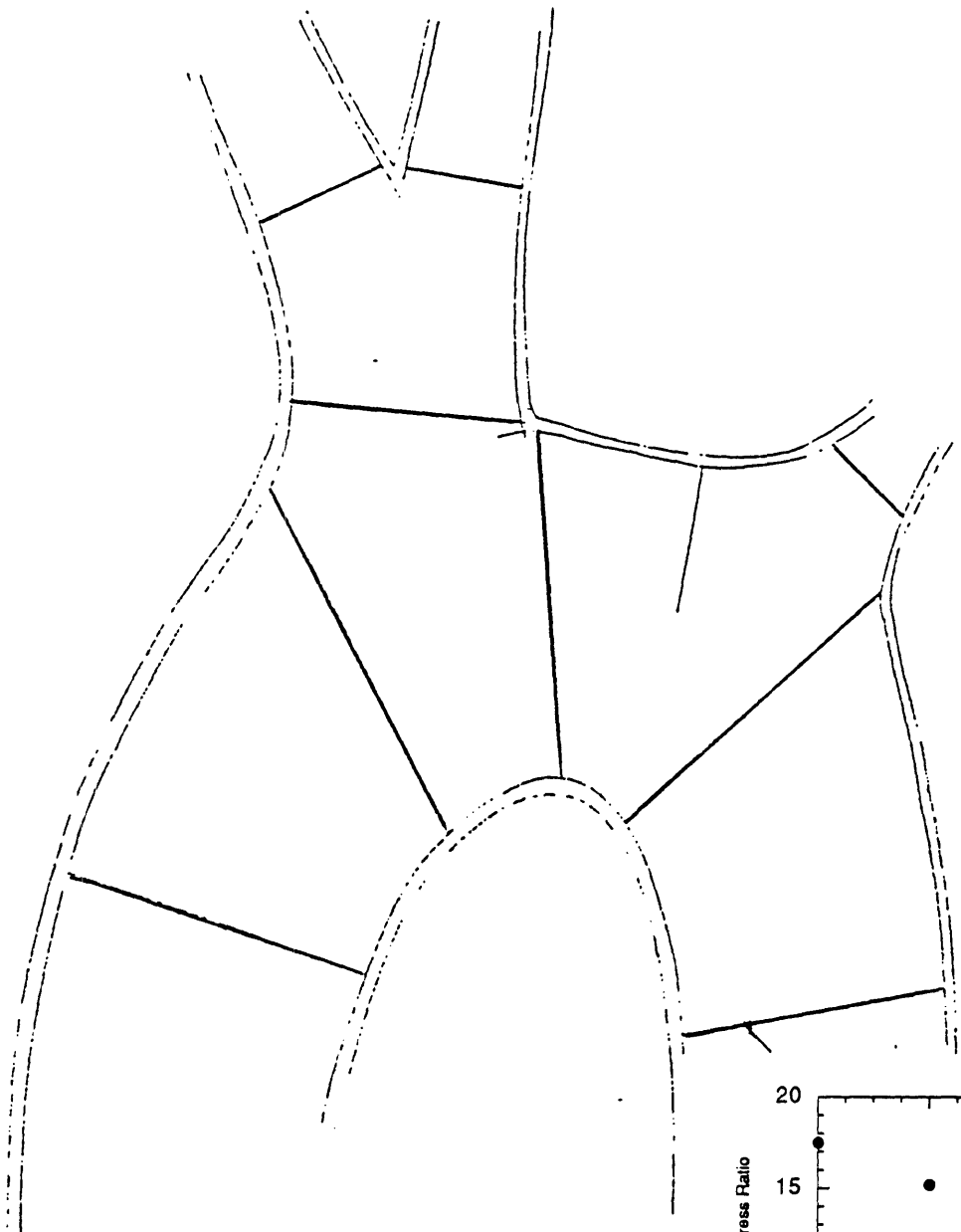

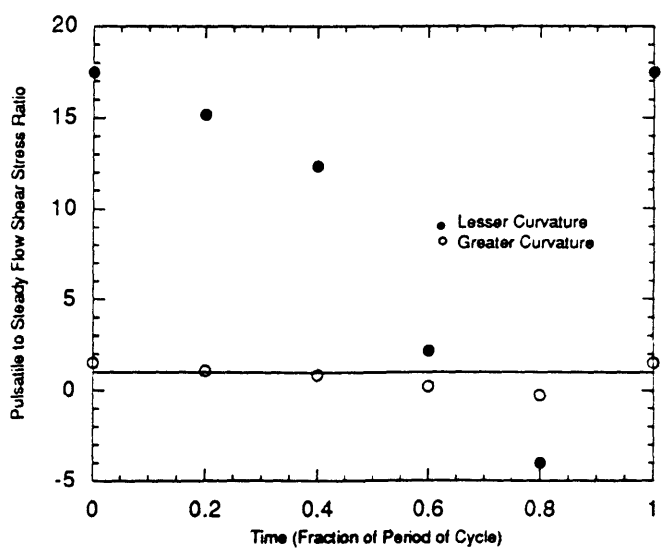
Pulsatile to Steady Flow Shear Stress Ratio
Time (Fraction of Period of Cycle)
Lesser Curvature
Greater Curvature
20
15
10
5
0
-5
0
0.2
0.4
0.6
0.8
1

Figure 4.7 (e)

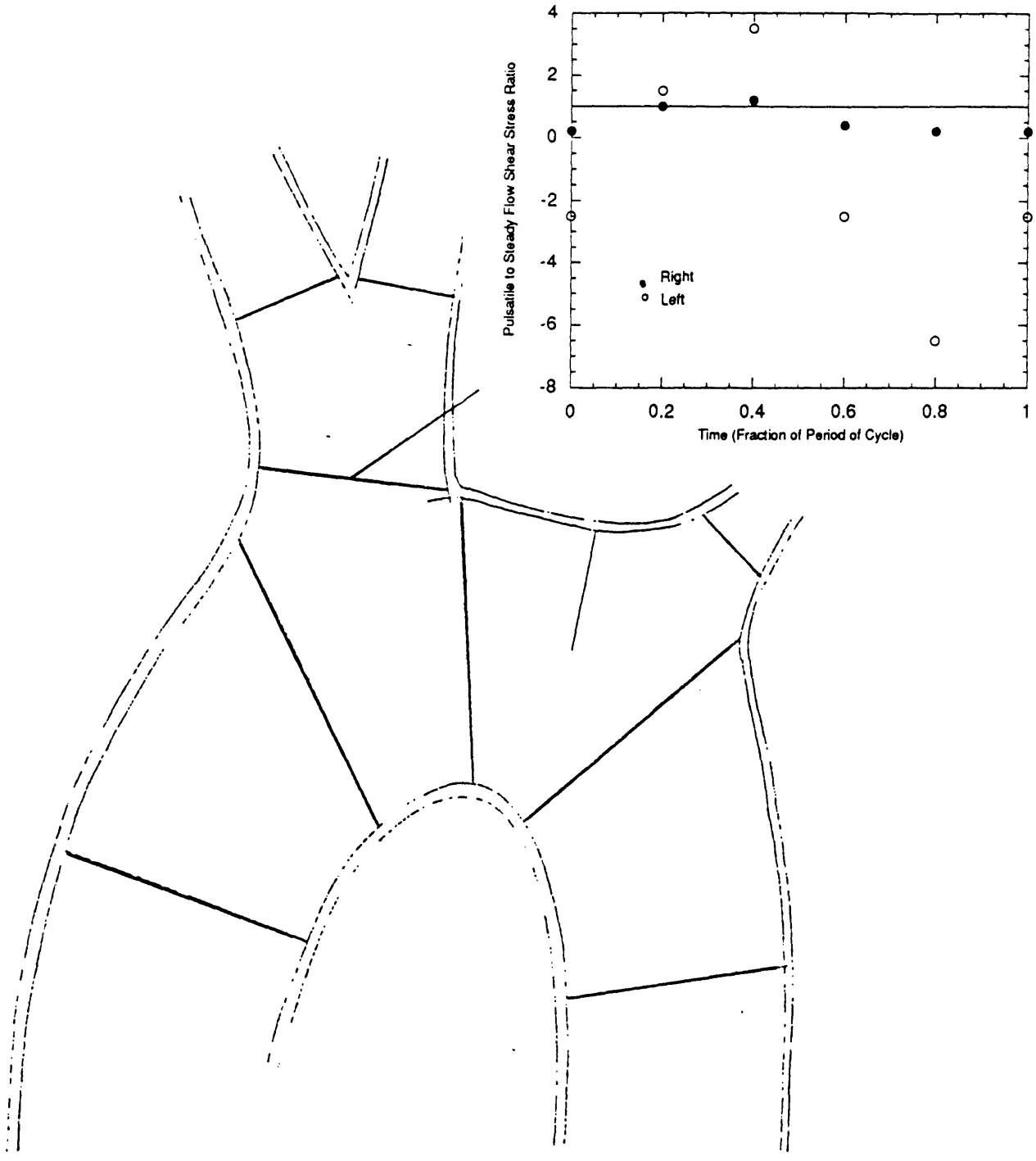
Pulsatile to Steady Flow Shear Stress Ratio
Time (Fraction of Period of Cycle)
Right
Left
4
2
0
-2
-4
-6
-8
0
0.2
0.4
0.6
0.8
1

Figure 4.7 (f)

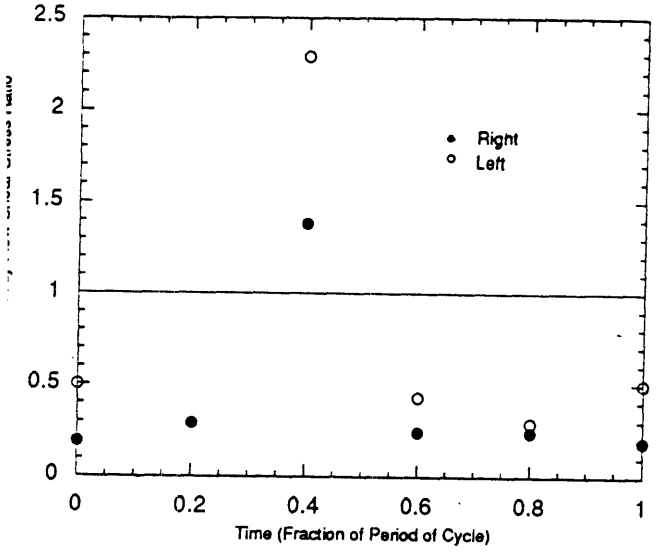
2.5
2
1.5
1
0.5
0
0
0.2
0.4
0.6
0.8
1
Right
Left
Time (Fraction of Period of Cycle)

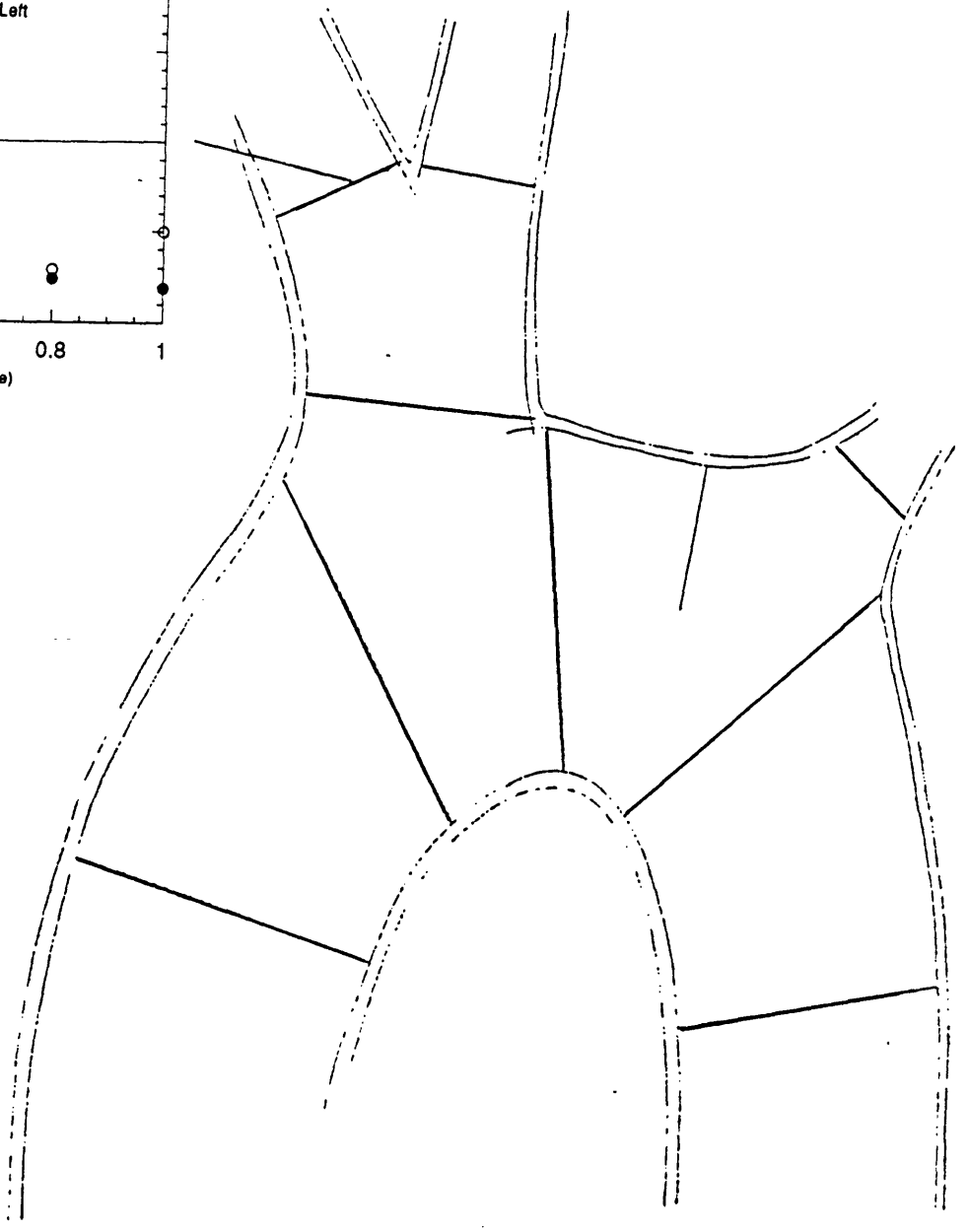

Figure 4.7 (g)

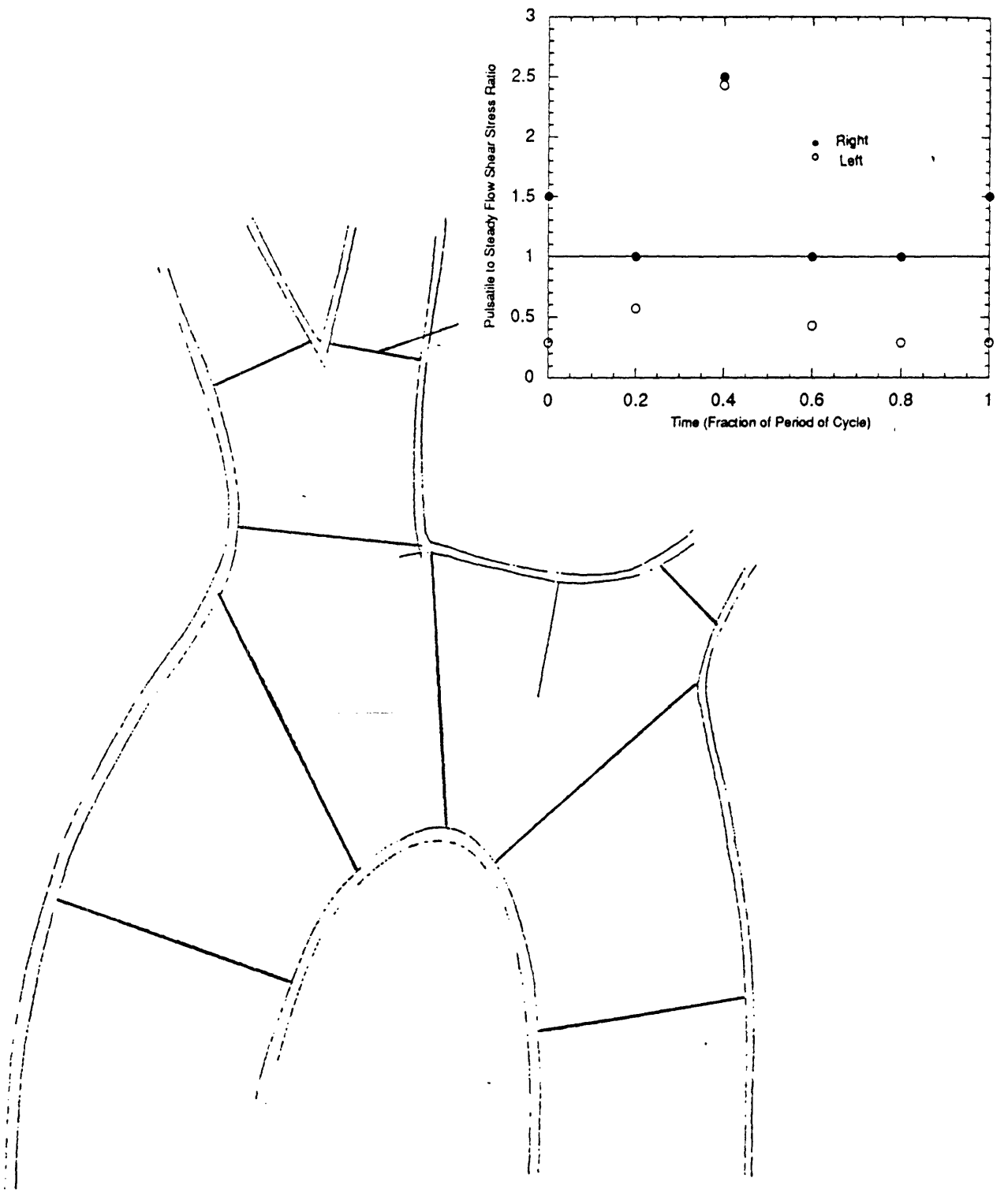
Pulsatile to Steady Flow Shear Stress Ratio
3
2.5
2
1.5
1
0.5
0
Right
Left
0
0.2
0.4
0.6
0.8
1
Time (Fraction of Period of Cycle)

Figure 4.7 (h)

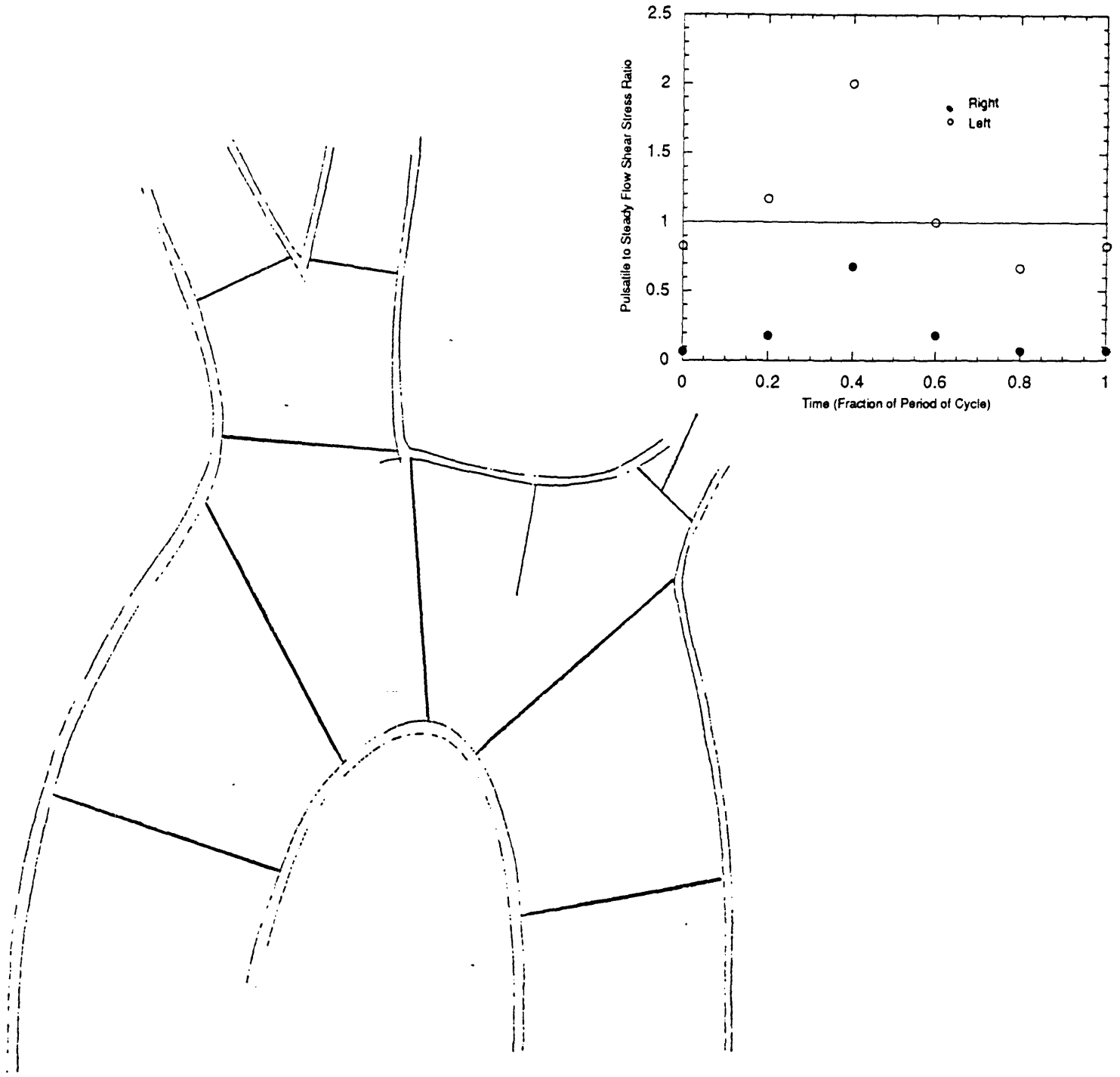
2.5
2
1.5
1
0.5
0
0
0.2
0.4
0.6
0.8
1
Right
Left
Pulsatile to Steady Flow Shear Stress Ratio
Time (Fraction of Period of Cycle)

Figure 4.7 (i)

Figure 4.8

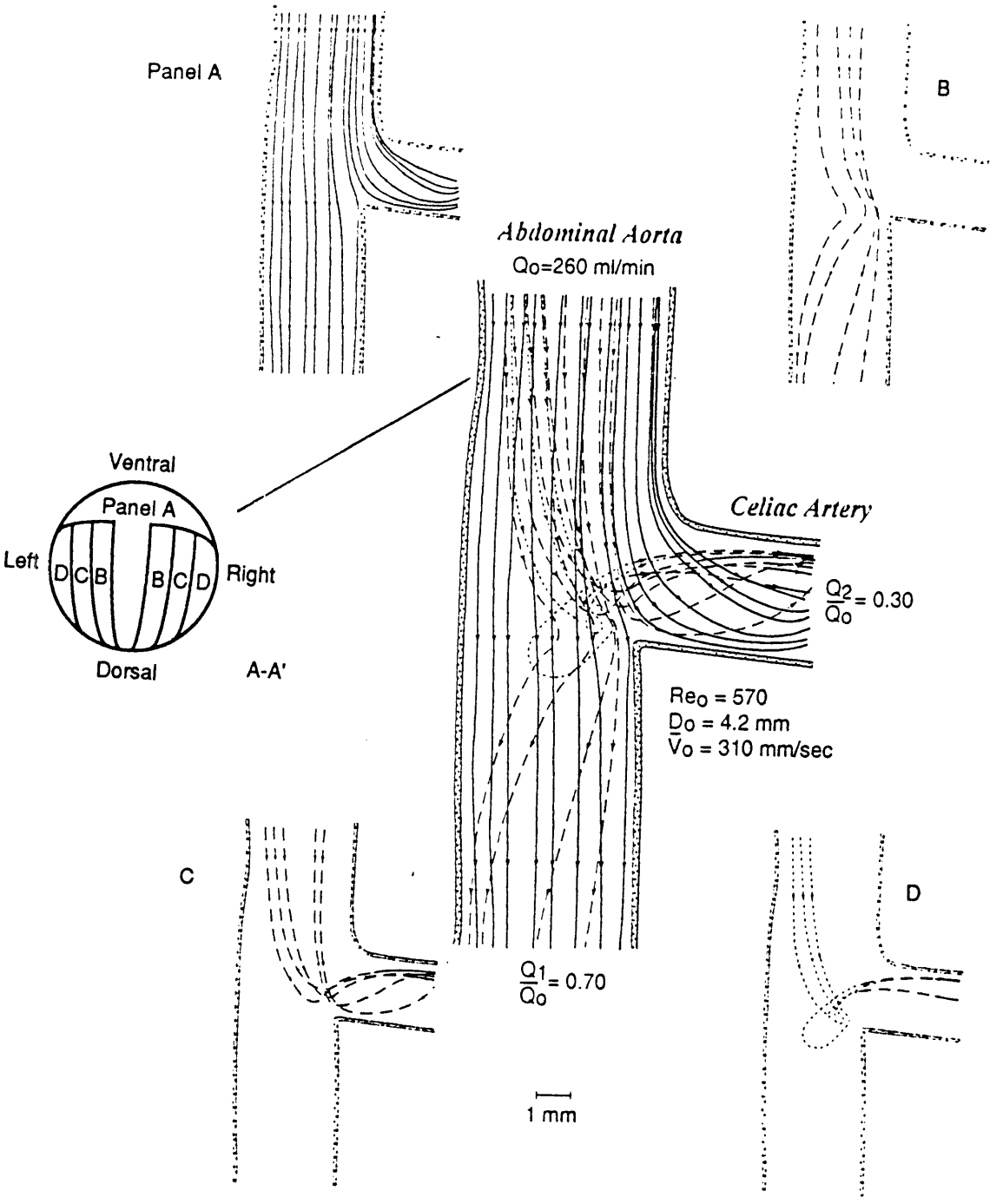
Panel A
B
Abdominal Aorta
Qo=260 ml/min
Ventral
Panel A
Left
D C B
B C D
Right
Dorsal
A-A'
Celiac Artery
Q2/Qo = 0.30
Reo = 570
Do = 4.2 mm
Vo = 310 mm/sec
C
D
Q1/Qo = 0.70
1 mm

Figure 4.9

STEADY FLOW IN TRANSPARENT AORTA

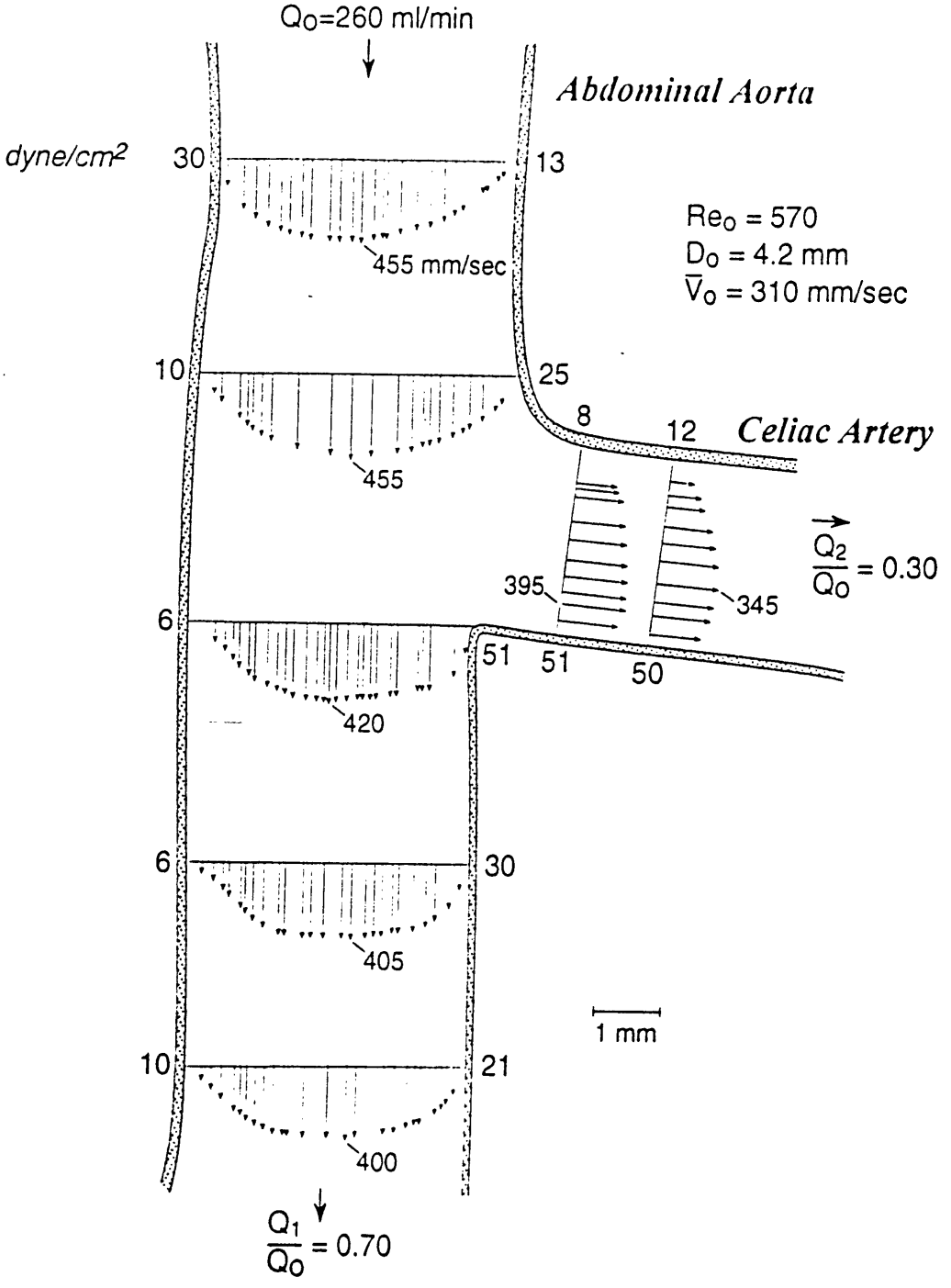

Figure 4.10

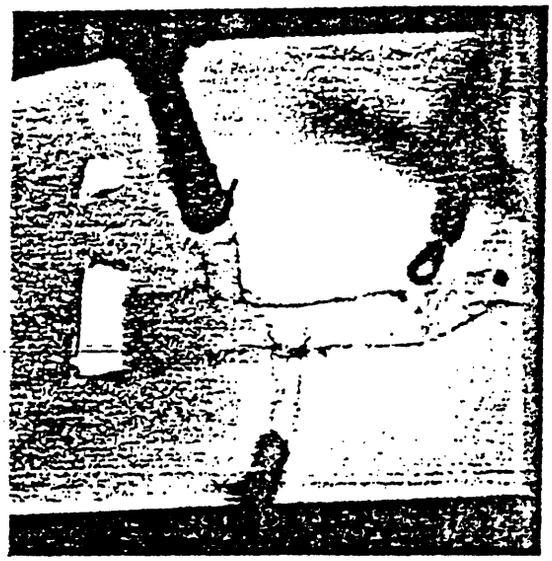

Figure 4.11

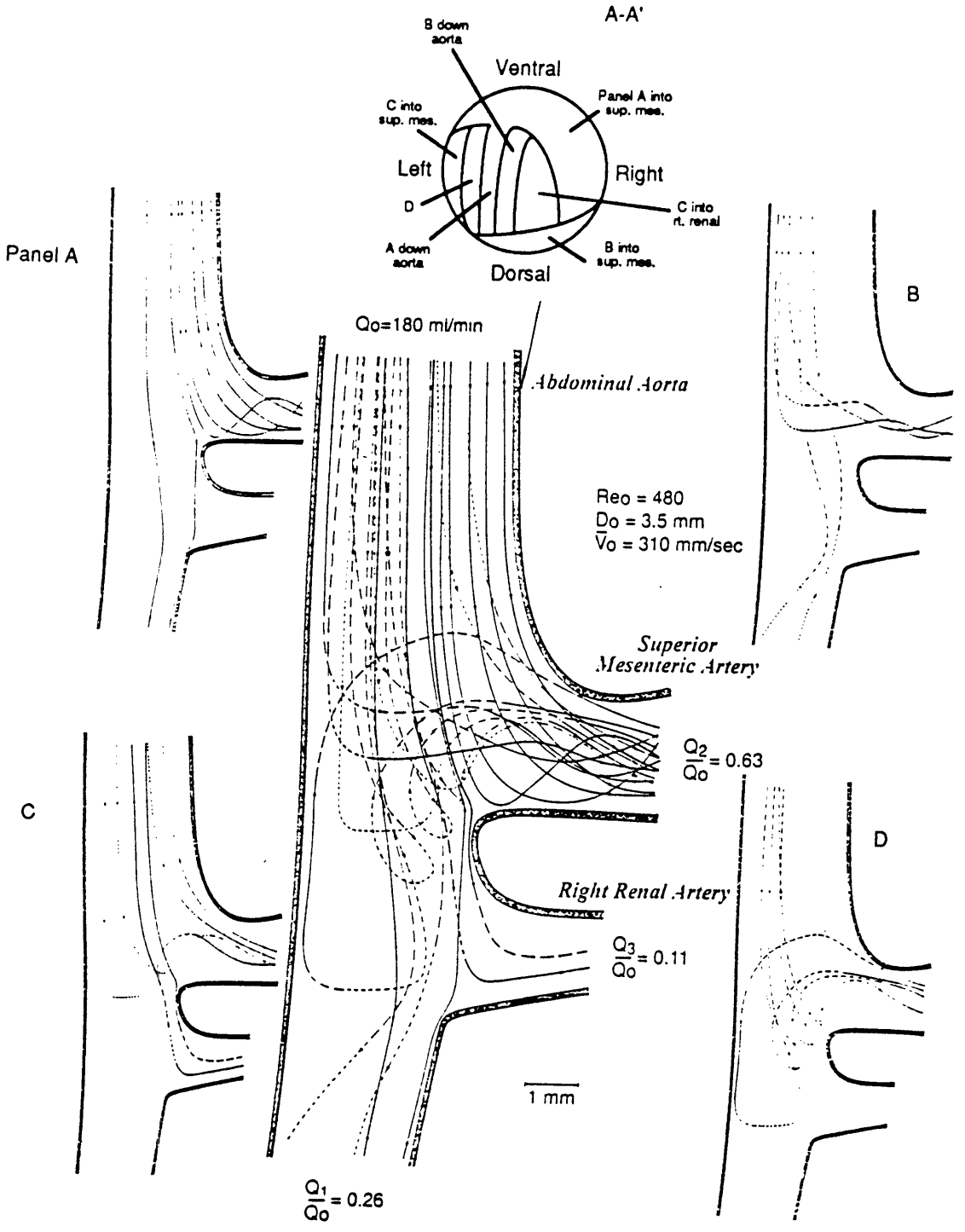
A-A'
B down aorta
Ventral
Panel A into sup. mes.
C into sup. mes.
Left
Right
D
C into rt. renal
A down aorta
B into sup. mes.
Dorsal
Panel A
B
Qo=180 ml/min
Abdominal Aorta
Reo = 480
Do = 3.5 mm
Vo = 310 mm/sec
Superior Mesenteric Artery
Q2/Qo = 0.63
C
D
Right Renal Artery
Q3/Qo = 0.11
1 mm
Q1/Qo = 0.26

Figure 4.12

STEADY FLOW IN TRANSPARENT AORTA

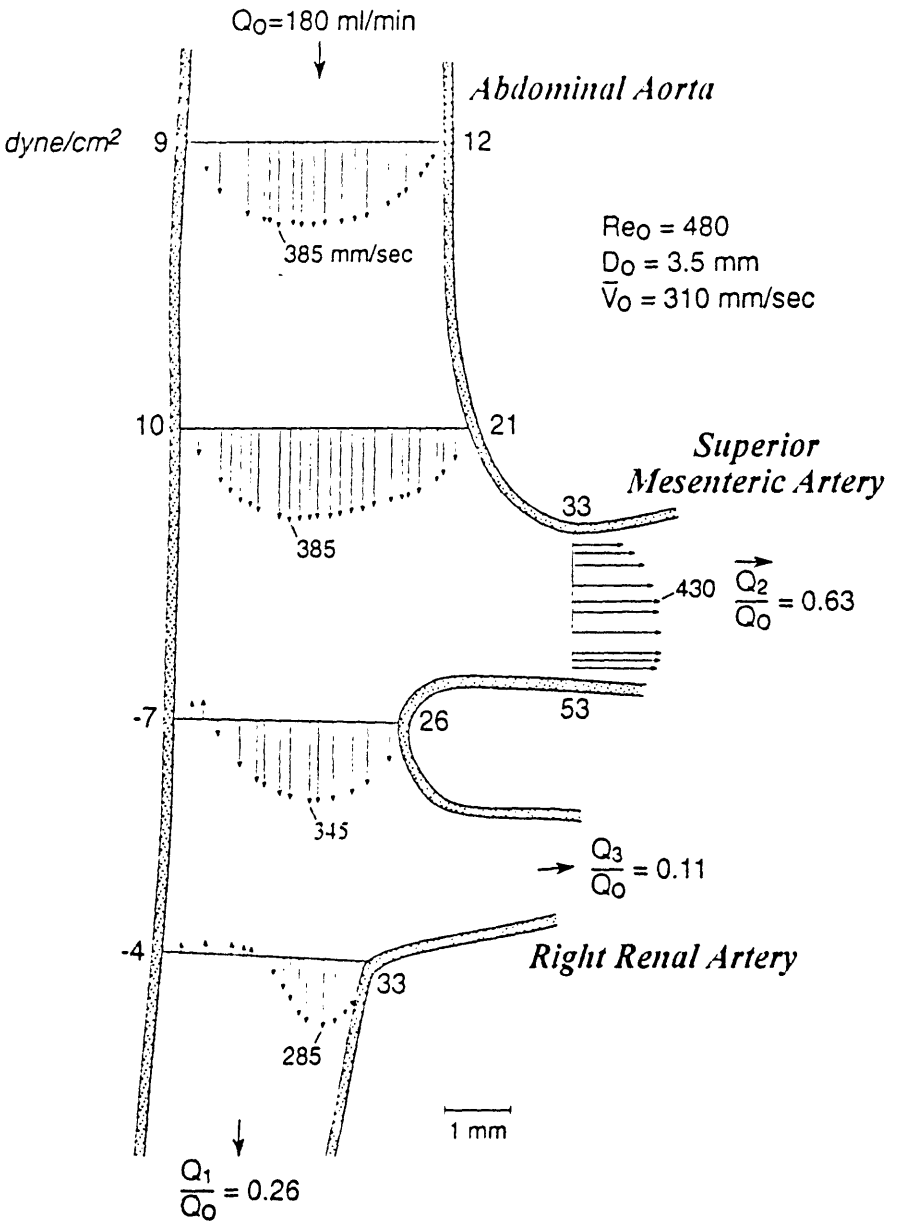

Figure 4.13

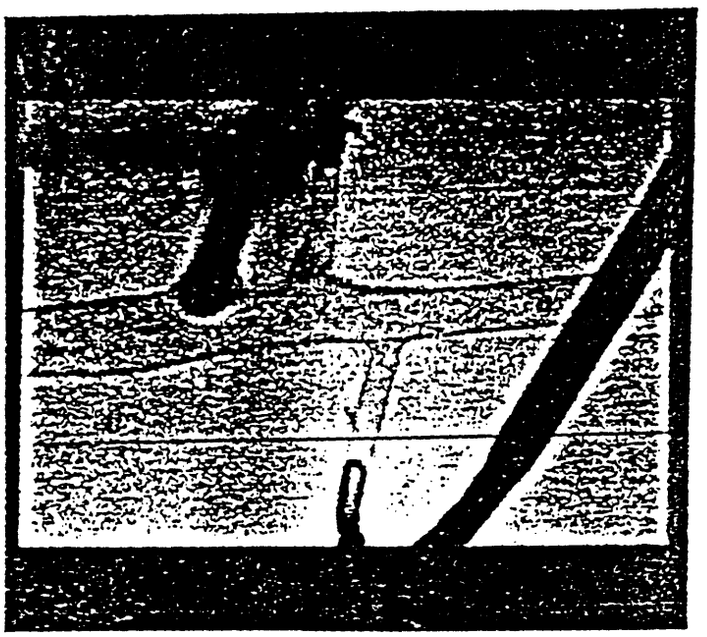

Figure 4.14

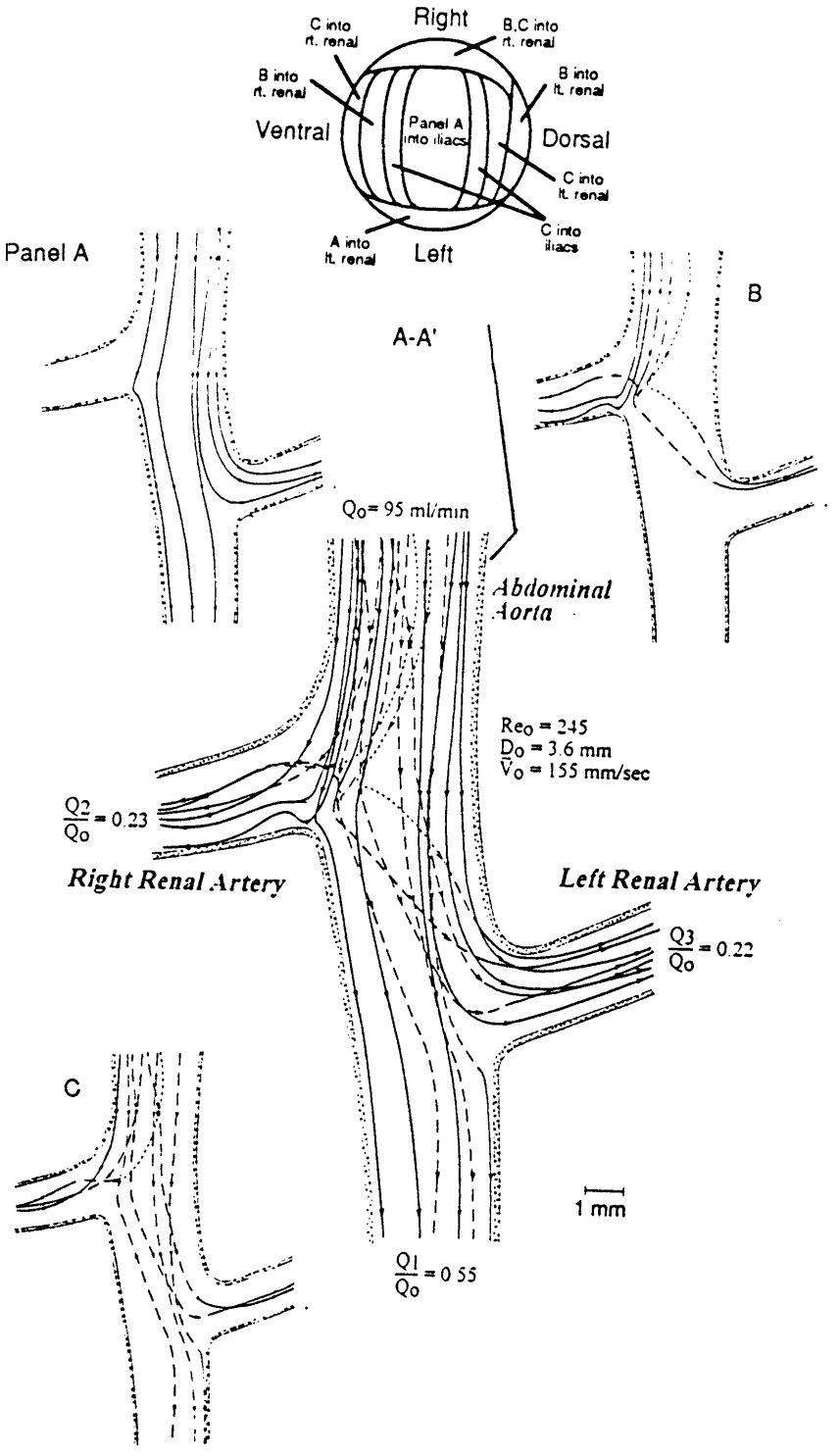
Right
C into rt. renal
B,C into rt. renal
B into rt. renal
B into lt. renal
Ventral
Panel A into iliacs
Dorsal
C into lt. renal
C into iliacs
A into lt. renal
Left
Panel A
B
A-A'
Qo= 95 ml/min
Abdominal Aorta
Reo = 245
Do = 3.6 mm
Vo = 155 mm/sec
Q2/Qo = 0.23
Right Renal Artery
Left Renal Artery
Q3/Qo = 0.22
C
1 mm
Q1/Qo = 0.55

Figure 4.15

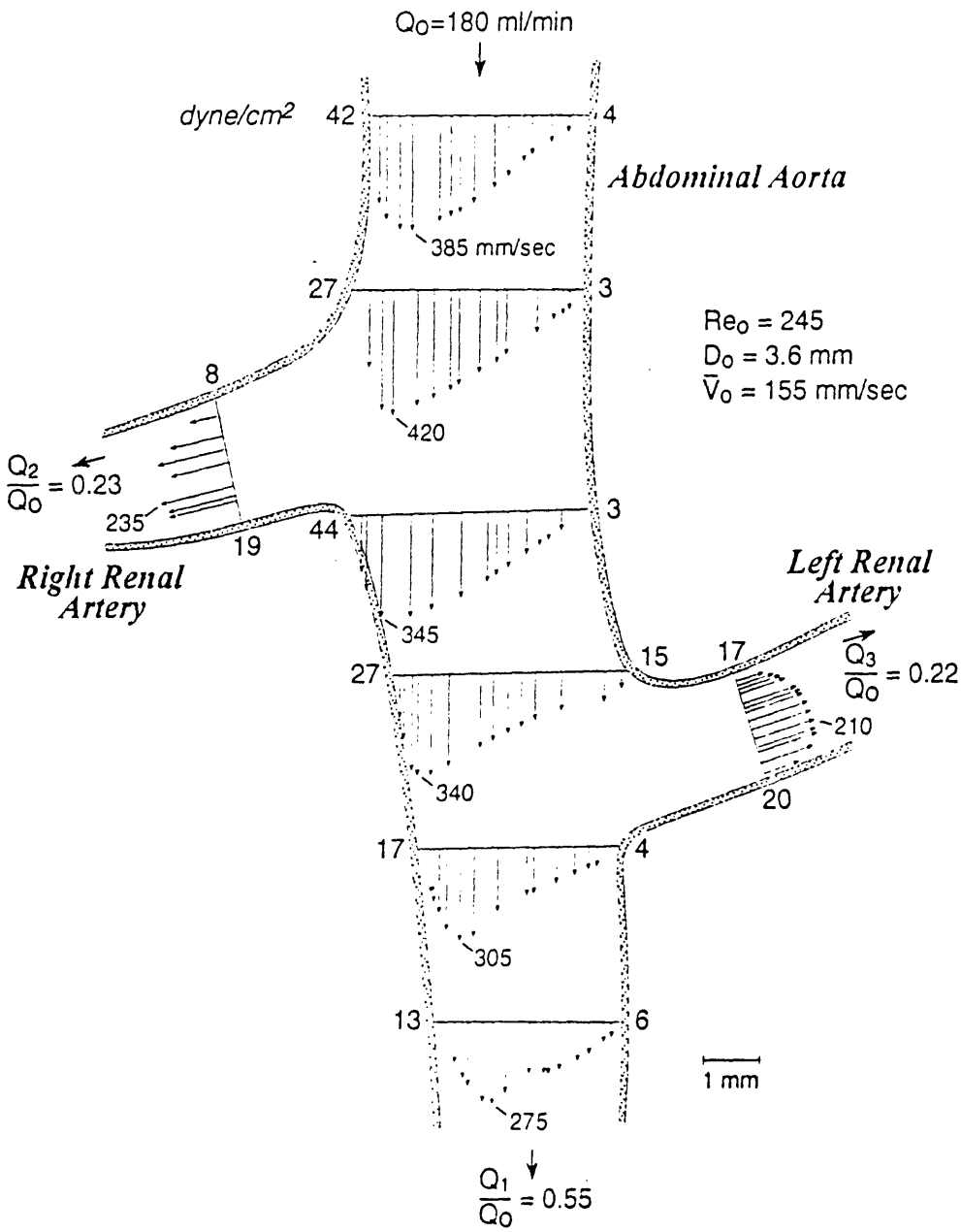
STEADY FLOW IN TRANSPARENT AORTA
Q0=180 ml/min
dyne/cm2
42
4
Abdominal Aorta
385 mm/sec
27
3
Re0 = 245
D0 = 3.6 mm
V̄0 = 155 mm/sec
8
420
Q2/Q0 = 0.23
235
19
44
3
Right Renal Artery
Left Renal Artery
345
15
17
Q3/Q0 = 0.22
27
210
340
20
17
4
305
13
6
1 mm
275
Q1/Q0 = 0.55

Figure 4.16

Chapter Five

Simulation of the Two-Dimensional Steady and Pulsatile Flow Field in a Model Arterial Branching

5.1 Introduction

The role that detailed arterial flow patterns may potentially play in the etiology and pathogenesis of atherosclerosis has motivated numerous experimental and numerical studies of the flow field in model arterial systems. Although these studies have shed some light on the complexity of arterial flow fields, very few generalizations regarding possible relationships between hemodynamics and atherosclerosis can be made. Atherosclerosis involves processes of macromolecular influx into and efflux from the arterial wall; therefore, it is generally assumed that any effect of bloodstream fluid dynamics on arterial endothelial function is mediated by the shear stresses imposed on the endothelium due to the motion of adjacent blood. Indeed, endothelial cells have been shown to exhibit humoral [1-3], metabolic [4-7], and structural responses [4,8-10] to various levels of shear stress. Disagreement persists, however, as to whether high [11], low [12,13], or rapidly changing [14] levels of shear stress represent the relevant hemodynamic culprit. The difficulty in making firm conclusions stems from the complexity of arterial fluid mechanics which has its basis in the very tortuous nature of arterial geometry, the pulsatility and hence time-unsteadiness of the flow, the complex viscoelastic motion of the arterial wall in response to physiological pressure pulses, and the non-Newtonian characteristics of blood. The possibility of the existence of bursts of turbulence at the end of the systolic phase of the cardiac cycle in larger animals further complicates the situation.

The limited spatial resolution of experimental techniques such as pulsed Doppler ultrasound velocimetry and magnetic resonance imaging in measuring the details of arterial flow fields has led to heightened interest in the formulation of sound numerical models. In addition to arbitrarily fine spatial and temporal resolution, a computational model allows the investigation of the effect of a wide range of geometric and fluid mechanical parameters on the details of the flow field. The advent of the finite element method has allowed the accurate modeling of complex geometries, and the spread of ultra-fast computers has rendered the solution of the inherently very computationally-intensive non-linear governing momentum equations feasible. Consequently, a number of computational investigations of the flow field in model arterial systems has recently emerged, and these models have progressively been made more sophisticated.

The vast majority of the computational studies in the literature are in models of either arterial stenoses of various degrees of severity or of bifurcations of different branching angles. The earliest studies were two-dimensional, steady flow computations which investigated regions of possible boundary layer separation and consequent flow recirculation as well as the wall shear stress distribution [15-20]. More recently, pulsatile flow simulations have become more common [21-27] as have three-dimensional models [28,29]. These studies have highlighted certain differences between steady and pulsatile flow behavior, and the three-dimensional investigations have demonstrated the existence of complex, secondary flow motion induced by regions of vessel curvature.

This paper involves the two-dimensional finite element simulation of the steady and pulsatile flow field in a 90° T-junction representing an idealized model of an arterial branching. The primary objective of the study is to

demonstrate fundamental differences that exist between steady and pulsatile flow conditions with regard to flow field details and resulting wall shear stress distribution. Important implications regarding the possible physiological relevance of the results are also discussed.

5.2 Numerical Model and Solution Procedure

The geometry in which the flow field is computed is the rigid-wall 90° T-junction shown in Figure 5.1. This specific geometry has been selected due to the availability of detailed experimental data in a glass model of an identical system [30]. Specifically, the parent vessel has a diameter of 3 mm, as do the two daughter branches. Flow enters the system with a fully-developed, parabolic profile at a mean velocity of 63.6 mm/s. The two daughter branches are sufficiently long for the establishment of parabolic flow at the outlets [31]. The total x-direction length simulated is 5.1 cm which corresponds to 17 tube diameters, while the y-direction simulation field spans a length of 2.7 cm corresponding to 9 tube diameters. 20% of the inlet flow is imposed into daughter branch 1, while branch 2 receives the remaining 80%. The working fluid is incompressible and Newtonian with a density of 1060 kg/m^3 and a dynamic viscosity of 2.0×10^{-3} kg/m-s (2.0 cP); therefore, the channel inlet Reynolds number is about 100. Both steady and sinusoidal pulsatile flows are simulated. The governing equations to be solved in the simulations are the two-dimensional equations of mass and momentum conservation given by:

$$\frac{\partial u}{\partial x} + \frac{\partial v}{\partial y} = 0$$

$$\rho\left(\frac{\partial u}{\partial t} + u\frac{\partial u}{\partial x} + v\frac{\partial u}{\partial y}\right) = -\frac{\partial p}{\partial x} + \mu\left(\frac{\partial^2 u}{\partial x^2} + \frac{\partial^2 u}{\partial y^2}\right)$$

and $$\rho\left(\frac{\partial u}{\partial t} + u\frac{\partial u}{\partial x} + v\frac{\partial u}{\partial y}\right) = -\frac{\partial p}{\partial x} + \mu\left(\frac{\partial^2 u}{\partial x^2} + \frac{\partial^2 u}{\partial y^2}\right)$$

where u and v are respectively the x- and y-components of the fluid velocity vector, p is the fluid pressure, t is time, and μ is the fluid dynamic viscosity. Under the assumption of parabolic velocity profiles at the flow inlet and both flow outlets and for the given values of channel diameter, relative flow splits, fluid density, and fluid dynamic viscosity, the flow boundary conditions are as shown in Figure 5.1.

In the steady flow simulations, the sinusoidal time-dependent term in the boundary conditions ($\cos \omega t$) is identically zero. In the pulsatile flow simulations, however, this term ranges from -1 to 1 so that the overall term ($1+\cos \omega t$) ranges from 0 to 2. This leads to a situation where there is no reverse flow at the fluid boundaries during any part of the pulsatile cycle. The value of the frequency of pulsatility ω is taken at a constant value of 15.7 s^{-1}. This value is not physiologically realistic; however, it is sufficiently high to allow the simulation of several pulsatile cycles during the course of a relatively short real simulation time. Moreover, this value of ω leads to a a value of the Womersley parameter α (defined as $D(\omega/\nu)^{1/2}$, where D is the channel diameter and ν is the fluid kinematic viscosity) of 6.1 which is typical of conditions in the abdominal aorta [32]. The fact that the pulsatile velocity shapes at all boundaries are in-phase reflects the situation that the simulation is performed on a rigid-wall system in which pressure pulses propagate infinitely fast through the flow system.

The computations are performed using the finite element computer code NEKTON [33,34]. NEKTON is a very robust and efficient code which is capable of solving the full unsteady, incompressible fluid, three-dimensional Navier-Stokes equations with forced or natural convection heat transfer in both stationary and time-dependent geometries. NEKTON possesses powerful pre- and post-processing packages which provide the capability to easily define the geometry in which the computations are to be performed and which allow the display of a wide array of parameters in multiple forms after the computations are completed. The code runs on a wide variety of computers ranging from personal workstations to supercomputers.

Briefly, the spatial discretization in NEKTON is based on the spectral element method, a high-order finite element method for partial differential equations. The computational domain is represented as a set of of disjoint macro-elements, with the solution, data, and geometry represented by high-order polynomial expansions within each macro-element. This approach offers high-order (spectral) accuracy, while maintaining the geometric flexibility of low-order finite-element techniques. In our two-dimensional computational domain, the isoparametric spectral element spatial discretization proceeds by first breaking the domain up into (non-degenerate) quadrangles, denoted as "macro-" or "spectral" elements. Within each element, a local Cartesian mesh is constructed corresponding to an NxN tensor-product Gauss-Lobatto Legendre collocation points. The Gauss-Lobatto points are clustered near elemental boundaries, and are chosen because of their accurate approximation, interpolation, and quadrature properties. Dependent variables are expanded in terms of $(N-1)^{th}$ order polynomial Lagrangian interpolants (through the Gauss-Lobatto Legendre collocation points).

Spatially discrete equations are generated by inserting assumed forms of the dependent variables into the governing equations and requiring that the residual vanish in some integral and weighted sense. The computed numerical variables correspond to values occurring at the collocation points of the mesh. Convergence is obtained by increasing the number of macro-elements (K) or the order of the interpolants (N) in the elements. The error decreases algebraically (like K^{-N}) as K is increased and exponentially for smooth solutions (like e^{-KN}) as N is increased. Further details on the code structure and numerical techniques can be found elsewhere [33,34].

In the computations reported in this paper, convergence is obtained in a domain that is divided into 96 macro-elements as shown in Figure 5.1 and with interpolants of order 7 in both the x- and y-directions. This leads to a situation where the field variables are computed at 49 independent nodes within each element thereby yielding a total problem size of 4704 nodes. The computations are performed on the MIT CRAY-II. The division of the computational domain into macro-elements has been selected to provide a high level of fluid mechanical detail in the immediate vicinity of the branching (defined as one channel diameter upstream and downstream of the branching within the horizontal portion of the T-junction and one channel diameter into the vertical portion) because it is this region that is of most interest within the context of potential relevance of the results to atherosclerosis.

5.3 Results

5.3.1 Steady Flow Simulations

The steady state computations are regarded by NEKTON as evolving transients so that the full time-dependent form of the governing equations is solved. The steady state solution is achieved as the time-asymptotic result of

the transient calculation. Convergence is attained when time changes in fluid velocity and pressure at selected points within the flow field become small. At the point of convergence in the steady flow simulations reported, the maximum change in the x-component of the velocity vector between the two last time steps is 0.34%, that in the y-component of the velocity is 0.79%, and that in pressure is 0.086%. The total cpu-time required to attain convergence is about 130 minutes.

The results of the steady state solution of the overall flow field in the two-dimensional system simulated under the conditions defined above is schematically shown in Figure 5.2. Inlet flow with a parabolic profile (imposed by the inlet boundary conditions) enters the T-junction. This velocity profile remains virtually unchanged until a short distance (about 2.1 D) upstream of the branching where the velocity profile becomes skewed towards the top wall of the parent vessel due to the presence of the branch. Downstream of the branch, the flow skewness persists for a length of about 3.9 D before becoming parabolic again. Within the branch, the velocity profile is skewed towards the downstream wall, and this skewness persists for a length of about 3.9 D.

Overall, the flow field contains two zones of boundary layer separation and consequent flow recirculation, labeled zones A and B in Figure 5.2. Figure 5.3 is a close-up view of the flow patterns in the high resolution region in the immediate vicinity of the branching. This figure more clearly illustrates the details of the two recirculation zones. Zone A results from flow separation at the upstream end of the branch as the fluid tries to negotiate its way around the sharp bend, while zone B has its origin in the deflection of the fluid due to the presence of the branch thereby leading to flow separation. Both these zones are closed, i.e. the fluid within the two zones does not communicate with fluid outside them, and the fluid velocity within the recirculation zones is significantly

lower than that outside. Recirculation zone A extends to a length of 2.0 D from the point of separation to the point of reattachment and has a maximum width of about 0.2 D. Zone B has a length of 1.5 D and a peak width of about 0.3 D.

Since the wall shear stress, or equivalently the shear rate since the fluid viscosity is constant, is the main parameter of interest, it is important to investigate the wall shear stress distribution in the simulation domain. Figure 5.4 illustrates the wall shear rate field in the horizontal section of the T-junction. Figure 5.4A represents the wall shear rate along the bottom wall of the channel. The flow at the inlet has a shear rate of about 129 s^{-1}, and this value remains relatively constant until a distance of about 2.1 D upstream of the branch where the shear rate begins dropping sharply as the fluid gets deflected towards the upper wall due to the presence of the branch. This decrease in shear rate continues until the shear rate drops to zero at a point about 0.3 D downstream of the proximal end of the branch at which point the flow separates from the wall and the shear rate values become negative due to fluid recirculation in the direction opposite to the main flow direction. The flow separation zone has a total length of about 1.5 D so that at a distance of about 1.8 D from the proximal (i.e. upstream) end of the branch, the flow reattaches (denoted by the second zero shear rate point). Beyond the reattachment point, the shear rate increases sharply until it attains a value of about 26 s^{-1} at a distance of about 3.0 D from the proximal end of the branch, and this value remains more or less constant until the channel outlet. One important observation regarding the shear rate field along the bottom wall is that practically all the changes in shear rate occur over a total length of about 5.1 D around the position of the branch (2.1 D upstream and 3.0 D downstream of the branch) although the total simulated length is 17 D. Moreover, the magnitude of the shear rate change over this length is large so that the spatial

shear rate gradients are very large. Specifically, proximal to the recirculation zone, the shear rate gradient is about 64.1 s^{-1}/mm, while that immediately distal to the recirculation zone is about 42.1 s^{-1}/mm. Since the fluid viscosity is constant at 2.0×10^{-3} kg/m-s, the corresponding shear stress gradients are 1.3 dyne/cm^2/mm proximal to and 0.8 dyne/cm^2/mm distal to the recirculation zone. These values should be compared to spatial gradients of about zero s^{-1}/mm in the straight flow regions away from the branch. Within recirculation zone B, the fluid moves very slowly, and the resulting wall shear rates are small (peak value of 15.6 s^{-1}). The spatial gradients of the shear rate, however, may be as large as about 25.3 s^{-1}/mm, which corresponds to a shear stress gradient of about 0.5 dyne/cm^2/mm.

Figure 5.4B illustrates the variation of wall shear rate along the top wall of the horizontal section in the region proximal to the branch. The shear rate remains relatively constant at about 126 s^{-1} until a distance of about 1.6 D proximal to the branch where it increases relatively slowly until a distance of about 0.5 D proximal to the branch where the shear rate begins increasing rapidly until it finally attains a peak value of 1326 s^{-1} at the proximal tip of the branch. The region of 0.5 D proximal to the branch exhibits a very large shear rate gradient of about 708.2 s^{-1}/mm (corresponding to a shear stress gradient of 14.2 dyne/cm^2/mm). Figure 5.4C displays the variation of upper wall shear rate with distance in the region distal to the branch. The point immediately distal to the branch has the highest shear rate, 245.9 s^{-1}. The shear rate then decreases rapidly so that by a distance of about 1 D from the branch apex, it attains a value of about 26 s^{-1} at which it remains virtually constant thereafter. The shear rate gradient within the distance of 1 D is therefore about 73.3 s^{-1}/mm (1.5 dyne/cm^2/mm).

Figure 5.5 illustrates the shear rate variation within the vertical section of the T-junction. Figure 5.5A exhibits the variation along the left (proximal) wall, while Figure 5.5B depicts the shear rate along the right (distal) wall. Along the left wall, the shear rate has a large positive value (393.0 s^{-1}) at the corner (point (0,0) in Figure 5.1) as this point lies just outside recirculation zone A. At a point 0.09 D from the corner, the recirculation zone is encountered, and the shear rate becomes negative and remains so for a distance of about 2 D at which point the separated fluid streamlines reattach. The shear rate then increases slowly until it attains its asymptotic value of about 101 s^{-1} at a distance of about 3.8 D. The sharp transition from positive to negative shear rate within a very short distance at point (0,0) leads to a very high spatial shear rate gradient of about 1836.9 s^{-1}/mm (36.7 dyne/cm^2/mm).

Along the right wall, the shear rate initially increases sharply as the curved incoming fluid streamlines bend to become parallel to the wall. The shear rate attains a peak value of 424.5 s^{-1} at a distance of 0.45 D from the corner (point (0.003,0) in Figure 5.1), and it then decreases gradually as the flow skewness towards the right wall progressively disappears and parabolic flow is reestablished. The asymptotic value of 101 s^{-1} is reached at a distance of about 2 D from the corner point.

5.3.2 Pulsatile Flow Simulations

In pulsatile flow, convergence is attained when changes in fluid mechanical conditions (velocities and pressure) at the same time points within consecutive pulsatile cycles are small. The total cpu-time required to simulate a single pulsatile cycle (about 0.4 seconds long since the angular frequency is 15.7 s^{-1}) is about 4 hours.

The details of the flow field under sinusoidal pulsatile conditions are significantly different from those in steady flow. The pulsatile flow cycle can be divided into the deceleration phase ($0 \leq \omega t \leq \pi$) and the acceleration phase ($\pi \leq \omega t \leq 2\pi$). Figure 5.6 represents a closeup-view of the flow field in the immediate vicinity of the branching during the course of a single pulsatile cycle which has been divided into 20 equally-spaced time intervals. The figure illustrates that recirculation zone A within the vertical branch is present throughout the course of the cycle although its length and width periodically increase and decrease. Specifically, this zone attains its maximum length of 2.4 D at $\omega t=0.5\pi$ and its minimum length of 0.05 D at $\omega t=1.3\pi$. Recirculation zone B along the bottom wall of the horizontal section disappears completely in the time interval $1.5\pi \leq \omega t \leq 1.7\pi$ after which it appears and progressively increases in length until it spans virtually the entire bottom wall at $\omega t=0.9\pi$.

While the two recirculation zones discussed here have also been observed in steady flow, there are additional periodically appearing and disappearing flow reversal zones observed in the pulsatile flow simulations which never occur under steady flow conditions. Specifically, in the interval $0.4\pi \leq \omega t \leq 1.3\pi$, there is flow reversal along the top wall of the horizontal portion of the T-junction distal to the branching. This reversal region initiates at $\omega t=0.4\pi$ at a distance of 1 D downstream of the branching and proceeds upstream with time to reach a point about 0.4 D distal to the branch at the end of deceleration ($\omega t=\pi$). This represents the point of farthest flow reversal penetration beyond which the region of flow reversal begins moving downstream, and it disappears completely at $\omega t=1.3\pi$. Therefore, the region between 0.4 D and 1 D distal to the branching is exposed to successive periods of forward and reverse flow within the course of a pulsatile cycle. The

0.4 D-long section immediately distal to the branching is exposed to forward flow throughout the pulsatile cycle.

In addition to this flow reversal region distal to the branch, the top wall of the horizontal section proximal to the branch is exposed to reverse flow in the interval $0.7\pi \leq \omega t \leq \pi$. Flow reversal begins at a distance of 1 D proximal to the branch at $\omega t = 0.7\pi$, extends downstream to a maximum penetration of 0.4 D proximal to the branch at $\omega t = 0.9\pi$, and then disappears at $\omega t = \pi$. Consequently, while the length of 0.4 D immediately proximal to the branch is exposed to forward flow throughout the course of the pulsatile cycle, the 0.6 D-long section between 0.4 D and 1 D proximal to the branch undergoes periodic flow reversal.

The periodic appearance and disappearance of recirculation and flow reversal zones in pulsatile flow leads to very interesting wall shear rate behavior. Within the context of a possible role of arterial fluid mechanics in atherosclerosis, the shear rate immediately proximal to and distal to branches is of interest due to conflicting experimental evidence of early lesion localization either proximal to or distal to aortic ostia in various species [35-38]. Figure 5.7 illustrates the time variation of the NEKTON-computed shear rates at both the proximal and distal corners of the T-junction (points (0,0) and (0.003,0)) during a single sinusoidal pulsatile cycle. The results indicate that the proximal shear rates vary over about four orders of magnitude during the course of the cycle, while the distal shear rates vary over about two orders of magnitude. Therefore, the temporal shear rate gradients are very steep. Also shown in Figure 5.7 are the constant proximal and distal shear rate values computed under steady flow conditions. Comparison of the pulsatile to steady conditions illustrates that, depending on the specific portion of the pulsatile

cycle under investigation, the pulsatile shear rates may be much larger or much smaller than their steady flow counterparts.

Figure 5.8 illustrates the variation of the magnitude of the distal to proximal shear rate ratio with time as well as the steady state value for this ratio. The results further emphasize the large differences that exist between steady and pulsatile flow conditions since at various points within the pulsatile cycle, the distal shear rate may be either much larger or much smaller than the proximal shear rate so that very few *a priori* generalizations regarding the relative magnitudes of these shear rates can be made in pulsatile flow (unlike the situation in steady flow where the distal to proximal shear rate ratio for the flow conditions studied has a constant value of 0.19).

In addition to the large time variations in shear rates proximal and distal to the branch, the spatial shear rate gradients and their variations with time are very large within the course of a single cycle. Figure 5.9 illustrates the magnitudes of the spatial shear rate and shear stress gradients during the pulsatile cycle immediately proximal and distal to the branch as well as the steady flow values for these gradients. The results indicate that the proximal gradient is generally larger than its distal counterpart except in the interval $0.8\pi \leq \omega t \leq 0.9\pi$. Furthermore, the extent of shear rate variation is much larger proximal than distal to the branch.

An additional parameter of interest is the global maximum shear rate within the horizontal section of the simulated flow field. This maximum always occurs at a point along the top wall of the horizontal section and is at the proximal tip of the branch during 80% of the pulsatile cycle ($0 \leq \omega t \leq 0.6\pi$ and $1.1\pi \leq \omega t \leq 2\pi$) but shifts to the distal tip during the interval $0.7\pi \leq \omega t \leq \pi$. These results are depicted in Figure 5.10 along with the constant steady state global maximum which occurs at the proximal tip. The results indicate that the

maximum shear rate changes over about two orders of magnitude during the course of the cycle and that it may be either significantly larger or smaller than its steady flow counterpart. Furthermore, the maximum always occurs in the immediate vicinity of the branch, and the periodic shift in its localization from the proximal to the distal tip during a portion of the pulsatile cycle further emphasizes the difficulty in making any *a priori* generalizations on the shear rates in pulsatile flow.

Figure 5.11 depicts the variation of the maximum value of the shear rate along the bottom wall of the horizontal section with time over a single cycle along with the constant steady flow value. The maximum always occurs in the vicinity of the branch. Moreover, during the interval $0.5\pi \leq \omega t \leq 1.1\pi$, the value of the maximum shear rate is actually within recirculation zone B. Figure 5.12 depicts the time variation of the ratio of the shear rate within recirculation zone B in pulsatile flow to the constant value of this parameter in steady flow (this constant value is 15.6 s^{-1}). The results indicate that flow pulsatility may lead to shear rates within the recirculation zone that are an order of magnitude larger than their steady flow counterparts.

5.4 Discussion

This paper has reported the two-dimensional numerical simulation of the steady and sinusoidal pulsatile flow field in a 90° T-junction using the finite element code NEKTON. Although this system has been studied by other investigators [26,27], there is a number of findings reported here which have not previously been reported in the literature.

The specific flow conditions (i.e. vessel dimensions, flow Reynolds number, and flow split ratios) simulated have been selected due to the availability of equivalent steady state experimental data in a glass model [30].

A comparison between the numerical and experimental results allows an overall assessment of the accuracy and predictive capabilities of the numerical model. This comparison illustrates that the computations accurately predict the overall qualitative nature of the flow field. Specifically, the velocity profiles upstream of the branch are significantly altered only a short distance proximal to the branch, where the flow gets skewed upwards due to the presence of the branch. Downstream of the branch, flow disturbance due to the branch persists for a longer length. The extent of upward skewness proximal to the branch in the simulations is significantly larger than its experimental counterpart; however, skewness in three-dimensional flows is typically smaller than that in two-dimensional flows [39].

The two recirculation zones A and B observed in the simulations are also observed experimentally, and their positions within the flow field are also accurately predicted. However, the lengths of the two recirculation zones are not correctly predicted as zones A and B are experimentally observed to have lengths of 0.7 D and 2.0 D, respectively (compared to 1.5 D and 2 D in the simulations). Another difference between the computations and the experiments is that while recirculation zones A and B are closed in the simulations, they are not in the experiments. Specifically, the experimental results indicate that the two recirculation zones interact as fluid from zone B recirculates within the common median plane of the test section for a given period of time before getting deflected out of the plane and tracing helical trajectories to enter zone A. This difference between simulations and experiments is not unexpected due to the two-dimensional nature of the computations where only the common median plane is simulated.

The higher upward skewness in the simulations proximal to the branch leads to a higher wall shear rate in that region. Specifically, the shear rate

along the upper wall immediately upstream of the branch is 1326 s^{-1}, while that experimentally observed is only 320 s^{-1}. The computed and experimentally observed distal shear rates are 246 and 310 s^{-1}, respectively. The maximum fluid velocity along the common median plane proximal to the branch is 97 mm/s in the simulations and 140 mm/s in the experiments, that distal is 33 mm/s in the simulations and 86 mm/s in the experiments. Finally, within recirculation zone B, the magnitude of the maximum shear rate computed is 16 s^{-1}, while a value of 50 s^{-1} is observed experimentally.

It is believed that the quantitative differences between the computational results and the experimental results are primarily due to differences between two-dimensional and three-dimensional flow conditions. Hence, although the two-dimensional simulations do not reproduce the exact quantitative values observed experimentally, the qualitative nature of the flow field is accurately predicted, and the essential features are captured.

The simulations have revealed some very fundamental differences between steady and pulsatile flow. Recirculation zones present in steady flow periodically appear and disappear in pulsatile flow. Furthermore, pulsatile flow reveals the presence of additional recirculation or flow reversal zones which are never observed in steady flow.

In pulsatile flow, shear rates and spatial shear rate gradients in the immediate vicinity of a branching vary over several orders of magnitude during the course of a single pulsatile cycle. The fact that the shear rates may be significantly larger or smaller than their constant steady flow counterparts emphasizes the need for incorporating pulsatility in model studies of possible relationships between hemodynamic phenomena and atherosclerosis. It also demonstrates the difficulty in making generalizations regarding the relative magnitudes of shear stresses proximal and distal to branches. In fact, it has

been demonstrated that the maximum shear rate within the simulated flow field oscillates between immediately proximal to and immediately distal to the branching during the course of a single cycle.

Whereas the wall shear rates within steady flow recirculation zones are always small, periodically appearing and disappearing recirculation zones in pulsatile flow exhibit shear rates that are comparable to the global maximum shear rates in the flow field.

If the same flow phenomena observed in our two-dimensional simulations occur *in-vivo,* then the results have important implications towards a potential role of arterial hemodynamics in the atherogenic process. The large variations in the magnitudes of shear rate to which underlying endothelial cells would be exposed within the course of a single cycle as well as the frequent reversal of flow direction that the cells "see" as a result of the periodic appearance and disappearance of recirculation and flow reversal zones may have important implications on details of endothelial cell molecular function. It is well-established that specific endothelial cell responses such as the activation of a K^+-selective ion channel and consequent cell membrane hyperpolarization occur over the course of very short time scales (milliseconds) [6] so that the sharp temporal gradients due to the quickly-varying hemodynamic conditions may be important in this regard. Furthermore, it has been shown that the cytoskeletal rearrangement of cultured endothelial cells in response to fluid flow depends strongly on whether the flow is unidirectional or directionally-unsteady [40]. Therefore, the periodic appearance and disappearance of recirculation and flow reversal zones may be important in influencing underlying endothelial cell cytoskeletal structure and hence possibly impacting permeability and metabolic characteristics of these cells.

One specific result of the computations that is of particular interest in view of existing physiological evidence is the presence of the periodically appearing and disappearing flow reversal zone a short distance distal to the branch. Okano and Yoshida [41] have studied the morphology of the endothelial cells in the normocholesterolemic rabbit aortic arch in the area distal to the brachiocephalic and left subclavian arteries. They have also investigated the localization of sudanophilic regions distal to these same branches in hypercholesterolemic rabbits. Their results indicate the presence of a region of long fusiform endothelial cells that spans a few hundred microns distal to the branches. Beyond this region, the cells become more ellipsoidal in shape. The region of ellipsoidal cells was typically sudanophilic, while the long fusiform cell zone was generally spared. These findings are consistent with the presence of a small flow reversal zone distal to the branches since experiments on cultured endothelial cells have shown that cells exposed to recirculating or non-unidirectional flow tend to be more ellipsoidal in shape, whereas those exposed to unidirectional flow tend to align in the bulk flow direction [4]. The length of the flow reversal zone observed in the computations (0.6 D or 1800 μm) is larger than the few hundred microns reported in [41], but the exact sizes depend on many flow and geometric parameters. The small size of this flow reversal zone emphasizes the difficulty of obtaining accurate experimental data on *in-vivo* flow fields since such a small recirculation zone will most likely be missed by the standard *in-vivo* velocity measurement techniques such as pulsed Doppler ultrasound velocimetry or magnetic resonance imaging. This, in turn, lends further support to the value of a sound numerical model.

The physiological relevance of the simulation results reported here remains unknown. The simulations are two-dimensional, the geometry is

idealized, the wall is rigid, and the pulse has a non-physiological sinusoidal shape. However, the results obtained provide insight into fundamental fluid mechanical differences that exist between steady and pulsatile flow. Efforts are under way to relax some of the simulation assumptions in order to render the computations more physiologically realistic.

5.5 References

1. Milner P, Kirkpatrick KA, Ralevic V, Toothill V, Pearson J, Burnstock G. Endothelial cells cultured from human umbilical vein release ATP, substance P and acetylcholine in response to increased flow. *Proc. R. Soc. Lond. B.* **241:** 245, 1990.

2. Massop DW, Wright JG, Smead WL, Sadoun ET, Cornhill JF. Interleukin-6 production by human aortic endothelial cells is regulated by shear stress. *Arteriosclerosis.* **10:** 760a, 1990.

3. Miller VM, Rud K, Heublein D. Chronic increases in blood flow modulate the production of nitric oxide and endothelin. *FASEB J.* **5:** A659, 1991.

4. Dewey CF, Bussolari SR, Gimbrone MA, Davies PF. The dynamic response of vascular endothelial cells to fluid shear stress. *J. Biomech. Eng.* **103:** 177, 1981.

5. Davies PF, Dewey CF Jr., Bussolari SR, Gordon EJ, Gimbrone MA Jr. Influence of hemodynamic forces on vascular endothelail function. In vitro studies of shear stress and pinocytosis in bovine aortic cells. *J. Clin. Invest.* **73:** 1121, 1984.

6. Olesen S-P, Clapham DE, Davies PF. Haemodynamic shear stress activates a K^+ current in vascular endothelial cells. *Nature.* **331:** 168, 1988.

7. Geiger R, Berk B, Alexander RW, Nerem RM. Spatial and temporal analysis of Ca^{2+} in single bovine aortic endothelial cells (BAECs) exposed to fluid flow. *FASEB J.* **5:** A529, 1991.

8. Flaherty JT, Pierce JE, Ferrans VJ, Patel DJ, Tucker WK, Fry DL. Endothelial nuclear patterns in the canine arterial tree with particular reference to hemodynamic events. *Circ. Res.* **30:** 23, 1972.

9. Frangos JA, Eskin SG, McIntyre LV, Ives CL. Flow effects on prostacyclin production by cultured human endothelial cells. *Science.* **227:** 1477, 1985.

10. Davies PF. Mechanical sensing mechanisms: Shear stress and endothelial cells. *J. Vasc. Surg.* **13:** 729, 1991.

11. Fry DL. Acute vascular endothelial changes associated with increased blood velocity gradients. *Circ. Res.* **22:** 165, 1968.

12. Caro CG, Fitz-Gerald JM, Schroter RC. Arterial wall shear and distribution of early atheroma in man. *Nature.* **223:** 1159, 1969.

13. Caro CG, Fitz-Gerald JM, Schroter RC. Atheroma and arterial wall shear: Observation, correlation and proposal of a shear dependent mass transfer mechanism for atherogenesis. *Proc. Roy. Soc. Lond. B.* **177:** 109, 1971.

14. Lutz RJ, Cannon JN, Bischoff KB, Dedrick RL, Stiles RK, Fry DL. Wall shear stress distribution in a model canine artery during steady flow. *Circ. Res.* **41:** 391, 1977.

15. Lew HS. Low Reynolds number equi-bifurcation flow in a two-dimensional channel. *J. Biomechanics.* **4:** 559, 1971.

16. Deshpande MD, Giddens DP, Mabon RF. Steady laminar flow through modelled vascular stenoses. *J. Biomechanics.* **9:** 165, 1976.

17. Gokhale VV, Tanner RI, Bischoff KB. Finite element solution of the Navier-Stokes equations for two-dimensional steady flow through a section of a canine aorta model. *J. Biomechanics.* **11:** 241, 1978.

18. Fukushima T, Azuma T, Matsuzawa T. Numerical analysis of blood flow in the vertebral artery. *J. Biomech. Eng.* **104:** 143, 1982.

19. Patil MK, Subbaraj K. Finite element analysis of two dimensional steady flow in model arterial bifurcation. *J. Biomechanics.* **21:** 219, 1988.

20. Thiriet M, Pares C, Saitel E, Hecht F. Numerical simulation of steady flow in a model of the aortic bifurcation. *J. Biomech. Eng.* **114:** 40, 1992.

21. Friedman MH, O'Brien V, Ehrlich LW. Calculations of pulsatile flow through a branch. *Circ. Res.* **36:** 277, 1975.

22. Daly BJ. A numerical study of pulsatile flow through stenosed canine femoral arteries. *J. Biomechanics.* **9:** 465, 1976.

23. Fernandez RC, De Witt KJ, Brown MR. Pulsatile flow through a bifurcation with applications to arterial disease. *J. Biomechanics.* **9:** 575, 1976.

24. O'Brien V, Ehrlich LW. Simulation of unsteady flow at renal branches. *J. Biomech.* **10:** 623, 1977.

25. Wille SO, Walloe L. Pulsatile pressure and flow in arterial stenoses simulated in a mathematical model. *J. Biomed. Eng.* **3:** 17, 1981.

26. Wille SO. Pulsatile pressure and flow in an arterial aneurysm in a mathematical model. *J. Biomed. Eng.* **3:** 153, 1981.

27. Tutty OR. Pulsatile flow in a constricted channel. *J. Biomech. Eng.* **114:** 50, 1992.

28. Perktold K, Florian H, Hilbert D, Peter R. Wall shear stress distribution in the human carotid siphon during pulsatile flow. *J. Biomechanics.* **21:** 663, 1988.

29. Deplano V, Rieu R, Extremet GP. Numerical simulations of the stationary flow of a viscous, incompressible fluid in a bifurcation model. *Proc. Third FIDAP Users Conference,* Evanston, Illinois, 1989.

30. Karino T, Kwong HHM, Goldsmith HL. Particle flow behaviour in models of branching vessels. I. Vortices in 90° T-junctions. *Biorheology.* **16:** 231, 1979.

31. Bejan A. *Convection Heat Transfer.* New York: John Wiley and Sons, pp.68-70, 1984.

32. McDonald D.A. *Blood Flow in Arteries.* 2nd ed., Englewood Cliffs, New Jersey: Prentice-Hall, 1974.

33. Ronquist EM, Patera AT. Spectral element multigrid. I. Formulation and numerical results. *J. Sci. Comput..* **2:** 389, 1987.

34. Maday Y, Patera AT. Spectral element methods for the incompressible Navier-Stokes Equations. In *State of the Art Surveys on Computational Mechanics*, Noor AK, Oden JT, eds., pp. 71-143, 1989.

35. Cornhill JF, Roach MR. A quantitative study of the localization of atherosclerotic lesions in the rabbit aorta. *Atherosclerosis.* **23:** 489, 1976.

36. Cornhill JF, Levesque MJ, Nerem RM. Quantitative study of the localization of sudanophilic coeliac lesions in the White Carneau Pigeon. *Atherosclerosis.* **35:** 103, 1980.

37. Sinzinger H, Silberbauer K, Auerswald W. A quantitative investigation of sudanophilic lesions around the aortic ostia of human fetuses, newborn, and children. *Blood Vessels.* **17:** 44, 1980.

38. Zeindler CM, Kratky RG, Roach MR. Quantitative measurements of early atherosclerotic lesions on rabbit aortae from vascular casts. *Atherosclerosis.* **76:** 245, 1989.

39. Pedley TJ. Personal Communication.

40. Dewey CF, Davies PF, Gimbrone MA Jr. Turbulence, disturbed flow, and vascular endothelium. In *Role of Blood Flow in Atherogenesis.* Yoshida Y, Yamaguchi T, Caro CG, Glagov S, Nerem RM, eds., pp. 201-204, Tokyo: Springer-Verlag, 1988.

41. Okano M, Yoshida Y. Endothelial cell morphometry of atherosclerotic lesions and flow profiles at aortic bifurcations in cholesterol fed rabbits. *J. Biomech. Eng.* **114:** 301, 1992.

Figure Captions:

Figure 5.1 Flow field simulation geometry illustrating the division of the computational domain into 96 macro-elements and the imposed parabolic velocity profile boundary conditions.

Figure 5.2 Steady state flow field illustrating the two recirculation zones A and B.

Figure 5.3 Close-up view of steady state fluid streamlines in the immediate vicinity of the branching.

Figure 5.4 Steady state wall shear rate field in the horizontal section of the T-junction along the bottom wall (4a), top wall proximal to the branching (4b), and top wall distal to the branching (4c). Positive values denote forward flow along the bottom wall and backward flow along the towall. Negative values denote backward flow along the bottom wall and forward flow along the top wall.

Figure 5.5 Steady state shear rate field in the vertical section of the T-junction along the left (5a) and right (5b) walls. Positive values denote forward flow along the left wall and backward flow along the right wall, while negative values denote backward flow along the left wall and forward flow along the right wall.

Figure 5.6 Close-up view of fluid streamlines in the immediate vicinity of the branching at 20 equally-spaced time intervals within the pulsatile cycle.

Figure 5.7 Time variation of shear rate at the proximal and distal corners of the branching during the course of the pulsatile cycle. Also shown are the constant values computed under steady flow conditions.

Figure 5.8 Time variation of the magnitude of the distal to proximal shear rate ratio during the course of the pulsatile cycle. Also shown is the constant value computed under steady flow conditions.

Figure 5.9 Magnitudes of the spatial shear rate and shear stress gradients in the immediate vicinity of the branching during the course of the pulsatile cycle.

Figure 5.10 Time variation of the global maximum shear rate within the horizontal section of the flow field during the course of the pulsatile cycle. Also shown is the constant value computed under steady flow conditions.

Figure 5.11 Time variation of the maximum shear rate along the bottom wall of the horizontal section of the T-junction during the course of the pulsatile cycle. Also shown is the constant value computed under steady flow conditions.

Figure 5.12 Time variation of the ratio of the shear rate within recirculation zone B in pulsatile flow to the constant value of this parameter in steady flow during the course of the pulsatile cycle.

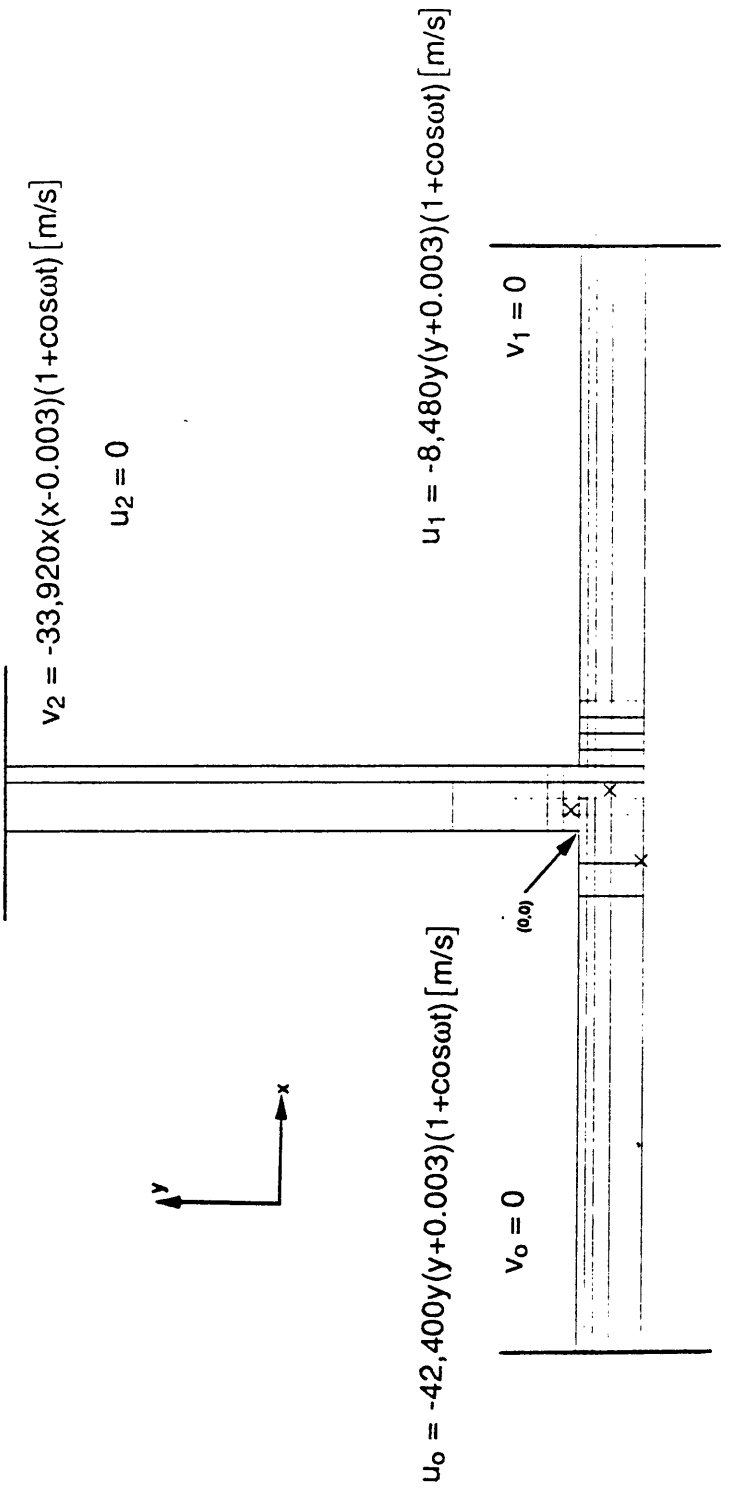
$v_2 = -33,920x(x-0.003)(1+\cos\omega t)$ [m/s]
$u_2 = 0$
$u_1 = -8,480y(y+0.003)(1+\cos\omega t)$ [m/s]
$v_1 = 0$
(0,0)
$u_o = -42,400y(y+0.003)(1+\cos\omega t)$ [m/s]
$v_o = 0$
x
y

Figure 5.1

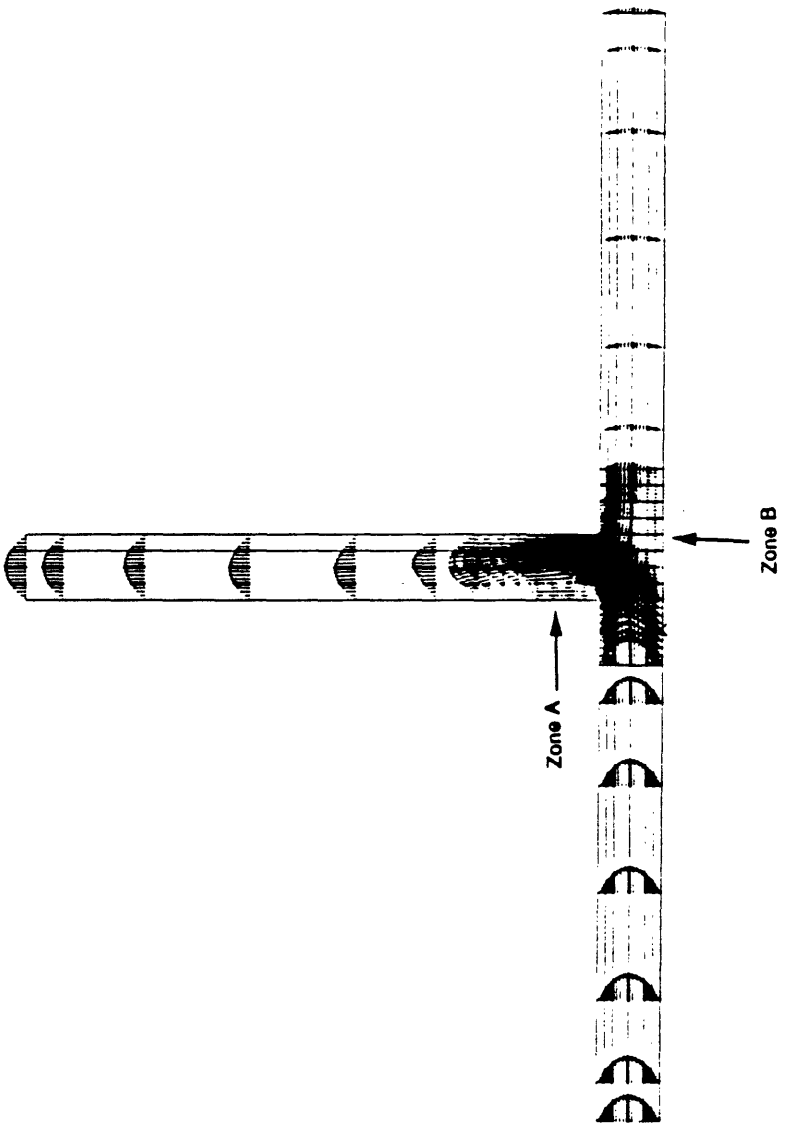

Figure 5.2

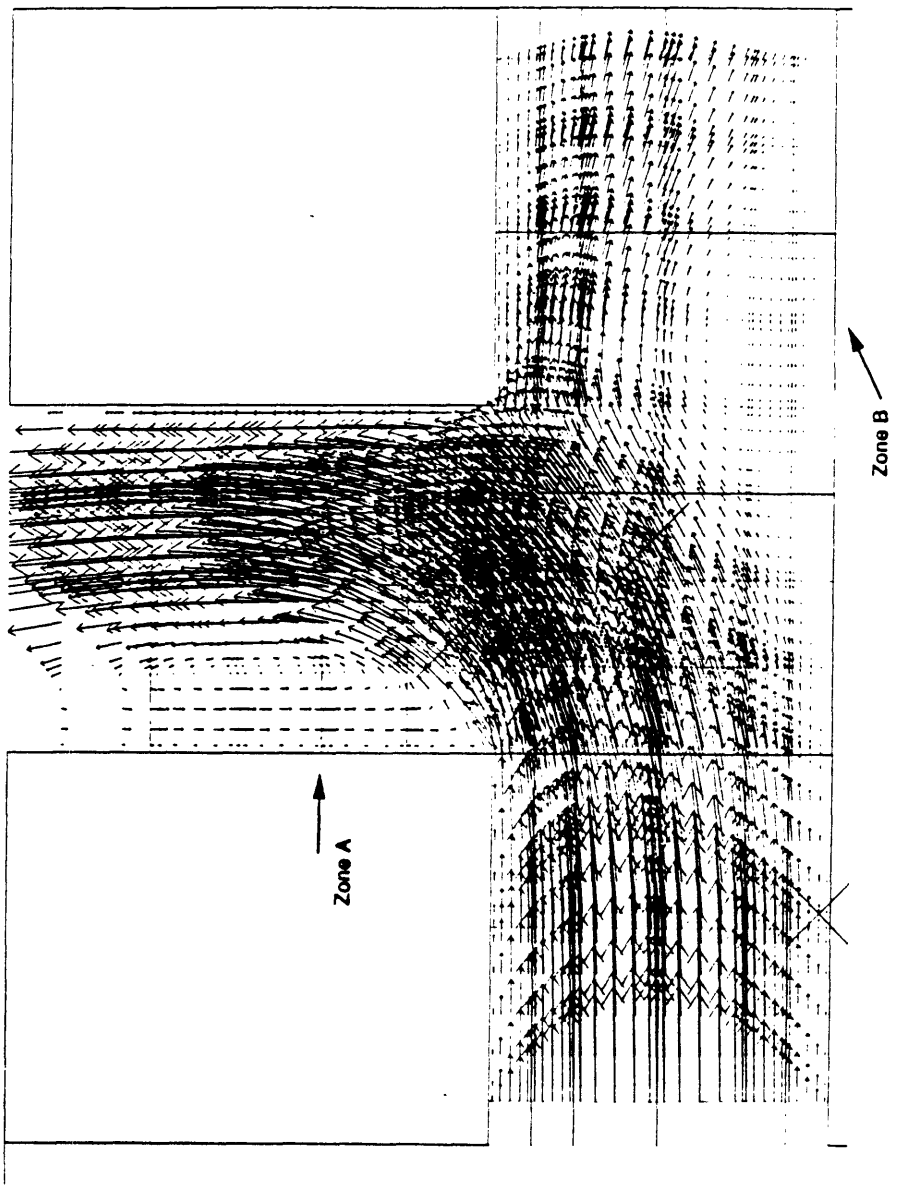

Figure 5.3

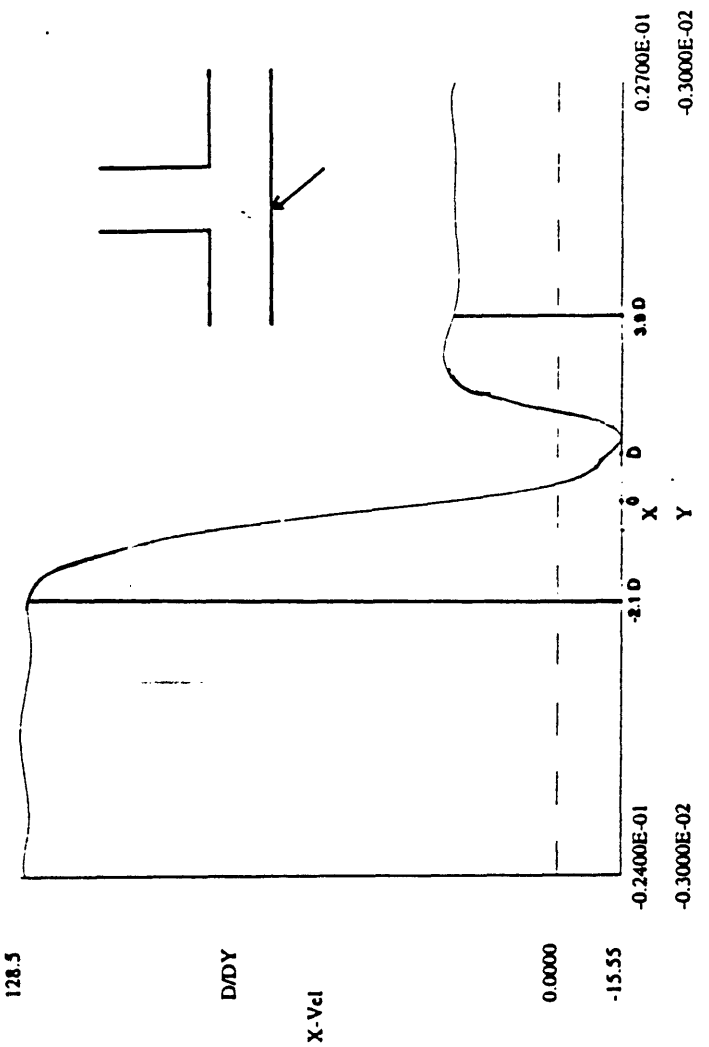
128.5
D/DY
X-Vel
0.0000
-15.55
-0.2400E-01
-0.3000E-02
-2.1 D
0
X
Y
D
3.9 D
0.2700E-01
-0.3000E-02

Figure 5.4 (a)

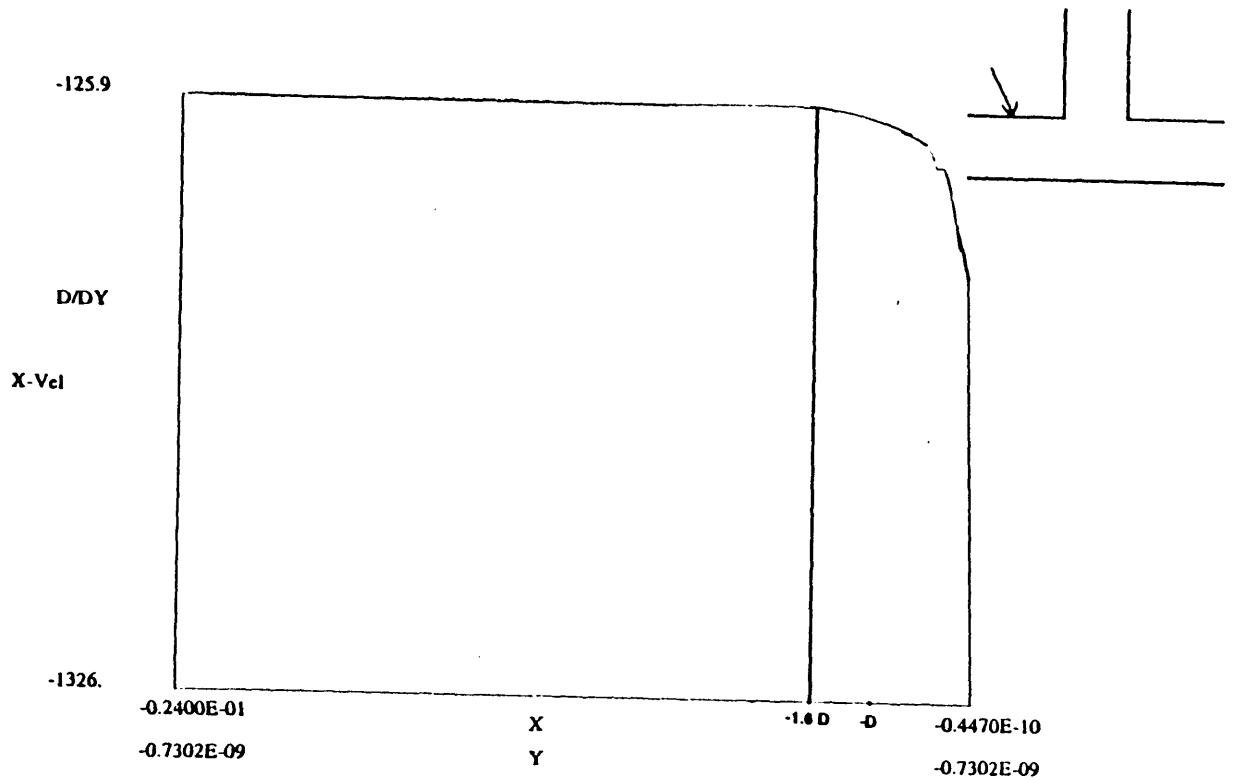
-125.9
D/DY
X-Vel
-1326.
-0.2400E-01
-0.7302E-09
X
Y
-1.0 D
-D
-0.4470E-10
-0.7302E-09

Figure 5.4 (b)

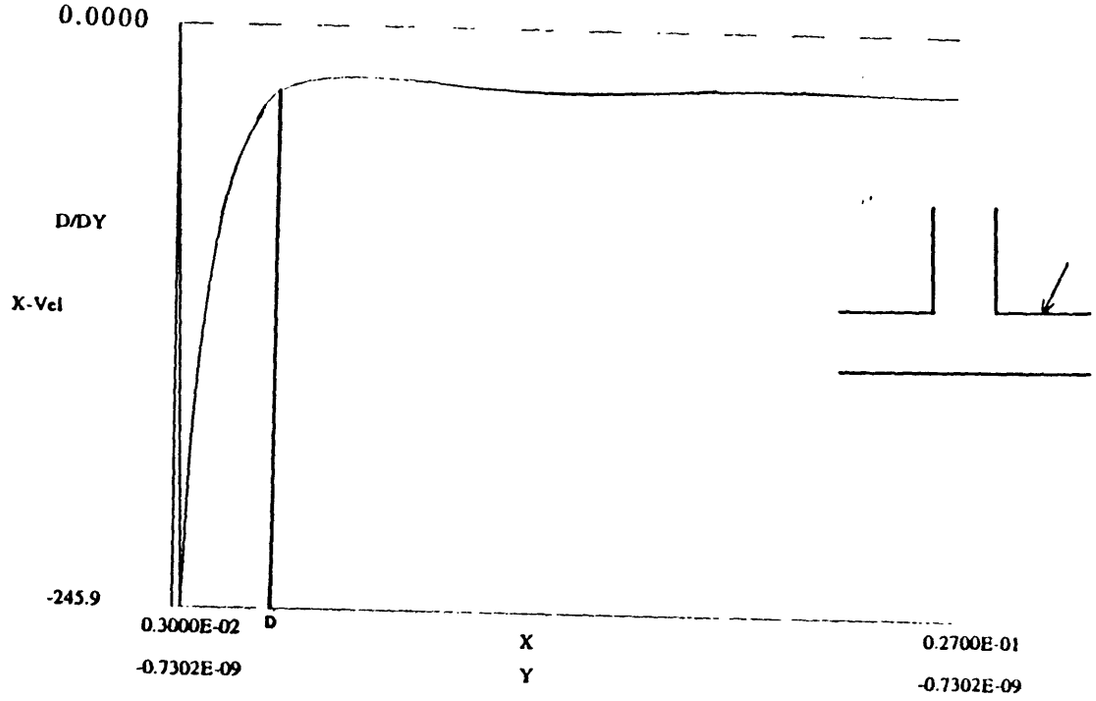
0.0000
D/DY
X-Vel
-245.9
0.3000E-02
-0.7302E-09
D
X
Y
0.2700E-01
-0.7302E-09

Figure 5.4 (c)

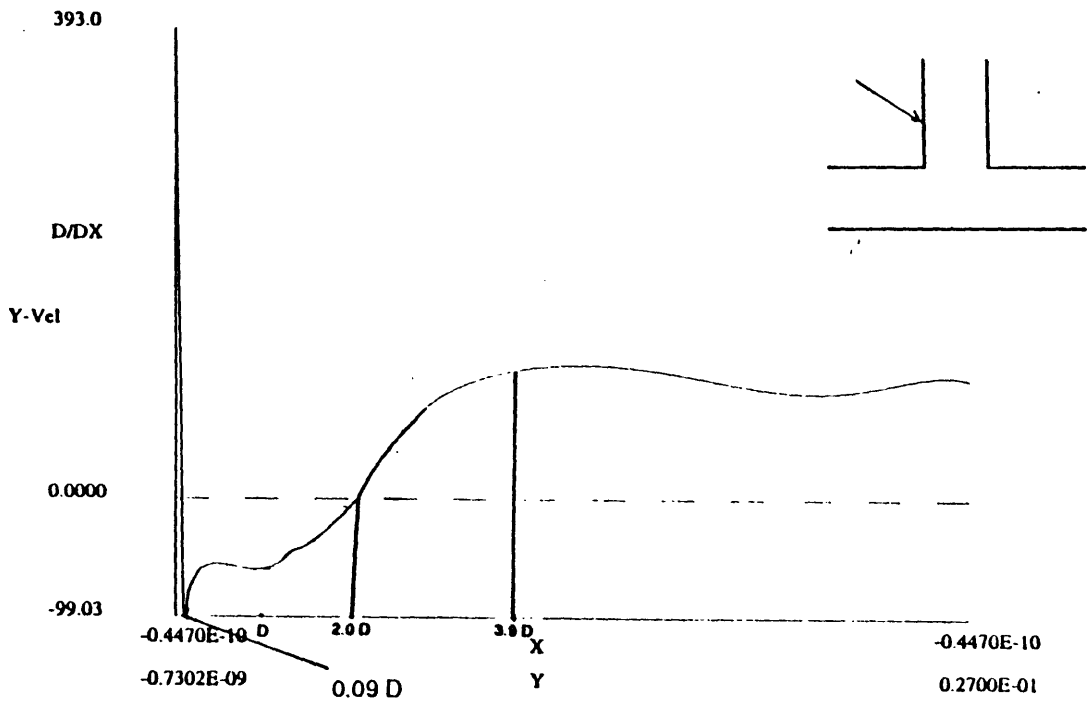
393.0
D/DX
Y-Vel
0.0000
-99.03
-0.4470E-10
D
2.0 D
3.0 D
X
-0.4470E-10
-0.7302E-09
0.09 D
Y
0.2700E-01

Figure 5.5 (a)

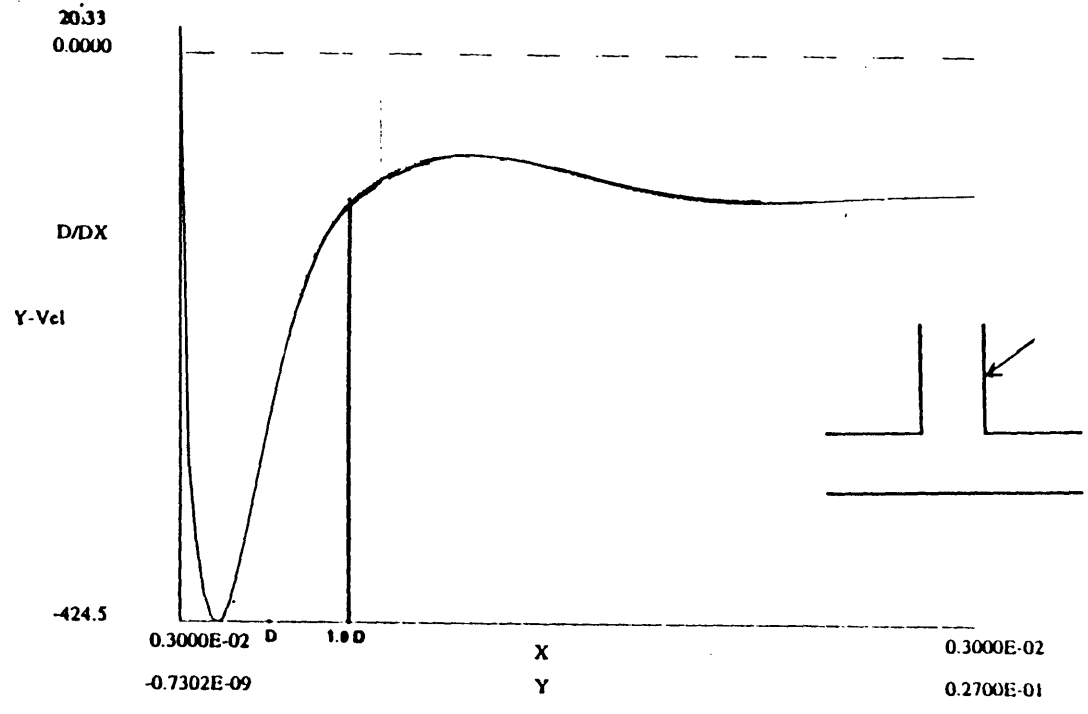
20.33
0.0000
D/DX
Y-Vel
-424.5
0.3000E-02
D
1.0 D
X
Y
-0.7302E-09
0.3000E-02
0.2700E-01

Figure 5.5 (b)

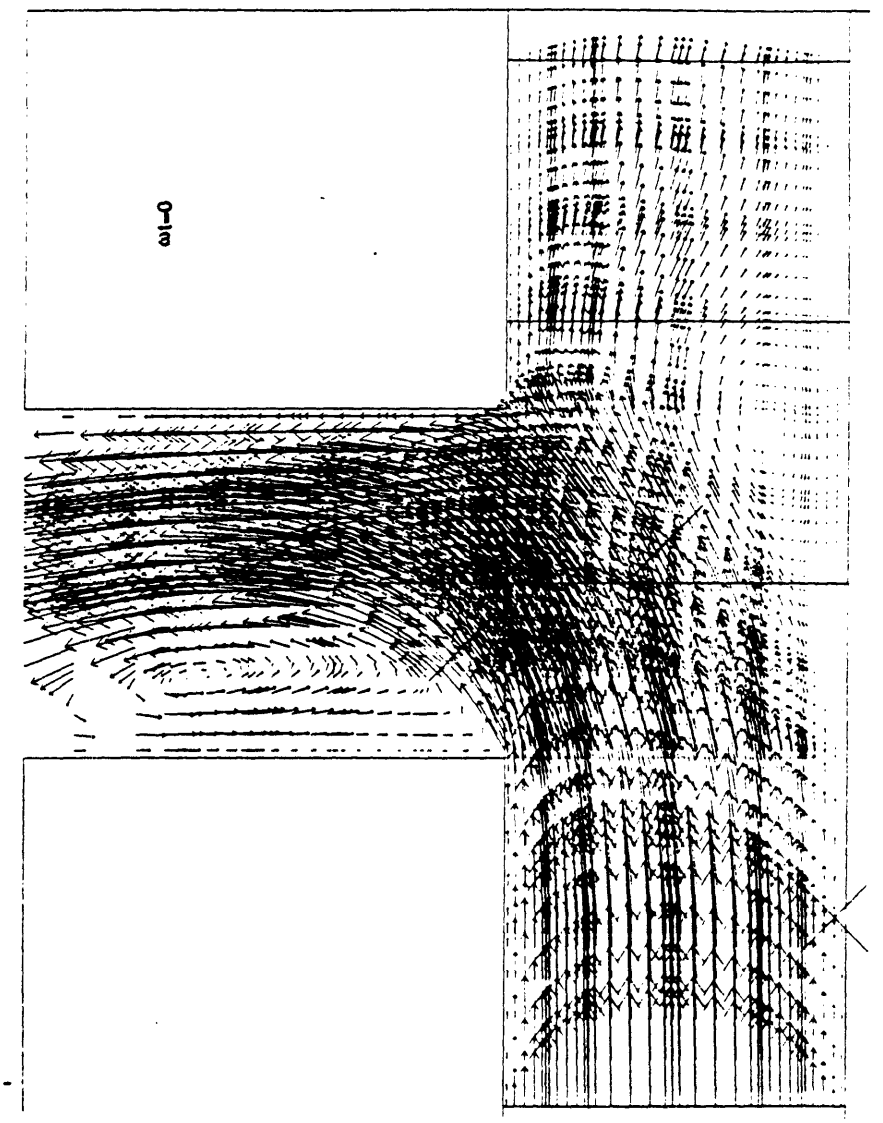

Figure 5.6 (a)

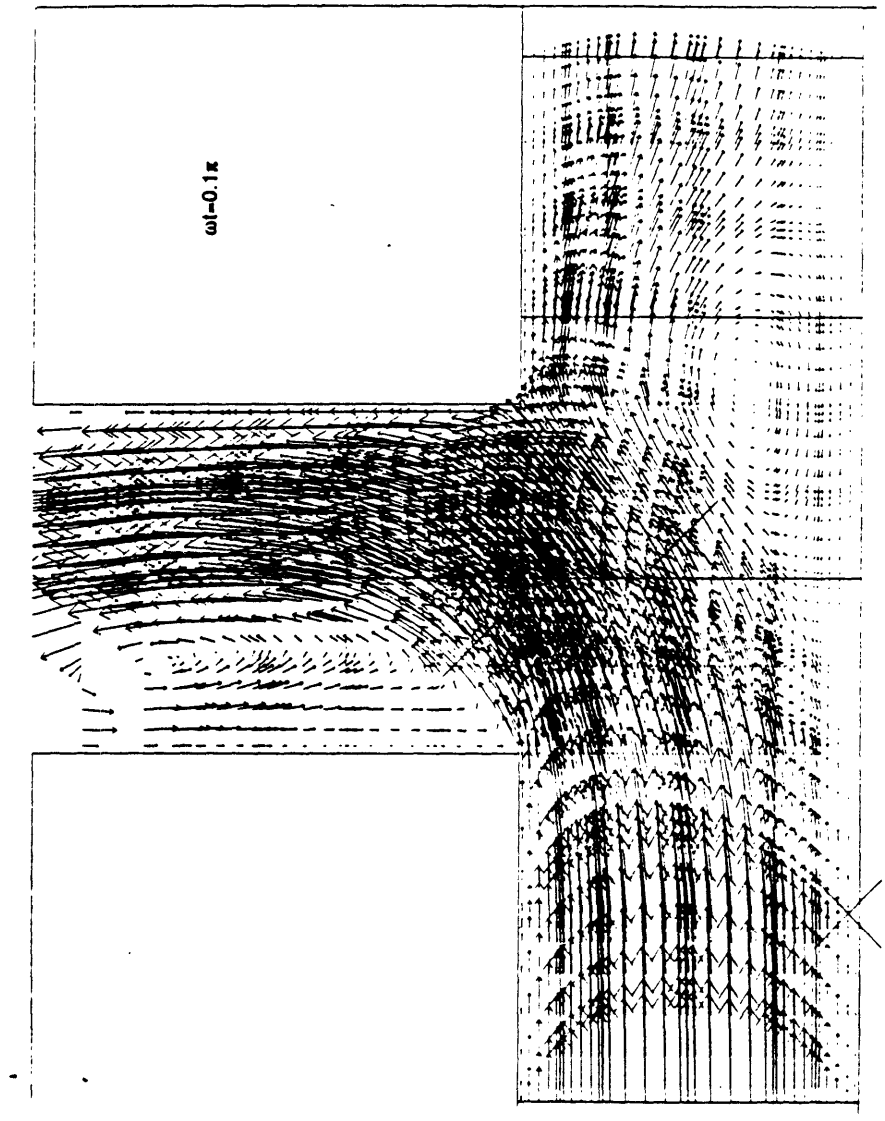

Figure 5.6 (b)

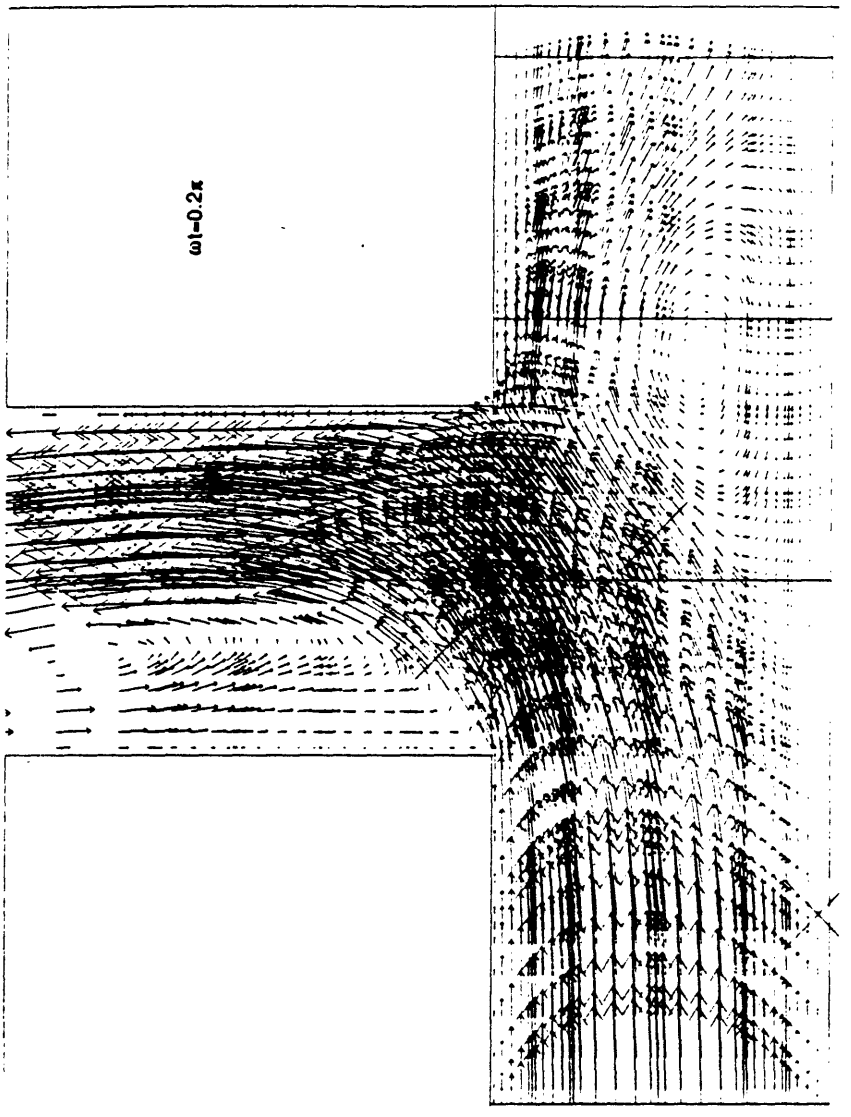

Figure 5.6 (c)

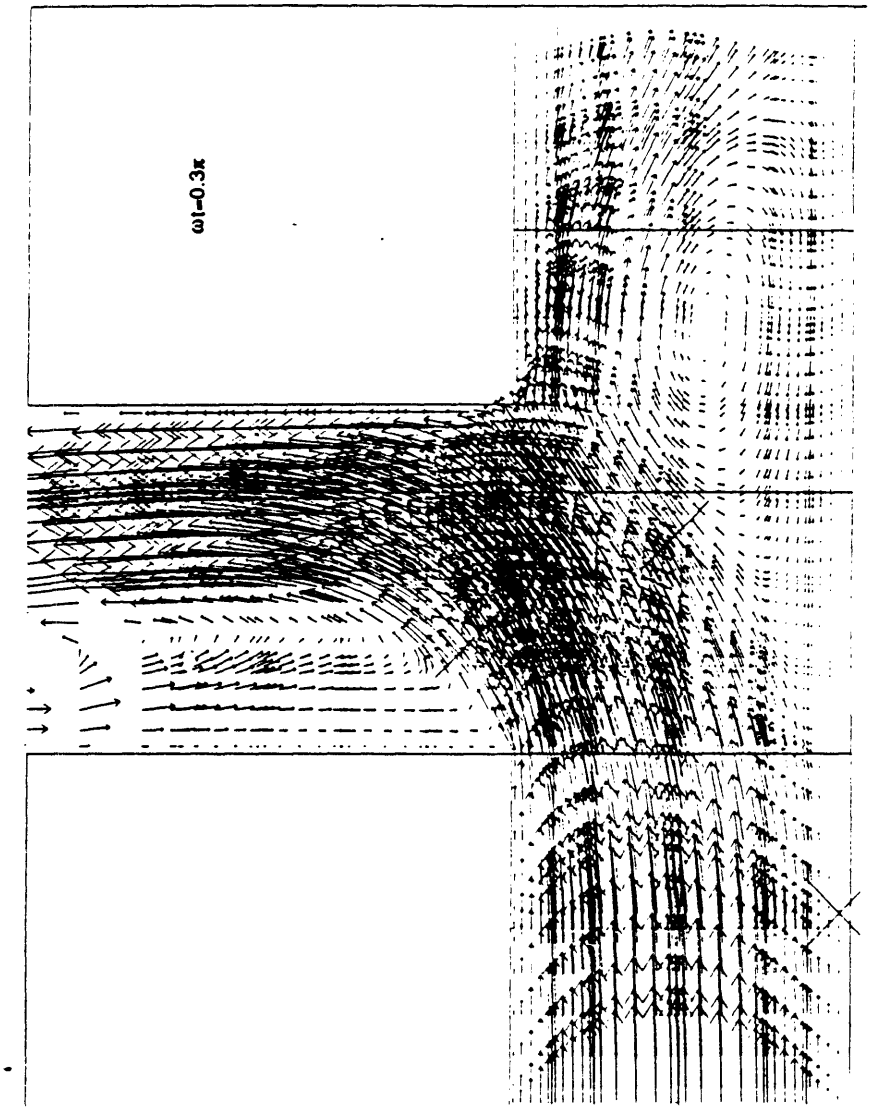

Figure 5.6 (d)

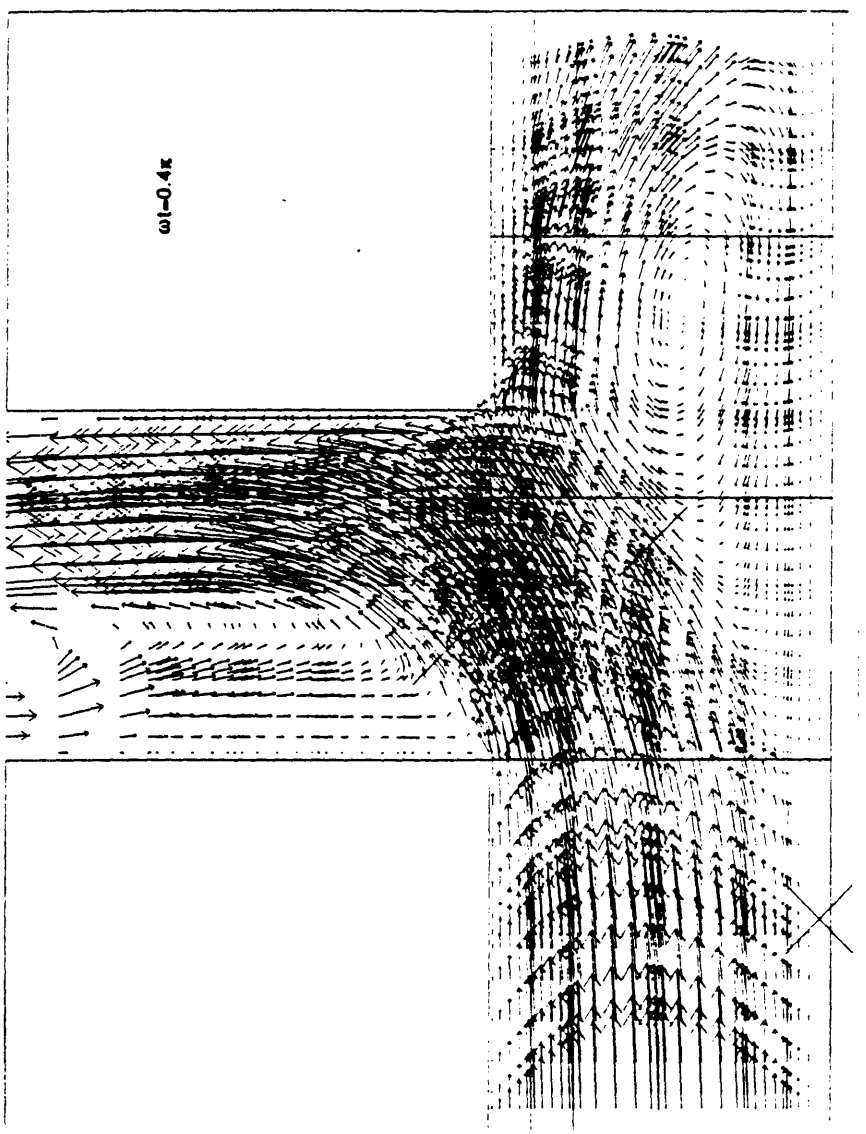

Figure 5.6 (e)

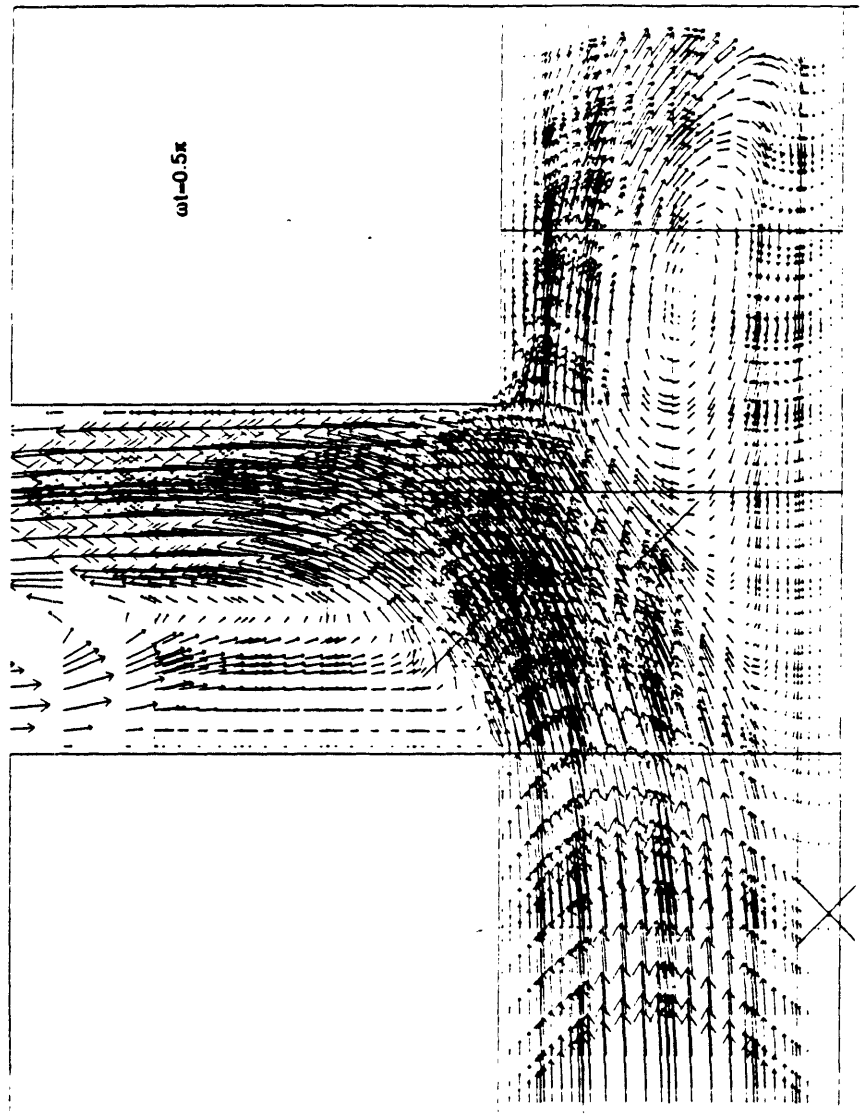

Figure 5.6 (f)

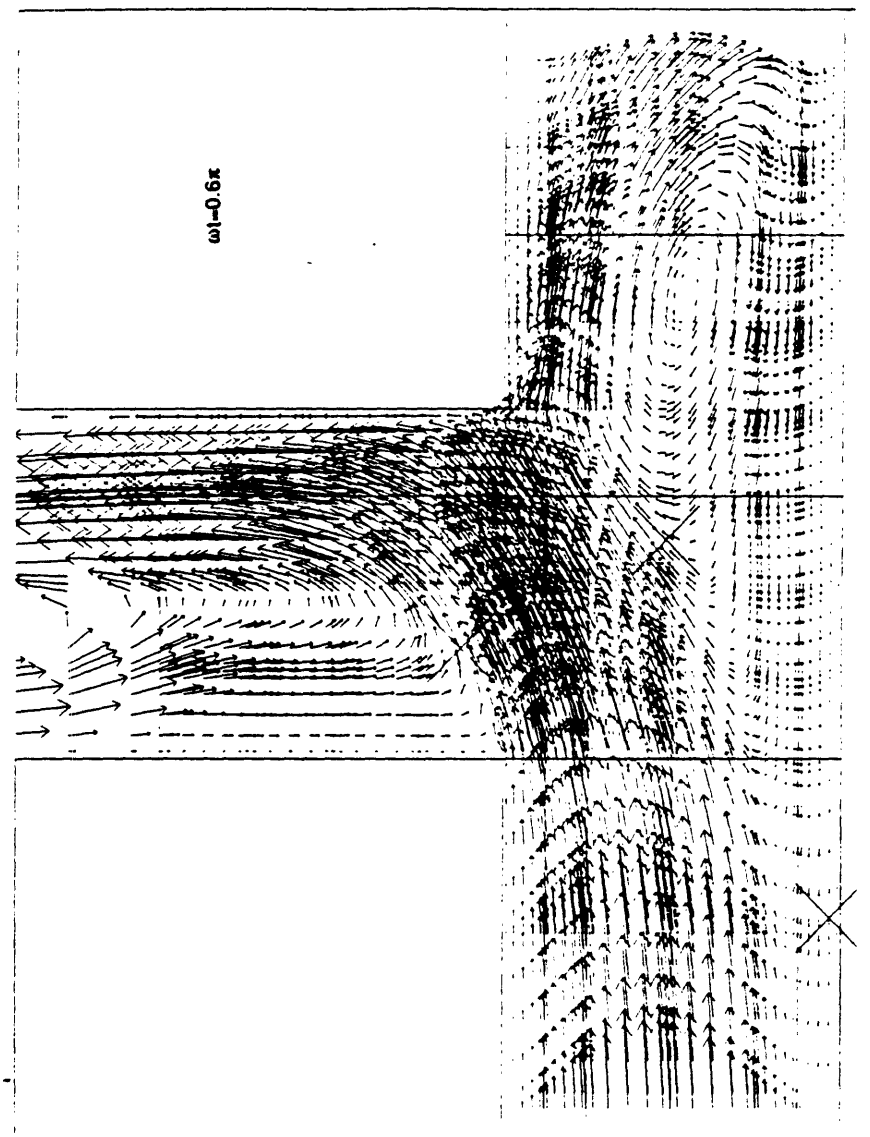

Figure 5.6 (g)

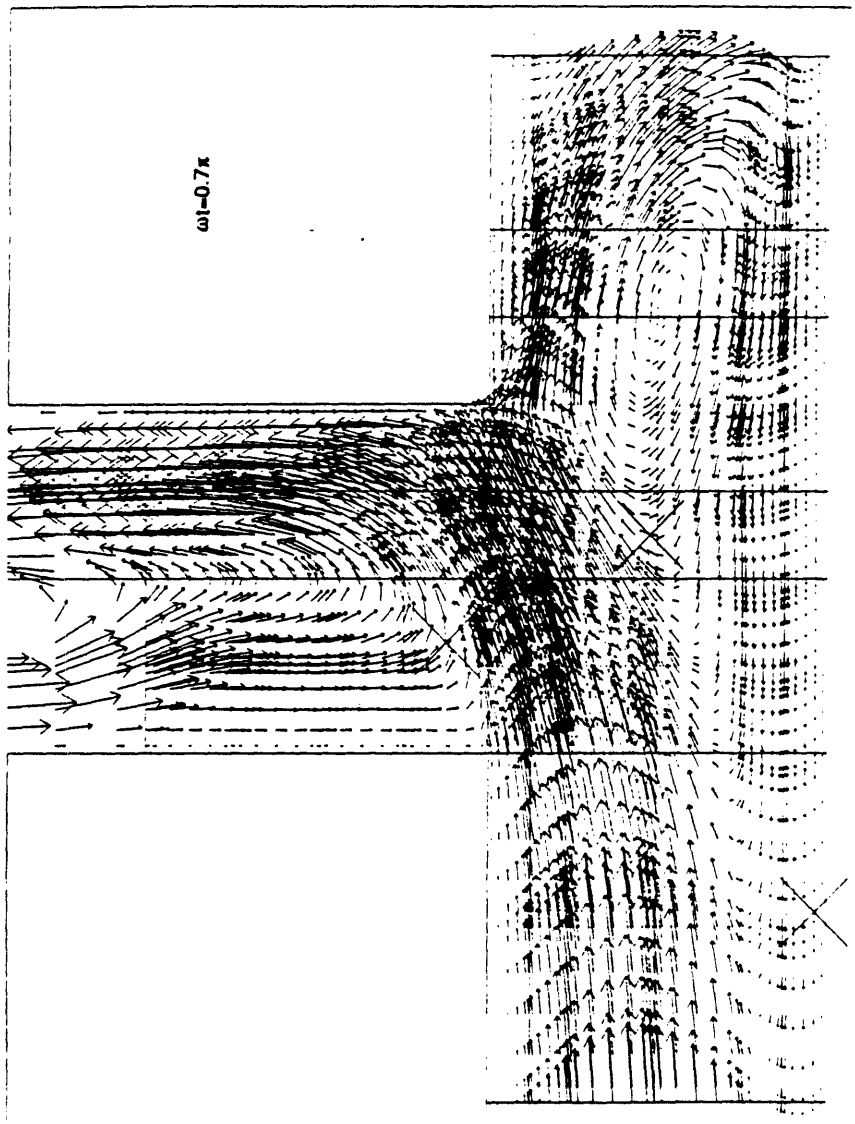

Figure 5.6 (h)

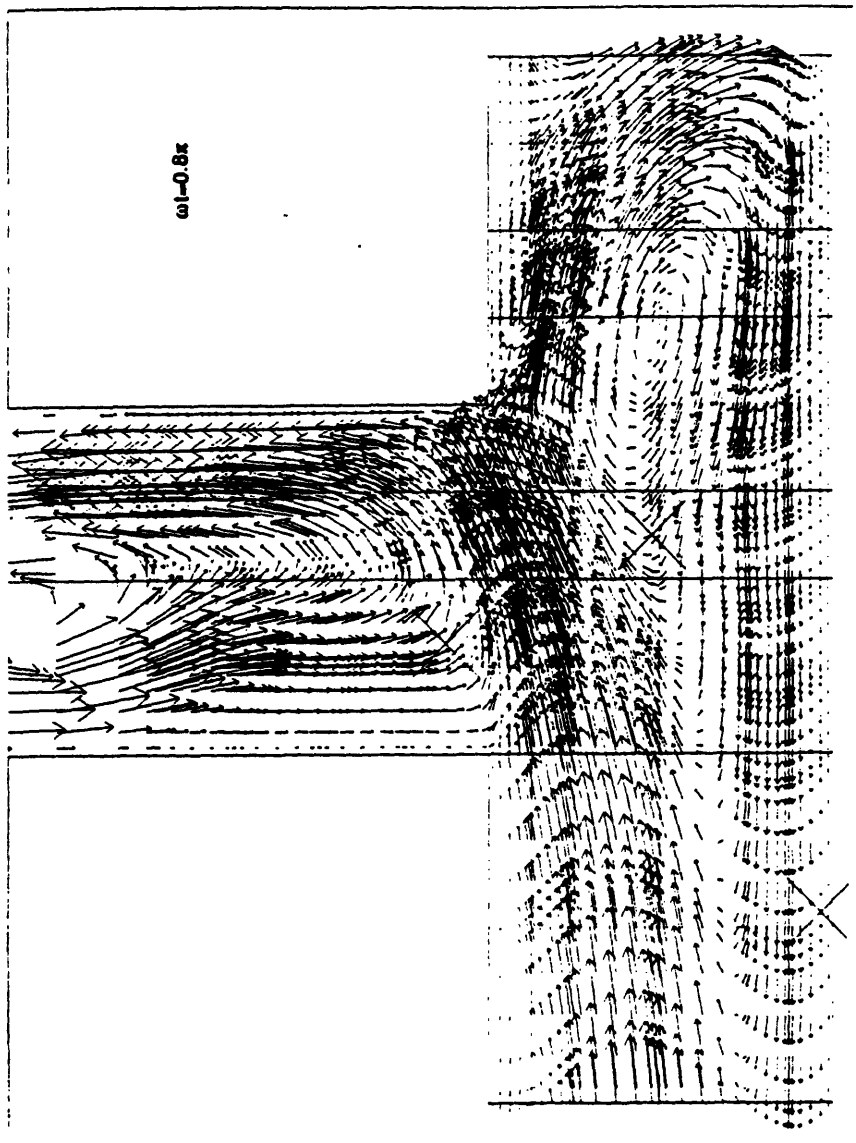

Figure 5.6 (i)

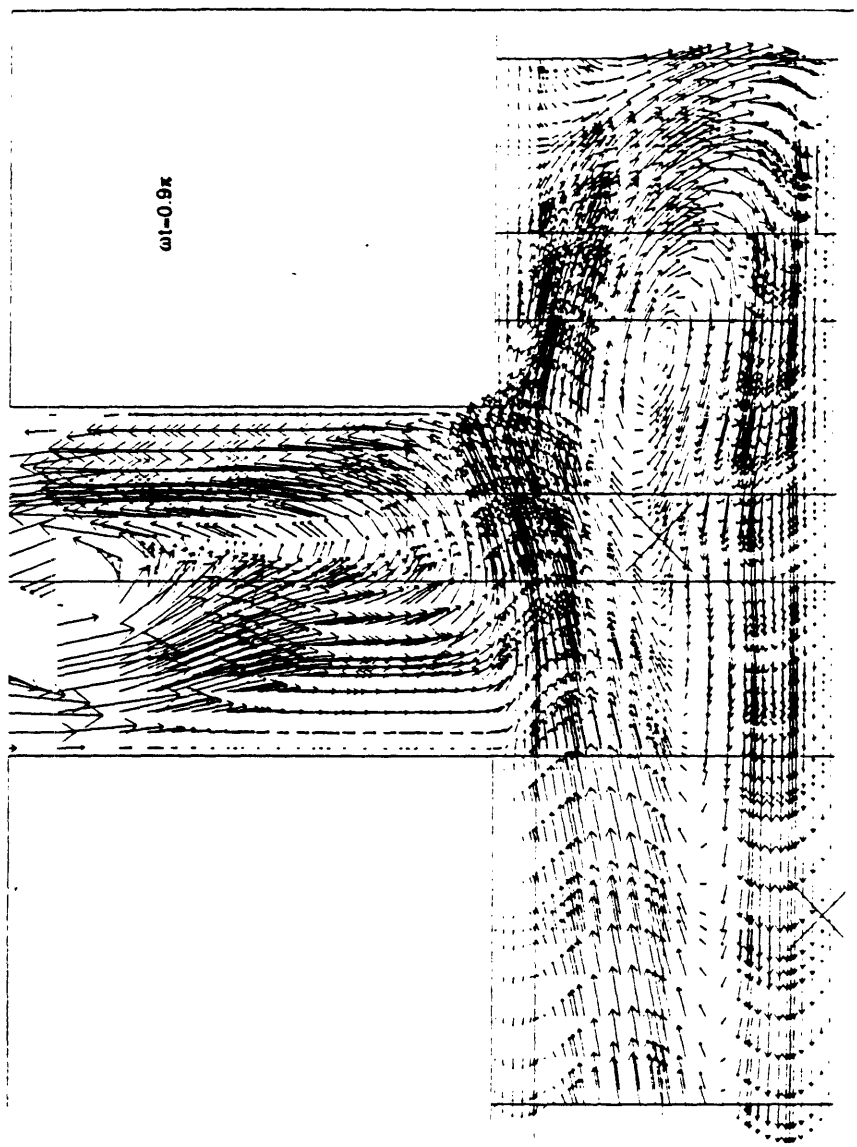

Figure 5.6 (j)

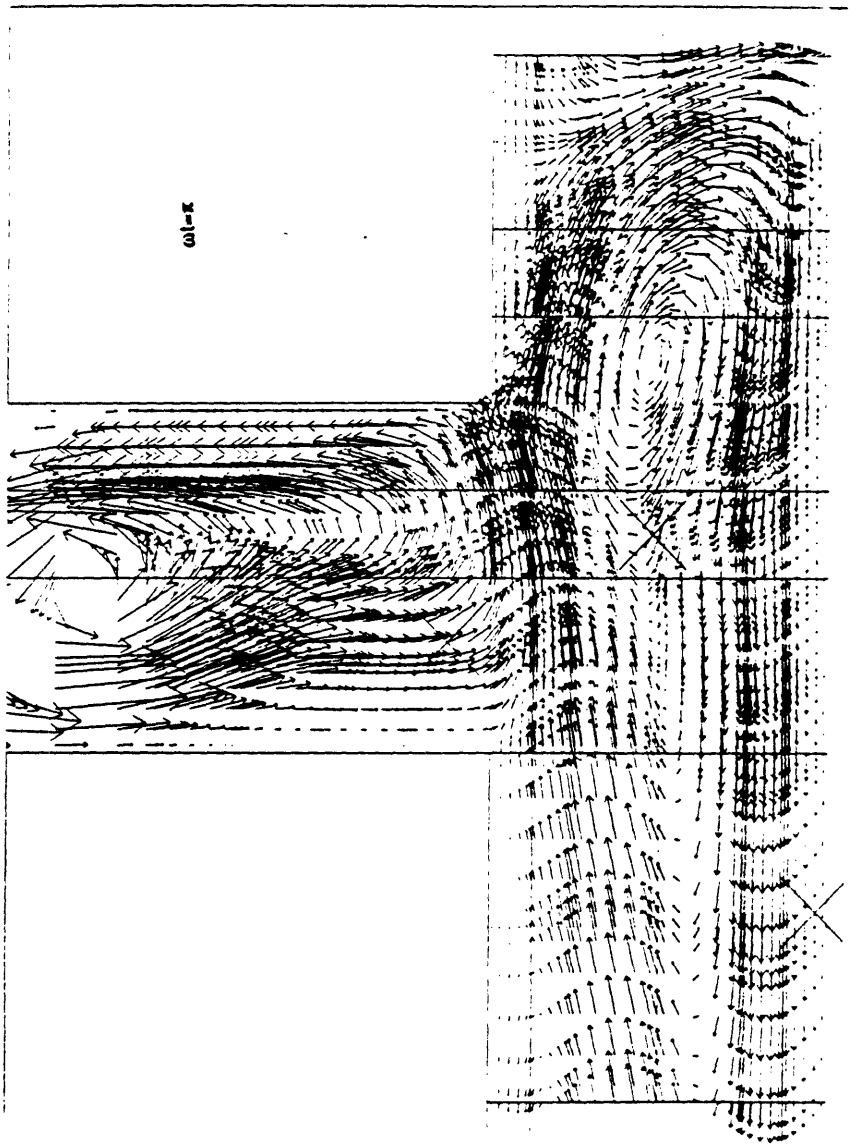

Figure 5.6 (k)

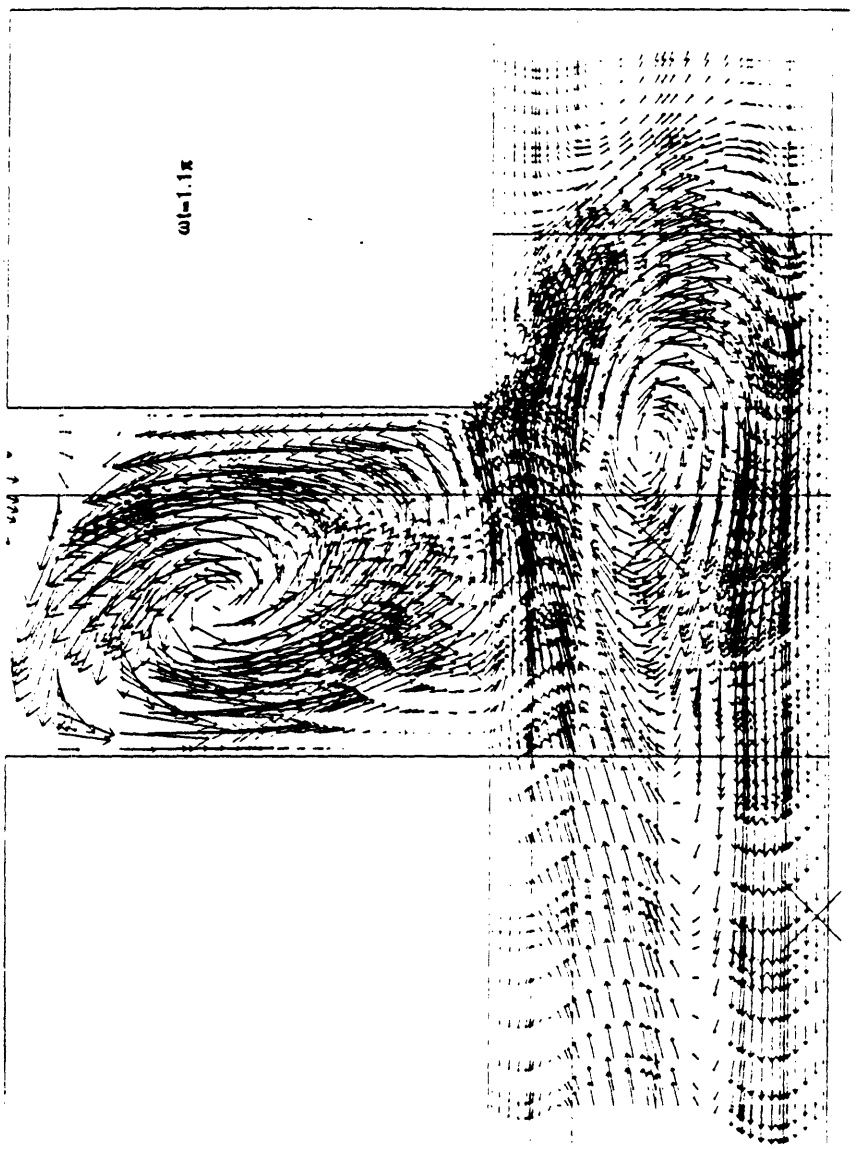

Figure 5.6 (l)

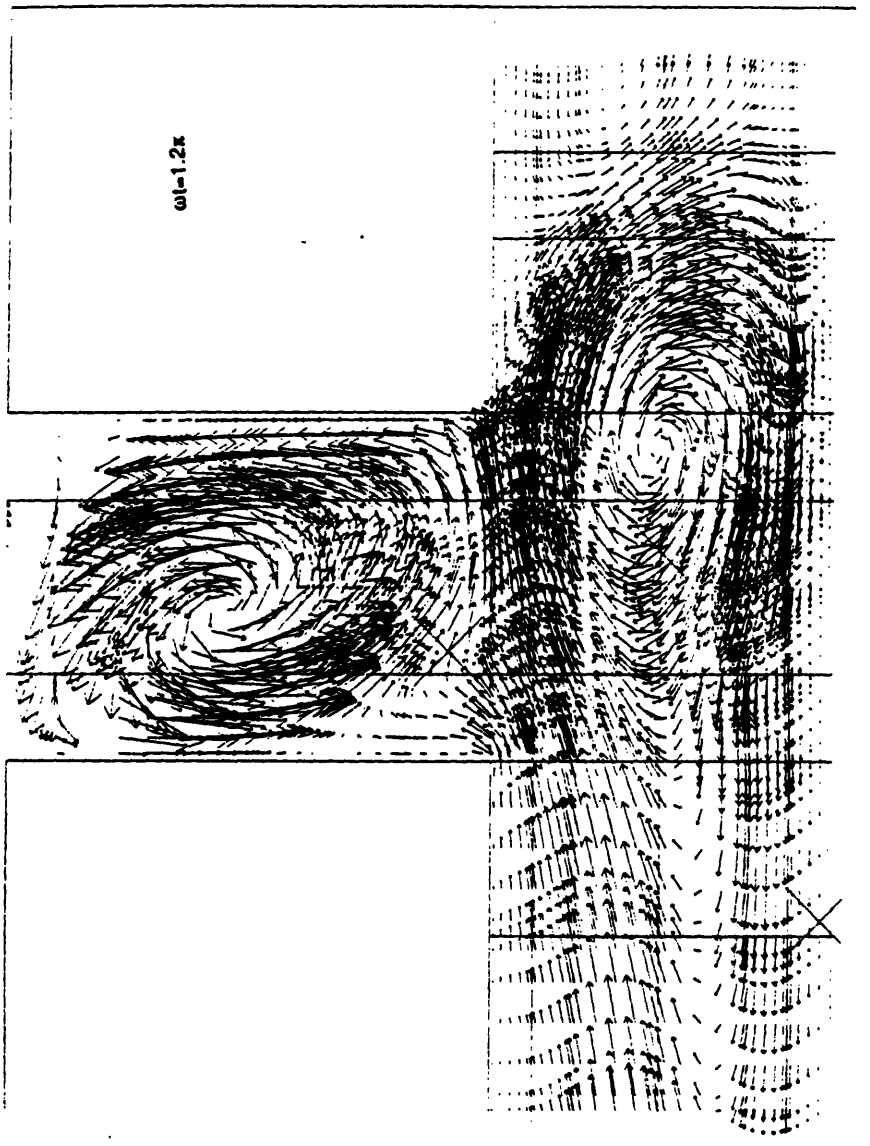

Figure 5.6 (m)

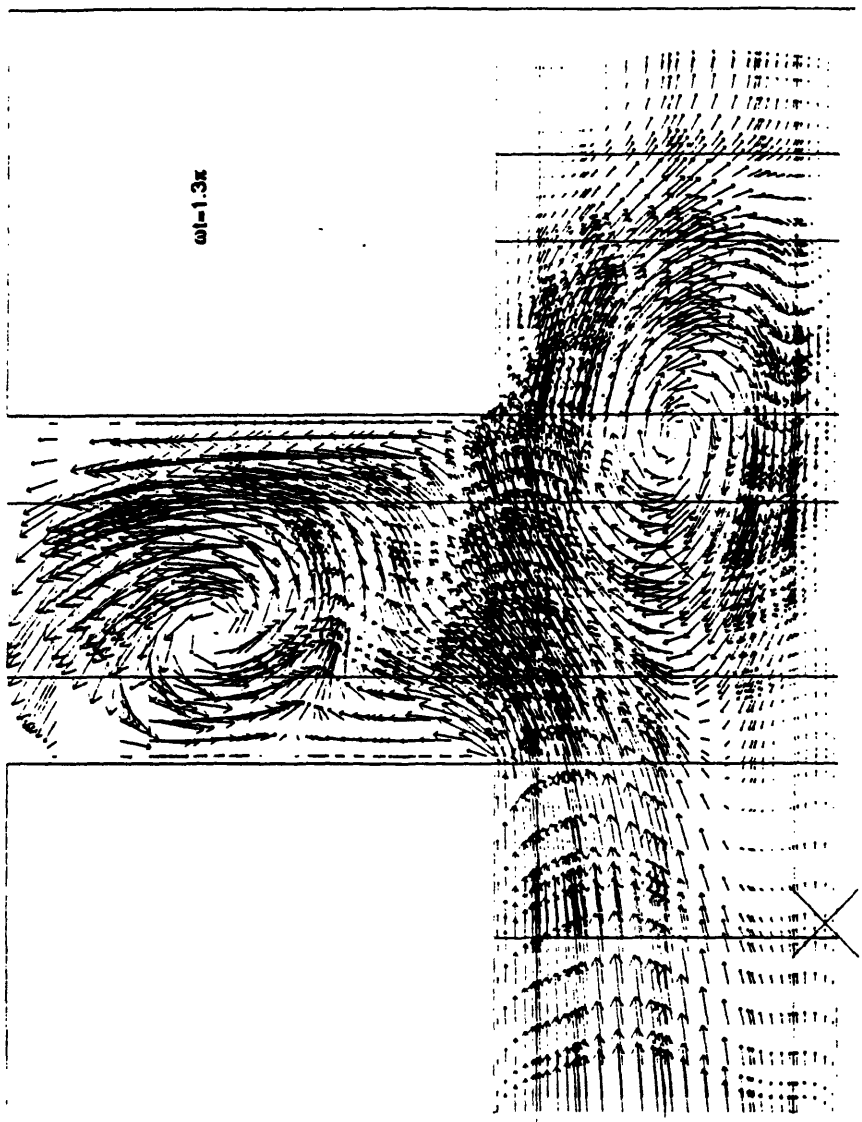

Figure 5.6 (n)

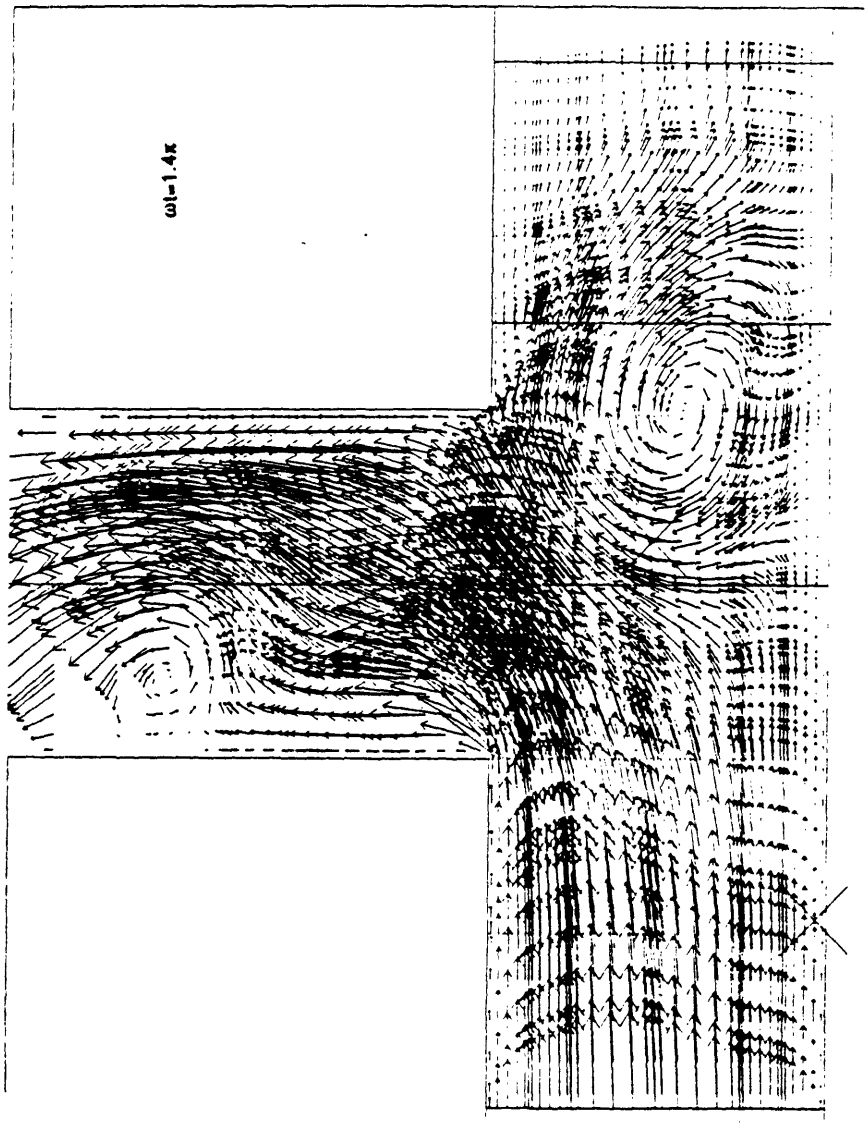

Figure 5.6 (o)

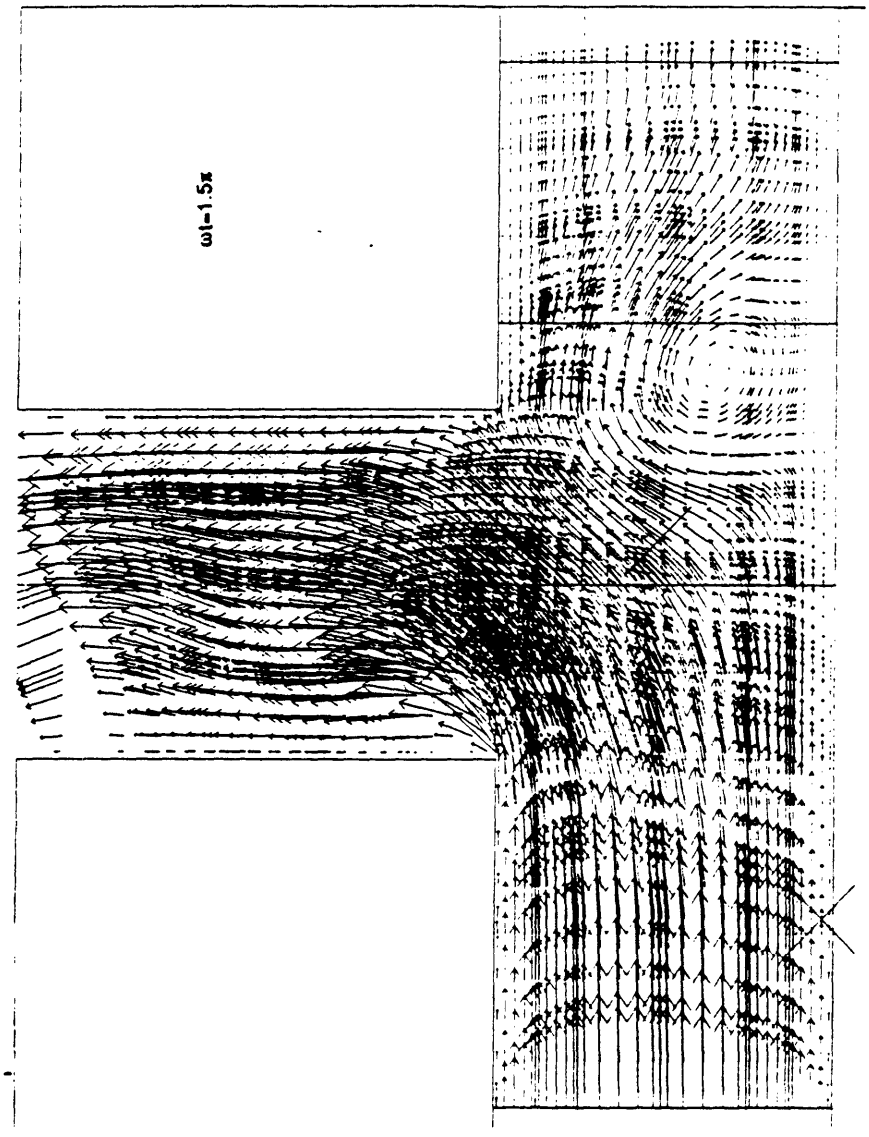

Figure 5.6 (p)

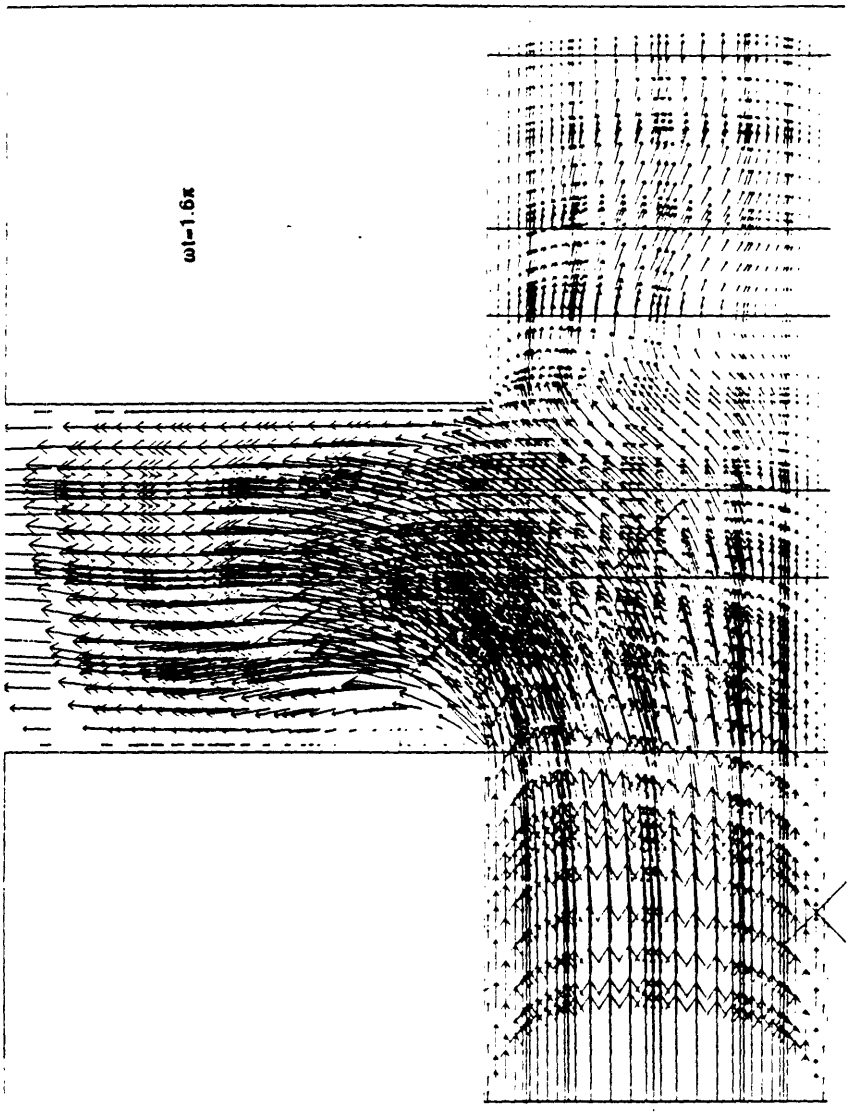

Figure 5.6 (q)

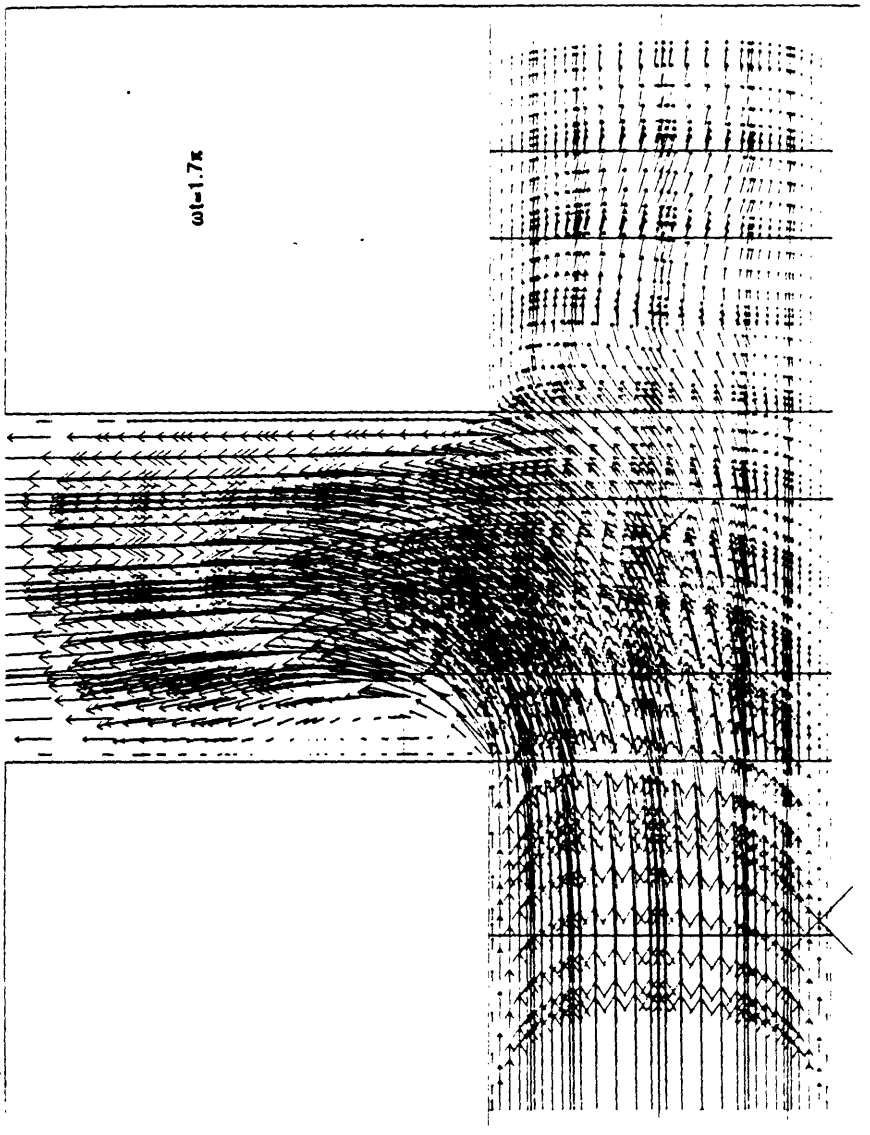

Figure 5.6 (r)

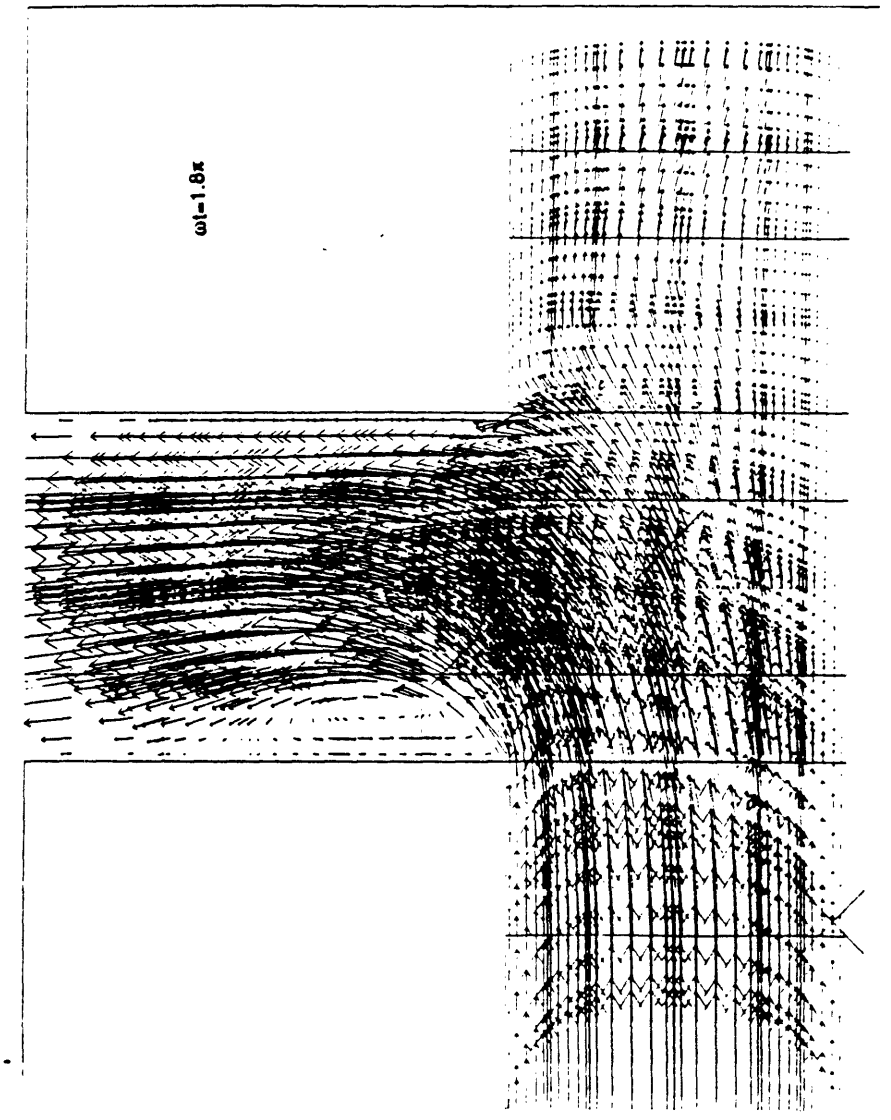

Figure 5.6 (s)

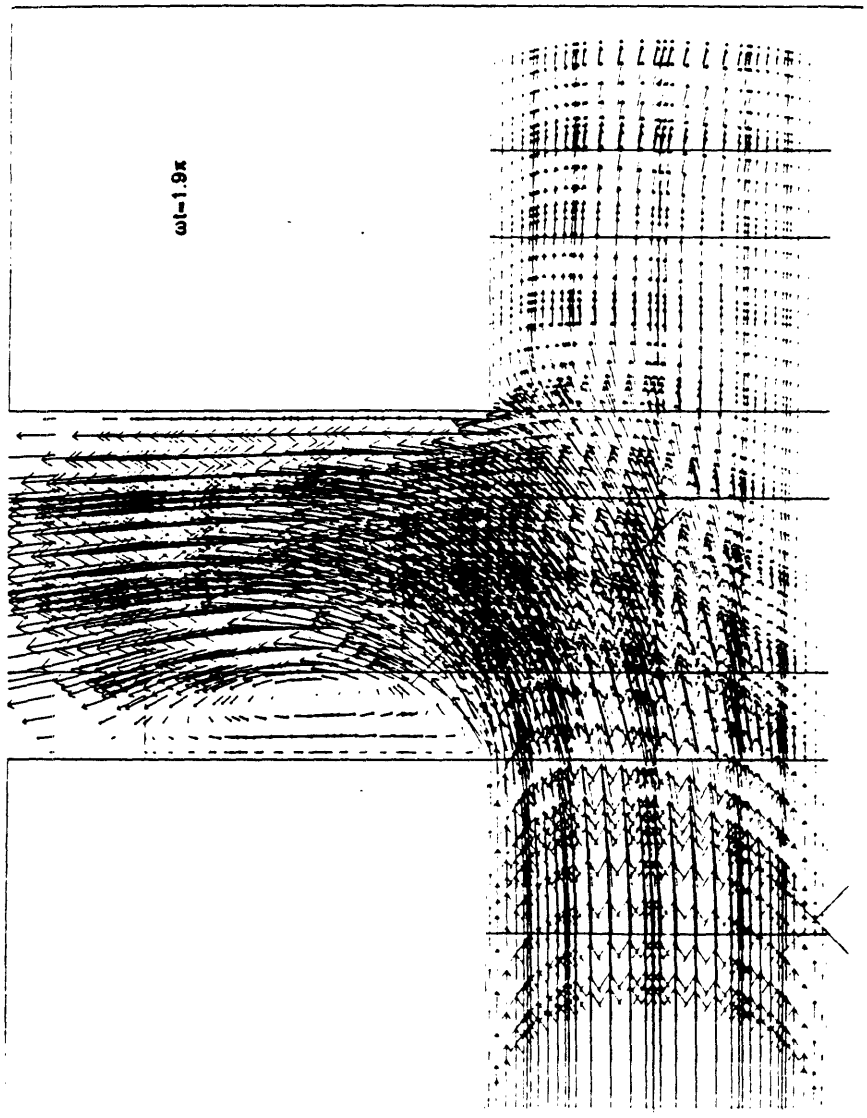

Figure 5.6 (t)

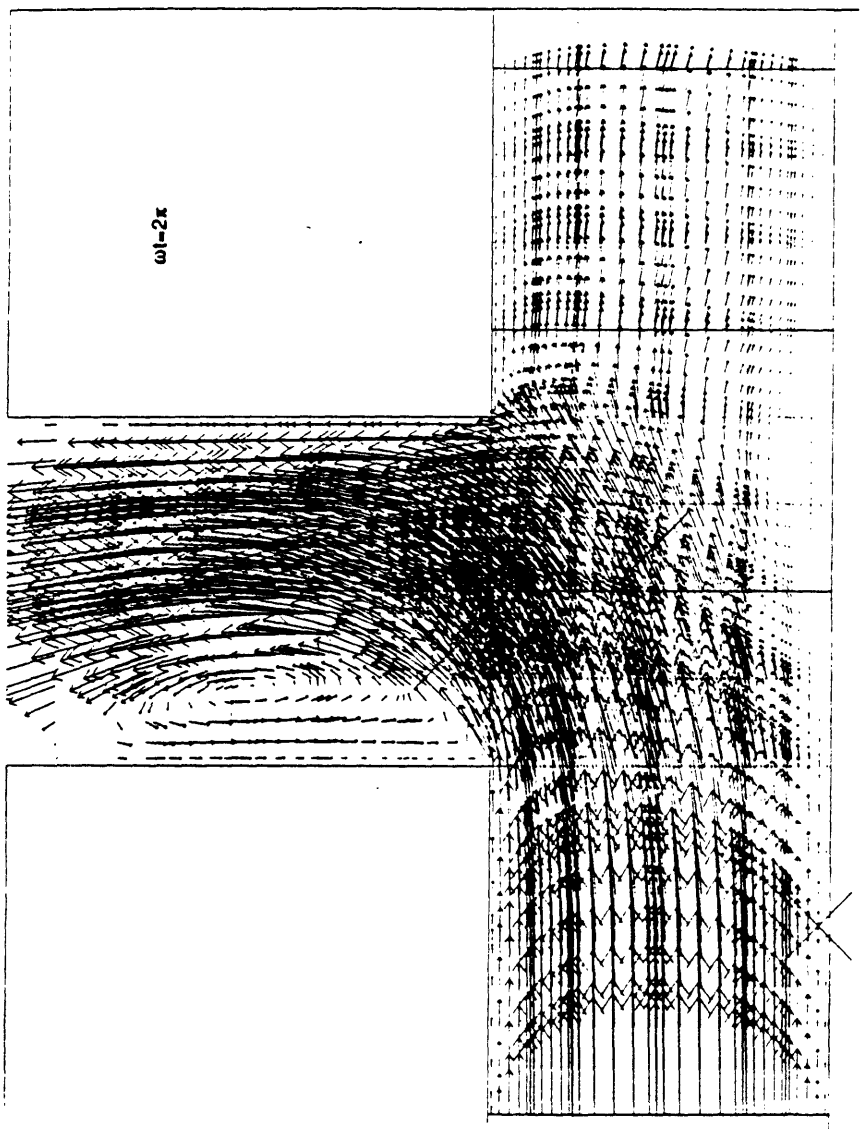

Figure 5.6 (u)

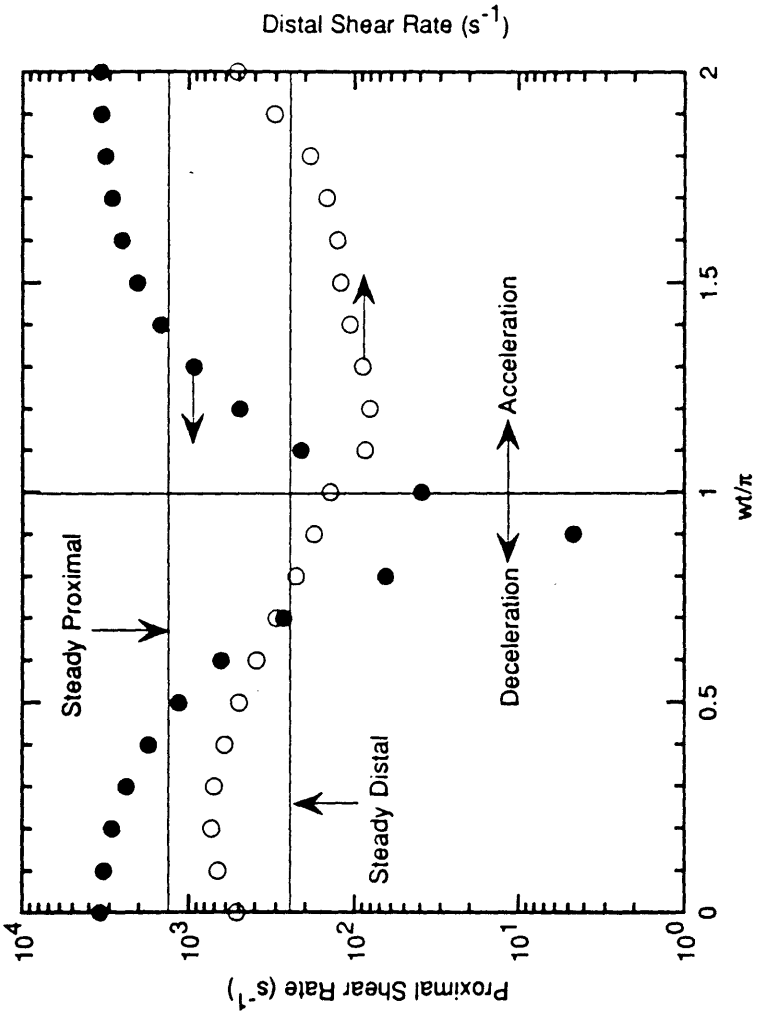
Distal Shear Rate (s^{-1})
Proximal Shear Rate (s^{-1})
10^4
10^3
10^2
10^1
10^0
0
0.5
1
1.5
2
wt/π
Steady Proximal
Steady Distal
Acceleration
Deceleration

Figure 5.7

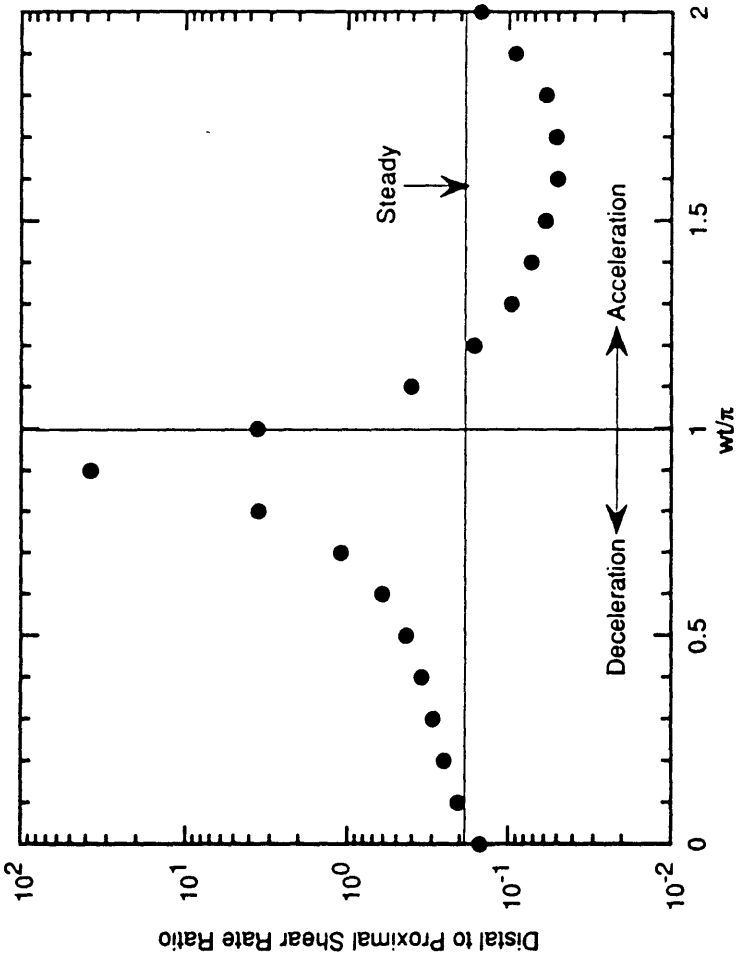
Distal to Proximal Shear Rate Ratio
10^{2}
10^{1}
10^{0}
10^{-1}
10^{-2}
0
0.5
1
1.5
2
$\omega t/\pi$
Steady
Acceleration
Deceleration

Figure 5.8

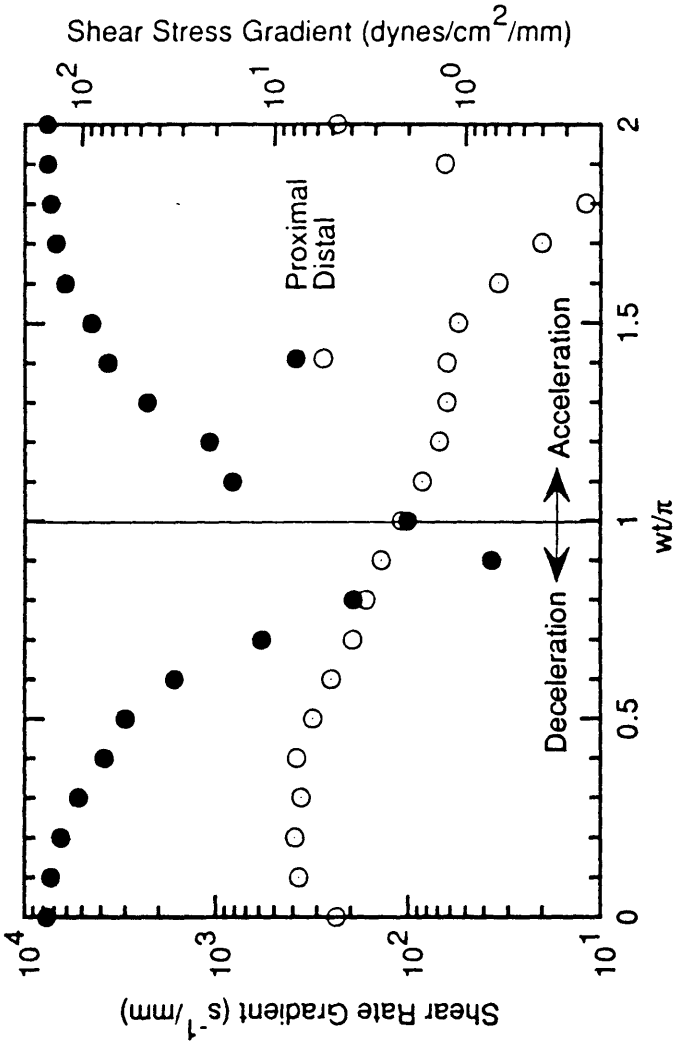
Shear Stress Gradient (dynes/cm^2/mm)
10^2
10^1
10^0
Proximal
Distal
Acceleration
Deceleration
2
1.5
1
0.5
0
wt/π
10^4
10^3
10^2
10^1
Shear Rate Gradient (s^{-1}/mm)

Figure 5.9

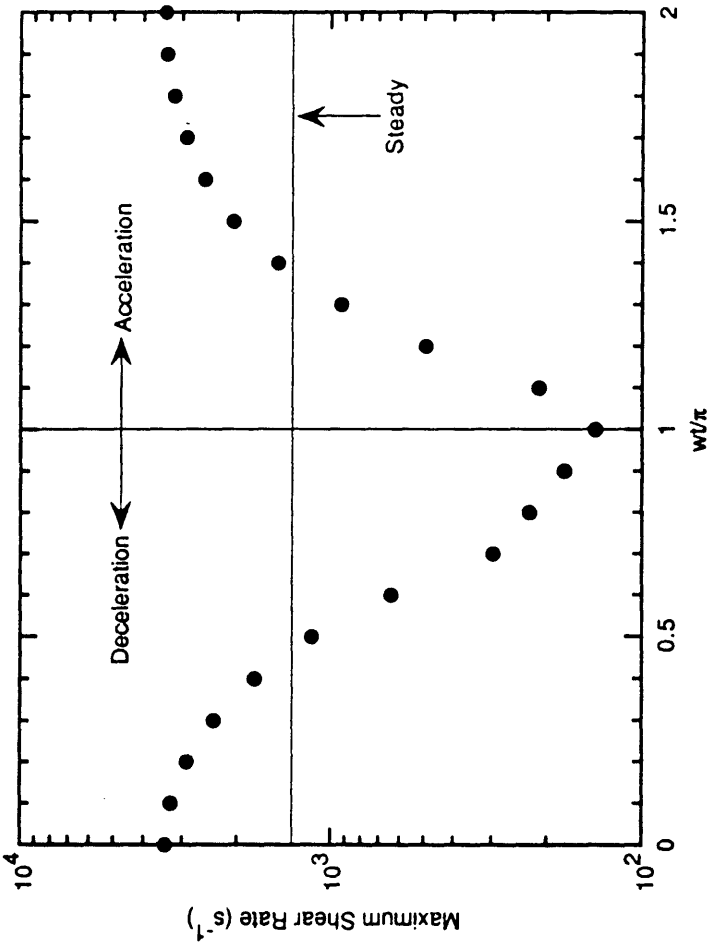
Maximum Shear Rate (s^{-1})
10^4
10^3
10^2
Deceleration
Acceleration
Steady
0
0.5
1
1.5
2
wt/π

Figure 5.10

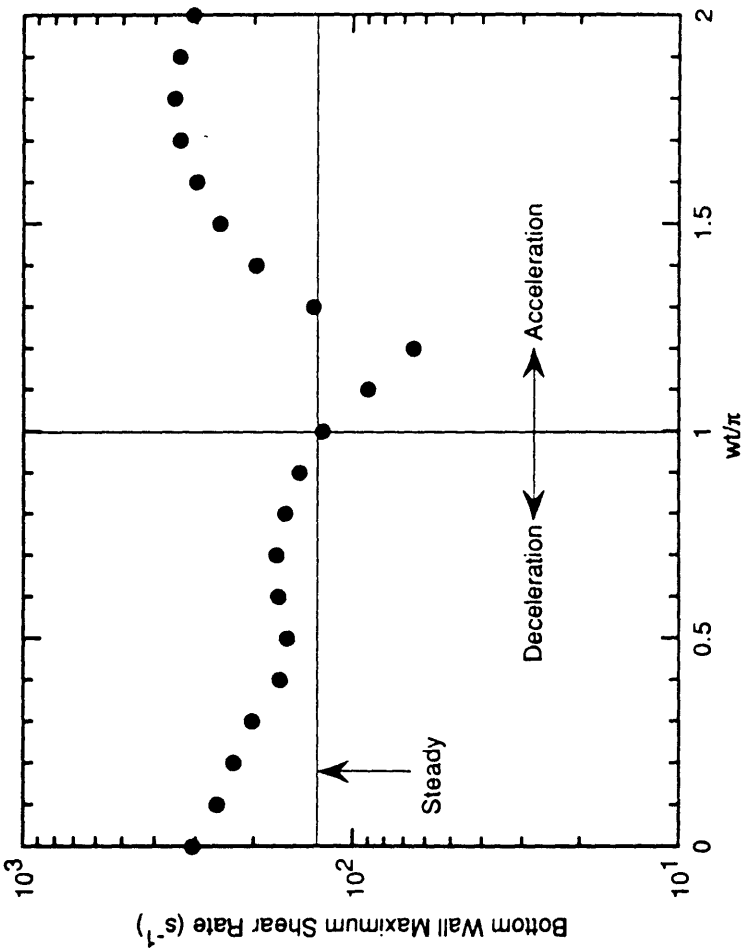
Bottom Wall Maximum Shear Rate (s^{-1})
10^3
10^2
10^1
0
0.5
1
1.5
2
wt/π
Steady
Deceleration
Acceleration

Figure 5.11

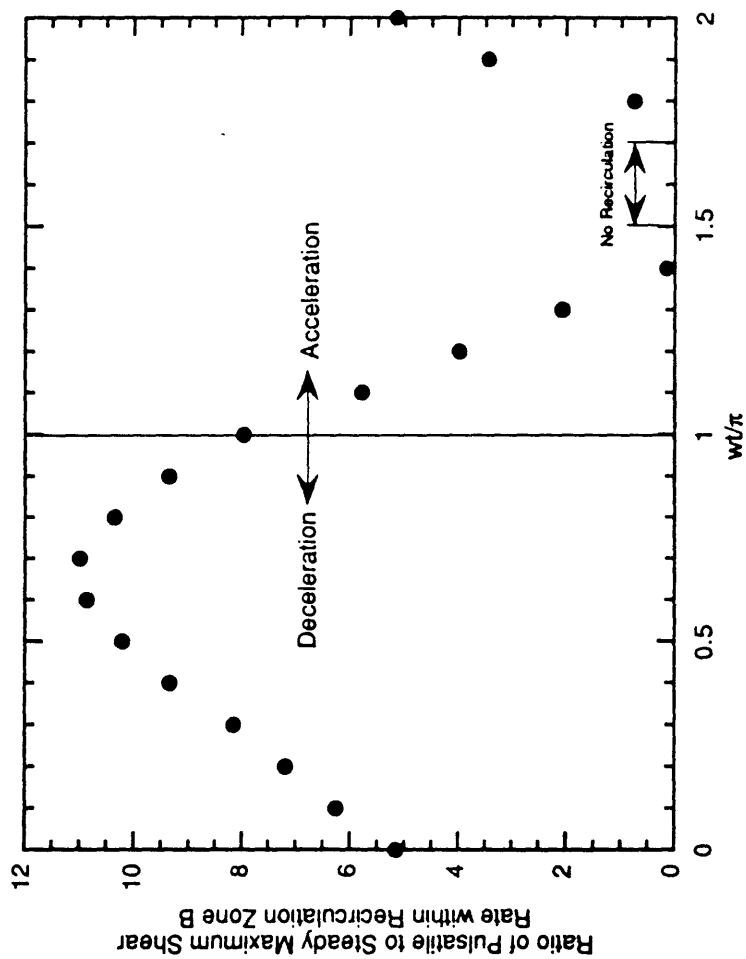
Ratio of Pulsatile to Steady Maximum Shear
Rate within Recirculation Zone B
12
10
8
6
4
2
0
0
0.5
1
1.5
2
wt/π
Deceleration
Acceleration
No Recirculation

Figure 5.12

Chapter Six

In Vivo Velocity Profiles in the Rabbit Abdominal Aorta

6.1 Introduction

Atherosclerosis is an arterial disease characterized by the focal accumulation of fatty and fibrous deposits within the arterial wall. The complicated lesions of atherosclerosis are thought to evolve from localized fatty streaks which progress to calcified fibrous plaques. It has long been recognized that atherosclerotic lesions do not occur randomly within the vasculature but rather preferentially in regions of arterial branching and curvature [1,2]. This focal nature has given rise to the notion of localizing factors in atherogenesis, most notably hemodynamics within the affected vessel [3,4].

Despite extensive study over the past three decades, very few generalizations can be made at this time regarding the potential role of hemodynamics in atherogenesis. The earliest theories expressed this role in terms of a response of the endothelium to hemodynamic injury caused by a wide range of fluid mechanical phenomena including high or low wall shear stress [5,6], low arterial blood pressure [7], boundary layer separation [8], turbulence [9], arterial wall fatigue and consequent loss of tensile strength [10], impedance mismatching [11], among other mechanisms. These studies, however, often failed to account for many of the subtle geometric and hemodynamic details which give rise to the tremendous complexity of arterial flow fields.

In light of pathological evidence that the earliest stages of atherosclerosis occur in the presence of an intact endothelium [12], the hemodynamic theories have evolved to a hypothesis of hemodynamic

endothelial dysfunction, thereby motivating a wide range of fundamental studies aims at elucidating endothelial cell response to fluid mechanical stresses. These studies have revealed that the endothelium, rather than being simply a non-thrombogenic surface and a selective barrier to macromolecular transport, is an active structure with sophisticated response mechanisms to stimuli. It possesses an extensive network of communication both with adjacent endothelial cells and subjacent smooth muscle cells. Endothelial cells exhibit specific humoral, metabolic, and structural responses which vary with shear stress level. Examples of phenomena that respond to shear stress are production of interleukin-6 [13]; expression of endothelin [14]; rate of prostacyclin production, intracellular Ca^{2+} concentration, and microtubule realignment [15]; pinocytotic rate, cell alignment in the flow direction, and redistribution of microfilaments or stress fibers [16]; endothelial cell proliferation and DNA synthesis [17]; deendothelialization and cell detachment [5]; redistribution of focal adhesion sites [18]; and reorientation of extracellular fibronectin deposition [19]. The endothelial cell responses to mechanical stimuli occur over time scales ranging from seconds to days [20]. Although their direct applicability to physiological situations is uncertain, these observations suggest that mechanical forces can stimulate endothelial cells *in vivo.*

Recent experimental investigations in glass models, vascular casts, and excised natural vessels have concentrated on capturing true arterial geometry, physiological pulsatility, and even wall compliance in some instances and have revealed the existence of complex flow fields, especially in the vicinity of arterial branches. For example, flow in models of the human abdominal aorta [21,22] demonstrated more complex flow patterns in the infrarenal than in the suprarenal section as well as time-varying helical vortex motion initiating at the

renal arteries and propagating to the iliac bifurcation. Furthermore, a region of boundary layer separation was observed along the posterior wall of the aorta extending from the renal arteries to the iliac bifurcation. Pulsatile flow experiments in models of the carotid artery [23,24] have shown that the common carotid and distal internal carotid arteries undergo axial, unidirectional flow, while the region within the carotid sinus undergoes boundary layer separation, helical flow, and reverse flow. Finally, within coronary arteries, disturbed flow patterns have been observed along the outer walls of bifurcations, while the inner walls remained generally exposed to unidirectional flow [25]. Comparison of the results of these hemodynamic investigations with the localization of early atherosclerotic lesions has suggested that lesion development correlates with regions of low or oscillatory wall shear stress, boundary layer separation, and/or flow reversal.

A relatively small number of *in vivo* studies of the flow and wall shear stress fields have been reported in the literature. Noninvasive pulsed Doppler [26] and magnetic resonance [27] measurements of velocity profiles have been made in peripheral arteries; however, the level of detail that can be resolved remains limited at this point. There have been several studies with invasive pulsed Doppler ultrasound in dogs, and these studies have shed some light on the arterial velocity profiles *in vivo.* For example, Farthing and Peronneau [28] studied the velocity profiles at several locations in the aortic arch at various points within the cardiac cycle and estimated wall shear stresses. Hutchison *et al.* [29] studied the flow patterns in the dog abdominal aorta and reported regions of transient flow recirculation opposite the superior mesenteric and left renal arteries in the post-systolic phase of the cardiac cycle. No recirculation was observed at peak systole although the velocity profiles were asymmetric. Bell *et al.* [30] examined the velocity profiles in the left cicumflex and left

anterior descending coronary arteries and consistently observed higher wall shear rates along the outer walls than along the inner walls.

The objective of this paper is to obtain quantitative information on the details of the flow field in the rabbit abdominal aorta *in vivo* using pulsed Doppler ultrasound velocimetry. In this preliminary study, we have concentrated exclusively on the region of the aorta between the celiac and superior mesenteric arteries because the ventral (i.e. anterior) wall within this region has previously been shown to reproducibly exhibit a streak of focal enhanced permeability sites to low density lipoprotein and other macromolecules [31]. The dorsal wall within this region is generally free of the enhanced permeability sites. It is desired to investigate whether or not this preferred localization has its basis in details of the *in vivo* flow field.

6.2 Materials and Methods

6.2.1 Flow Rate Measurement System

The system used for measuring the *in vivo* velocity profiles in the rabbit abdominal aorta is a high resolution pulsed Doppler ultrasound velocimeter and associated perivascular probes [32]. The velocimeter has a transmission frequency of 15 MHz, and a pulse repetition frequency of 60 kHz. The quoted spatial resolution of the system is 0.1 mm. The uniqueness of this system lies in the design of the probes each of which is equipped with two transducers. Each transducer is oriented at an angle of approximately 60° relative to the bulk flow direction. This double-transducer probe design permits the measurement of both the axial and transverse components of the velocity vector within the measurement volume [33,34]. Commercially available pulsed Doppler systems are equipped with single-transducer probes which measure only the component of the velocity parallel to the ultrasound beam. Each

transducer has a diameter of 2 mm, and the center-to-center distance between the two transducers is 5 mm. The total width of each probe, i.e. the two transducers and their support bracket, is 8 mm.

The details of pulsed Doppler ultrasound velocimetry can be found elsewhere [35,36], but the basic principle is that the two ferro-electric transducers are successively activated by a series of ultrasound pulses. These pulses penetrate the vessel and are partially reflected by the various objects within their paths, namely the vessel walls and the cells within the bloodstream. Between pulses, each transducer acts as a receiver for the reflected signals. An electronic gate is used to specify the distance from the transducer of a measurement volume within which data are collected, so that the radial position or depth sampled within the vessel is known. The Doppler frequency shift of the recorded reflected signal is proportional to the fluid velocity within the measurement volume. The generation of a velocity profile within a vessel thus consists of scanning the entire depth of the vessel along the ultrasonic beam by electronically displacing the measurement volume from the near wall to the far wall in successive intervals (i.e. at various radial positions) and measuring the Doppler frequency at each radial position. This process is followed for each of the two transducers, and the measurements from the two transducers are combined to yield the axial and transverse components of the velocity vector. One fundamental assumption made in using this technique is that the fluid velocity does not change appreciably over the separation distance between the two transducers.

6.2.2 Animal Experiments

6.2.2.1 Animal Preparation

Five specific pathogen-free male, New Zealand White rabbits Hra:(NZW) SPF, *Onyctolagus Cunniculus* (Hazleton Research Products, Inc., Denver, PA) ranging in weight from 2.6 to 3.8 kg were used. The rabbits were individually housed in stainless steel cages (24"x30"x17"), fed a commercial rabbit diet (Purina Rabbit Chow HF5326, Ralston Purina Company, St. Louis, MO) and water *ad libitum,* and maintained in a controlled environment of 68-72 °F, relative humidity of 40-65%, and 12 hours light/12 hours dark. Ventilation was 100% fresh air with 12 complete room air changes per hour. Initial anesthesia was induced by the intramuscular injection of 50 mg/kg ketamine and 10 mg/kg xylazine. After the rabbit lost consciousness, both ears were shaved. A 24 ga catheter (2 in Intracath, Deseret Pharmaceutical Co., Sandy, VT) was inserted through one of the marginal ear veins of the left ear, and a 22 ga catheter (2 in Intracath, Deseret Pharmaceutical Co., Sandy, VT) was inserted through the central artery of the right ear. Both catheters were secured in place with tape and tightly capped. The animal was then intubated with an uncuffed endotracheal tube (3 mm internal diameter) which was inserted approximately 4 cm into the trachea. The ventral surface of the rabbit was shaved, prepped with 70% isopropyl alcohol, and secured with limb ties in dorsal recumbancy. The ear vein catheter was then connected to a bag of warm, sterile lactated Ringer's solution positioned about 100 cm above the operating table that provided continuous fluid administration averaging 10 ml/kg/hr throughout the experiment. The ear artery catheter was connected to a pressure transducer (Statham Gould P231D, Gould Inc., Medical Products Division, Oxnard, CA) and monitor (Statham Gould Model SP14053, Gould Inc.) for continuous blood pressure monitoring. Animals were maintained on circulating hot water

heating pads (37.8 °C). ECG electrodes connected to the animal's four limbs provided continuous monitoring of heart rate.

6.2.2.2 Surgical Procedures

All procedures described here were reviewed and approved by the Committee on Animal Care at MIT. The intubation tube was connected to a respirator providing oxygen at about 1.5 liters/min. The respirator delivered a tidal volume of 25-50 ml of oxygen containing 0.5 to 2% isoflurane at 30 breaths per minute. Attempts were made to maintain heart rate and blood pressure constant by decreasing the administration rate of isoflurane and increasing the rate of lactated Ringer's solution infusion in response to decreased heart rate and blood pressure.

A ventral midline laperotomy was performed. The abdominal contents were retracted to the rabbit's left side and maintained moist by covering them with saline-soaked gauze. The portion of the abdominal aorta between the celiac and superior mesenteric arteries was isolated with a combination of blunt and sharp dissections, as were lengths of the celiac and superior mesenteric arteries.

6.2.2.3 Velocity Profile Measurements

Within the aortic segment between the celiac and superior mesenteric arteries, velocity profiles have been recorded at three different axial positions: a short distance distal to the celiac artery, a point about halfway between the two branches, and a short distance proximal to the superior mesenteric artery. Figure 6.1 illustrates how the velocity profile measurements in the abdominal aorta at each of these three locations are made. Two probes, 1 and 2 in the figure, are used, each for a different position. Probe 1 is placed along the

ventral surface of the aorta, and it measures the velocity profile along the midplane of the vessel from the ventral to the dorsal walls. Probe 2 is positioned along the right lateral wall of the aorta, and it measures the velocity profile in the midplane connecting the right lateral to the left lateral walls. Each probe contains two transducers, and information from both transducers is combined to yield the axial and transverse components of the velocity vectors along the two orthogonal planes of measurement. The sign convention for each probe is that velocity is positive in the direction away from the probe and negative in the direction toward the probe.

The probes are actually not mounted on the aortic wall. Rather, they are mounted on a mechanical micromanipulator which allows great flexibility in accurately positioning the probes and which avoids any problems that may result from the probes being in direct contact with the aorta. An acoustic couplant (aquasonic gel) was used to ensure that the ultrasound beam travels continuously through a medium whose acoustic properties resemble those of animal tissue.

Briefly, the measurement procedure is as follows: the zero baseline and voltage calibration signals are initially recorded. Probe 1 is then positioned along the ventral wall of the aorta, and the positions of the near and far, i.e. anatomical ventral and dorsal, walls are established for each of the two transducers. This is accomplished by adjusting the electronic gate of the velocimeter so that the frequency signal at each wall is virtually zero. The rabbit aorta is a small-diameter vessel; therefore, it is difficult to ascertain that the probe positioning is exactly along the midplane of the vessel. In order to verify this positioning, the micromanipulator is used to displace the probe laterally in small intervals, and at each interval the positions of the near and far walls are recorded using the electronic gate. The position corresponding to

the maximum value of the distance between the two walls, i.e. the diameter of the aorta, is taken as the midplane position. Once the positions of the two walls are established for each transducer, the electronic gate is used to progressively displace the measurement volume in small intervals within the vessel lumen until the entire diameter of the aorta is scanned. At each interval, the Doppler frequency is recorded over 15 to 25 cardiac cycles, and these frequencies, after being converted to fluid velocities, then yield the desired profile in the midplane connecting the ventral and dorsal walls. The process is then repeated for probe 2 to construct the velocity profile in the plane connecting the right and left lateral walls.

All data recording was performed automatically using a PC-based data acquisition software (Datalog, National Software, CA) loaded onto an IBM 386-PC. Two recording channels were used: the first recorded the voltages corresponding to the Doppler frequencies, while the second recorded a pulse signal of an ECG trigger which demarcated the beginning of every recorded cardiac cycle. The probe positioning and data recording for each of the two orthogonal positions at each axial location between the celiac and superior mesenteric arteries required about one hour.

Following completion of the measurements, the animal was euthanized with an overdose (about 3 ml) of sodium pentobarbital (6 g/ml, Lemmon Co., Sellersville, PA) injected either into the marginal ear vein catheter. The animal died immediately.

6.3 Results

6.3.1 Straight Tube Velocity Profiles

A number of control experiments were performed to validate the performance of the pulsed Doppler system. We studied steady, fully

developed flow in a straight tube. Polyethylene tubing with an inner diameter of about 4.2 mm was used in these experiments. Steady flow was imposed using a small tubing pump. The working fluid was water seeded with starch which acted as the reflecting medium for the ultrasound pulses. The flow rate tested was 420 ml/min which corresponds to a flow Reynolds number of about 2100 (assuming the viscosity of water is unchanged by the added starch). The measurements were made at an axial position 18 cm (about 43 tube diameters) downstream of the tube entrance, so that the flow was fully developed [37]. Both probes 1 and 2 were used to measure the velocity profiles in two orthogonal midplanes of the tube.

Figure 6.2 illustrates the probe 1 axial and transverse velocity profiles within the tube. The axial velocity profile is nearly parabolic, the shape that would be expected for steady, laminar, fully developed flow in a straight tube. The transverse velocity profile exhibits no systematic structure, and the transverse velocities are small relative to the axial velocities (peak transverse velocity is about 13% of the peak axial velocity) indicating the presence of predominantly axial flow with limited secondary flow motion. The small secondary flow components may have been caused by electronic noise in the measurement system, by small-scale disturbances in the flow field induced by the pump's inability to deliver perfectly steady flow, or by the flow Reynolds number being close to transition to turbulence.

Figure 6.3 illustrates the probe 2 axial and transverse velocity profiles in the straight tube. The peak transverse velocity is about 7% of the peak axial velocity, and the same general conclusions described in the case of the probe 1 profiles apply in this case.

6.3.2 Abdominal Aorta Velocity Profiles

The velocity profiles in the abdominal aortas of five rabbits have been studied in this preliminary effort. As has already been mentioned, we have chosen to focus our attention on the region of the abdominal aorta between the celiac and superior mesenteric arteries. We have measured the *in vivo* velocity profiles in two orthogonal midplanes at three axial positions within the region of interest: shortly distal to the celiac artery, midway between the celiac and superior mesenteric arteries, and shortly proximal to the superior mesenteric artery.

Figure 6.4 illustrates typical probe 1 axial and transverse velocity profiles within the aorta shortly distal to the celiac artery as a function of time for a single "average" cardiac cycle. The profiles actually represent data averaged over 16 cardiac cycles, and 28 separate time points were recorded within each cycle. Data have been acquired at 13 radial positions within the vessel lumen (in addition to the two wall data points). The peak axial velocity is reached at the 9th time point, and the axial profiles demonstrate that the flow is skewed towards the ventral wall of the aorta during a portion of the cardiac cycle. The axial velocities are positive throughout the cardiac cycle indicating that the flow in the midplane connecting the ventral and dorsal walls is in the forward direction throughout the cycle with no regions of flow recirculation along either wall.

The transverse velocity profiles indicate that the transverse velocities are relatively large; the peak transverse velocity is about 25% of the peak axial velocity. This indicates significant secondary flow motion within the flow field. Moreover, at the beginning of the cardiac cycle and until the 7th recorded time point (corresponding to one-fourth of the cardiac cycle), the transverse velocity has a negative value along the entire midplane connecting the ventral and

dorsal walls of the aorta indicating the presence of secondary flow motion directed towards the ventral wall (since the sign convention, as has already been described, is positive in the direction away from the probe and negative toward it). At the 8th time point, the transverse velocity becomes positive within a small distance near the ventral wall but remains negative along most of the midplane. This indicates secondary flow motion near the ventral wall that is directed toward the dorsal wall, while the secondary flow motion throughout the remainder of the midplane remains directed toward the ventral wall. The extent of the region of positive transverse velocity increases with time until it spans the entire midplane at about the 19th time point and remains so until the end of the cycle although its magnitude progressively decreases until it disappears completely at the end of the cycle before becoming negative again at the start of the next cycle.

Figure 6.5 illustrates typical probe 2 axial and transverse velocity profiles within the aorta shortly distal to the celiac artery as a function of time for a single "average" cardiac cycle (average of 16 recorded cycles). 28 time points have been recorded within the course of each cycle, and measurements have been made at 15 radial positions within the vessel lumen (in addition to the two wall measurements). The peak axial velocity is attained at the 12th time point. The axial velocity profiles are skewed towards the right lateral wall during a large portion of the cycle, and, as in the case of the probe 1 data, the axial velocities are always positive indicating forward flow in the midplane connecting the right and left lateral walls of the aorta.

The transverse velocities are once again relatively large (maximum transverse velocity is 16% of the maximum axial velocity) indicating the existence of extensive helical motion. The transverse velocity is negative along the entire midplane at the beginning of the cycle indicating secondary

flow motion directed toward the right lateral wall. This continues to be the case until the 9th time point when the transverse velocity remains negative near the right lateral wall but becomes positive near the left lateral wall. This behavior continues until the 12th time point when the transverse velocity becomes positive throughout the entire midplane thereby indicating secondary flow directed toward the left lateral wall. The transverse velocity remains fully positive until the 24th time point when it becomes positive near the right wall and negative near the left wall and remains so until the end of the cycle at which point it disappears completely before becoming fully negative to begin the next cycle.

The combination of the transverse velocity data from both probes leads to complex secondary flow behavior within the vessel cross-section during the course of a cycle. Figure 6.6 illustrates vessel cross-sections at four time points within the cycle along with the directions of the transverse velocities measured in the two orthogonal midplanes at those time points. Also shown are the simplest flow patterns within the vessel cross-section that are consistent with the measured midplane information. The results indicate the presence of multiple cells of vortical motion within the aorta, and the exact structure of this vortical flow behavior undergoes several changes within the course of a single cardiac cycle. Given that the axial velocities are in the forward direction throughout the course of the cycle, the secondary flow results represent forward-moving helical zones. The four time points displayed in Figure 6.6 represent selected points at which the flow field is most structured. Intermediate time points may include additional zones of helical motion as the flow undergoes transition from one of the structures shown in Figure 6.6 to a subsequent one.

Figures 6.7 and 6.8 depict respectively the probe 1 and probe 2 axial and transverse velocity profiles within the abdominal aorta midway between the celiac and superior mesenteric arteries. The probe 1 data are the average of 15 cycles with 30 time points per cycle, while the probe 2 data are the average of 16 cycles with 28 time points per cycle. Measurements have been made at 12 radial points within the vessel lumen (in addition to the two wall data points) for both probes 1 and 2. Generally similar observations are made at this location to those at the region shortly distal to the celiac artery. In particular, the axial velocities in the two orthogonal midplanes measured are in the forward direction throughout the course of the cardiac cycle, and the transverse velocities are large indicating extensive secondary flow motion. The details of the transverse velocity behavior are somewhat different than those discussed in the region shortly distal to the celiac artery, and the helical motion structures consistent with the specific results are illustrated in Figure 6.9. Finally, Figures 6.10 and 6.11 illustrate the probe 1 and probe 2 axial and transverse velocity profiles during the course of a cardiac cycle shortly proximal to the superior mesenteric artery. The probe 1 data represent the average of 19 cycles with 28 time points per cycle, while the probe 2 data are the average of 24 cycles with 22 time points per cycle. Probe 1 measurements have been made at 14 radial positions within the vessel lumen (in addition to the two wall data points), while the probe two measurements have been made at 12 radial positions (in addition to the two wall data points). The general conclusions are similar to the other two cases, and the structures depicting the flow field helical motion at selected time points are shown in Figure 6.12.

Figures 6.13, 6.14, and 6.15 illustrate the *in vivo* wall axial shear stress as a function of time during the course of a cardiac cycle at the ventral, dorsal, right lateral, and left lateral walls at the three axial measurement locations

between the celiac and superior mesenteric arteries. In these computations, the shear rate at each wall is computed as the slope of a straight line connecting the measured velocity at the wall to that at the point within the bloodstream closest to the wall, and the blood viscosity is assumed constant at 4 cP. The results indicate that the axial shear stresses to which the four walls are exposed are not significantly different in magnitude or overall behavior. The shear stresses generally increase as the flow accelerates, and then decrease as the flow decelerates. The ventral wall shear stress may be smaller or larger than that at the dorsal wall, and the right lateral wall shear stress may likewise be smaller or larger than the left lateral wall shear stress. Therefore, no generalizations regarding relative magnitudes can be made. As has already been mentioned, enhanced permeability sites in the region between the celiac and superior mesenteric arteries consistently localize along the ventral wall of the aorta. The lack of a clear distinction in axial wall shear stress behavior between the ventral and dorsal walls indicates that no correlation can be drawn at this point between the axial wall shear stress behavior and enhanced permeability site localization.

The existence of prominent transverse velocity components suggests the presence of significant circumferential shear stresses. These, however, cannot be directly inferred from the current measurements.

In addition to the measurements in the abdominal aorta, the velocity profiles within the superior mesenteric artery of one rabbit was studied. The axial and transverse velocity profiles in the superior mesenteric artery as a function of time are illustrated in Figure 6.16. The most interesting feature of the axial velocity profiles is that they become negative for a small portion of diastole. This indicates reverse flow from the superior mesenteric artery into the aorta. This reverse flow will have important implications on the wall shear

stress in the aorta in the immediate vicinity of the superior mesenteric artery. Although the preliminary data reported here on branch flow reversal are limited, they are supportive of previous observations we have made in studies of *in vivo* flow rates in the rabbit aortic branches using transit-time ultrasound flowmetry [38]. The relatively large transverse velocities within the superior mesenteric artery are consistent with the presence of extensive helical motion within the branch. This is also in agreement with previous results we have obtained in flow visualization studies in rabbit aortas that had been rendered transparent [39].

6.4 Discussion

The study reported here is the first known investigation of *in vivo* velocity profiles in the rabbit aorta. This represents important information in trying to understand the physiological aortic flow field and how it may relate to the localization of enhanced permeability sites and early atherosclerotic lesions. We have used a high resolution pulsed Doppler ultrasound system to measure the velocity profiles in two orthogonal midplanes at three locations within the abdominal aortas of five rabbits in the regions between the celiac and superior mesenteric arteries. The uniqueness of the system used here lies in the design of the perivascular probes each of which is equipped with two ultrasonic transducers. The combination of recorded information from both transducers allows the deduction of both the axial and transverse velocities in the plane of measurement. Commercially available systems permit the measurement of only the axial component of the velocity vector.

The axial velocity results have consistently revealed the presence of forward flow in the aortic segment under investigation throughout the course of the cardiac cycle. The axial velocity profiles are occasionally skewed towards

one of the aortic walls. Relatively large transverse velocities have been measured in the aortas of all five rabbits indicating the presence of extensive secondary flow motion. The transverse velocity information from the two orthogonal planes of measurement at each site is consistent with the existence of multiple zones of forrward-moving helical motion within the aortic cross-section. The exact structure of this motion changes significantly within the course of a single cardiac cycle. Specific helical zones appear at particular points within the cycle, grow with flow acceleration until they reach a maximum size after which they begin decreasing in size and eventually disappear entirely.

Axial wall shear stresses have been computed along the ventral, dorsal, right lateral, and left lateral walls of the aorta as a function of time. No clear differences in axial shear stress behavior is observed among the four aortic walls. Furthermore, the relative magnitudes of the shear stresses depend on the specific portion of the pulsatile cycle investigated. The extensive helical motion in the aorta in all likelihood leads to significant circumferential wall shear stresses, but these shear stresses could not be measured in this study.

It should be noted that the magnitudes of the axial wall shear stress measured here are significantly smaller than those obtained from steady flow visualization studies previously performed in rabbit aortas that had been made transparent while the peak velocities are comparable [39]. It is well-established that Doppler velocimetry measurements are least accurate very close to the aortic wall. As the vessel lumen is scanned by the electronic displacement of the measurement volume in order to construct the velocity profile, the situation is frequently encountered near the vessel wall that the measurement volume straddles both fluid and wall so that the measurements become muddled. The wall motion adds further noise to the recorded signals.

Unfortunately, it is precisely the near-wall fluid mechanical conditions that are believed to be relevant in investigating a potential role for hemodynamics in atherogenesis. Therefore, the shear stresses reported here are considered questionable. Further system validation experiments on well-behaved flows in straight tubes should be performed before confidence is established in the *in vivo* wall shear stress levels.

The axial and transverse velocity profiles within the superior mesenteric artery of one rabbit were measured, and the preliminary results revealed the presence of extensive helical motion within the superior mesenteric artery as well as the occurrence of reverse flow from the branch back into the aorta during a portion of diastole. This reverse flow is expected to have a significant effect on the shear stress to which the aortic wall is exposed during the course of a cardiac cycle.

The segment of the abdominal aorta between the celiac and superior mesenteric arteries has been selected for these initial studies because the ventral wall within this region is a site of localization of early atherosclerotic lesions experimentally induced in hypercholesterolemic rabbits [40]. Moreover, in the normocholesterolemic rabbit, this region reproducibly exhibits predilection for the occurrence of focal sites of enhanced macromolecular permeability [31]. The dorsal wall within this region is invariably spared of similar localization. The finding of no clear differences in the magnitudes or the temporal gradients of axial shear stresses between the ventral and dorsal walls suggests that, if hemodynamics play a role in the localization of early lesions, then it may be the circumferential components of the wall shear stress that may be most relevant.

Although no previous data have been reported on the rabbit, there exist limited data on the *in vivo* flow field in the dog abdominal aorta. Hutchison *et*

al. [29] used pulsed Doppler ultrasound velocimetry to measure the axial velocity profiles in the dog abdominal aorta shortly distal to the superior mesenteric and left renal arteries. They reported the existence of flow recirculation in diastole along the walls opposite to the branches. No flow recirculation was observed during systole although the velocity profiles were asymmetric. Moore *et al.* [21] and Pedersen *et al.* [22] performed dye injection flow visualization studies of the steady and pulsatile flow fields in models of the human aorta and reported complex vortical flow behavior. No quantitative information on the magnitudes and exact nature of the transverse velocities were reported. Thiriet *et al.* [41] performed three-dimensional steady flow finite element simulations of the flow field in a model of the aortic bifurcation and observed prominent secondary flow motion within the two iliac branches. Our results indicate that this secondary flow motion is also prominent in the rabbit aorta *in vivo,* and our measurement technique allows the quantitation of the transverse velocity components within the planes of measurement.

In addition to measurement inaccuracy near the wall, a limitation of the measurements reported here is the difficulty of making measurements in the immediate vicinity of branches. Okano and Yoshida [42] have reported significant endothelial cell shape differences distal to the rabbit brachiocephalic and left subclavian arteries over length scales of 100-200 μm. Although the probes used here are relatively miniature and are mounted on a micromanipulator, it remains very difficult to make accurate measurements within such small length scales. It is believed that the results here provide an understanding of the macroscopic structure of the *in vivo* aortic flow field, and this would then need to be combined with more microscopic studies to investigate very localized phenomena. Finally, the measurements reported here were made on two orthogonal midplanes in the aorta. The inference of

the entire three-dimensional flow field from sparse two-plane data is both difficult and inaccurate; therefore, data in additional orthogonal planes at each measurement site are desirable. Efforts in this direction are currently underway.

6.5 References

1. Schwartz CJ, Mitchell JRA. Observations on localizations of arterial plaques. *Circ. Res.* **11**: 63, 1972.

2. Spain DM. Atherosclerosis. *Scientific American.* **215**: 48, 1966.

3. Nerem RM. Vascular fluid mechanics, the arterial wall, and atherosclerosis. *J. Biomech. Eng.* **114**: 274, 1992.

4. Nerem RM, Levesque MJ. Fluid dynamics as a factor in the localization of atherogenesis. *Annals of the New York Academy of Science.* **416**: 719, 1983.

5. Fry DL. Acute vascular endothelial changes associated with increased blood velocity gradients. *Circ. Res.* **22**: 165, 1968.

6. Caro CG, Fitzgerald JM, Schroter RC. Arterial wall shear and distribution of early atheroma in man. *Nature.* **223:** 1159, 1969.

7. Texon M. *Hemodynamic Basis of Atherosclerosis.* Washington: Hemisphere Publishing Corp., 1980.

8. Fox JA, Hugh AE. Localization of atheroma: A theory based on boundary layer separation. *Br. Heart J.* **28**: 388, 1966.

9. Wesolowski SA, Fries CC, Sabini AM, Sawyer PN. The significance of turbulence in hemic systems and in the distribution of the atherosclerotic lesion. *Surgery.* **57**: 155, 1965.

10. Stehbens WE. Hemodynamics and atherosclerosis. *Biorheology.* **19**: 95, 1982.

11. Gosling RG, Newman DL, Bowden NLR, Twinn KW. The area ratio of normal aortic junctions: aortic configuration and pulse-wave reflection. *Brit. J. Radiol.* **44**: 850, 1971.

12. Goode TS, Davies PF, Reidy MA, Bowyer DE. Aortic endothelial cell morphology observed *in situ* by scanning electron microscopy during atherogenesis in the rabbit. *Atherosclerosis.* **27**: 235, 1977.

13. Massop DW, Wright JG, Smead WL, Sadoun ET, Cornhill JF. Interleukin-6 production by human aortic endothelial cells is regulated by shear stress. *Arteriosclerosis.* **10**: 760a, 1990.

14. Malek A, Izumo S. Physiological fluid shear stress causes downregulation of endothelin-1 mRNA in bovine aortic endothelium. *Am. J. Physiol.* **263** (Cell Physiol. 32): C389, 1992.

15. Frangos JA, Eskin SG, McIntyre LV, Ives CL. Flow effects on prostacyclin production by cultured human endothelial cells. *Science.* **227**: 1477, 1989.

16. Dewey CF, Bussolari SR, Gimbrone MA, Davies PF. The dynamic response of vascular endothelial cells to fluid shear stress. *J Biomech. Eng.* **103**: 177, 1981.

17. Davies PF, Remuzzi A, Gordon EJ, Dewey CF, Gimbrone MA. Turbulent fluid shear stress induces vascular endothelial turnover in vitro. *Proc. Natl. Acad. Sci. USA.* **83**: 2114, 1986.

18. Davies PF. Mechanical sensing mechanisms: Shear stress and endothelial cells. *J. Vasc.Surg.* **13**: 729-731,1991.

19. Wick TM, Doty SD, Nerem RM. Influence of fluid mechanical stresses on vascular cell adhesion. *Biomedical Transport Processes,* NY: Plenum Press, pp.283-292, 1990.

20. Davies PF, Tripathi SC. Mechanical stress mechanisms and the cell: An endothelial paradigm. *Circ. Res.* **72**: 239-245, 1993.

21. Moore JE, Ku DN, Zarins CK, Glagov S. Pulsatile flow visualization in the abdominal aorta under differing physiologic conditions: Implications for increased susceptibility to atherosclerosis. *J. Biomech. Eng.* **114**: 391, 1991.

22. Pedersen EM, Yoganathan AP, Lefebvre XP. Pulsatile flow visualization in a model of the human abdominal aorta and aortic bifurcations. *J. Biomechanics.* **25**: 935, 1992.

23. Ku DN, Giddens DP. Pulsatile flow in a model carotid bifurcation. *Arteriosclerosis.* **3**: 31, 1983.

24. Zarins CK, Giddens DP, Bharadvaj BK, Sottiurai VS, Mabon RF, Glagov S. Carotid bifurcation atherosclerosis: Quantitative correlation of plaque localization with flow velocity profiles and wall shear stress. *Circ. Res.* **53**: 502, 1983.

25. Asakura T, Karino T. Flow patterns and spatial distribution of atherosclerotic lesions in human coronary arteries. *Circ. Res.* **66**: 1045, 1990.

26. Simon AC, Levenson J, Flaud P. Pulsatile flow and oscillating wall shear stress in the brachial artery of normotensive and hypertensive subjects. *Cardiovascular Res.* **24**: 129, 1990.

27. Moore JE, Ku DN. Wall shear stress measurements in model abdominal aorta using magnetic resonance imaging. *ASME BED Advances in Bioengineering.* **20**: 375, 1991.

28. Farthing S, Peronneau P. Flow in thoracic aorta. *Cardiovascular Res.* **13**: 607, 1979.

29. Hutchison KJ, Karpinski E, Campbell JD, Potemkowski AP. Aortic velocity contours at abdominal branches in anesthetized dogs. *J. Biomechanics.* **21**: 277, 1988.

30. Bell DR, Sabbah HN, Stein PD. Profiles of velocity in coronary arteries of dogs indicate lower shear rate along inner arterial curvature. *Arteriosclerosis.* **9**: 167, 1989.

31 Barakat AI, Uhthoff PAF, Colton CK. Topographical mapping of sites of enhanced HRP permeability in the normal rabbit aorta. *J. Biomech. Eng.* **114**: 283, 1992.

32. Delouche A, Dimicoli JL, Peronneau P. In vitro study of modifications of blood flow patterns induced by a bifurcation. *Biorheology.* **22**: 55, 1985.

33. Peronneau P. *Analyse de l'ecoulement sanguin dans les gros vaisseaux par methode ultrasonore.* These Science Nat. Universite de Paris, 1977.

34. Peronneau P, Nakache M. Relationship between hydrodynamic forces and vascular wall phenomena - I. Measurement of parietal friction by pulse type Doppler velocimeter. *Biorheology.* **16**: 257, 1979.

35. Baker DW. Pulsed ultrasonic doppler blood flow sensing. *I. E .E. E. Trans. Sonics Ultrason..* **17**: 170, 1970.

36. Peronneau P, Delouche A, Bui-Mong-Hung, Hinglais J. Debitmetrie sanguine par ultrasons. Developpement et applications experimentales. *Eur. Surg. Res.* **1**: 147, 1969.

37. Bejan A. *Convection heat transfer.* John Wiley and Sons, NY, 1984.

38. Barakat AI, Marini RP, Colton CK. Measurement of flowrates through aortic branches in the rabbit in vivo. (Manuscript in preparation).

39. Barakat AI, Colton CK. Detailed flow pattern in the transparent rabbit aorta. (Manuscript in preparation).

40. Schwenke DC, Carew TE. Quantification in vivo of increased LDL content and rate of LDL degradation in normal rabbit aorta occuring at

sites susceptible to early atherosclerotic lesions. *Circ. Res.* **62**: 699, 1988.

41. Thiriet M, Pares C, Saltel E, Hecht F. Numerical simulations of steady flow in a model of the aortic bifurcation. *J. Biomech. Eng.* **114**: 40, 1992.

42. Okano M, Yoshida Y. Endothelial cell morphometry of atherosclerotic lesions and flow profiles at aortic bifurcations in cholesterol fed rabbits. *J. Biomech. Eng.* **114**: 301, 1992.

Figure Captions

Figure 6.1 Method of velocity measurement in two orthogonal midplanes of the aorta. Two probes (1 and 2), each equipped with two transducers, are used. Data from the two transducers are combined to yield both axial and transverse velocity components.

Figure 6.2 Probe 1 axial and transverse velocity profiles for steady, fully developed flow in a straignt polyethylene tube.

Figure 6.3 Probe 2 axial and transverse velocity profiles for steady, fully developed flow in a straignt polyethylene tube.

Figure 6.4 Position 1 (corresponding to probe 1) axial and transverse velocity profiles as a function of time during the course of a cardiac cycle in the rabbit abdominal aorta shortly distal to the celiac artery. "V" refers to the ventral wall of the aorta and "D" to the dorsal wall.

Figure 6.5 Position 2 (corresponding to probe 2) axial and transverse velocity profiles as a function of time during the course of a cardiac cycle in the rabbit abdominal aorta shortly distal to the celiac artery. "R" refers to the right lateral wall of the aorta and "L" to the left lateral wall.

Figure 6.6 Aortic cross-sections indicating directions of transverse velocities in the two orthogonal measurement midplanes at selected time points within the cardiac cycle shortly distal to the celiac artery. Also shown are helical flow patterns consistent with the measured transverse velocities.

Figure 6.7 Position 1 (corresponding to probe 1) axial and transverse velocity profiles as a function of time during the course of a cardiac cycle in the rabbit abdominal aorta midway between the celiac and superior mesenteric arteries. "V" refers to the ventral wall of the aorta and "D" to the dorsal wall.

Figure 6.8 Position 2 (corresponding to probe 2) axial and transverse velocity profiles as a function of time during the course of a cardiac cycle in the rabbit abdominal aorta midway between the celiac and superior mesenteric arteries. "R" refers to the right lateral wall of the aorta and "L" to the left lateral wall.

Figure 6.9 Aortic cross-sections indicating directions of transverse velocities in the two orthogonal measurement midplanes at selected time points within the cardiac cycle midway between the celiac and superior mesenteric arteries . Also shown are helical flow patterns consistent with the measured transverse velocities.

Figure 6.10 Position 1 (corresponding to probe 1) axial and transverse velocity profiles as a function of time during the course of a cardiac cycle in the rabbit abdominal aorta shortly proximal to the superior mesenteric artery. "V" refers to the ventral wall of the aorta and "D" to the dorsal wall.

Figure 6.11 Position 2 (corresponding to probe 2) axial and transverse velocity profiles as a function of time during the course of a cardiac cycle in the rabbit abdominal aorta shortly proximal to the superior mesenteric artery. "R" refers to the right lateral wall of the aorta and "L" to the left lateral wall.

Figure 6.12 Aortic cross-sections indicating directions of transverse velocities in the two orthogonal measurement midplanes at selected time points within the cardiac cycle shortly proximal to the superior mesenteric artery. Also shown are helical flow patterns consistent with the measured transverse velocities.

Figure 6.13 Axial velocity shear stresses at the ventral, dorsal, right lateral, and left lateral aortic walls shortly distal to celiac artery as a function of time during the course of a cardiac cycle.

Figure 6.14 Axial velocity shear stresses at the ventral, dorsal, right lateral, and left lateral aortic walls midway between the celiac and superior mesenteric arteris as a function of time during the course of a cardiac cycle.

Figure 6.15 Axial velocity shear stresses at the ventral, dorsal, right lateral, and left lateral aortic walls shortly proximal to superior mesenteric artery as a function of time during the course of a cardiac cycle.

Figure 6.16 Axial and transverse velocity profiles in the superior mesenteric artery. Note that the axial velocity becomes negative during a portion of diastole indicating reverse flow from the branch into the aorta.

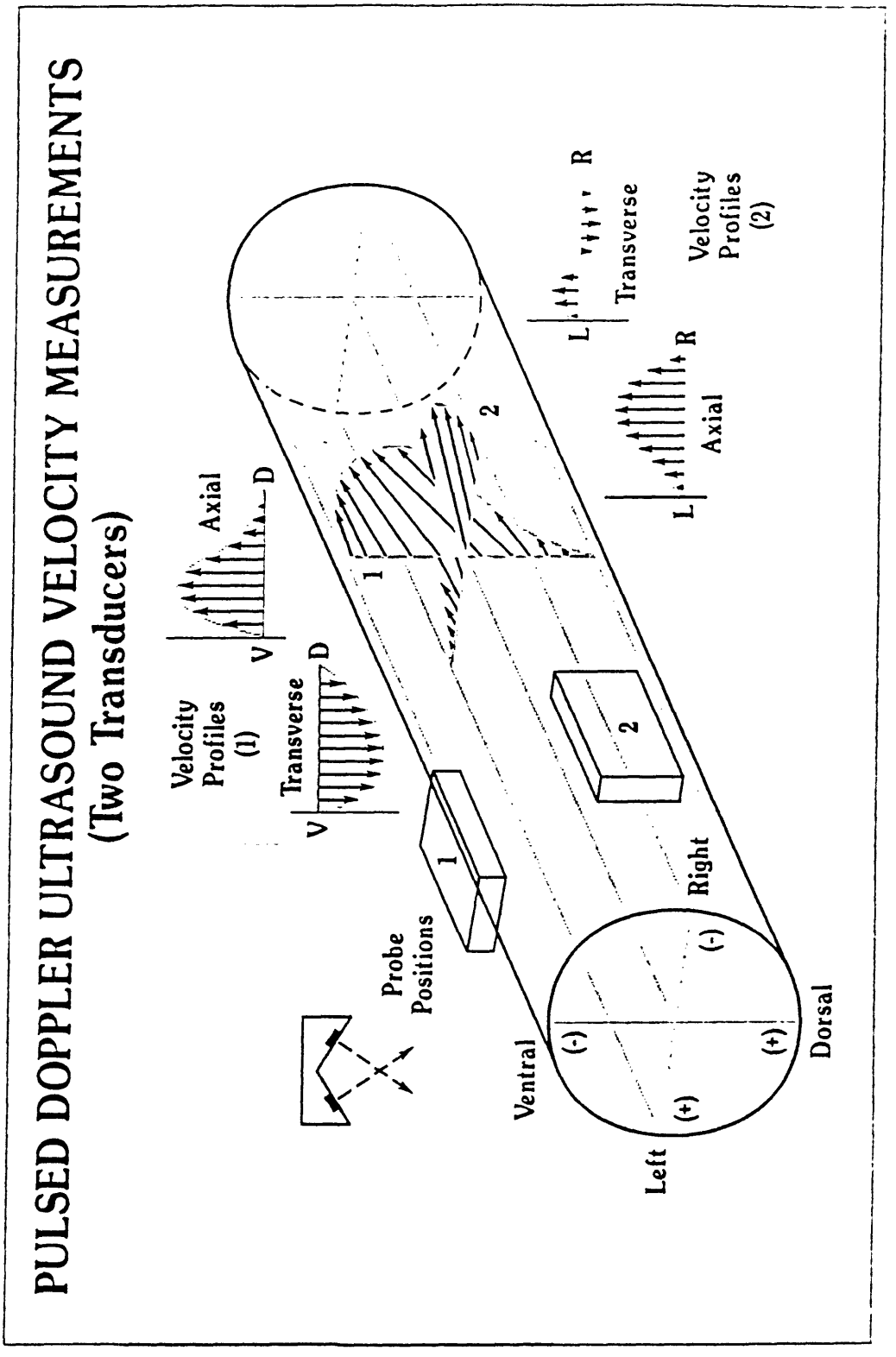
PULSED DOPPLER ULTRASOUND VELOCITY MEASUREMENTS
(Two Transducers)
Velocity Profiles (1)
Axial
V
D
Transverse
V
D
Probe Positions
1
2
Ventral
Dorsal
Left
Right
(-)
(+)
(+)
(-)
L
R
Axial
L
R
Transverse
Velocity Profiles (2)

Figure 6.1

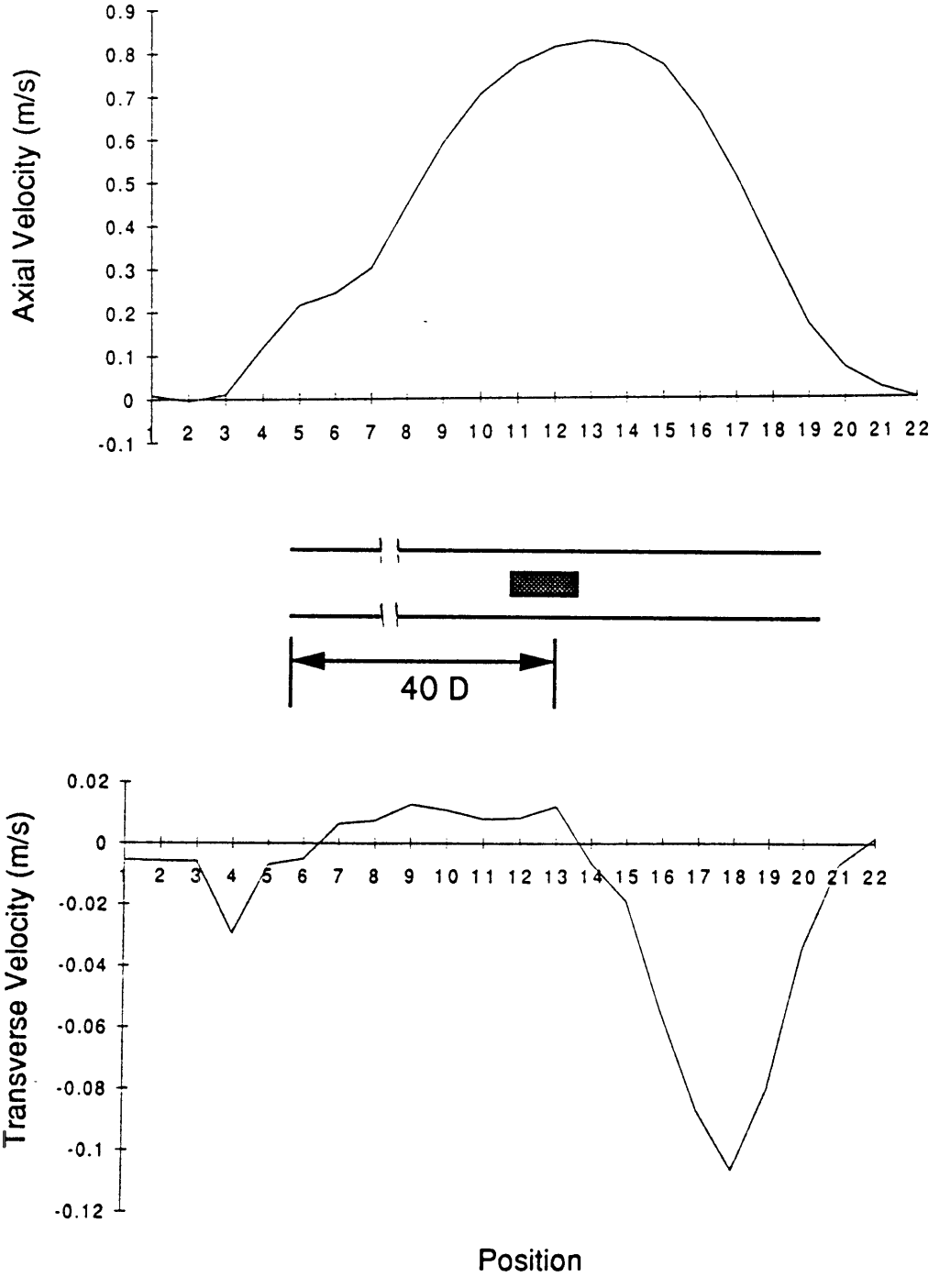
Axial Velocity (m/s)
0.9
0.8
0.7
0.6
0.5
0.4
0.3
0.2
0.1
0
-0.1
1 2 3 4 5 6 7 8 9 10 11 12 13 14 15 16 17 18 19 20 21 22
40 D
Transverse Velocity (m/s)
0.02
0
-0.02
-0.04
-0.06
-0.08
-0.1
-0.12
1 2 3 4 5 6 7 8 9 10 11 12 13 14 15 16 17 18 19 20 21 22
Position

Figure 6.2

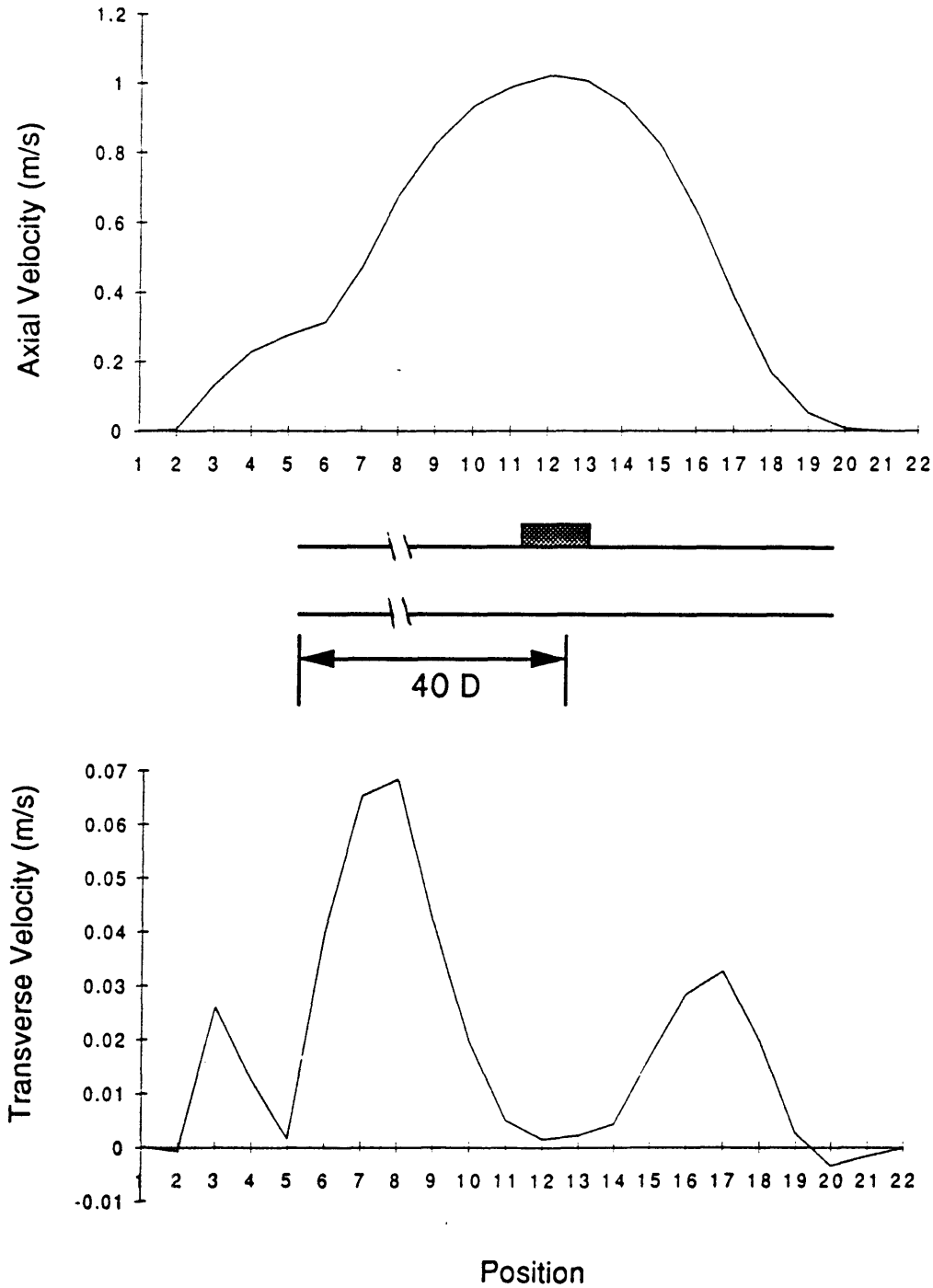
Axial Velocity (m/s)
1.2
1
0.8
0.6
0.4
0.2
0
1 2 3 4 5 6 7 8 9 10 11 12 13 14 15 16 17 18 19 20 21 22
40 D
Transverse Velocity (m/s)
0.07
0.06
0.05
0.04
0.03
0.02
0.01
0
-0.01
1 2 3 4 5 6 7 8 9 10 11 12 13 14 15 16 17 18 19 20 21 22
Position

Figure 6.3

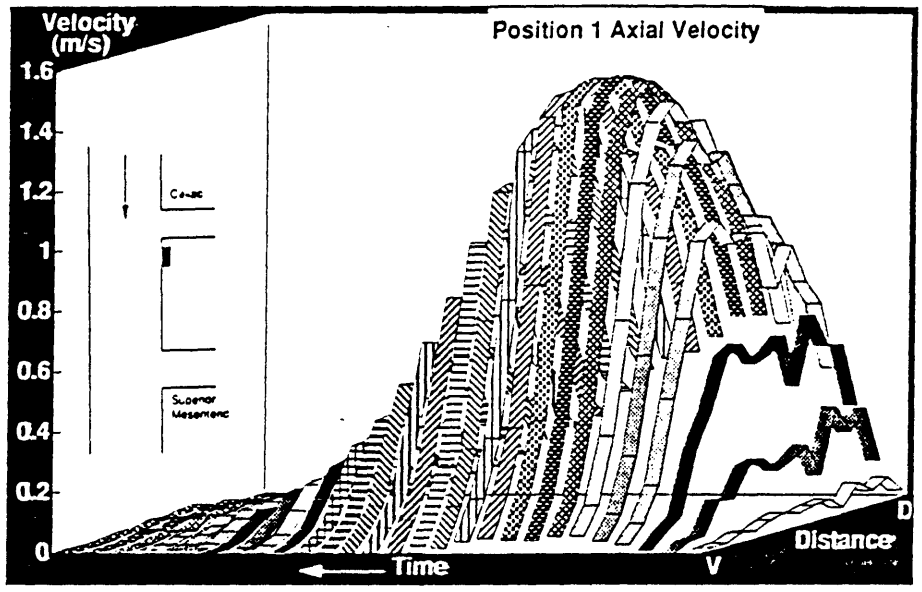
Velocity (m/s)
Position 1 Axial Velocity
1.6
1.4
1.2
1
0.8
0.6
0.4
0.2
0
Time
V
D
Distance

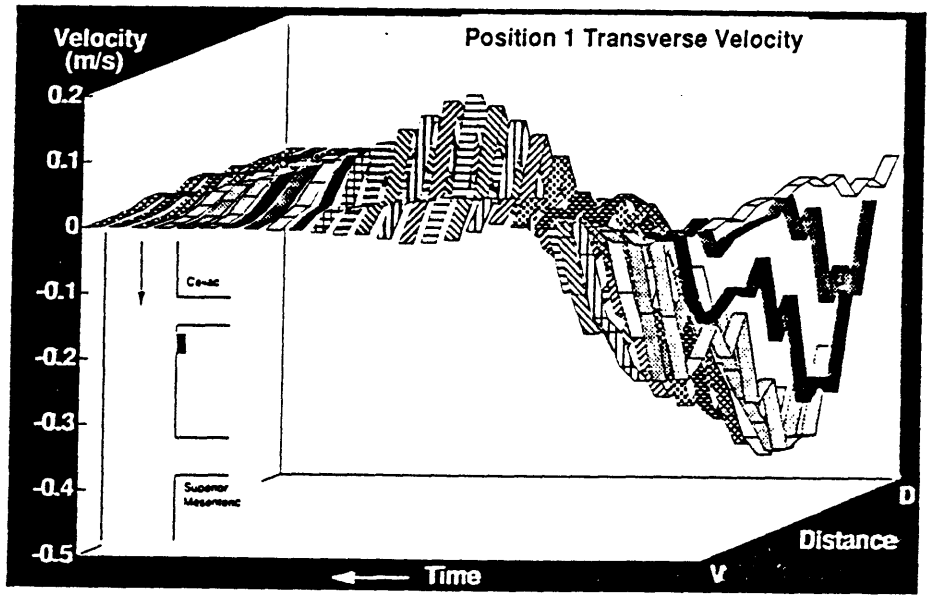
Velocity (m/s)
Position 1 Transverse Velocity
0.2
0.1
0
-0.1
-0.2
-0.3
-0.4
-0.5
Time
V
D
Distance

Figure 6.4

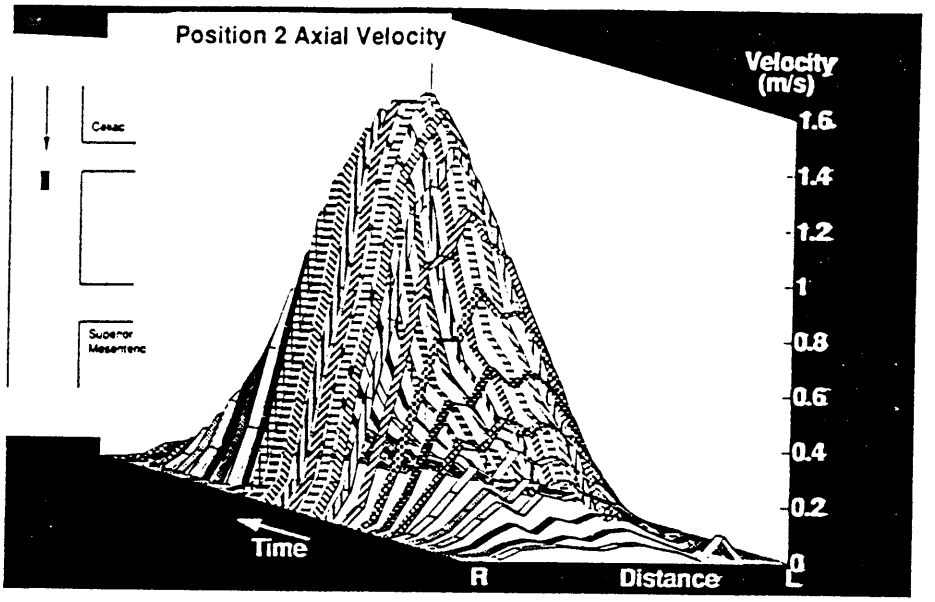
Position 2 Axial Velocity
Velocity (m/s)
1.6
1.4
1.2
1
0.8
0.6
0.4
0.2
0
Time
R
Distance
L

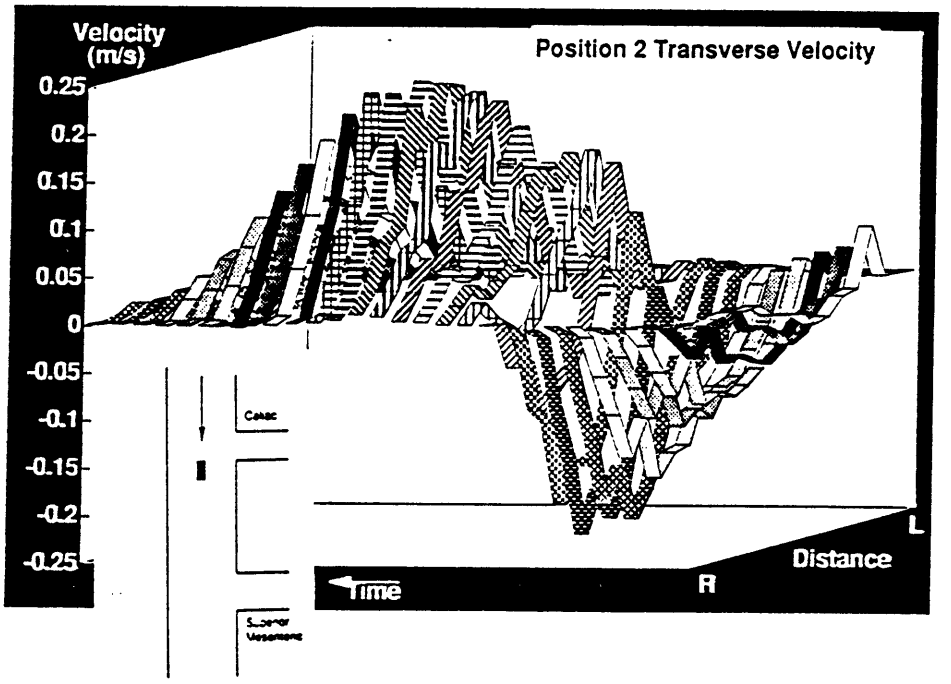
Velocity (m/s)
Position 2 Transverse Velocity
0.25
0.2
0.15
0.1
0.05
0
-0.05
-0.1
-0.15
-0.2
-0.25
Time
R
Distance
L

Figure 6.5

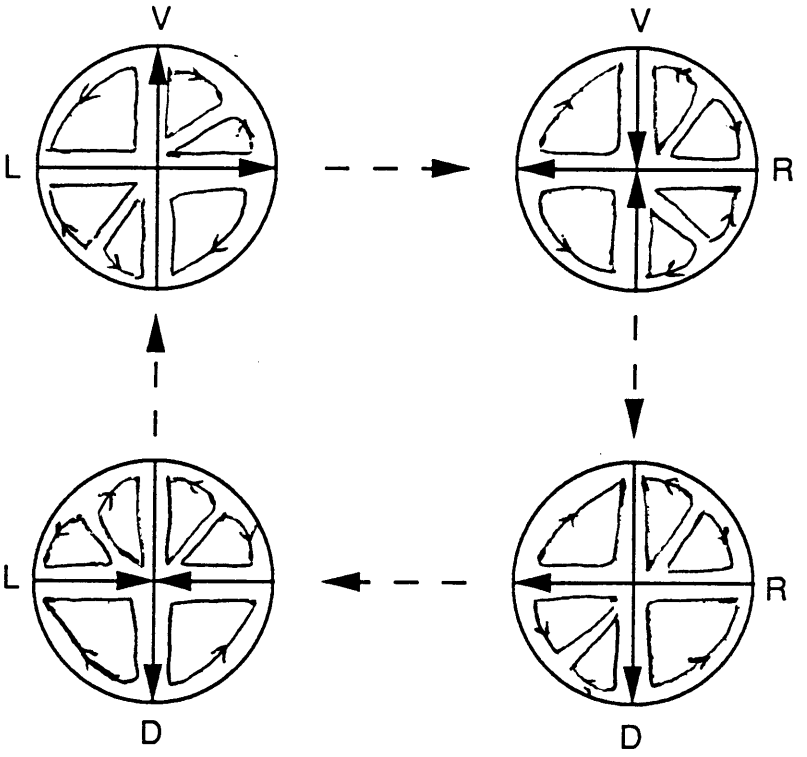

Figure 6.6

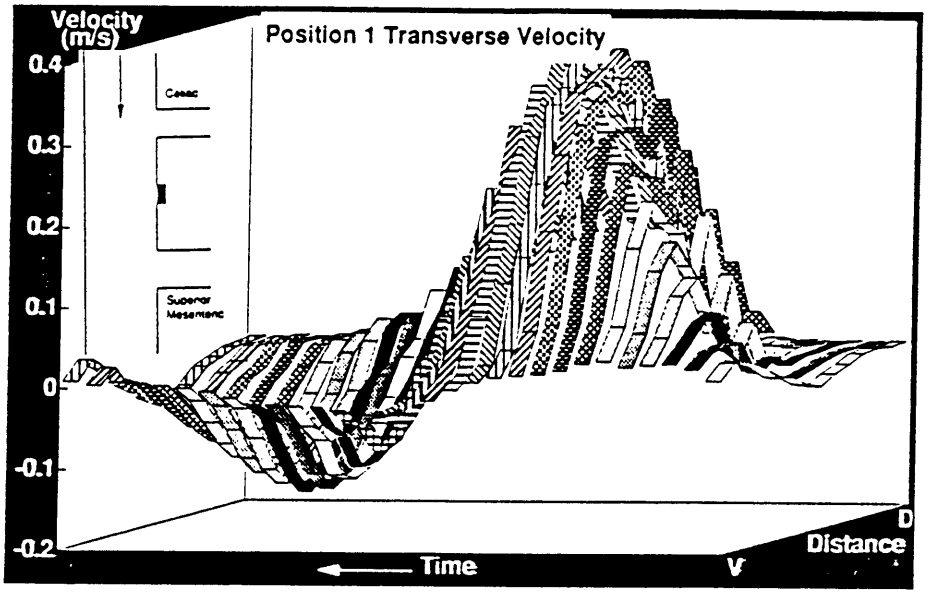
Velocity
(m/s)
Position 1 Transverse Velocity
0.4
0.3
0.2
0.1
0
-0.1
-0.2
Coeac
Superior
Mesenteric
Time
V
D
Distance

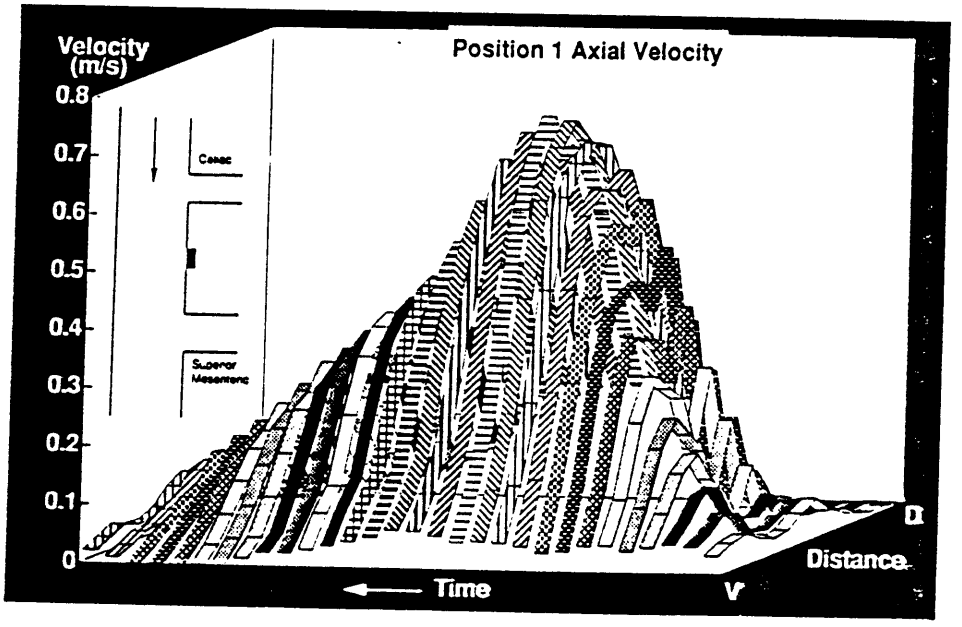
Velocity
(m/s)
Position 1 Axial Velocity
0.8
0.7
0.6
0.5
0.4
0.3
0.2
0.1
0
Coeac
Superior
Mesenteric
Time
V
D
Distance

Figure 6.7

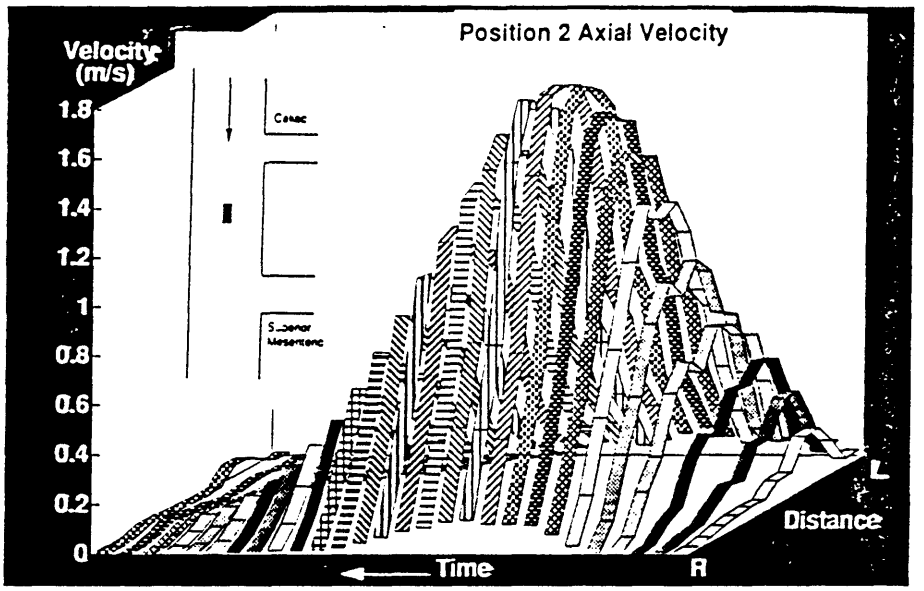
Position 2 Axial Velocity
Velocity (m/s)
1.8
1.6
1.4
1.2
1
0.8
0.6
0.4
0.2
0
Time
R
L
Distance

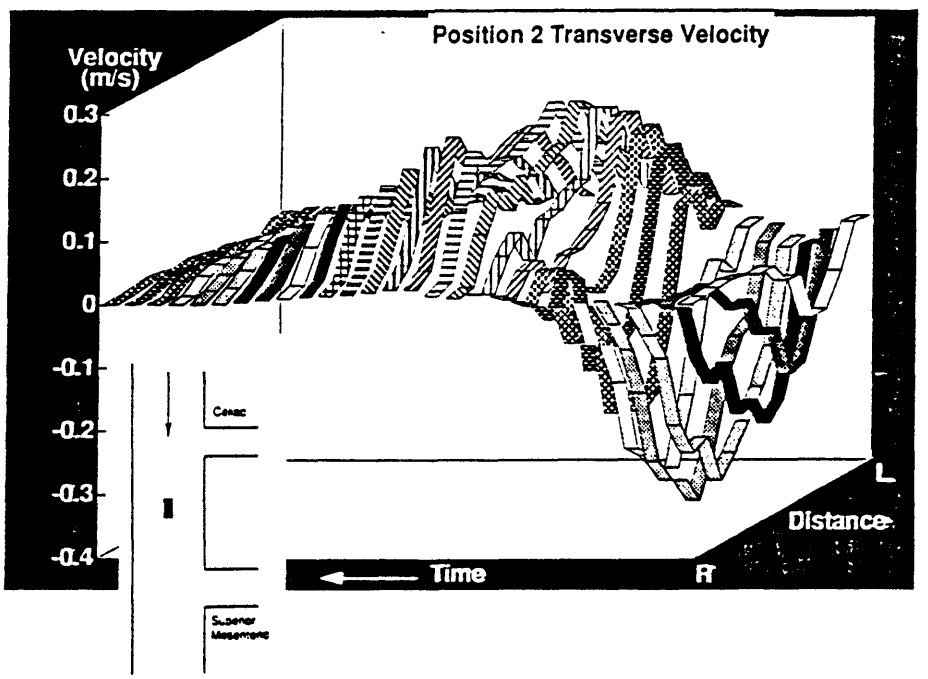
Position 2 Transverse Velocity
Velocity (m/s)
0.3
0.2
0.1
0
-0.1
-0.2
-0.3
-0.4
Time
R
L
Distance

Figure 6.8

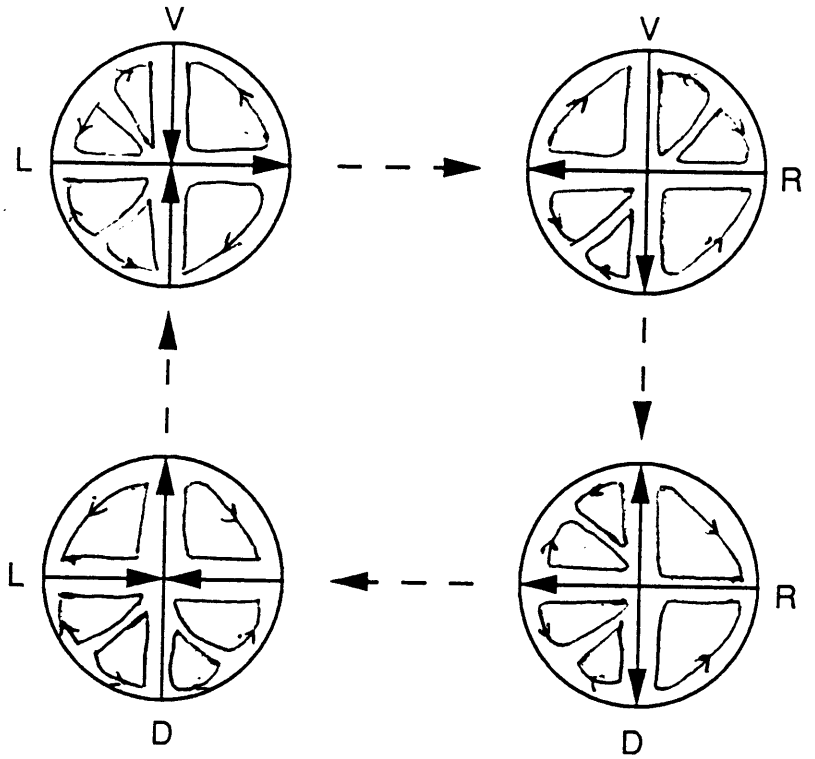

Figure 6.9

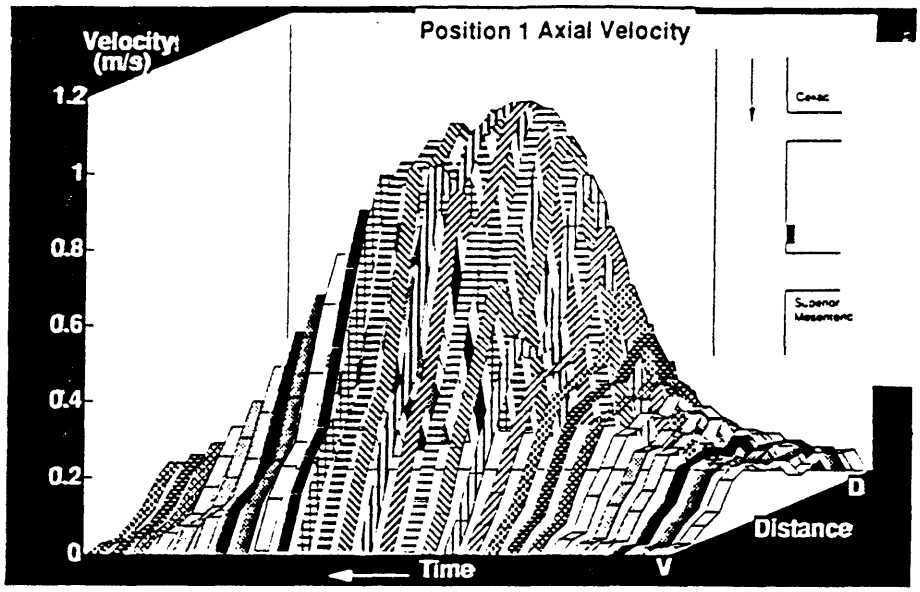
Position 1 Axial Velocity
Velocity (m/s)
1.2
1
0.8
0.6
0.4
0.2
0
Time
V
D
Distance

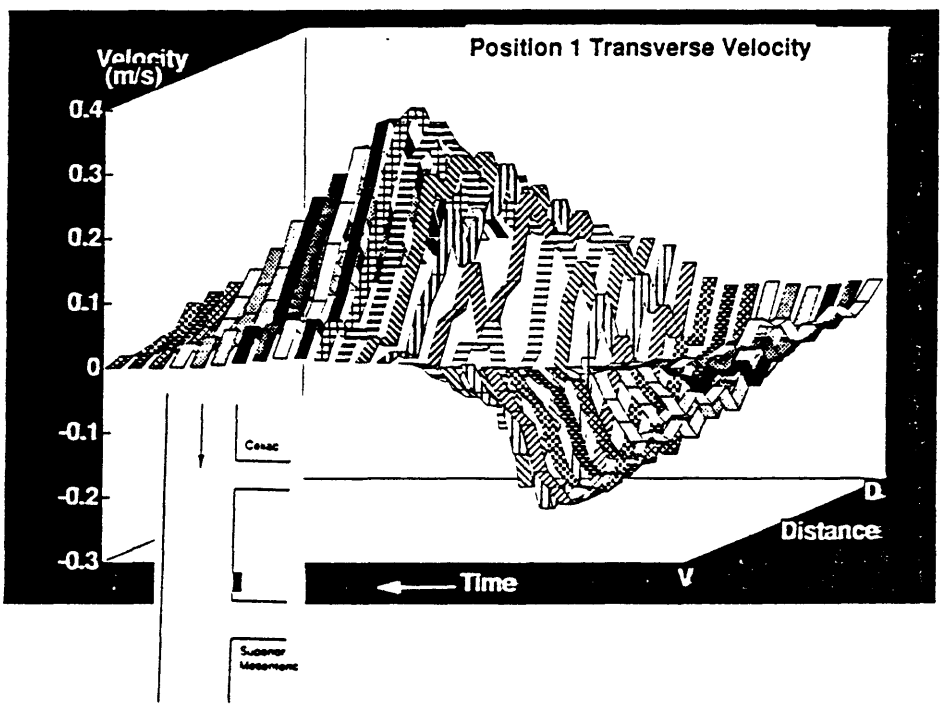
Position 1 Transverse Velocity
Velocity (m/s)
0.4
0.3
0.2
0.1
0
-0.1
-0.2
-0.3
Time
V
D
Distance

Figure 6.10

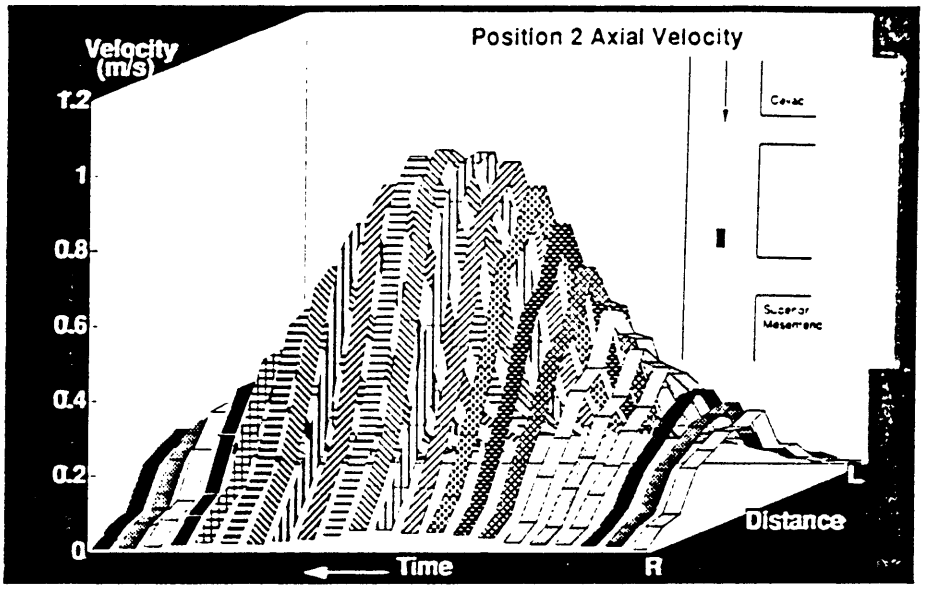
Position 2 Axial Velocity
Velocity (m/s)
1.2
1
0.8
0.6
0.4
0.2
0
Time
R
L
Distance

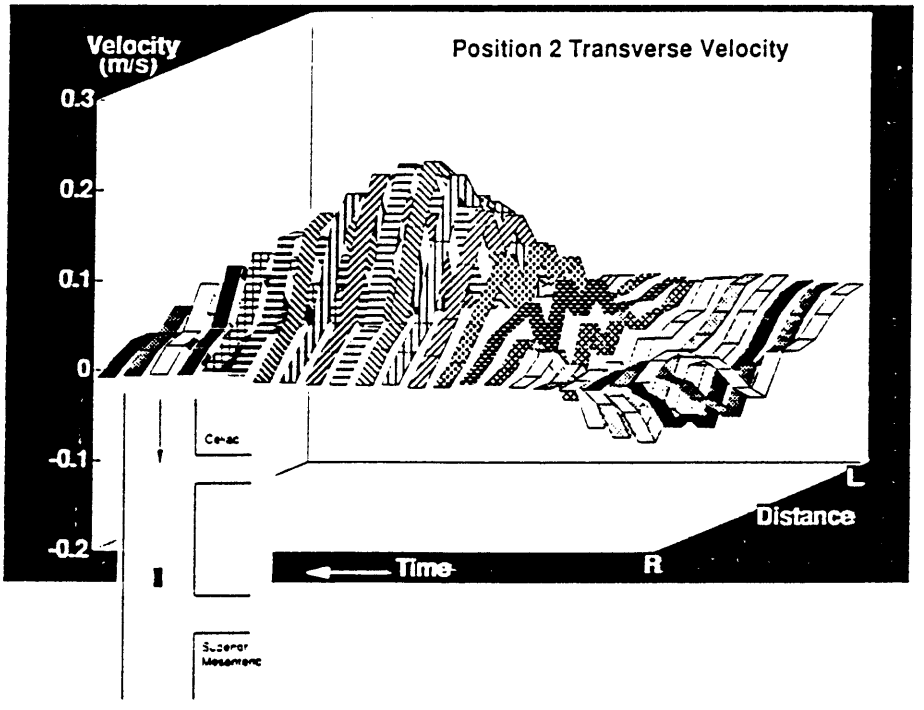
Position 2 Transverse Velocity
Velocity (m/s)
0.3
0.2
0.1
0
-0.1
-0.2
Time
R
L
Distance

Figure 6.11

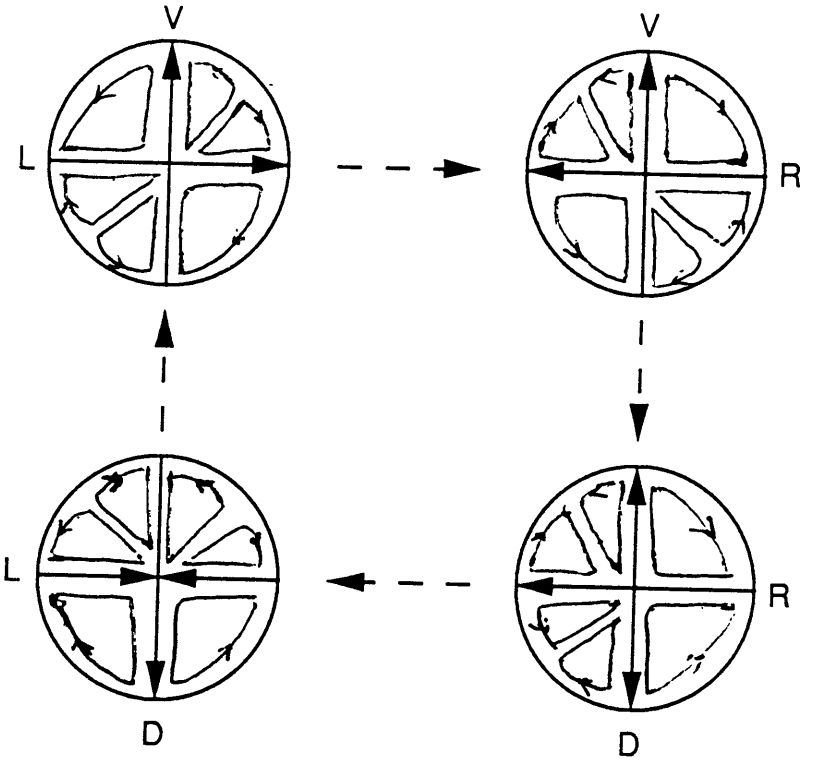

Figure 6.12

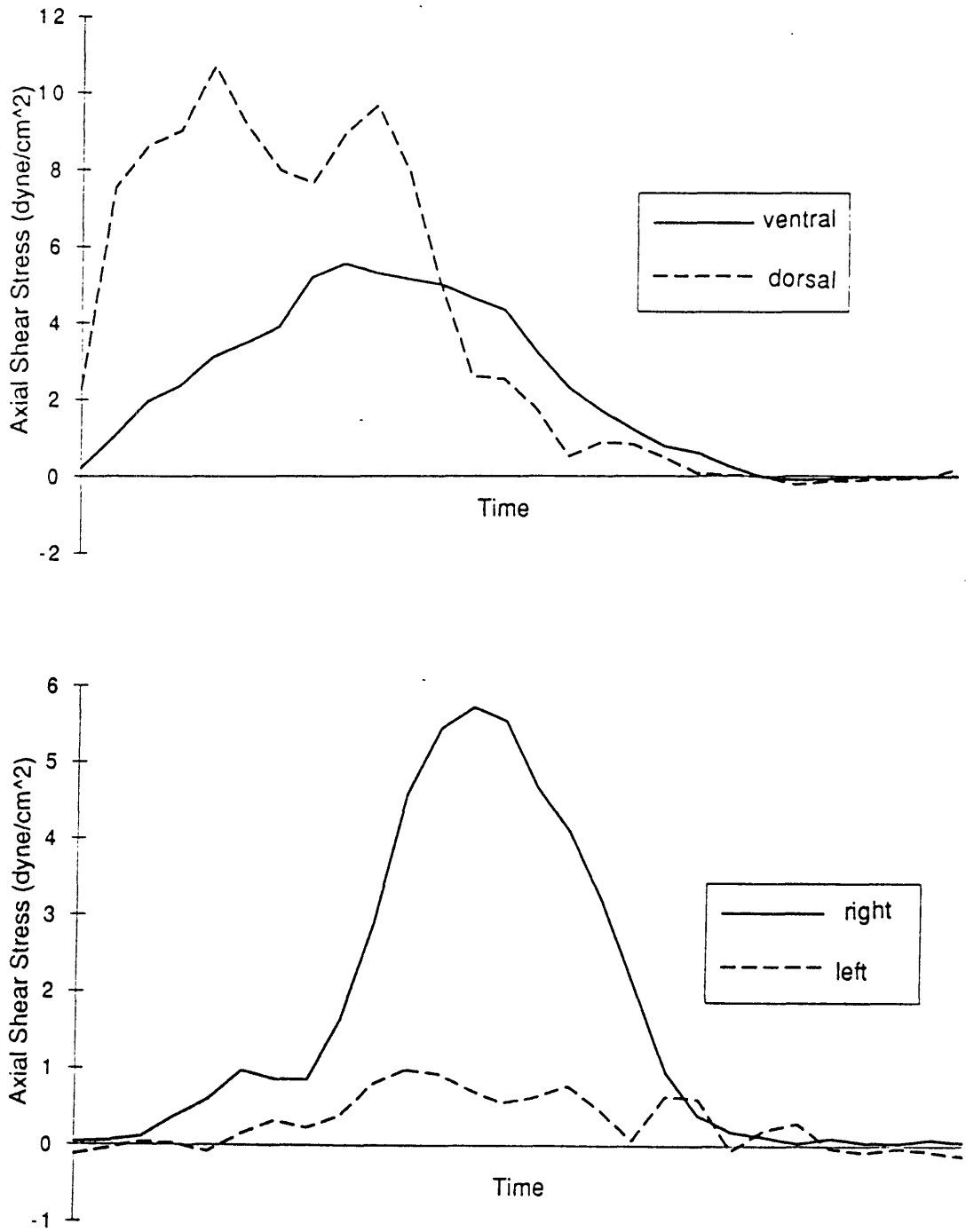
12
10
8
6
4
2
0
-2
Axial Shear Stress (dyne/cm^2)
Time
ventral
dorsal
6
5
4
3
2
1
0
-1
Axial Shear Stress (dyne/cm^2)
Time
right
left

Figure 6.13

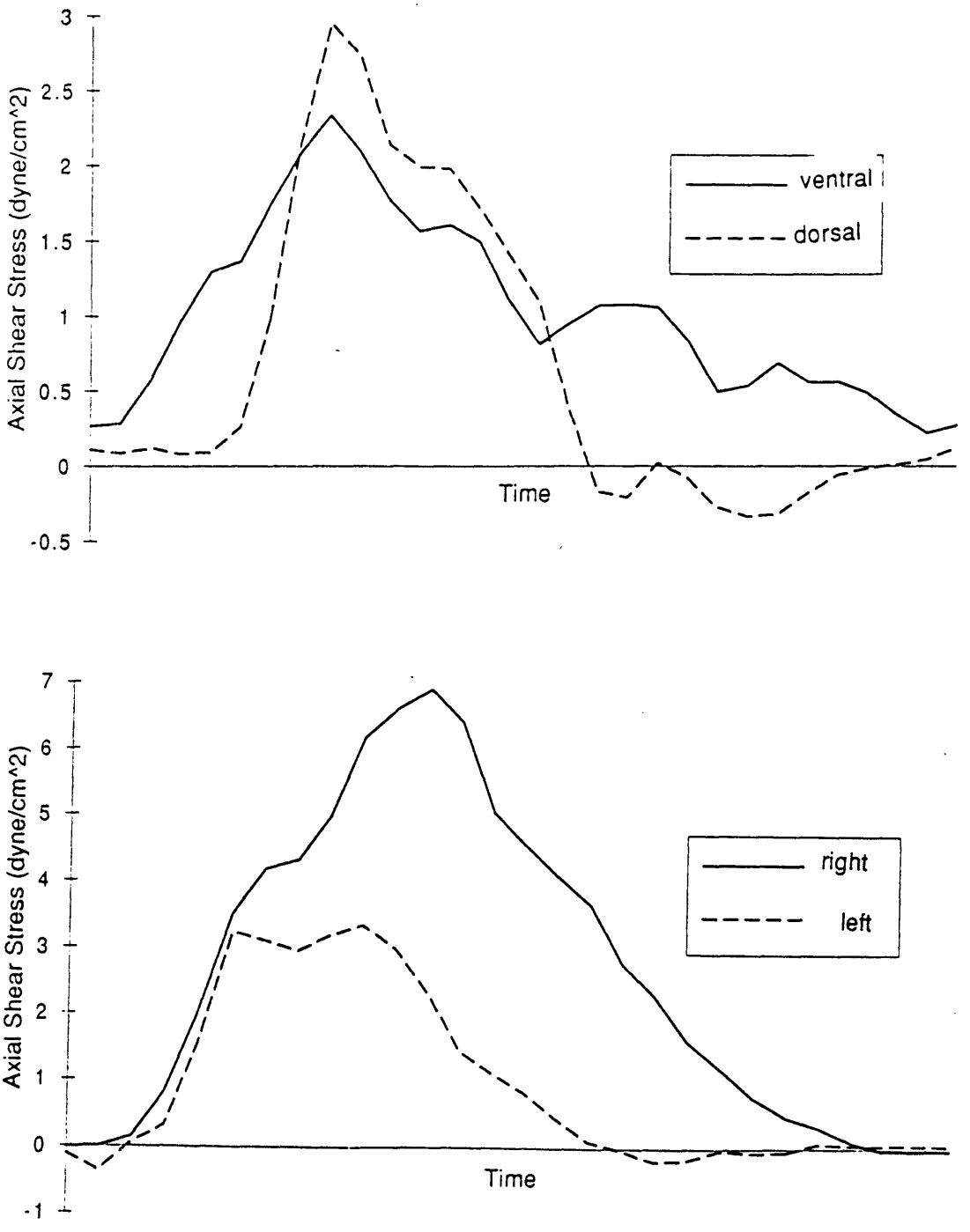
Axial Shear Stress (dyne/cm^2)
3
2.5
2
1.5
1
0.5
0
-0.5
Time
ventral
dorsal
Axial Shear Stress (dyne/cm^2)
7
6
5
4
3
2
1
0
-1
Time
right
left

Figure 6.14

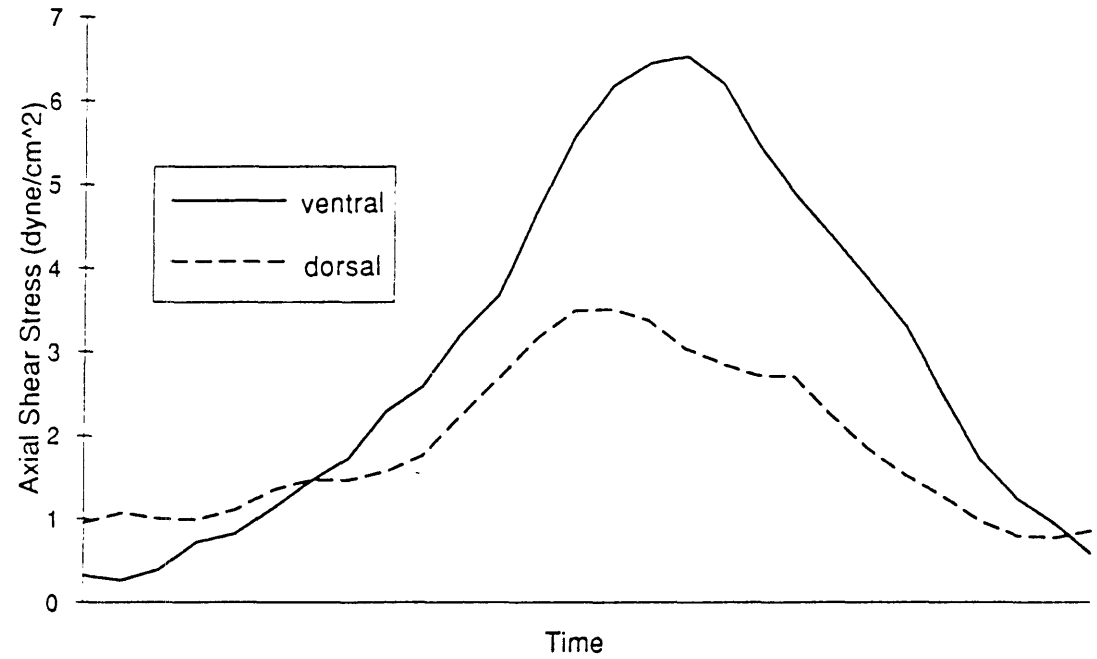
7
6
5
4
3
2
1
0
Axial Shear Stress (dyne/cm^2)
ventral
dorsal
Time

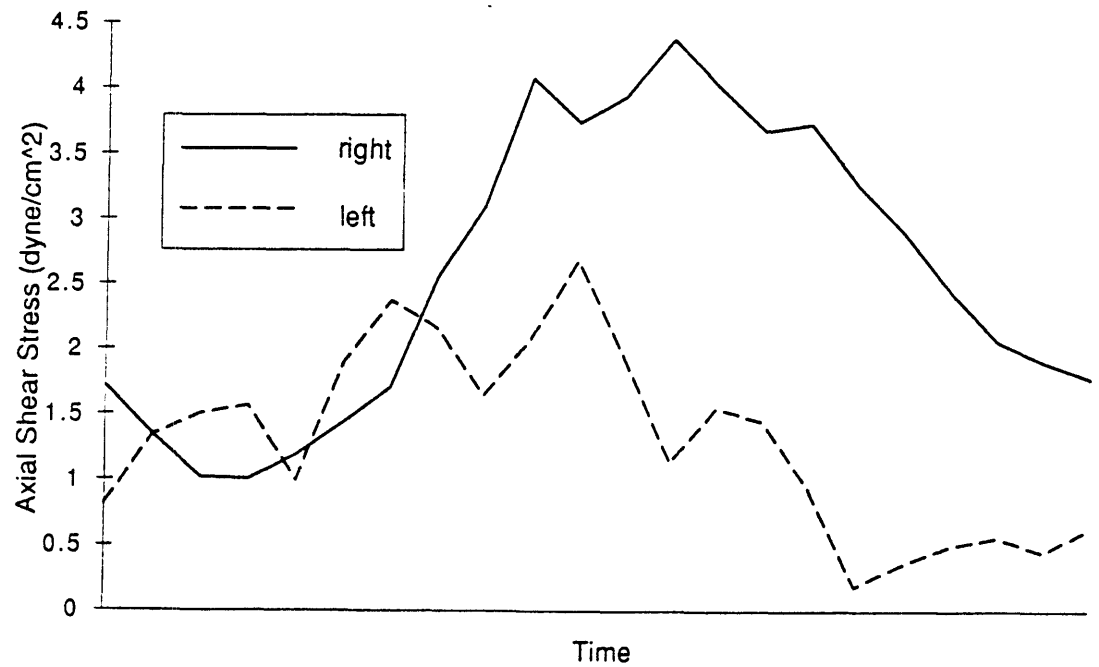
4.5
4
3.5
3
2.5
2
1.5
1
0.5
0
Axial Shear Stress (dyne/cm^2)
right
left
Time

Figure 6.15

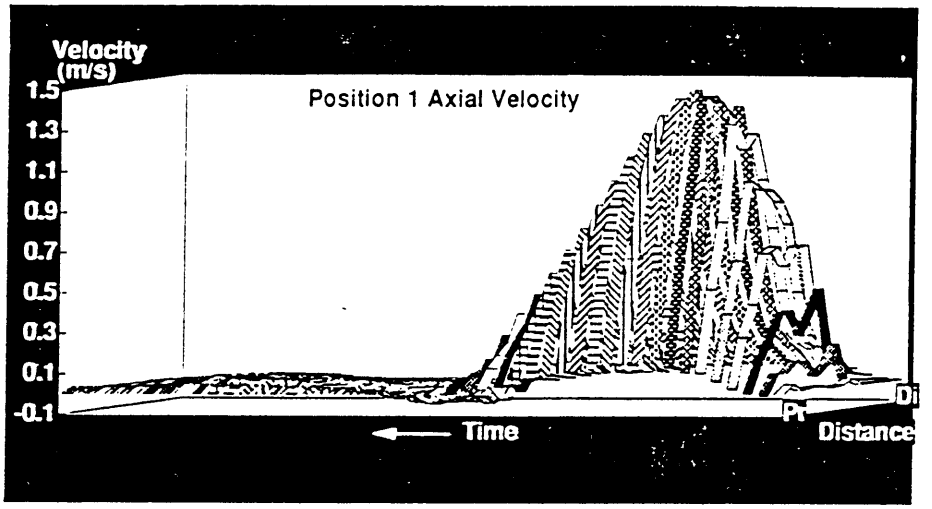
Velocity
(m/s)
1.5
1.3
1.1
0.9
0.7
0.5
0.3
0.1
-0.1
Position 1 Axial Velocity
Time
Pr
Distance

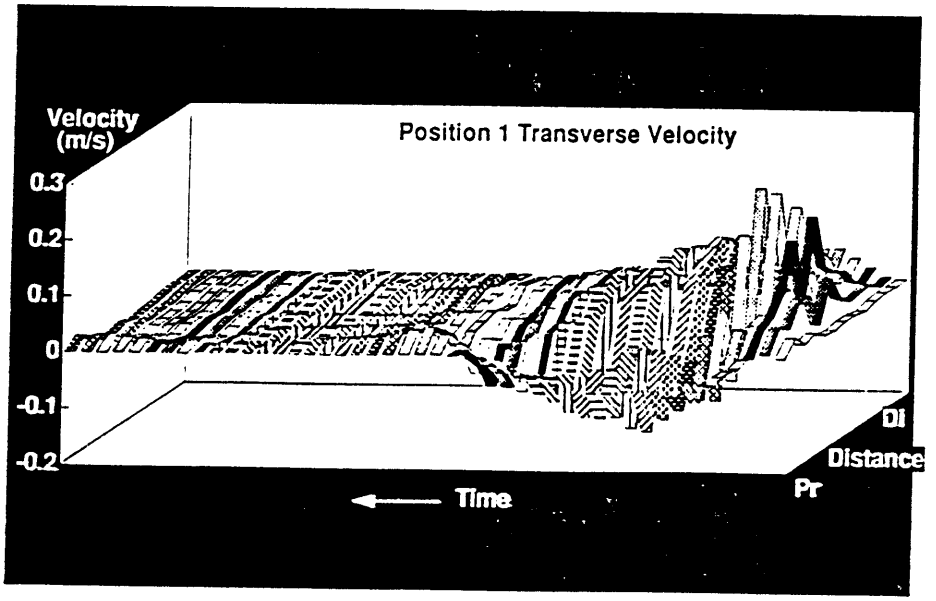
Velocity
(m/s)
0.3
0.2
0.1
0
-0.1
-0.2
Position 1 Transverse Velocity
Time
Pr
Distance

Figure 6.16

Chapter Seven

Conclusions and Recommendations for Future Work

7.1 Conclusions

The focal nature of early atherosclerotic lesions has motivated the notion of the importance of localizing factors including detailed hemodynamics within the affected vessel. Despite a large number of investigations, very few generalizations regarding the potential role of arterial fluid mechanics in atherogenesis can be made at the present time.

The overall objectives of this thesis were to quantitatively establish the topography of sites of enhanced macromolecular permeability previously identified in the normal rabbit aorta, to compare this topography with that of early atherosclerotic lesions experimentally induced in hypercholesterolemic rabbits, and to investigate whether the localization of the enhanced permeability sites is associated with specific features of the macroscopic flow field in the rabbit aorta. The flow field in the aorta was studied both in excised natural aortas rendered transparent to allow high speed cinematographic flow visualization and *in vivo* by high resolution pulsed Doppler ultrasound velocimetry. Numerical simulations in idealized models of arterial branching were performed to provide additional fundamental fluid mechanical insight. The specific contributions of the various studies are next described.

The topographical mapping study revealed that the density of the enhanced permeability sites is consistently highest in the region of the aortic arch, decreases as one proceeds distally reaching a minimum in the region of the intercostal arteries, and then increases again in the abdominal aorta. The region of highest site density in the arch follows a clockwise helical pattern. Outside the arch, the enhanced permeability sites occur in streaks oriented in

the bulk flow direction. The density of the enhanced permeability sites is elevated in the vicinity of aortic ostia with the region of highest density being distal to most ostia. The distribution of the enhanced permeability sites around most ostia is similar to that of early atherosclerotic lesions experimentally induced in the hypercholesterolemic rabbit. This study represents the most extensive quantitative investigation to date of the localization of focal sites in the rabbit aorta.

High speed cinematographic flow studies were performed in excised natural rabbit aortas rendered transparent to allow flow visualization. The details of the flow field in the cinematographic experiments are expected to be sensitive to the flowrates imposed through the various aortic branches. Hence, prior to performing the flow visualization experiments, these flowrates were studied in the rabbit *in vivo* using transit-time ultrasound flowmetry. These studies established that the celiac and superior mesenteric arteries receive the bulk of the aortic flow, while the other branches receive significantly less flow. An additional observation was the occurrence of reverse flow from some of the branches back into the aorta during a portion of diastole. This reverse flow may have important implications on the time-varying aortic wall shear stress in the immediate vicinity of the branches.

The measured branch flowrates were imposed on the transparent aorta preparations to visualize the flow field. Both steady and pulsatile flow experiments were performed in the aortic arch, while studies in the abdominal aorta were confined to steady flow. The steady flow results revealed a very complex flow field including regions of boundary layer separation and flow recirculation. Clockwise helical motion is present at the ventral wall of the aortic arch, and a pair of slowly-moving recirculation zones is observed lateral to most aortic ostia. Flow separation generally occurs at the entrance of aortic

branches, but the flow separation zones are most commonly occupied by helical motion originating from the lateral recirculation zones. Vessels in close anatomic proximity exhibit extensive fluid mechanical interaction resulting in very complex flow patterns. Pulsatility in the aortic arch leads to the periodic appearance and disappearance of flow recirculation zones as well as to reverse flow primarily along the lesser curvature of the arch. No generalizations can be made regarding the relative magnitudes of wall shear stress proximal and distal to ostia due to the complexity and asymmetry of the flow field. No correlation is observed between the steady flow wall shear stress behavior and the distribution of enhanced permeability sites. This study represents the most extensive investigation to date of the flow field in the rabbit aorta.

The velocity profiles in the rabbit abdominal aorta between the celiac and superior mesenteric arteries were also studied *in vivo* using a high resolution 15 MHz pulsed Doppler ultrasound velocimeter and associated perivascular probes. This region between the celiac and superior mesenteric arteries is of particular interest due to the consistent observation of a streak of enhanced permeability sites along the ventral wall within this region. Each probe was equipped with two transducers thereby allowing the resolution of the velocity vector within the measurement volume into its axial and transverse components. The results revealed the presence of large transverse velocity components indicative of extensive secondary flow motion within the aorta. The measured velocity profiles are consistent with the presence of multiple zones of helical flow within the aortic cross-section. Wall shear stresses based on the axial component of the velocity are not significantly different along the ventral, dorsal, right lateral, and left lateral walls and hence do not correlate with the localization of enhanced permeability sites. However, the presence of

extensive helical flow points to significant circumferential wall shear stresses which could not be measured in this study. The reported results provide the first *in vivo* data on the velocity profiles in the rabbit aorta.

Finally, two-dimensional finite element simulations using the computer code NEKTON were performed in an idealized model of an arterial branching. Both steady and sinusoidal pulsatile computations were performed. The results revealed important fundamental differences between steady and pulsatile flow. In particular, steady flow recirculation zones periodically appear and disappear with pulsatility. Moreover, additional recirculation zones not present in steady flow are observed in pulsatile flow. Pulsatile wall shear stresses may be significantly larger or smaller than their steady flow counterparts depending on the specific portion of the pulsatile cycle under consideration. Finally, while steady flow wall shear stresses within recirculation zones are always low, no such generalization can be made in the case of pulsatile flow.

7.2 Recommendations for Future Work

There is a number of natural extensions to the work reported in this thesis. Additional *in vivo* pulsed Doppler measurements need to be made within the other regions of the aorta. Moreover, the numerical simulations need to be extended to the three-dimensional case in order to make the results more physiologically relevant. The incorporation of aortic geometric details as well as the imposition of physiological pulsatility are examples of possible additional improvements on the computational model.

The results of this thesis suggest that the flow field in the rabbit aorta needs to be probed at a microscopic level in order to establish meaningful correlations with localized aortic wall phenomena. Two possible approaches

to accomplish this goal are suggested. The first is the performance of detailed numerical simulations which, in principle, offer arbitrarily fine spatial and temporal resolution. Hence, the formulation of a sound predictive numerical model will allow probing the hemodynamic environment at very localized levels. The more macroscopic flow field information obtained in this thesis will provide appropriate flow boundary conditions as well as important data for the validation of any such computational model. The second approach is based on the sensitivity of endothelial cell shape to imposed fluid mechanical stresses so that cell shape can be used as a local marker for the near-wall flow field in the regions of interest. This approach, however, is an indirect way of deducing the flow field and hence has limitations. In particular, various hemodynamic environments may lead to generally similar cell shapes which makes it very difficult to draw conclusions on the potential role of specific hemodynamic phenomena in atherogenesis.